DESIGNING BIO-INK FOR EXTRUSION BASED BIO-PRINTING PROCESS

A Dissertation
Submitted to the Graduate Faculty
of the
North Dakota State University
of Agriculture and Applied Science

By

MD Ahasan Habib

In Partial Fulfillment of the Requirements
for the Degree of
DOCTOR OF PHILOSOPHY

Major Department:
Industrial and Manufacturing Engineering

June 2019

Fargo, North Dakota

North Dakota State University
Graduate School

Title

DESIGNING BIO-INK FOR EXTRUSION BASED BIO-PRINTING PROCESS

By

MD Ahasan Habib

The Supervisory Committee certifies that this ***disquisition*** complies with North Dakota

State University's regulations and meets the accepted standards for the degree of

DOCTOR OF PHILOSOPHY

SUPERVISORY COMMITTEE:

Dr. Bashir Khoda

Chair

Dr. Val R. Marinov

Dr. Chad Ulven

Dr. Yiwen Xu

Approved:

July 3, 2019	Dr. David Grewell
Date	Department Chair

ABSTRACT

Tissue regeneration using in-vitro scaffold becomes a vital mean to mimic the in-vivo counterpart due to the insufficiency of animal models to predict the applicability of drug and other physiological behavior. Three-dimensional (3D) bio-printing is an emerging technology to reproduce living tissue through controlled allocation of biomaterial and cell. Due to its bio-compatibility, natural hydrogels are commonly considered as the scaffold material in bio-printing process. However, repeatable scaffold structure with good printability and shape fidelity is a challenge with hydrogel material due to weak bonding in polymer chain. Additionally, there are intrinsic limitations for bio-printing of hydrogels due to limited cell proliferation and colonization while cells are immobilized within hydrogels and don't spread, stretch and migrate to generate new tissue. The goal of this research is to develop a bio-ink suitable for extrusion-based bio-printing process to construct 3D scaffold. In this research, a novel hybrid hydrogel, is designed and systematic quantitative characterization are conducted to validate its printability, shape fidelity and cell viability. The outcomes are measured and quantified which demonstrate the favorable printability and shape fidelity of our proposed material. The research focuses on factors associated with pre-printing, printing and post-printing behavior of bio-ink and their biology. With the proposed hybrid hydrogel, 2 cm tall acellular 3D scaffold is fabricated with proper shape fidelity. Cell viability of the proposed material are tested with multiple cell lines i.e. BxPC3, prostate stem cancer cell, HEK 293, and Porc1 cell and about 90% viability after 15-day incubation have been achieved. The designed hybrid hydrogel demonstrate excellent behavior as bio-ink for bio-printing process which can reproduce scaffold with proper printability, shape fidelity and higher cell survivability. Additionally, the outlined characterization techniques

proposed here open-up a novel avenue for quantifiable bio-ink assessment framework in lieu of

their qualitative evaluation.

ACKNOWLEDGEMENTS

I would like to express my sincere gratitude to my advisor Dr. Bashir Khoda for the invaluable guidance, support, and training he provided throughout this research. It's been a privilege for me to work in advanced manufacturing lab under his guidance.

I am very grateful to Dr. Val R. Marinov for invaluable instructions, sharing knowledge on material and manufacturing, being my committee member, and reviewing this thesis.

I want to sincerely thank Dr. Chad Ulven for being my committee member, and providing valuable advice, insights, and reviewing this thesis.

I would like to thank Dr. Yiwen Xu for being my committee member, and providing valuable suggestion, insights, and reviewing this thesis.

Thanks to my lab colleague AMM Nazmul Ahsan for being supportive and collaborative in accomplishing various tasks of this thesis.

Finally, I express my deepest gratitude to my mother, father and wife for continual support, love, encouragement, sacrifice, and all the opportunities one can desire for.

DEDICATION

To my parents

TABLE OF CONTENTS

LIST OF TABLES

LIST OF FIGURES

1. INTRODUCTION

Bio-printing is a revolutionary technology which uses a three dimensional (3D) printing discipline to fabricate a 3D scaffold. In this technique, living cell is encapsulated into the bio-material and deposited layer-upon-layer [1-4]. Engineered scaffold is a highly porous 3D construct that serves as a temporary structural support for growing the isolated cells, providing nutrient to new tissues, facilitating the healing process, restoring the tissue function, and minimizing the wound scar [5]. To fabricate the engineered scaffold using bio-printing technique, appropriate bio-material selection is crucial. The selected bio-material should support certain criteria such as providing structural integrity and shape fidelity of the fabricated scaffold, facilitating cell viability and proliferation during incubation period [6]. The living cell can be encapsulated into material during fabrication of scaffold, or seeded on the scaffold after fabrication. Materials encapsulating living cell during fabrication is normally defined as bio-ink. On the other hand, materials that can be printed and subsequently seeded with cells after deposition, but not directly encapsulated with cells is defined as bio-material ink [7]. Bio-ink facilitates more cell delivery and controlled cell to material distribution compared to bio-material ink [4]. To construct the porous scaffold with well-defined pore size and geometry, porosity, pore connectivity, mechanical properties, cell viability and proliferation, the development of novel and versatile bio-inks will have crucial implications [8, 9].

Three common bio-printing strategies are commonly used to fabricate the 3D tissue scaffold and they are inkjet bio-printing [10, 11], extrusion-based bio-printing [12, 13], and laser-assisted bio-printing [14-16]. Among them, the extrusion-based system is compatible with a diverse range of materials printing including hydrogels, biocompatible co-polymers and their composition including heterogeneous bio-ink, and cell spheroid [17]. Even though the spatial

1

resolution in extrusion based fabrication system is in micron level, the shape fidelity of the printed scaffold structure is still a challenge. In other words, extrusion-based bio-additive manufacturing (bio-AM) technique often demonstrates the significant disparity between design and fabricated part due to the material characteristics. Thus, identifying appropriate biomaterials for extrusion-based bio-printing to fabricate the 3D controlled porous structure using bio-AM to ensure shape fidelity and mechanical integrity is an active area of research. A number of characteristics, i.e., biocompatibility, printability, shape fidelity, degradation kinetics, and byproducts should be considered before selecting biomaterials for scaffold fabrication [1].

Due to adjustable physical and chemical properties, hydrogels become one of the major candidates in tissue repair and drug delivery application [18]. The hydrophilic functional groups attached with the polymer enable the hydrogels to retain a high percentage (>90%) of water content and makes hydrogel especially attractive for cell delivery and encapsulation [19, 20]. Therefore, hydrogel is used to prepare the bio-ink which provides high cell density, achieves uniform cell distribution and ensures suitable microenvironment for the cell. However, achieving the intricate internal porous architecture with predefined shape, size and dimensional integrity using hydrogels material is severly limited. It is reported in several works that designing the scaffold architecture with porosity has a positive impact on the cell viability, proliferation and migration [21-25]. In terms of viability, the porous cell-laden scaffold shows more than 30% improved cell viability than non-porous scaffold [26]. Hence, the architecture of the 3D scaffold should be designed and fabricated addressing the tissue specific structural, mechanical and biological constraints [27-29]. The capability of fabricating 3D scaffold using bio-printing technique assuring uniform pore geometry with less discrepancy compared to the designed pore geometry is defined as printability [30]. Continuation of proper printability throughout the

2

whole structure i.e. shape fidelity [31] can ensure the specific geometrical, mechanical and biological constraints [32]. Selection of appropriate hydrogel during bio-printing process can ensuring the proper printability and shape fidelity of the fabricated scaffold [33]. Since, single hydrogel often struggles to achieve printability and shape fidelity, multiple hydrogels are mixed together to formulate hybrid hydrogels [34-36] for achieving the desired properties.

To achieve the proper printability and shape fidelity of the fabricated scaffold, several materials related properties i.e. rheology [24, 37], pH [38] and printing process related parameters i.e. nozzle diameter, air pressure, print speed, print distance, build plane temperature [32, 39, 40] are important as shown in Figure 1. After deposition from the nozzle tip, the filament should preserve the shape morphology having enough mechanical strength to support the forthcoming layers [41]. Proper printability of various hydrogels with extrusion-based bio-printing is associated with three main characteristics. Those are: (i) hydrogels should be highly thixotropic, (ii) it should have sufficient mechanical strength to support the printed structure and (iii) should have enough layer to layer interaction to prevent failure during and after printing [24]. Rheological properties of hydrogels i.e. viscoelasticity and yield strength are critical for providing proper extrudability, bonding between layers and supporting the self-weight [42]. Moreover, the proper controlling of shear thinning behavior of hybrid hydrogels is necessary to assure the smooth flow of materials and to retain mechanically strong filament morphology after deposition.
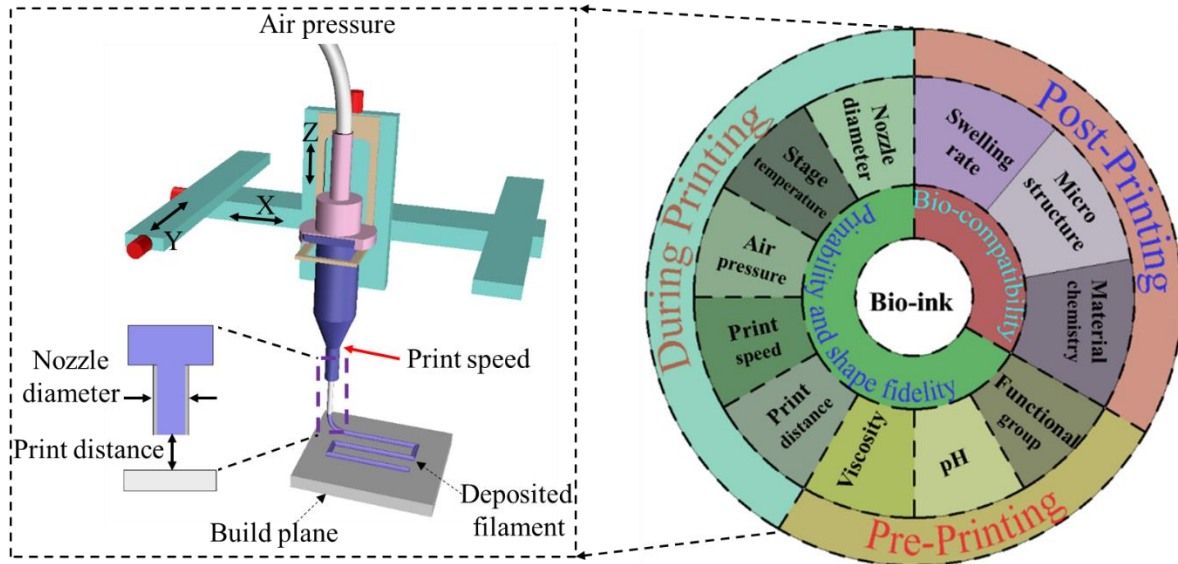
Figure 1: Various factors affecting printability, shape fidelity and bio-compatibility.

Pneumatic, piston-driven, or screw-driven system are used in extrusion based bio-printing process to exert force to release material from the nozzle [1]. In pneumatic extrusion-based system, air pressure is the most important parameter since it determines the extrusion output and defines the extruded filament width [43]. The applied air pressure should be higher than the surface tension of extrusion hydrogel. The requirement of air pressure mainly depends on the hydrogel viscosity and nozzle diameter [32, 37, 38]. Hydrogel with higher viscosity requires higher air pressure to dispense through a constant nozzle diameter. On the other hand, the width of the dispensed filament decreases with increasing the viscosity of the hydrogel with a constant air pressure [44]. Increase in viscosity increases the mechanical strength of the fabricated scaffold [45]. Therefore, to achieve a good printability and shape fidelity, viscosity plays a significant role [46].

During bio-printing process, inconsistent air pressure and print speed lead to a uncontrolled dispensing volume of hydrogel disrupting the printability [37, 38]. The filament width and pore geometry can be affected by the distance between nozzle tip and print platform.

During material deposition, change in nozzle direction may cause change in the speed (acceleration and deaccelaration) which also introduces inconsistency in deposited material geometry [32]. Temperature can also affect the printability. For an example, a temperature sensitive bio-ink (gelatin) creates nozzle clog and dispenses discontinuous filament at lower temperature which eventually leads to poor printability [47].

Another important selection criteria of bio-ink is its bio-compatibility i.e. the encapsulated cell should show viability and proliferation at the incubation or post-printing period.
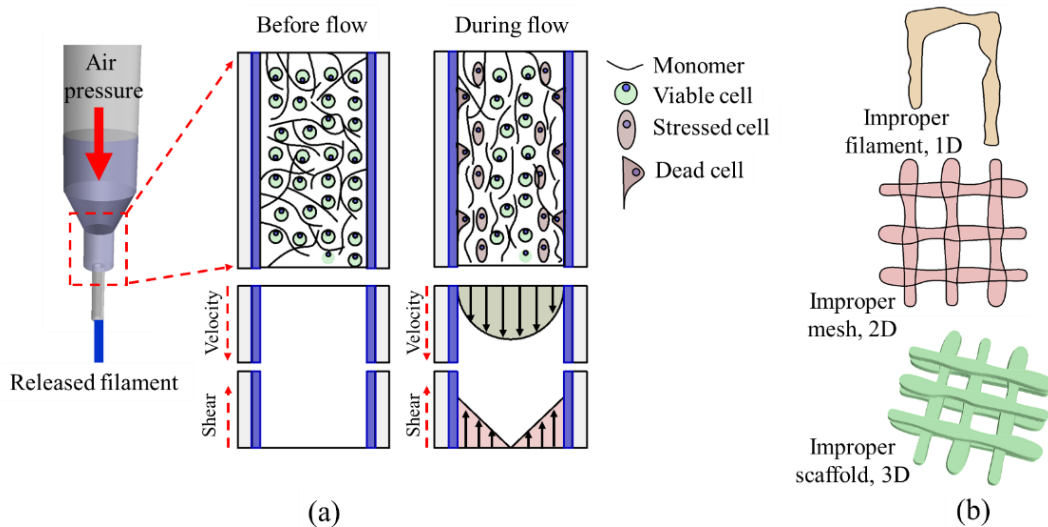
Figure 2: (a) Cell damage due to high shear stress (b) Improper filament, mesh and scaffold geometry due to low viscous hydrogel.

Even though, the extrusion based bio-printing process exerts force to release bio-ink [48, 49], the effect of this force on cell viability is overlooked often time. The biological studies show that living cells are a dynamic structure and can manipulate their growth, locomotion, and differentiation under external influence [50]. Moreover, the alteration of mechanical signals caused by changes of cell geometry can change in chemical signals that may undermine cellular development [51]. During deposition through nozzle, the encapsulated cell near nozzle wall

experiences more shear stress and results cell death as shown in Figure 2 (a). The exerted share force profile is dependent upon the nozzle geometry and can affect the cell viability [39]. Therefore, to prepare an effective bio-ink in pre-printing process, the selected hydrogel should have an optimum level of viscosity which will be able to hold the filament shape after deposition and can protect the cells from rupture. Often time, the viscosity of the hydrogel materials becomes a conflicting characteristic to achieve proper bio-compatibility. For example, the less viscous hydrogel precursor, i.e. less than 300 cps limits the mechanically stable structure [32] as shown in Figure 2 (b). Increasing the viscosity of the hydrogel ($\leq$ 100000 cps) will bring the mechanical integrity but reduces the cell viability and proliferation [52]. Thus, selection of appropriate process parameters during bio-printing is imperative to achieve the proper printability and shape fidelity of the fabricated scaffold.

1.1. Goal and aim of the research

The goal of this research is to develop a bio-ink suitable for extrusion based bio-printing process to construct 3D scaffold. The objective of this research is to design a quantifiable framework for bio-ink assessment which is highly qualitative in nature. The research will focus on factors associated with pre-printing, printing and post-printing behavior of bio-ink and their bio-logy. To accomplish the objective following tasks are performed:

Task 1: Study the bio-materials and their potentials as bio-ink.

Task 2: Establish a cell-laden bio-ink assessment protocol for extrusion based bio-printing.

Task 3: Investigate the rheological behavior of bio-materials and compositions.

Task 4: Determine the bio-printability of 3D structure through a quantitative analysis.

A bio-ink composed with a hybrid hydrogel will be identified in this research having the intention of fabricating large scaffold preserving proper printability, shape fidelity and better cell

6

viability. The extrusion-based in-house developed bio-printing system will be used in this research to fabricate 3D scaffold structure with features. Dispensing material used in this technique requires suitable viscosity and density as well as the shape fidelity retaining capability and high cell viability during and after printing [53]. A set of systematic qualitative and quantitative characterization tests such as rheological and mechanical test, microstructural test, filament collapse and fusion test, the effects of air pressure and print distance on filament width are conducted to validate printability, shape fidelity of the identified hybrid hydrogel. Moreover, the survivability of multiple cell lines e.g. BxPC3 (pancreatic cancer cell), human embryonic kidney cell (HEK 293), prostate stem cancer cell, Porc1 (functional cell) is determined into the scaffold fabricated with the proposed hybrid hydrogel at the post-printing stage i.e. at incubation period.

1.2. Overview of the research

This thesis is organized as follows: Section 2 represents the background and review of literature on scaffold based 3D bio-printing techniques and bio-materials. Section 3 describes the extrusion based bio-printing process. Section 4, 5, and 6 focus on three proposed hybrid hydrogels. Section 7 describes the overall discussion of the proposed materials. Finally section 8 concludes the work and future recommendation of this research work.

2. LITERATURE REVIEW

2.1. 3D bio-printing technologies

Tissue engineering aims to regenerate artificial organs or tissues to replace damaged or sick ones in the human body. Since this is a multidisciplinary field including medicine, engineering, material sciences, chemistry and biology, it achieves a great interest of research enlightening the hope of bridging the gap between organ shortage and transplantation requirement. In the fabricated engineered tissues and organs, cells can be used directly from the patients to regenerate the parts which minimizes the immunization and rejection concern. The fundamental steps of tissue engineering includes cell extraction, cell incubation and proliferation by 2D culture, fabrication of engineered scaffold, cell maturation in scaffold i.e. tissue generation, and implantation. Cell can be collected from blood or solid tissues. Depending on the bio-material properties, cell can directly attach with the material or the attachment can be promoted by external molecules [54]. Since cells are environment-sensitive, the cell behavior can be guided by material properties [55, 56], scaffold geometry [57, 58], surface treatment [59, 60], growth factors [61, 62], and property degradation kinetics [63, 64]. Therefore, the proper selection of candidate materials, appropriate designing of scaffold and fabrication technologies are imperative to achieve the success in tissue engineering.

To fabricate the scaffold for tissue engineering, several fabrication technologies have been developed such as solvent casting [65-67], freeze drying [68-70], gas foaming [71-73], electrospinning [74-76], and bio-printing [34, 44, 77]. However, recent development of 3D printing processes revolutionized the scaffold fabrication processes which is often called 3D bio-printing [1, 78]. Compared with traditional tissue engineering approaches, where cells are seeded after the scaffold fabrication, bio-printing enables the cell encapsulation into the

biomaterials during the fabrication. Several advantages of bio-printing are enlisted in literatures e.g. large scale fabrication of scaffold [46], precise allocation of multiple cells and biological agents [2], enabling tissue reconstruction with a high level of 3d cell density [79], incorporating the vascularization into the scaffold [2, 80].

The bio-printing process can be classified into three categories. They are inkjet bio-printing, laser-assisted bio-printing, and extrusion based bio-printing as shown in Figure 3. Depending on the nature of droplet generation, inkjet bio-printing is classified as continuous inkjet-based bio-printing and drop-on-demand inkjet-based bio-printing where it delivers controlled volume of liquid to predefined location [81, 82] as shown in Figure 3(i). This printer produces pulses of pressure using heat that forms the droplet around 50-300 μm from the nozzle [83]. Some advantages of inkjet printer are high print speed, low cost and wide availability.. However, low droplet directionality, risk of heat exposed with cell and biomaterial, mechanical stress on cell, frequent clogging of nozzle are considerable disadvantages of this printer to use in bio-printing [1].

Laser-assisted bio-printing (LAB), which is less common compared to other two bio-printing strategies, is increasingly being used for tissue engineering as shown in Figure 3 (ii). A typical LAB consists of pulsed laser beam, focusing system, a ribbon, and a layer of biological material. This strategy is not using nozzle, therefore there is no nozzle clogging and it can print mammalian cell with negligible effect on cell viability [84-86]. However this has some drawbacks such as lower gelation kinetics, complex ribbon preparation process for different material, difficult to target the accurate cell position, and finally the metallic residues are presented in the final construct due to vaporization of metallic laser-absorbing layer during printing [1].

In extrusion-based bio-printing, material is deposited on a substrate parallel to XY plane following a vectorized tool-path and the subsequent z-axis movement ensures the progressive build height of the construct. Various materials are compatible with this printing techniques including hydrogels, biocompatible copolymers, and cell spheroid [17]. Two most common methods named pneumatic [39, 43, 87] and mechanical (piston and screw) [88, 89] are used to deposit the materials as shown in Figure 3 (iii). Though mechanical dispensing system has more direct control over pneumatic, pneumatic has simpler drive-control mechanism. Wide range of biomaterials, viscosity range from 30 mPa/s to 6×10^7 mPa/s are suitable for pneumatic extrusion system [90]. High viscous material gives structural support to the construct where low viscous materials maintain the microenvironment for high cell viability. The main advantage of extrusion-based bio-printing is maintaining high cell density which is one of the challenges in other bio-printing modal [1]. Sometimes multi-cellular cell-spheroids are deposited and controlled to self-assemble into the required 3D structures [91, 92]. The wide range of cell type has been printed with extrusion based system and cell viability has been reported from 40-86% [93]. The lower viscous material and bigger nozzle size may increase the cell viability [39, 94]. However bigger nozzle diameter restrict the resolution of the printing, which may be important for mimicking the native tissue structure. With the improvement of dispensing system (i.e. nozzle, chamber or motor-control system) as well as designing of new material system might ease these challenges [89]. The aforementioned advantages of extrusion-based bio-printing technique and potential to improve this technique encourage us to choose this technique as our fabrication tool. The overall steps of 3D bio-printing process for tissue regeneration is shown in Figure 3.
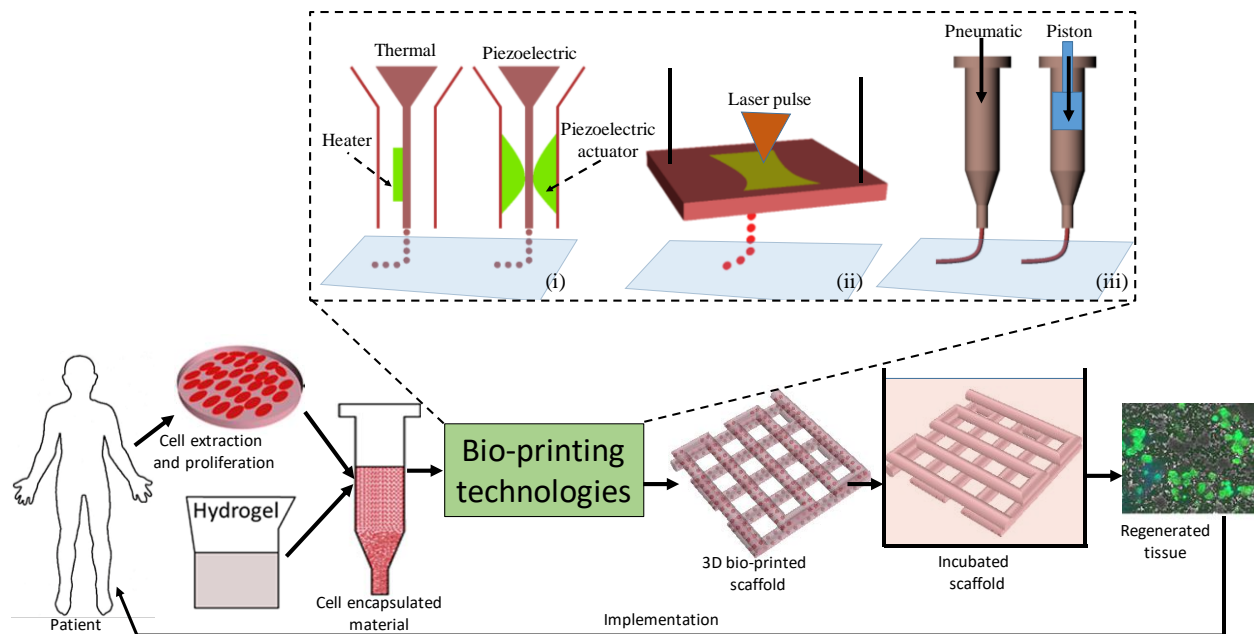
Figure 3: Overall steps in 3D bio-printing process and tissue engineering.

It is challenging to maintain the cell viability for a longer span time. In the current state-of-art, the cell viability is tested for a short range of time frame i.e. from few hours to couple of days [39, 95, 96]. In addition, due to the lack of mechanical integrity, the soft printed scaffolds dissolve in a short time through hydrolysis process [91, 96, 97] . Therefore this is really a big challenge to fabricate human scale tissue construct using the bio-printing process. The proper selection of biomaterial and process plans may help to fabricate thicker tissue construct.

2.2. Bio-materials for 3D bio-printing

In the literature, biomaterials are defined as "any substance (other than a drug) or combination of substances, synthetic or natural in origin, which can be used for any period of time, as a whole or part of a system, which treats, augments, or replaces any tissue, organ or function of the body" [98]. A major challenge in extrusion-based bio-printing is to identifying appropriate material from a limited bio-material pool [43]. Materials selected for bio-printing should maintain or induce the desired function of the incorporated cell. Functions including

11

interaction with endogenous tissues and immune system, supporting appropriate cellular activity followed by facilitation of molecular or mechanical signaling systems are strictly important for successful transplantation and function [99]. Most importantly, these materials must support the cellular attachment, proliferation and micro-environmental function [18]. Therefore, a pilot test of biocompatibility can be done prior to heading bio-printing process, which will warrant the material functionality into fabrication process.

In extrusion-based system, material pushed through the nozzle in semi-solid or gel state. Once extruded through the nozzle, the material must regain its shape. The desired transformation can occur via additives (e.g. cross-linker [100] and gelling agents [39]) or via external stimulus (e.g. UV exposure [101], humidity and temperature [96]). . For cell-laden material printing, materials that requires excessive form of stimulus (e.g. high or low temperature) or non-bio-compatible additives (e.g. toxic binder or solvent) for transformation critical point drying should be avoided [43]. Below is a chart (Figure 4) that shows the list of polymeric material (both natural and synthetic) that satisfies the stringent requirement of bio-materials[1, 43].
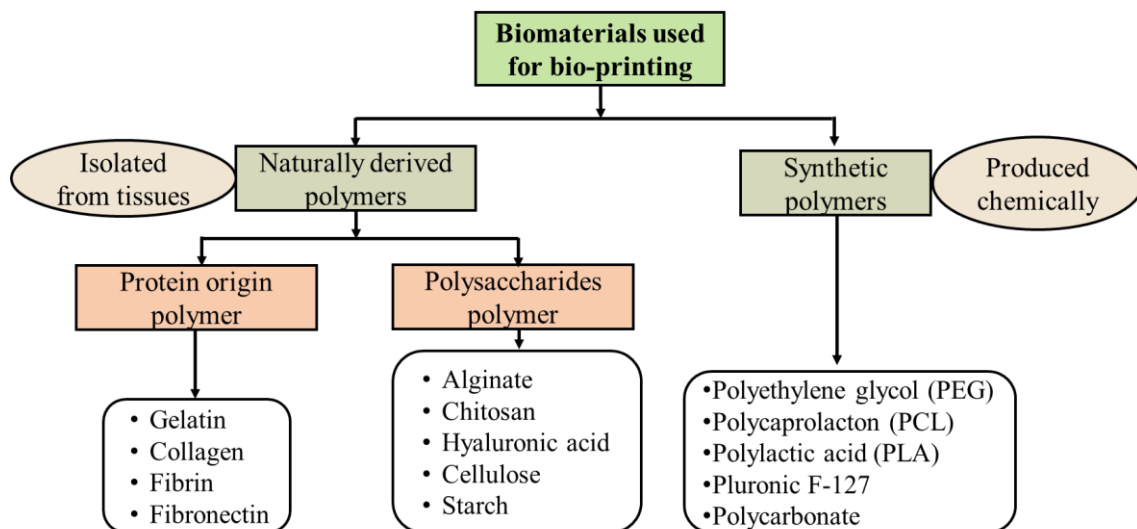
Figure 4: Biomaterial used for bio-printing.

Naturally derived polymers exhibit advantages for 3D bio-printing due to their similarity to human extra-cellular matrix (ECM) and their inherent bioactivity. On the other hand, synthetic polymers can be tailored to specific physical properties for stimulating particular cell/tissue activities. Even though, material presented in Figure 4 displayed cell viable characteristic, but their performance as bio-material varies in areas such as biocompatibility, byproducts produced and loss of mechanical properties during degradation.

To maintain the cell viability, the degradation kinetics of the materials must be understood and controlled. Among a several aspects, the degradation rate of the materials should be matched with the cell ability to replace the materials with the ECM. This is really challenging to match the degradation rate of a specific material with various cells and vice versa. Moreover, the byproduct of the material should be non-toxic, readily metabolized and rapidly cleared from the body because they often direct the biocompatibility of any degradable material. The toxic byproducts can include small proteins and molecules, non-physiological pH, increased temperature or other detrimental factors on cell viability.

Additionally, the physical changes in materials i.e. swelling and contractile generate from extrusion process needs to be study [102]. Materials with high swelling rate can potentially absorb the fluid from surroundings and their contractions may close the pores or vessels that are necessary for cell migration and nutrients delivery. It becomes more challenging when multiple materials come into action having various swelling and contraction rates. To mimic the native tissue, the incorporated endogenous and exogenous cells should be attached, migrated, proliferated and functioned into the bio-printed construct. Several works have been published demonstrating the effects of materials on cell attachment [84, 103], cell sizes and shape [104].

13

Moreover, the addition of external ligands on the material substrate has potential to increase the cell attachment and proliferation [103].

The categories of bio-material can be generalized as i) cell-laden biomaterial i.e. bio-ink and ii) acellular biomaterial ink [7]. Printing with bio-material (non-living) is commonly used to create acellular porous 3D scaffolds in which post-fabrication cell seeding is performed. Building a tissue construct with cell-laden bio-ink is relatively new strategy [105, 106]. The exerted force on the material to extrude through the nozzle are generated with pneumatic [39, 43, 87] or mechanical via piston and screw [88, 89] system. Finally, crosslinking agent, temperature or photo initiator curing is commonly applied on bio-ink for making the 3D scaffold structures. The printing parameter, as well as material preparation, can be significantly different based on the bio-ink. For example, exerted energy (i.e., pressure, temperature) on cell-laden bio-ink during printing needs to be lower for maintaining cell viability [107]. These materials can be classified further as shown in Figure 5 and reviewed accordingly in the upcoming five subsections from 2.2.1 to 2.2.5.
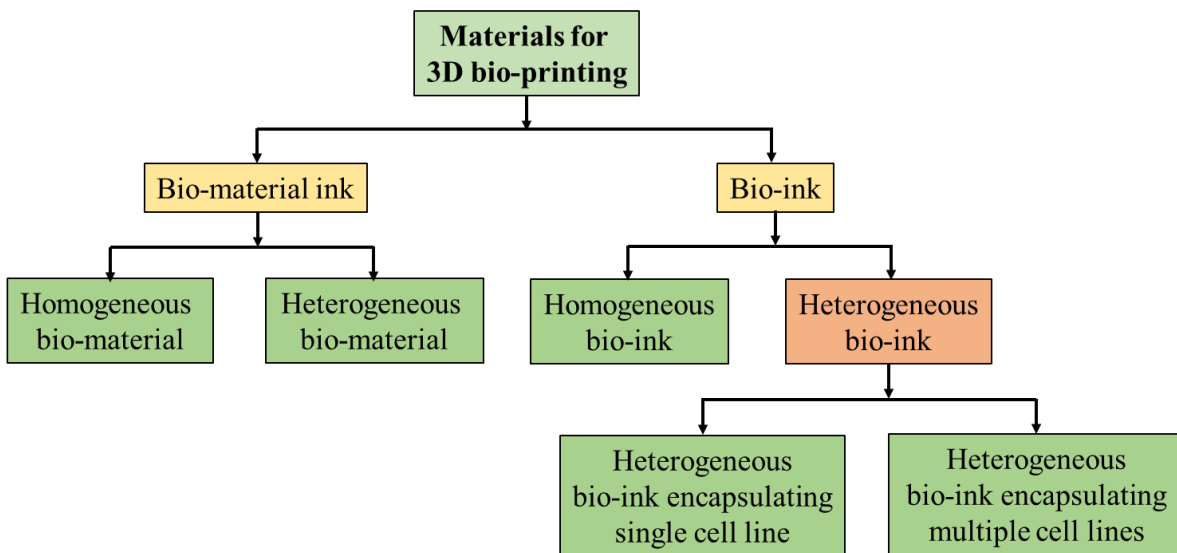
Figure 5: Classification of bio-material and bio-ink.

2.2.1. Homogeneous bio-material

Several works have been published to demonstrate homogeneous material scaffold fabrication. The porous cell free scaffold provides the inhabitation of seeded cell for necessary nutrient and metabolic transport without significant compromising of mechanical stability of the scaffold. Moreover, the proper degradation rate of the scaffold material with respect to the new matrix production of the tissue will allow the successful tissue regeneration. To analyze the degradation of the fabricated scaffold over time, PLA was casted into the polydimethylsiloxane (PDMS) molds [9]. In the same study, alginate is used to fabricate a lumber vertebra model to demonstrate the effect of the internal architecture on fluid flow. Alginate has also been used to demonstrate to fabricate functionally gradient variational porous scaffold architecture [5, 108, 109]. PCL is one of the frequently used synthetic polymers in bio-printing, mainly targeted for bone tissue regeneration application [110-112]. Poly (ethylene glycol) (PEG) micro-gel has been used to fabricate degradable scaffold to deliver bioactive nerve growth factor [113]. Various natural polymers e.g. collagen, agar and synthetic polymers e.g. Poly-l-lactic acid (PLLA), poly (glycolic acid) (PGA), have been used as scaffold material to fabricate soft and hard implants using 3D bio-printing technique [114]. A non-exhaustive list of bio-polymer that have been used for tissue engineering are listed in the Table 1. However, to analyze the combined effect of various materials into the solution, multiple materials are mixed together i.e. hybrid material to fabricate the cell free scaffold.

Table 1: Synthetic polymers used for tissue engineering.

Polymer	Application	References
Poleanhydride	Bone, controlled drug release	[115-117]
Polycarbonate	Bone, degradable fixation device, controlled drug release	[118, 119]
Ployfumarate	Bone	[120]
Poly (lactide-cogycolide) (PLGA)	Bone, drug delivery	[121-124]

2.2.2. Heterogeneous bio-material

To achieve the desired properties e.g. mechanical strength, layer-to-layer adhesion, better rheological property, multiple bio-materials are mixed together which are defined as heterogeneous bio-material here. After fabricating the scaffold, live cell are seeded on the scaffold to determine the cytotoxicity of the structure. A hybrid scaffold has been fabricated using PCL and alginate to ensure the mechanical strength of the construct and better biological properties [125]. In another work, alginate was mixed with acrylamide to fabricate the cell free scaffold to perform the mechanical strength of the fabricated scaffold [126]. Co-polymer of poly(ethyleneglycol)-tetraphthalate/poly(butylene terephthalete) (PEGT/PBT) has been used to fabricate engineered cartilage and later bovine articular chondrocytes cell was seeded into this construct [127]. Gelatin, lysin and polyurethane (PU) were used together and liver cells were seeded to demonstrate the regeneration of implantable liver tissue [128]. PCL-HA matrix was used to fabricate the bone construct and hMSC cell was seeded into this fabricated scaffold [110]. To demonstrate the influence of porosity, molecular network mesh size and swelling in aqueous media, scaffold is fabricated using poly(ethylene oxide terephthalate)-poly-(butylene terephthalate) (PEOT/PBT) [129]. A prefabricated PCL scaffold was immersed into chitosan and hyaluronate solution to fabricate PCL/chitosan and PCL/hyaluronate hybrid scaffold and

chondrocytes were seeded into this construct for further analysis [130]. Alginate scaffold was prepared by coating it on 3D printed PCL scaffold and later hUCS was coated on the alginate scaffold to demonstrate the enhanced osteogenesis [131]. A 3D anatomical data-based rabbit femoral scaffold was fabricated using PCL/HA composite and the mechanical test was performed afterward [132]. Poly (ethylene glycol) diacrylate (PEGDA) and acrylic acid (AA) have been used as scaffold material where PEGDA served as cross linker and AA used for absorbing protein [133]. To enhance the mechanical strength of cartilage scaffold, cellulose nano-crystal (CNC) was reinforced into PCL/chitosan matrix. The overall tensile strength of the scaffold was improved significantly using this composition [134]. Chitosan was also mixed with hydroxyapatite and alginate to prepare the scaffold and MC3T3-E1 and hASC cells were encapsulated respectively to demonstrate the fabrication of bone and damaged tissue [135, 136]. Alginate and gelatin have been used in several works to fabricate cell free structure and later cell has been seed on the scaffolds [137, 138]. However, to increase the cell density and proper distribution of cell into the material, various types of cell have been encapsulated into the biomaterials to fabricate the cell-laden scaffold.

2.2.3. Single-material bio-ink

The mostly used homogeneous material encapsulating single type cell is alginate. Hepatocytes cells were mixed with alginate and bio-printed the scaffold to exhibit the potential of the fabrication of micro-organ [139]. To accommodate the fast gelation and slow degradation kinetics, various cell lines are encapsulated with alginate to fabricate the cell laden scaffold [140-142]. To demonstrate the direct bio-printing of implant, articular chondrocytes [143] and rat heart endothelial cells (RHECs) [52] were seeded into alginate and fabricated the scaffold. However, due to the poor mechanical properties and scarcity of cell adhesion site, other

biomaterials are mixed with alginate to improve the mechanical integrity and better cell survivability. Recently a work has been published where several single material bioink e.g. agarose, alginate, gelatin methacryloyl (GelMA) and poly (ethylene glycol) methacrylate (PEGMA) are used with single type mesenchymal stem cells (MSCs) to fabricate fibrocartilage and hyaline cartilage. Among them alginate and agarose hydrogels support the development of hyaline-like cartilage where GelMA and PEGMA support to develop more cartilage-like tissue [144]. A work related to direct printing of cartilage tissue using Poly (ethylene glycol) dimethacrylate (PEGDA) with human chondrocytes has been reported to repair human cartilage repair [82]. Human articular chondrocytes cell has been encapsulated into PEGDMA (polyethylene glycol di-methacrylate) solution to prepare the bio-ink and scaffold has been fabricated to demonstrate the regeneration of human cartilage. Gelatin methacrylamide along with two photon-initiator was used to encapsulate the HepG2 cell to prepare the bio-ink. This work demonstrated the effect of bio-printing process parameters and scaffold fabrication pattern on overall cell viability. Scaffold having higher cell viability showed the expression of liver specific functions [145]. In another work, brain cell is mixed with gelatin and a 3D model is fabricated using the bio-printing technique to establish the regeneration of injured nerve tissue [146]. However, the overall result showed that the combination of gelatin and hyaluronan has better potential than only gelatin to regenerate the nerve tissue. HUVEC cell is encapsulated with gelatin to regenerate hollow tube to facilitate the vascularization [147]. However, often time multiple materials are mixed together as heterogeneous material and single type cell is encapsulated to identify the effect of hybrid material composition on the overall mechanical integrity of scaffold and cell activity.

2.2.4. Heterogeneous bio-ink (multiple bio-material) encapsulating single cell line

Several works have been published where authors encapsulated single cell line into multiple material composition to execute the fabrication of cell-laden scaffold. Most recently, one of the widely reported hybrid hydrogels is alginate-gelatin which shows better achievement of scaffold architecture and improved cell bio-activity [6, 44, 148-150]. Alginate and gelatin are also mixed with different types of material to prepare the hybrid hydrogel and encapsulated with single type cell to accomplish various applications as enlisted in Table 2.

Two different types of lung cancer cells e.g. A549 and 95-D have been used separately in the matrix of alginate and gelatin and demonstrates the possibility of tumor model regeneration to explore the cancer treatment [166]. Recently, a hybrid hydrogel containing alginate, methyl cellulose and laponite nano-clay is used with human mesenchymal stem cell line to validate the cytotoxicity of this hybrid hydrogel [46]. To identify the effect of 3D bio-printing process parameters on fabricated scaffold, mouse embryonic stem cell (ESC) has been encapsulated into alginate and gelatin and dispensed [6]. Chitosan grafted with lactic acid and methacrylate initiator has been used to encapsulate the chondrocytes cell to fabricate the scaffold. A covalent cross-linking technique and enzymatic degradation mechanism have been used during printing process and in incubation period respectively [167]. Gelatin and chitosan were mixed together to prepare the hybrid hydrogel and hepatocytes were encapsulated to analyze the biological function of the cell and their potentials to regenerate the artificial liver tissue [168]. Cinnamon basil plant cell has been used with alginate, agarose and methylcellulose matrix to simulate an immobilization environment to identify the capability to produce the secondary metabolites in-vitro [169]. Mouse fibroblast cell has been used into alginate and gelatin mixture to fabricate high resolution 3D cell-laden scaffold to explore the cell activity into the structure [148].

19

Table 2: Various materials mixed with alginate and gelatin encapsulating single type cell.

Material	Other materials mixed	Cell type encapsulated	Application	References
Alginate	RGD, PEGMA, GELMA	Chondrocytes	Engineering of whole bones for orthopedic and craniofacial medicine	[151]
	Nano-cellulose	Human nasoseptal chondrocytes (hNC)	Growth of cartilage tissue	[152]
	PCL, growth factor	Chondrocytes	Regeneration of cartilage tissue	[153]
	Oxidation, RGD	hADSC	New tissue regeneration	[154]
	Methyl cellulose	hMSC	Large scaffold fabrication	[155]
	Agarose, gelatin	SaOS-2	Bone tissue regeneration	[29]
	Fibrinogen, gelatin	HeLa	Tumor model	[156]
	Collagen, PCL	MSC	Bone tissue regeneration	[157]
	PCL	Primary chondrocytes	Cartilage regeneration	[158]
	Acidic media, agarose and methylcellulose	Bone marrow stromal cells (BMSCs)	Bone tissue regeneration	[159]
Gelatin	Fibrinogen,	Hepatic cell	Functional proliferation and liver-specific functions	[160]
	Nano-silica	MC3T3 preosteoblasts	Bone tissue regeneration	[161]
	PCL, fibrinogen, hyaluronic acid and glycerol	human amniotic fluid-derived stem cells (hAFSC)	Bone, cartilage and skeletal muscle tissues	[162]
	Alginate, hydroxyapatite	hMSC	Drug delivery, microsphere deposition or soft tissue engineering	[163]
	Alginate, RGD	MG-63		[164]
	Hydroxyapatite	Chondrocytes	Regeneration of cartilage tissue	[165]

By blending the thermos-responsive polymer poly(N-isopropylacrylamide) grafted hyaluronan (HA-pNIPAAM) with methacrylated hyaluronan (HAMA), high-resolution scaffolds with good viability of bovine chondrocytes were printed [170]. A 3-D printable formulations of

hybrid hydrogels were developed, based on methacrylated hyaluronic acid (Me-HA) and methacrylated gelatin (Me-Gel). The formulated bio-ink was used to bio-print heart valve conduits containing encapsulated human aortic valvular interstitial cells (HAVIC) [171]. After seven incubation days, the encapsulated HAVIC showed enhanced production of collagen and glycosaminoglycan, indicating ECM remodeling. Electro-spinning of PCL fibers was combined with printing of rabbit elastic chondrocytes encapsulated in a fibrin-collagen gel and the scaffold was able to produced cartilage extracellular matrix even in vivo [172]. However, native tissue contain multiple cell type and mimicking the functional tissue regeneration, multiple cells are encapsulated to achieve the combined effect of each cell which is discussed in the next section.

2.2.5. Heterogeneous bio-ink (multiple bio-materials) encapsulating multiple cell lines

Fabricating and recapitulating a tissue construct like the native tissue microarchitecture comprising the multiple cell types along with multiple extra cellular matrix components still remain challenging [173]. Alginate and gelatin are commonly mixed to prepare the hybrid hydrogel and encapsulated with multiple type cells to accomplish various applications as enlisted in Table 3. Two different cell lines SaOS-2 and RAW 264.7 are encapsulated into alginate-silica composite to demonstrate the programmable bio-ink preparation [180]. GelMA, alginate, and poly (-ethylene glycol)-tetra-acrylate (PEGTA) were used with endothelial and stem cell to demonstrate the tissue scaffold fabrication with vascularization [2]. In another work, human umbilical vein endothelial cells (HUVEC) and hiPSC-cardiomyocytes were encapsulated into GelMA, alginate and photoinitiator Irgacure 2959 to demonstrate the fabrication of cardiovascular tissue [181]. Porcine aortic valve interstitial cells (VIC) and aortic root sinus smooth muscle cells (SMC) cells were encapsulated into alginate and gelatin to exhibit the in-vitro fabrication of aortic valve [95].

Table 3: Various materials mixed with alginate and gelatin encapsulating multiple type cell.

Material	Other materials mixed	Cell type encapsulated	Application	References
Alginate	PCL	Osteoblasts and chondrocytes	Regeneration of cartilage tissue	[174]
	Nano-cellulose	Articular cartilage and medial condyle	Growth of cartilage tissue	[175]
	Fibrin	Functional and HUVEC	New tissue regeneration	[176]
	Carboxymethyl-chitosan, agarose	hESCs and hiPSCs	Artificial 3D neural tissue	[177]
	Collagen, fibrin	C2C12 and MC3T3	Mechanically robust and complex scaffold fabrication	[178]
	PEGDA, nanoclay	hMSC, HEK	endure high stress in both tension and compression	[49]
Gelatin	Polyethylene glycol, fibrinogen	hMSC, HUVEC	Tissue regeneration with vascularization	[179]
	Methacrylate, photo initiator	MC3T3, HUVEC	Microchannel to facilitate vasculature	[80]

PCL and PEGDA were used as supportive material and collagen type 1 was used as hydrogel material along with encapsulating HUVEC and mouse mesenchymal stem cells to fabricate the hybrid tissue construct [182]. HUVEC and hMSC cells were encapsulated into multifunctional PEG (PEGX)-gelatin bio-ink to mimic the tissue more close to native one. Taken together, this hybrid hydrogel was a facile and effective approach for obtaining desirable bio-ink characteristics without compromising cell viability. The result showed that hMSC approached towards skin like tissue reconstruction [179]. Another hybrid hydrogel was formulated with gelatin, fibrinogen, HA and glycerol with different weight percentages for encapsulating various cells e.g. human AFSC, chondrocytes, and C2C12 to demonstrate the reconstruction of bone, cartilage and skeletal muscle [183]. To establish the extrusion into the hydrogel support bath, a

novel bio-ink was developed containing carbopol and irgacure and HAECs, MDCK and MCF10A cells were encapsulated into the bio-ink. After fabrication, the support bath was removed to leave the scaffold containing multiple cell [184].

From the above discussion it is clear that, bio-ink prepared with hybrid hydrogel may bring advantages over bio-ink prepared with single hydrogel but become a delicate process. Even though, various biomaterial inks and bio-inks are developed with hybrid hydrogel for bio-printing process, the bio-ink assuring proper printability, shape fidelity for large scale scaffold (cm scale) and cell survivability into the printed scaffold for a longer period (more than 15 days) of time is still challenging. Moreover, controlling the cell proliferation direction with bio-ink component in extrusion-based bio-printing is still not explored. In this research, a hybrid hydrogel will be developed which will assure the proper printability, shape fidelity for large scale scaffold and cell will be safely encapsulated for a longer period of time. This research will also explore the controlling of cell proliferation direction using appropriate bio-ink component.

2.3. Printability and shape fidelity

2.3.1. Material properties affecting printability and shape fidelity

Printability is an important concept as the fabricated scaffold of the bio-printing process must mimic both the cellular architecture and geometry [185]. To fabricate a tissue scaffold with intricate architecture, this is particularly important. Geometry is as important in tissue structure as its function. For an example, heart valves have to be durable whilst allowing appropriate blood flow at varying valvular pressures. For this reason, spatial and mechanical heterogeneity is needed. Understating the importance of printability and shape fidelity, a number of works have been published in recent past. Recently, few bio-ink papers have characterized their hydrogels

23

for printability with any of the suggested standardized methods, which include viscosity/shear thinning [8, 186], yield strength [187], recovery [186, 188].

Thixotropic Hydrogels may provide sufficient mechanical strength to support the printed structure and layer to layer interaction to prevent failure during and after printing [24]. Rheological properties including viscoelasticity and sufficient yield strength, the hydrogel may produce proper extrudability, binding of consecutive layers together and supporting the weight of deposited layers [42]. Moreover, to assure the smooth flow of materials and mechanically strong morphology after deposition, the proper controlling of shear thinning behavior of hydrogels is necessary. These rheological properties in general are linked and cannot be verified separately [189]. Achieving predefined shape, size, dimensional integrity and intricate internal porous architecture i.e. good shape fidelity using single material is limited due to its viscosity. Hence, multiple materials are mixed together to prepare hybrid hydrogel to assist large scale scaffold fabrication [46, 95, 131, 155, 190, 191]. The hybrid hydrogel enables to achieve physical gelation characteristics and uniform filament morphology after extrusion to support the successive layers. Besides, the mixing of multiple biomaterials may offer more suitable cell-friendly microenvironment to support and improve various cell activities, i.e., proliferation, migration and differentiation [6]. Carboxymethylcellulose (CMC) [34], methyl cellulose [24, 155], TEMPO-mediated nano fibrillated cellulose (TO-NFC) [192], gelatin [193], nano clay [46] have been used as viscosity modifier to prepare a hybrid hydrogel and improve printability.

The printability and shape fidelity of a hybrid hydrogel is defined by the material loss modulus and a predictive air pressure model is developed in term of loss and storage modulus [33]. They demonstrated that the lower loss modulus can define good printability. Recently in another work, the printability of HA based hydrogel precursor is determined based on yield

stress, viscosity and storage modulus [194]. This work has shown that, the higher molecular weight with lower concentration of hydrogel provides better storage modulus and eventually better printability. The yield stress is one of the most important parameters to characterize because a yield stress is required for a material to hold its shape after bio-printing and support the weight of the added layers. The printability of a synthetic polymer (poloxamer) has been determined by yield stress and it is stated that this material shows good printability at the yield stress value around 300 Pa [188]. In another work, the printability of collagen hydrogel was determined by the riboflavin photo-crosslinking and pH. This study showed that riboflavin increased the storage modulus of the hydrogel but the degree of enhancement was less pronounced at higher collagen concentration. The higher value of pH also increased the printability and shape fidelity of the hydrogel in this work [195]. The mechanical properties and eventually the printability of single filament fabricated with dECM was tailored by vitamin B2 and UVA irradiation [196]. This works showed that the inclusion of vitamin B2 with dECM increased the rheological stiffness. However, the increased amount of vitamin B2 decreased the rheological stiffness due to aggregation of this element to form photo-inactive aggregates. To improve the printability, alginate was mixed with genetically engineered M13 phages which includes the integrin-binding and calcium-binding domains. Hence, the shape fidelity of the fabricated filament was preserved better during crosslinking and in incubation period for a longer period of time [197]. There are other methods of quantifying the printability and shape fidelity such as using image analysis of software to measure pore area, circularity of pore [6], strut size [198], print area [199], and filament fusion and collapse [31].

2.3.2. Dispensing factor affecting cell viability and printability

The effects of several dispensing factors shown in **Figure 1** have been studied in various works. During, extrusion-based strategy, the dispensing pressure is applied to deposit the cell-laden filament through nozzle orifice by pneumatic and mechanical assistance (as referred earlier), thereby the effects of dispensing pressure and nozzle diameter on the cell viability needs to be identified. Even though, the mechanical effects on cell viability is not considered, the biological studies show that living cells are dynamic structure and manipulate their growth, locomotion, and differentiation under external influence [50]. Moreover, the changes of cell geometry can alter the mechanical signals which may cause the change in chemical signals and subsequently undermine cellular development [51]. Specifically, the reduction of syringe nozzle diameter and increasing the dispensing pressure will increase the shear force on the cell during deposition and reduce the cell viability. Moreover, the cell inside the solution may experience additional compressive or tensile forces due to the nozzle head movement with respect to substrate. The outcome of the experiment may vary with respect to different time frames i.e. short term (hour) and long term (day) [39]. However, material, stage temperature and nozzle speed effects have not been studied i.e. at room temperature a single material (sodium alginate) is used. Others reported the effect of extrusion pressure, nozzle speed along with humidity and stage temperature [96]. The viability of cell is significantly increased when material was deposited on bed in room temperature applying humidity comparing with the deposition on hot bed without employing humidity. Nonetheless, the material effect has not been considered (only collagen is used) in this experiment. In another work, a framework of determining the optimum process parameters has been proposed for alginate and gelatin hydrogel encapsulating mouse embryonic stem cell (ESC) [6]. A set of shape fidelity and printability experiments has been

26

done to design a candidate material for 3D bio-printing. The related process parameters have been determined on cell free scaffold [31].

In this research, different dispensing factors such as nozzle diameter, nozzle speed, dispensing pressure, print distance with various biomaterials is studied at different time frame to increase the cell viability. This study anticipates an effective improvement in bio-printing horizon and finally in overall 3D printed engineering tissue scaffold.

2.4. Vascularized tissue scaffold

The capability to fabricate 3D vascularized tissues on demand would enable scientific and technological advances in tissue engineering, drug screening and organ repair. Several key components e.g. cell, extra cellular matrix (ECM), and vasculature need to be patterned in precise geometries to generate 3D engineered tissue constructs that mimic the native grafts and eventually the organs. Each of these elements imprints vital role in imparting, supporting, and sustaining the biomimetic function of the engineered tissue construct, respectively. Among them perhaps vasculature plays most important role as they provides sufficient nutrients, growth/signaling factor, waste transport. Without the proximity to a perfused microvasculature; most cell within the bulk tissue will not remain viable. The structure of vascular tube is formed consisting of three different layers named intima contains a monolayer of endothelial cell, medial layer contains a multiple layers of smooth muscle cells (SMCs) and adventitia contains fibroblastic cells [200]. A recent work has been published demonstrating the effects of microchannel into the cell-laden tissue structure [80]. The microchannel was bio-printed using the agarose and the cell-laden hydrogel consisted of other types of photo-cross-linkable polymers e.g. GelMA, SPELA, PEGDMA and PEGDA was casted upon of these microchannel. The bio-printed agarose was aspirated by light vacuum or removed manually to get the microchannel.

The cell viability of tissue structure embedded with microchannel was almost 90%, which was greater than the construct without microchannel (77%). Recently, a heterogeneous bio-printing process has been demonstrated where two different types of cell line, Human Neonatal Dermal Fibroblast (HNDFs) and 10T1/2 mixing into GelMA are deposited along with pluronic F-127 into pure GelMA solution [201]. Pluronic F-127 is liquefied and removed from the construct, which imprints the vasculature to assist different growth factors and nutrients to flow. These cell-laden bio-printing process shows 81% and 82% cell viability for HNDF and 10T1/2 cell lines respectively. Another work has been published demonstrating the bio-fabrication of functional vascular channels where the collagen and cell-laden gelatin were deposited. Once the HUVEC cell was attached with the inner surface of collagen, the gelatin was washed out to generate the vascular channel [147]. This process showed almost 90% cell viability. However, the cell-free gelatin deposition to make vascular channel and later injecting cell increased cell viability due to less mechanical stress on cell, higher cell density and less encapsulation of gelatin. A heterogeneous printing process using PCL/alginate struts coated by osteoblast-like cell-laden alginate has been demonstrated to maintain the mechanical strength of the fabricated scaffold [191]. Compared with non-coated alginate, the proposed construct shows more cell viability (almost 93%) and good alkaline phosphatase (ALP) activity. This work demonstrates the optimum alginate-calcium chloride mixing ratio to get suitable coat-ability.

Recently, a single nozzle extrusion based heterogeneous bio-printing technique has been published where HUVEC cell-laden alginate/GelMA hydrogels are deposited simultaneously with Ca^{2+} crosslinking solution [202] . The GelMA is cross-linked by UV light. The appropriate concentration of Ca^{2+} (0.3M) solution and amount of exposure time (30 s) of UV light, suitable for cell viability (almost 80%) are reported here. This work concluded with the possibility of co-

culture by seeding primary cardio-myocytes on top of the heterogeneous bio-printed tissue. However, due to the free radical produced by photo-initiator, high stiffness of cross linked material, prolonged exposure of UV undermine the cell viability. Other than printing the microchannel and removing later, a perfusable vascular construct fabrication has been demonstrated where a novel blend of ink consisting of GelMA, alginate and PEGTA has been developed [2]. HUVEC and MSC cell-laden ink is deposited through a co-axial nozzle containing concentric channel to create continuous hollow interiors. The result (80% cell viability) demonstrates the endothelial proliferation and ultimately the vasculature channel into the tissue. However due to the degradation of GelMA component of proposed ink, it was difficult to maintain the perfusability more than 21 days. Another work related to built-in microchannel to deliver nutrients has been published where a co-axial nozzle has been used to deposit L929 cell-laden alginate as scaffold material and $CaCl_2$ as cross-linker. The greater cell viability of the scaffold having built-in micro-channels compared without micro-channel illustrates the significance of vascular channels [203]. Hence, to regenerate the tissue, proper vasculaturization into the scaffold is important.

2.5. Remarks

The above discussion clarifies that even though extrusion-based bio-printing has good potential on in-vitro tissue fabrication, the related material design, geometry of the fabricated scaffold, determining optimum process parameters, and vascularization are important to successfully fabricate the thick tissue scaffold. Among them, the designing of an appropriate bio-ink for extrusion based bio-printing and related printing process parameters will be focused in this research.

3. EXTRUSION BASED BIO-PRINTING: EQUIPMENT AND PROCESS PLAN

3.1. Extrusion based bio-printer

Extrusion-based bio-printing systems basically rely on dispensing of larger polymer or hydrogel strands through a dispensing micro-nozzle and positioning them via computer-controlled motion either of the printing heads or collecting stage. To accomplish bio-printing using this technique, polymer or hydrogel is generally loaded in metallic or plastic barrel and dispensed via either pneumatic, piston-driven, or screw-driven force on a building platform as shown in Figure 6 (b).
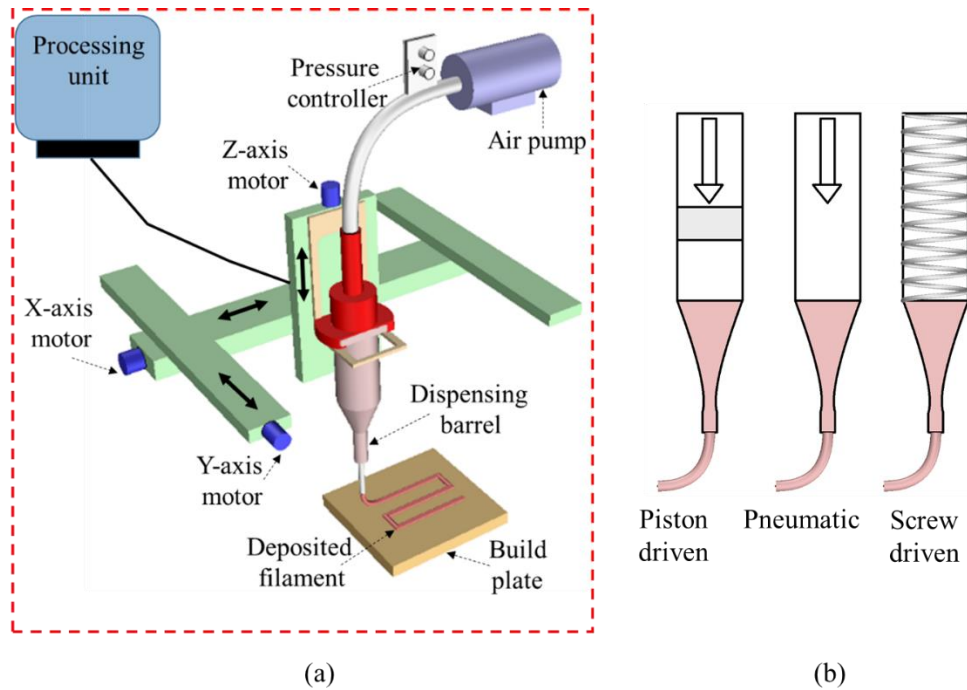
Figure 6: (a) Schematic diagram of extrusion based bio-printer, and (b) Driving force to release material.

The resolution that can be achieved with extrusion-based printing is in the range of about 80 µm, which is considerably low compared to laser- or inkjet-based systems which can be in few microns [204]. But the fabrication speed is significantly higher and wide range of materials can be printed with extrusion based system [92]. Based on pneumatic, piston-driven, or screw-

driven force, the released materials show different merits and demerits. Normally, materials dispensed by pneumatic systems are associated with a delay in dispensing due to the compressed gas. However, they work better for highly viscous molten polymer. On the contrary, the piston-driven deposition generally offers more direct control over the flow of the hydrogel from the nozzle. Finally, screw-based systems provide more spatial control and are valuable for the dispensing of hydrogels with higher viscosities. It should be noted here, the encapsulated cell within the hydrogels can be deposited with high viability using both pneumatic and piston-driven systems. Material deposited by the screw-driven system can generate larger pressure drops at the nozzle which can be detrimental for the encapsulated cells. This issue can be minimized by designing the screw-pitch geometry. In contrast, pneumatic system is quiet simple, easy to use and can deliver delicate material without damaging them. Therefore, in this research we have selected pneumatic system in this research.

The 3D printing philosophy used in extrusion based bio-printing is similar to fused deposition modeling (FDM), one of the 3D printing technologies [204]. This technology was developed in late 1980s which was successfully commercialized in 1990 [205]. Traditionally, the FDM system consists of three axis namely x, y, and z-axis where the nozzle or the build plane move on XY-plane and the build height is achieved by the z-direction movement. The main function of the nozzle or dispensing barrel is to extrude the filament materials onto the building platform following a preprogrammed path, essentially based on computer aided manufacturing (CAM). After completing the fabrication of a single layer, the nozzle moves up or xy-plane moves down one step along z-direction to deposit the next layer creating 3D structures. The bio-printing technique that we used in this research use the same process plan which has been build in our lab and explained in the following section.

3.2. Development of a 3D bio-printer

In this research, a three-axis 3D bio-printer is developed in-house as shown in Figure 7 and used to fabricate the acellular and cell-laden scaffold under sterile condition. The reason to develop the 3D printer is to ensure the user-end full control over fabrication process and optimizing related process parameters. The optimized process parameters will assist towards achieving designed architecture of the scaffold. For fabricating cell-laden scaffold without contamination, the working envelop is properly sterilized by spraying 70% ethyl alcohol. The machine uses compressed air to exert the force on material. It has a controller assuring the consistent air pressure during extrusion and a HEPA filter is attached with the tube for sterile air flow. Other process parameters such as nozzle speed, needle diameter, material flow rate, print distance are investigated and characterized for scaffold fabrication.
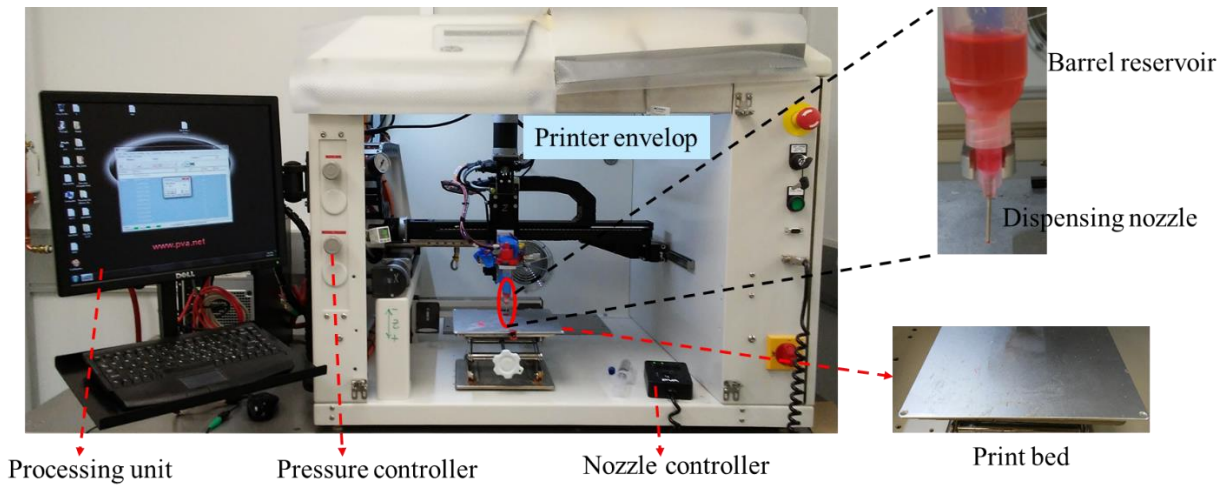
Figure 7: 3D bio-printer developed in-house for this research.

The simultaneous coexistence of various cell types into biomaterials is necessary to mimic the architecture of native tissue construct. To do this, we have also develop a multi-nozzle system with the developed 3D bio-printer in our lab. The existing nozzle holder of our 3D printer is shown in Figure 8 (a). This nozzle holder is modified for holding multiple nozzles as shown in

Figure 8 (b). To hold three dispensing nozzles of 10cc simultaneously, an attachment is manufactured using aluminum as shown in Figure 9.
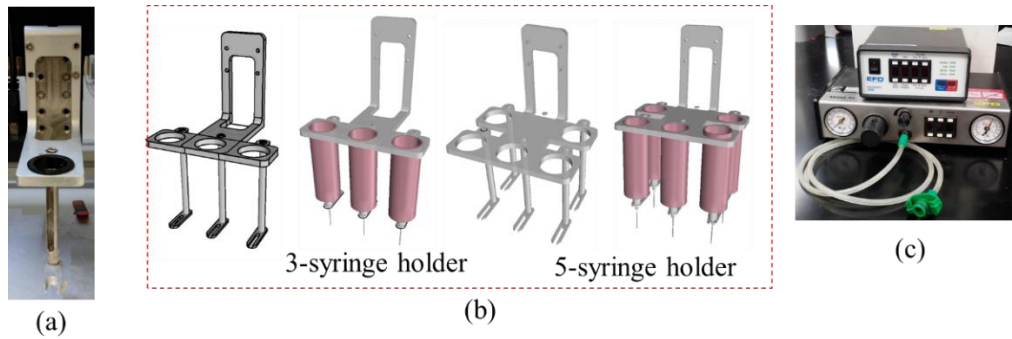
Figure 8: (a) Existing nozzle holder, (b) Proposed nozzle holders, (c) External air pressure controllers.
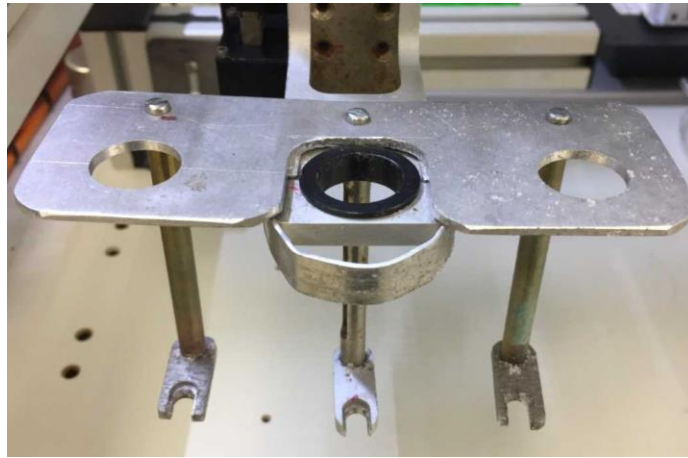
Figure 9: Attachment to hold three dispensing nozzles simultaneously.

For heterogeneous (two or more dissimilar materials) material printing, co-axial dispensing nozzle with various gauges and materials (i.e. plastic, stainless steel) are assembled in-house. A co-axial dispensing nozzle is manufactured with a 20 gauge stainless steel needle by drilling with 0.75 mm drill bit as shown in Figure 10 (a). Another needle is attached seamlessly as shown in Figure 10 (b,c) with this drilled needle to ensure the material flow through single nozzle. A schematic diagram of co-axial nozzle is shown in Figure 10 (d) to fabricate filament having micro-

channel.
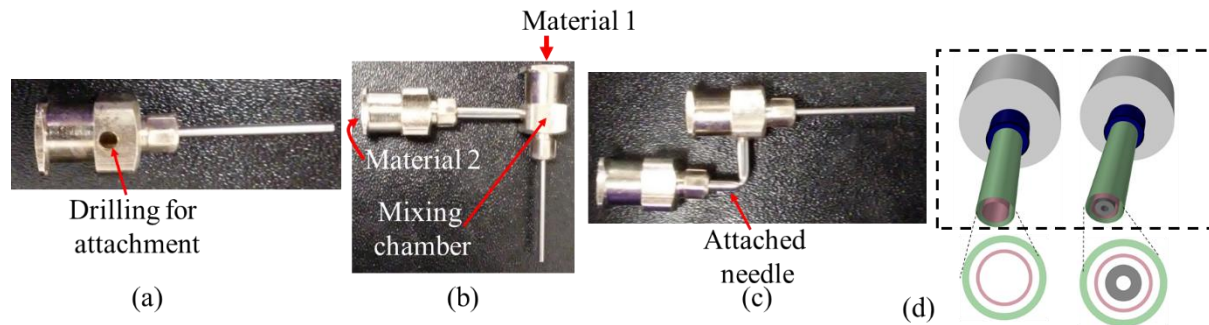
Figure 10: (a) Drilled needle, (b, c) attaching another needle with drilled needle, (d) Multi-layered co-axial nozzle with cross-section.

3.3. Pre-process plan of 3D bio-printing

The overall framework of 3D bio-printing process plan is classified into three stages as pre-processing, processing and post-processing [206] as shown in Figure 11.
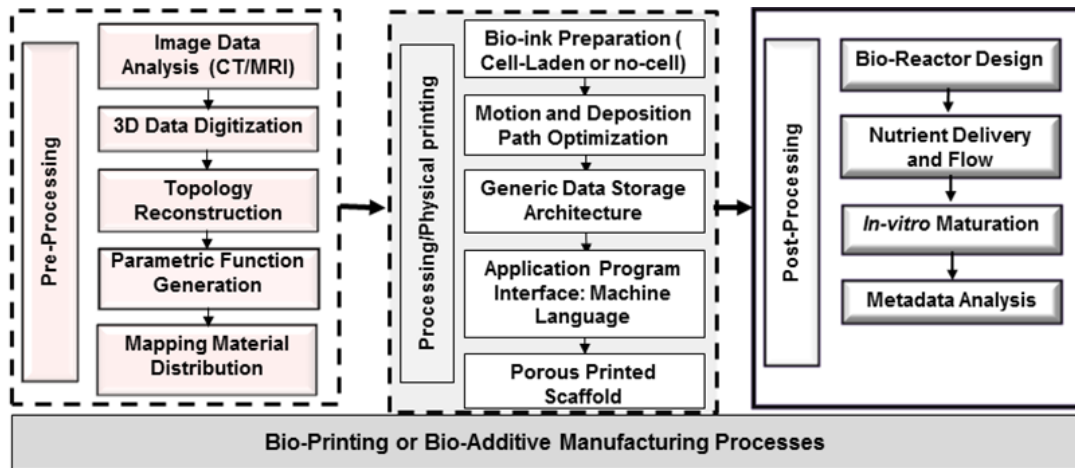
Figure 11: Framework of the bio-printing process.

A hierarchical pre-process plan of 3D bio-printing starts with a digital model designed by CAD software or obtained from reverse engineering as shown in Figure 11, which is used as the digital input of the machine, leads towards the end product. Before feeding the digital input to AM machines, several pre-process plans such as selecting appropriate build direction [207-211],

slicing [212, 213], tool-path design and generation [214, 215] can define the efficiency and product quality of this fabrication process.
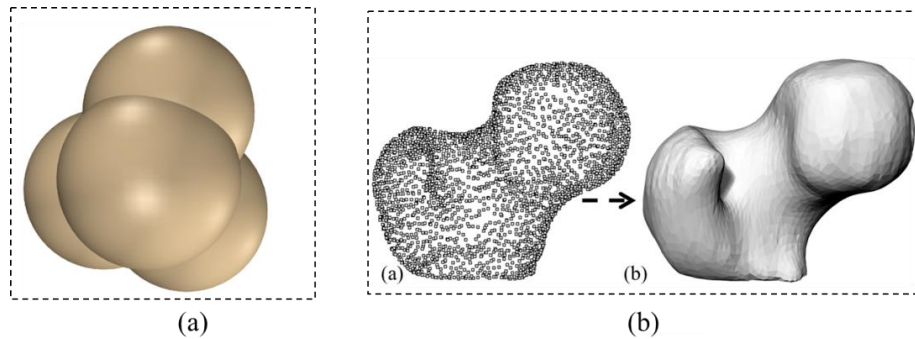
Figure 12: 3D model digitization by (a) CAD modeler (b) Reverse Engineering.
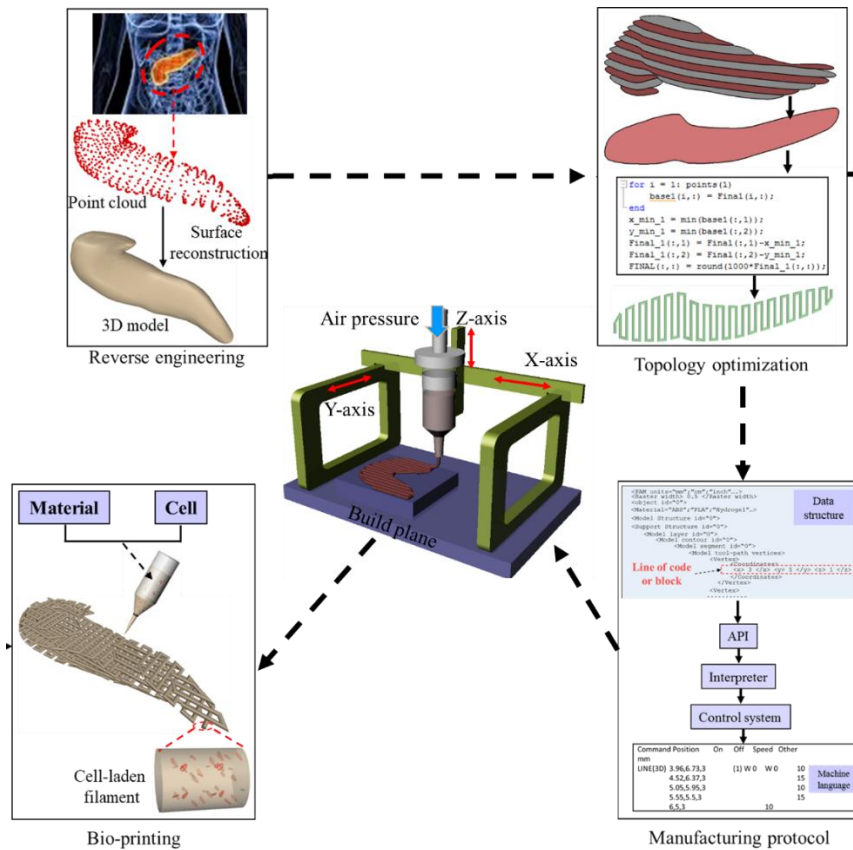
Figure 13: The schematic diagram of overall process plan of 3D bio-printing.

3.3.1. Designing of scaffold tool-path

The overall pre-process plan is shown in Figure 13 where a 3D model is sliced at a specific layer height. This slice generates a set of closed contours. The vectorized toolpath is programmed and generated into closed contours to deposit material layer-upon-layer. The nozzle head needs to be guided along the generated path with a selected raster width i.e. filament to filament distance and deposition angle to fill the interior of the layer. In order to ensure the geometric quality, strength and stiffness of a model and overall build efficiency, the tool-path needs to be designed properly. Both zig-zag/direction parallel and spiral/contour parallel deposition path are commonly used in combination to fill the contour periphery and curing the interior material [216]. The contour parallel tool-path has high spatial filling accuracy but complicated generation algorithm and less infill efficiency. On the other hand, zig-zag tool-path has relatively high infill efficiency but less accuracy [217]. A tool-path planning approach for functionally graded material has been proposed considering the zig zag and contour parallel tool-path [218]. This work has focused more on region-based material distribution by tool-path planning than build efficiency. A laser-based (selective laser sintering, SLS) tool-path planning has been proposed to scan and cure large contour area [219]. To expedite the efficiency, a dual laser has been employed on discretized contour area. In [219], authors focused on the zig zag tool-path planning strategy to balance and optimize the build efficiency. In zig zag tool-path, the nozzle/tool tip/print head will fill or cure the material in a continuous line-by-line fashion along a specific direction. Since each fabricated layer is supported by its preceding layer, a 0°-90° raster angle pattern among successive layers is usually used to ensure structural integrity [220]. However, other pre-determined layout patterns were also investigated for the structural integrity [221]. Adaptive material laying patterns have recently been proposed by Khoda *et al.* [222] to

36

achieve the desired porosity of the functionally gradient porous internal architecture of additively

manufactured tissue scaffolds. A multi-directional parametric material deposition orientation

[223] is also demonstrated considering the accessibility and porosity of the internal region. An

adaptive tool-path algorithm has been proposed for interior of the object with zig-zag pattern

[224]. Here, the deposition direction is determined via changing the direction parallel slope that

provides the minimum build time. After this discussion, it is clear that continuous zigzag

toolpath is efficient for extrusion based printing process. Therefore, zigzag toolpath pattern is

used in this research to fabricate the scaffold.
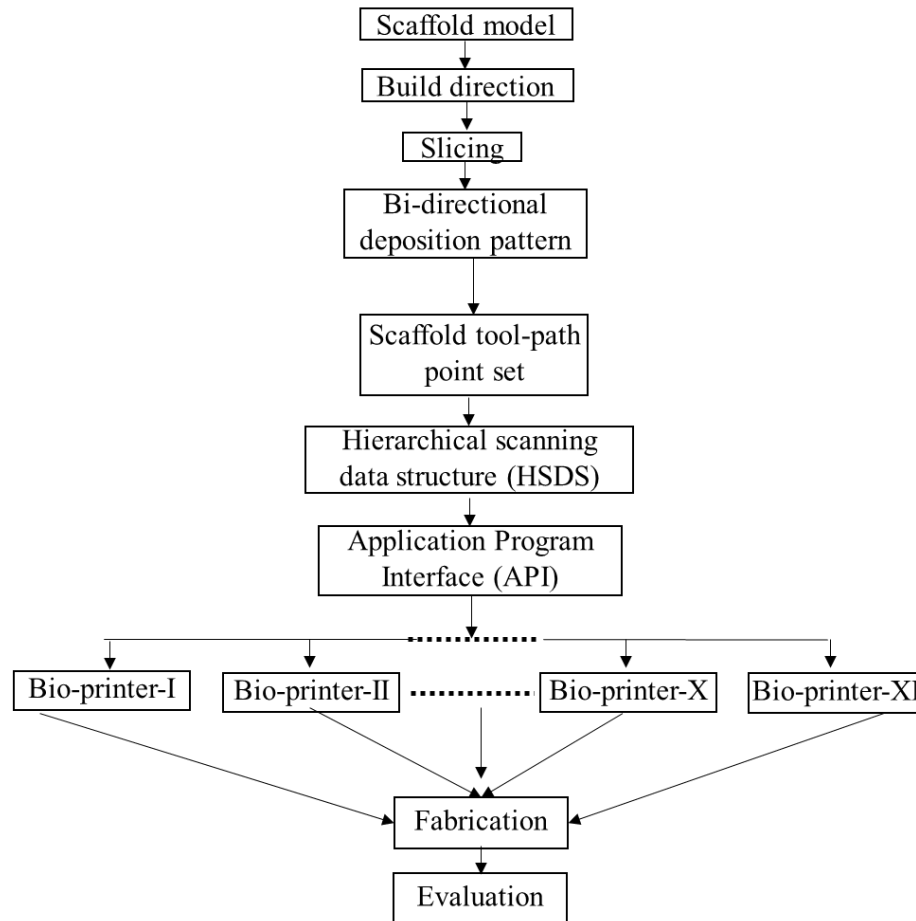
Figure 14: Process flow diagram of the proposed methodology.

37

The process flow chart of the proposed methodology is shown in Figure 14. Normally, a technology-independent de facto file format called STL (STerioLithography) is used to transfer the digital information of the scaffold model to bio-printers. The actual polynomial surface of the scaffold model is converted into STL model using first order piece-wise linear approximation. This causes loss of geometrical and topological information and introduces error to the actual scaffold model. This error is known as chordal error or chordal height deviation as shown in Figure 15.
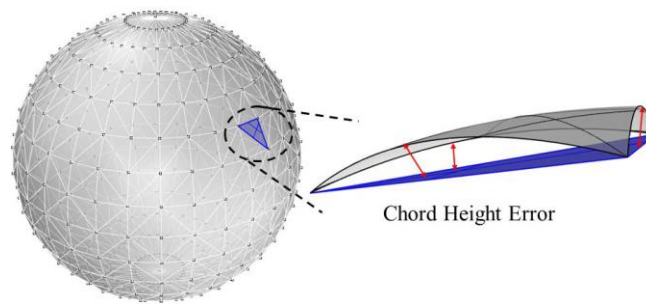
Figure 15: Chordal error

Moreover during surface approximation, it causes several errors such as holes or cracks, non-manifolds, overlapping facets and incorrect normal, hence the loss of geometrical and topological information and introduces error to the digital model [225]. Since it represents the object surface by thousands of triangles, it does not provide an efficient memory storage compared to the higher level spline, NURBS (B-Rep) representations [226]. Therefore, STL representation may be cumbersome in term of digital memory and computational requirements. The memory and computational issues can be resolved by reducing the number of input data points. That will aggravate the loss of surface information and consequently the chordal deviation and finally erroneous digital model information. Besides, the approximated model volume differs from the actual model due to the approximation error in each layer as shown in

Figure 16. Figure 17 demonstrates the effect of change of number of triangles on the scaffold model quality.
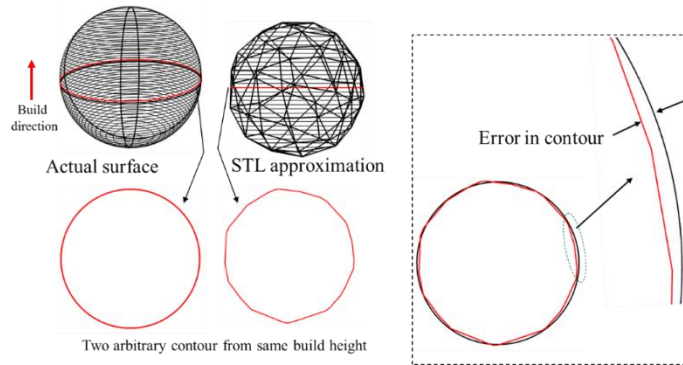
Figure 16: Error in contour generated from STL model.
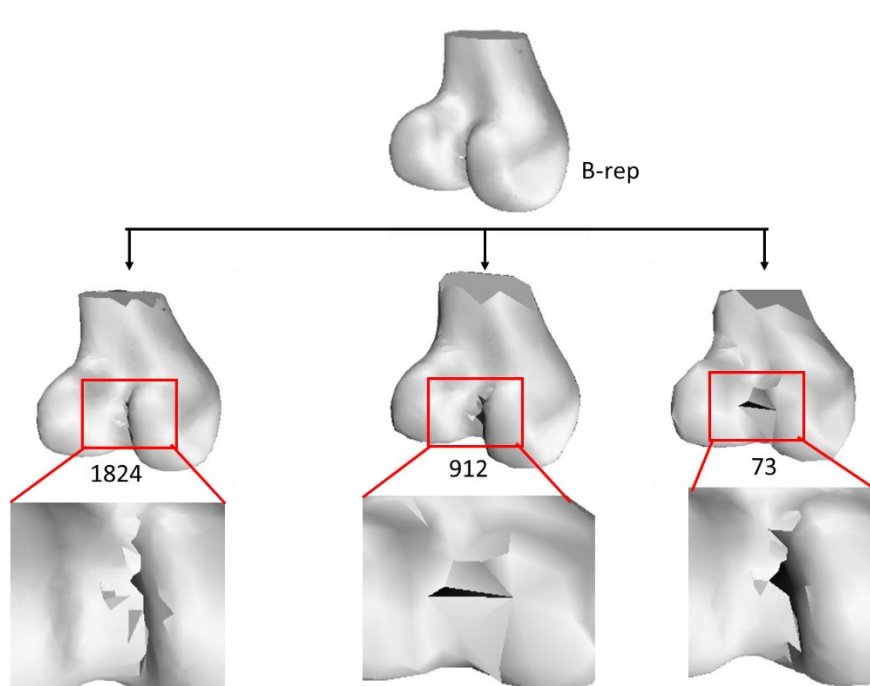
Figure 17: Effect of changes of triangle number on scaffold quality.

Hence, the platform-specific data conversion during process plan step transition from 3D model digitization towards the end product results in error accumulation. Finally, this error introduces extrinsic and intrinsic variability in the end fabricated scaffold. Thus the repeatability between bio-printers with various data processing engines will be undermined.

To resolve the STL issues, several attempts have been taken by the researchers. Some works have been done to repair the existing erroneous STL file [227, 228]. A new rapid prototyping interface file format has been proposed including the topological information and discarding the redundant information that contained in STL file [225]. Other standard type of file format have been proposed to represent the 3D model instead of STL file. Each of them have different characteristics as listed in Table 4.

Table 4: Characteristics of different file formats.

File Format	Geometry	Material	Color
STL [229, 230]	✓	×	×
.MF [231, 232]	✓	✓	✓
.TEP [233, 234]	✓	✓	✓
.MF [235, 236]	✓	✓	✓
.RML, PLY, OBJ [237]	✓	×	✓

These standard files are approximating function-specific digital information of the model, but existing bio-AM machines are not capable to read all of this information. Attempts have been taken to make some of these file machine readable. An assessment has been done about the AM file format directing the development of new representation [229]. Nassar et al. [237] proposed an extensible markup language (XML)-based file formats describing the record and data transfer of AMF file at every stage of AM process. Another file format has been published for universal multi-material AM process [238].

To resolve the STL related issues, a systematic file format i.e. hierarchical scanning data structure (HSDS) [239] is proposed in this research. The NURBS (B-Rep) file of 3D scaffold model is directly sliced which creates a set of closed contours. The zigzag toolpath is generated into each closed contour. Each toolpath contains a set of information of a sequential number of points. The information of those sequential points will be stored into HSDS. A common

application program interface (API) platform is also proposed here, which can access the HSDS and generate machine readable file for different existing 3D bio-printers. This proposed file format system will be a new data feeding protocol for existing 3D bio-printers.

3.3.2. File format for STL free scaffold model

The scaffold is directly sliced and a similarity index is determined between any two consecutive contours. Once a set of sequential tool-path points of a specific scaffold-layer is generated, it is stored in HSDS. The chronological bottom-up or top-down visit to each layer of the scaffold will result in a sequential tool-path points for this scaffold. Hence, a generic HSDS file will be generated for the whole scaffold. A common application program interface (API) platform contacts the HSDS and generate machine readable file for different existing bio-printer control systems considering the similarity index and machine specific layer thickness. The data stored in HSDS can be retrieved remotely and be used by different existing bio-printers controller supporting the cloud/remote manufacturing process. That's how the platform-independent object repeatability can be ensured. Among four main service models such as Infrastructure-as-a-Service (IaaS), Platform-as-a-Service (PaaS), Hardware-as-a-Service (HaaS) and Sortware-as-a-Service (SaaS) of cloud based design and manufacturing (CBDM) [240], SaaS can be replaced by the HSDS to make the proposed methodology cloud based design and manufacturing enable. An overview of the proposed methodology including the potential of the cloud manufacturing is shown in Figure 18.
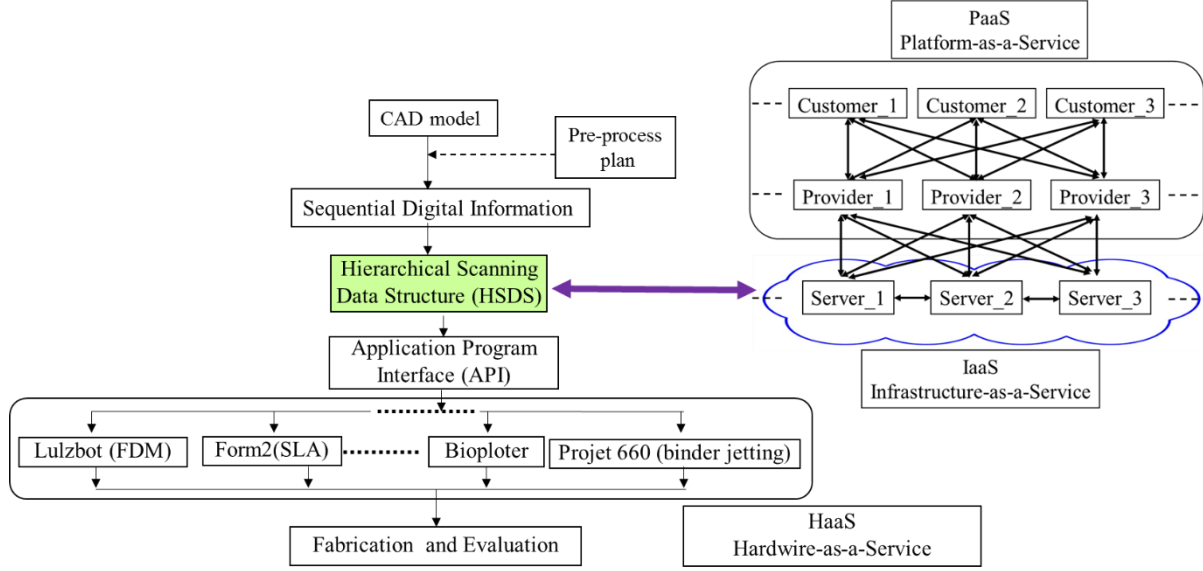
Figure 18: Overview of the process including cloud manufacturing possibility.

3.3.2.1. Direct slicing of the scaffold

The 3D parametric surface (NURBS surface) of scaffold model is sliced by a set of planar surfaces (parallel to XY plane) to find the layer contours to be used for additive manufacturing processes. Surface-surface intersection algorithm is used to identify the boundary contours of the cross-sectional area of the object to be filled with material as shown in Figure 19. Depending on the object geometry, the resultant closed boundary contour may be composed with a single curve or with a set of smoothly connected piecewise curves. A NURBS surface can be represented by the following equation:

$$S(u,v) = \frac{\sum_{i=0}^{n}\sum_{j=0}^{m}N_{i,p}(u)N_{j,q}(v)w_{i,j}P_{i,j}}{\sum_{i=0}^{n}\sum_{j=0}^{m}N_{i,p}(u)N_{j,q}(v)w_{i,j}} \qquad 0 \leq u,v \leq 1 \qquad (1)$$

Where $\{P_{i,j}\}$ are the control points, $\{w_{i,j}\}$ are the weights and the $\{N_{i,p}(u)\}$ and $\{N_{j,q}(v)\}$ are the nonrational B-Spline basis function defined on the **U** and **V** knot vectors. In general the object surface and the cutting surface can be represented respectively as follows:

42

$$S_{Obj}(u,v) = \begin{bmatrix} x_{obj}(u,v) \\ y_{obj}(u,v) \\ z_{obj}(u,v) \end{bmatrix} \text{ and } S_{CP}(s,t) = \begin{bmatrix} x_{cp}(s,t) \\ y_{cp}(s,t) \\ z(s,t)_{cp} = C \end{bmatrix} \text{where } 0 \leq s,t \leq 1 \tag{2}$$

The problem of intersection can be solved by computing the set

$$\begin{aligned} Int &= \{S_{Obj(u,v)} - S_{CP}(s,t)\} \\ &= F(u(\gamma),v(\gamma),s(\gamma),t(\gamma)) \\ &= \begin{bmatrix} x_{Obj}(u,v) - x_{cp}(s,t) \\ y_{Obj}(u,v) - y_{cp}(s,t) \\ z_{Obj}(u,v) - z_{cp}(s,t) \end{bmatrix} = \begin{bmatrix} f_1(u,v,s,t) \\ f_2(u,v,s,t) \\ f_3(u,v,s,t) \end{bmatrix} = \begin{bmatrix} 0 \\ 0 \\ 0 \end{bmatrix} \end{aligned} \tag{3}$$

Where γ is any parameter. This function can be interpreted as a pair of two curves as follows:

$$C_{Obj} = (u(\gamma),v(\gamma))^T \subseteq [0,1]^2 \text{ and } C_{CP} = (s(\gamma),t(\gamma))^T \subseteq [0,1]^2 \tag{4}$$

Which represent the path of intersection on each of the surface in the corresponding parameter space. The intersected curve can also be determined applying k-Nearest Neighbors [241] on the points results from the following parametric equation:

$$C(u,v,s,t) = \frac{N_{Obj} \times N_{CP}}{\|N_{Obj} \times N_{CP}\|} \text{ where } N_{Obj} = \frac{S_{Obj(u)} \times S_{Obj(v)}}{\|S_{Obj(u)} \times S_{Obj(v)}\|} \text{ and } N_{CP} = \frac{S_{CP(s)} \times S_{CP(t)}}{\|S_{CP(s)} \times S_{CP(t)}\|} \tag{5}$$

After applying the same technique successively in bottom-up or top down fashion with a specific layer thickness, a set of closed object contour is generated $OB\_Cont = \{Cont_i\}_{i=1,2\ldots R}$. Since they do not intersect themselves other than at their start and end points and have the same (positive) orientation generally these can be represented as:

$$Cont_i(\gamma) = \{x(\gamma), y(\gamma), z(\gamma)\}^T ; \forall \ \gamma \in [a_i,b_i] \rightarrow \Re^2 ; Cont_i|_{\gamma=a_i} = Cont_i|_{\gamma=b_i} ; \ i = 1,2\ldots R \tag{6}$$

43
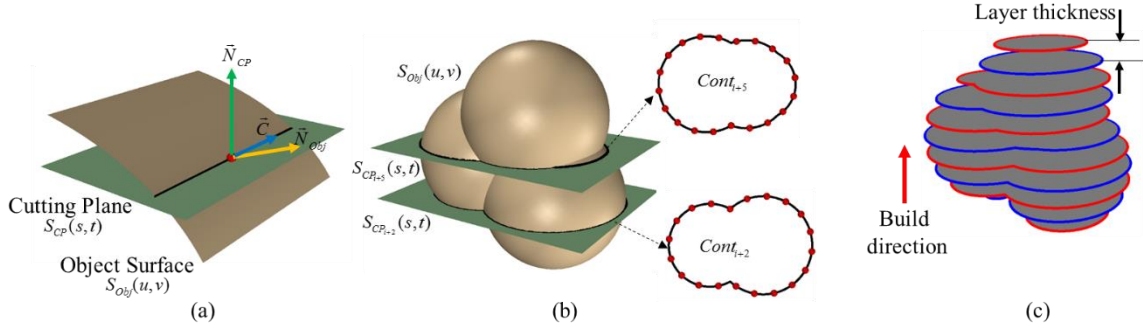
Figure 19: (a) Surface-surface intersection and resultant curve, (b) Contour generation at different build height, (c) Resultant object contour.

To make the HSDS compatible for each bio-AM machine with different resolutions, a similarity index between any two consecutive contours is determined. Depending on the similarity index a set of contours can be eliminated from the similar contour group within a specific layer thickness or a set of contours can be added in between of the consecutive layers by doing the linear interpolation without hampering the object geometry. Thus machine-specific HSDS can be generated. To determine the similarity index, three factors such as distance factor (DF), curvature factor (CF) and area factor (AF) are considered. A set of finite number of points $PT = \{pt_w\}_{w=1,2..W}$ are considered on any two consecutive contours $Cont_i, Cont_{i+1}$ respectively and projected them on build plane considering z-component zero, i.e. $pt_w = \{x_w, y_w, 0\}$ as shown in Figure (8 (a)) . The corresponding point of pt_w^i, i.e. pt_w^{i+1} is determined based on the minimum distance from pt_w^i to $PT^{i+1} = \{pt_w^{i+1}\}_{w=1,2..W}$, i.e. $d_w = min\{d_{w,w}^{i,i+1}, d_{w,w+1}^{i,i+1}...d_{w,W}^{i,i+1}\}$. Then the summation of all normalized minimum distance is defined as distance factor (DF), i.e. $DF = \sum_{w=1}^{W} nd_w$. A set of curvature $CR = \{\kappa_w\}_{w=1,2..W}$, is determined on each point pt_w on $Cont_i, Cont_{i+1}$ contours respectively and the difference of curvature between two corresponding points i.e. $diff_w^{\kappa} = |\kappa_w^i - \kappa_w^{i+1}|$ are stored as shown in Figure (8 (b)). The summation of normalized curvature difference is defined as

44

curvature factor (CF) , i.e. $CF = \sum_{w=1}^{W} ndiff_w^{\kappa}$. The ratio of the area difference between two

consecutive contours and the area of bottom surface of the object bounding box $A_{bottom,BB}$ is defined

as the area factor, i.e. $AF = |A_i - A_{i+1}| / A_{bottom,BB}$. A weighted factor (WF$_i$) of similarity index between

$Cont_i, Cont_{i+1}$ contours is determined consisting of these three factors as follows:

$$WF_i = \omega_{DF} \times DF + \omega_{CF} \times CF + \omega_{AF} \times AF; 1 \leq i \leq R - 1; \omega_{DF} + \omega_{CF} + \omega_{AF} = 1, DF = \frac{d_w - d_{w,min}}{d_{w,max} - d_{w,min}} \qquad (7)$$

Here ω_{DF}, ω_{CF} and ω_{AF} are three associated user defined weights for distance factor, curvature

factor and area factor respectively. These three weights reflect the relative importance of these

three factors. Once a set of weighted factor (WF) of similarity index is determined, they are

classified into a finite number (L) of similar contour groups (SCG) using equation (8) as shown

in Figure 20 (c).

$$SCG = \{scg_l\}_{l=1,2...L}; wf_l \leq WF_i \leq wf_{l+1} \qquad (8)$$

Where wf_l and wf_{l+1} are user defined minimum and maximum range of WF$_i$. Some scenario

of similarity index is shown in Figure 21. Therefore the candidate contours are identified to be

eliminated from HSDS or added to HSDS depending on the AM machine resolution once the

similarity index between contours are determined
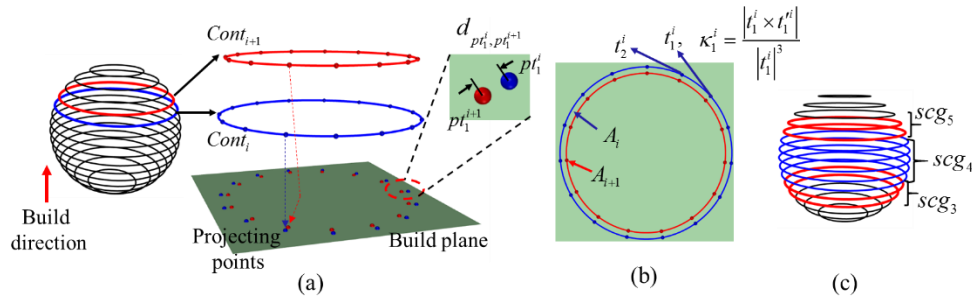
Figure 20: (a) Identification of corresponding points and distance factor, (b) Determination of area factor and curvature factor, (c) Group of similar contours.

45
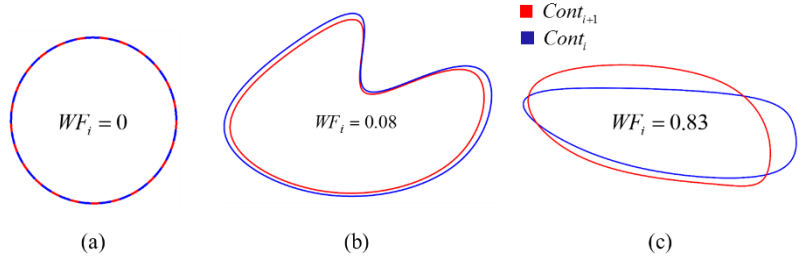
Figure 21: Similarity Index of two consecutive contours (a) Same contours, WFi=0, (b) Smaller difference, WFi=0.11, and (c) Larger difference, WFi=0.83.

3.3.2.2. Hierarchical scanning data structure

Once all the sequential points of the whole scaffold are determined, this information is stored in a hierarchical order into HSDS file as shown in Figure 22. Different 3D bio-printers will generate different HSDS data structures as shown in Figure 23 where HSDS will contain all the information of the scaffold, layers, contours, and sequential path coordinates.
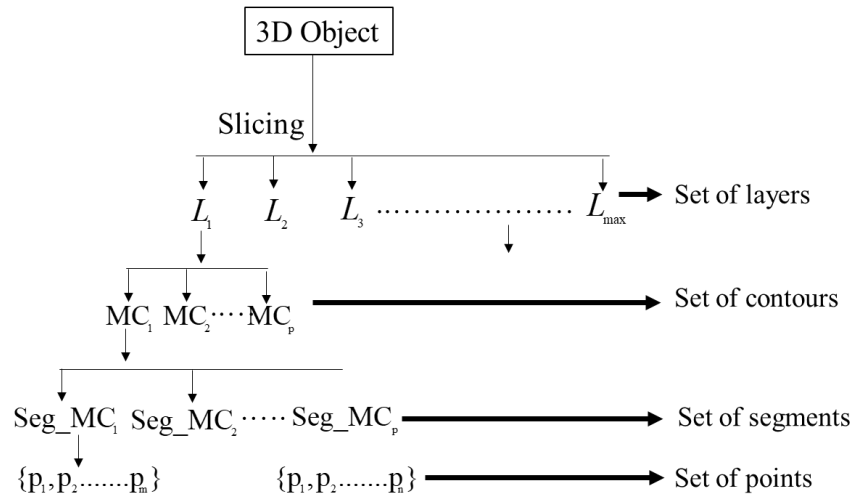
Figure 22: Data storage hierarchy of HSDS.

```
<PAM units="mm";"µm";….>
<Raster width> 0.1 </Raster width>
<object id="0">
<Material="alginate";"gelatin";"alg-gel"…>
<Scaffold Structure id="0">
    <Scaffold layer id="0">
        < Scaffold contour id="0">
            < Scaffold segment id="0">
                < Scaffold tool-path vertices>
                    <Vertex>
                            <Coordinates>
                            <x> 3 </x>
                            <y> 5 </y>
                            <z> 1 </z>
                            </Coordinates>
                        </Vertex>
                    <Vertex>
                    ...........
            </ Scaffold layer id="0">
            .............
     < Scaffold layer id="1">
            .............
    </ Scaffold layer id="1">

        .............
    </ Scaffold Structure >
        </object>
```

Figure 23: Data structure of HSDS.

3.3.2.3. *Application program interface (API)*

The part and process related information i.e. coordinated linear or non-linear motion;

depositing and non-depositing control points; flow rate, speed, raster etc. are stored in this file.

To construct the physical 3D scaffold with any bio-printers, the stored data in HSDS needs to be

converted into the controller specific language. A common API (Application Program Interface)

platform is also proposed in this research, which can access the HSDS and generate machine

readable file for different existing 3D printers as shown in Figure 24. The metadata section of the

file will assure the readability by different existing 3D printing interpreters. Each line of this file

will be called as "line of code" or "block". The API will read this line of code and send back

signal to driver telling it was readable or not. If it is readable, the driver will tell interpreter to

execute this line. The interpreter will generate a message using its own function and send it to the

control system.

47
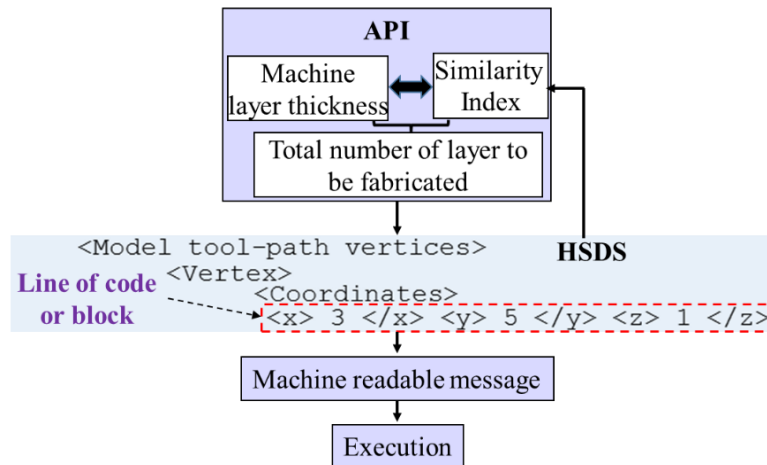
Figure 24: API working principle

Likewise, the control system receives a set of messages which is queued up and executed. Thus, the consecutive execution of those lines of code will result in a final printer executable path-plan sequence for the 3D scaffold as shown in Figure 25. This proposed file format system can be applied on existing 3D printers as shown in Figure 26.
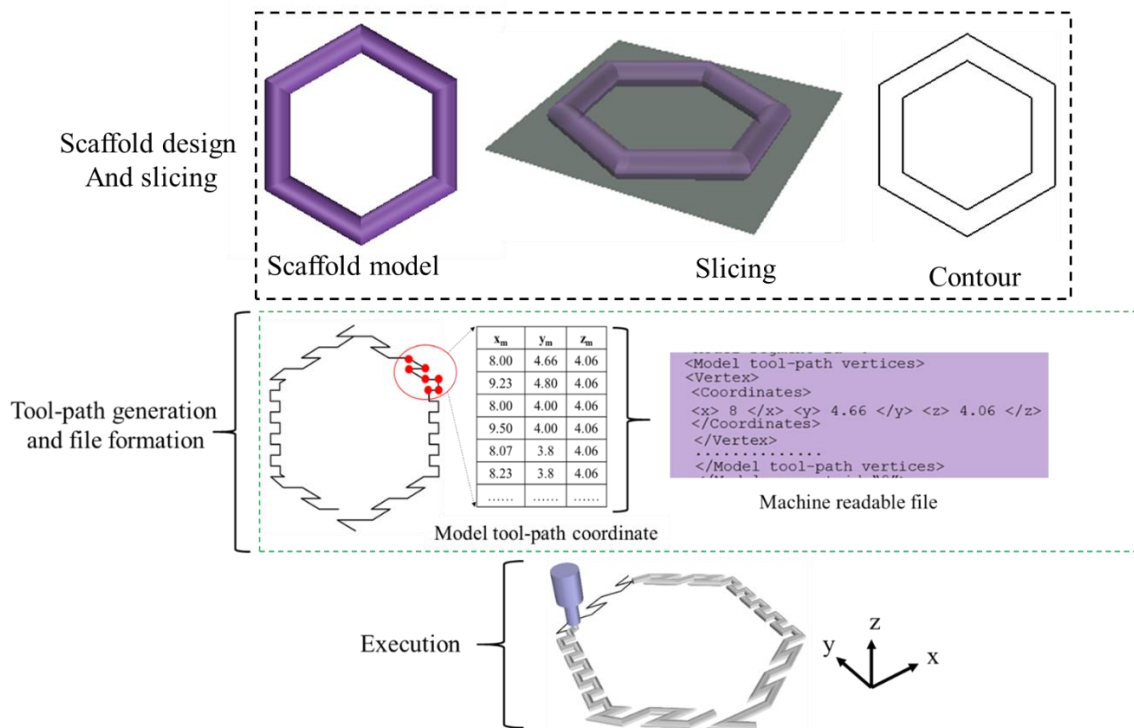
Figure 25: Executing the API for a specific bio-printer
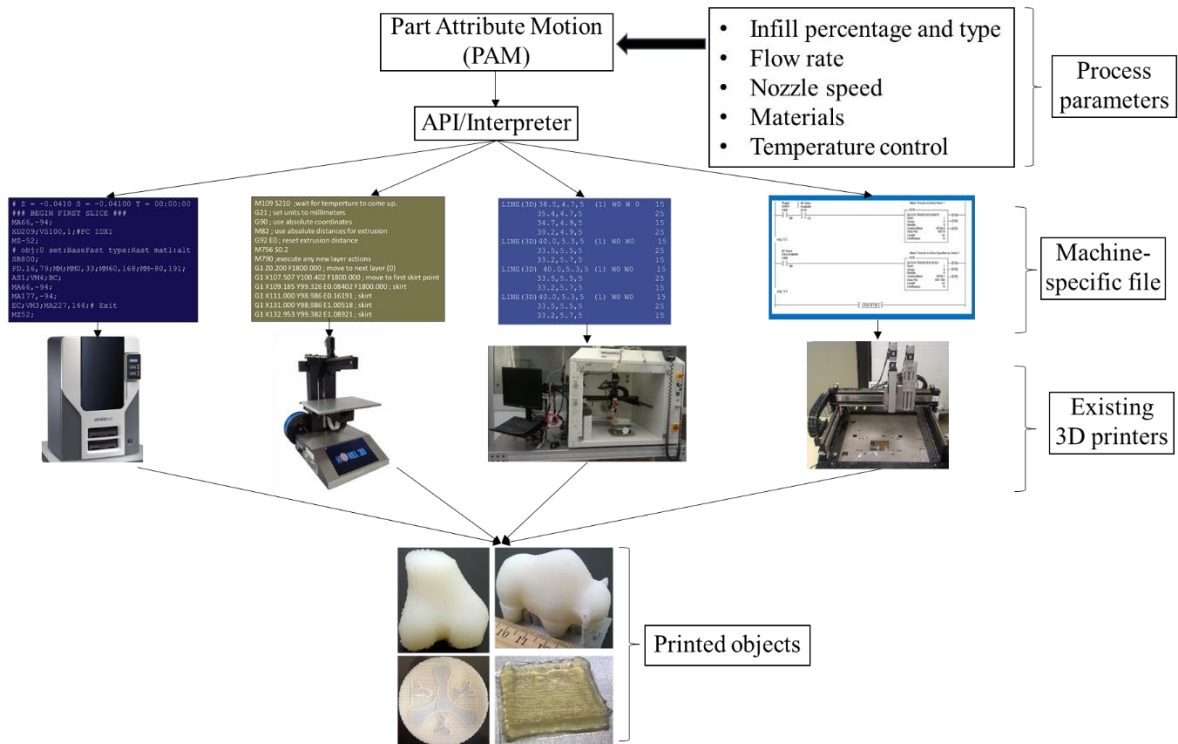
Figure 26: Executing HSDS for existing 3D printers.

3.4. Results and discussion

3.4.1. Implementation

The proposed file format system is implemented on four example scaffolds with a Core i7 @ 3.4 GHz CPU equipped with 8 GB RAM using Visual Basic scripting language. The layer thickness for existing AM machines are enlisted in Table 5 where Form1 has least layer thickness than other machines.

Table 5: Layer thickness of different AM machines

Stratasys FDM (in)		MakerBot (in)		Hyrel (in)		Form1 (in)		Projet 660 (in)	
LT_{min}	LT_{max}	LT_{min}	LT_{max}	LT_{min}	LT_{max}	LT_{min}	LT_{max}	LT_{min}	LT_{max}
0.007	0.014	0.004	0.013	0.004	0.02	0.001	0.004	0.004	0.004

49

To execute the fabrication of the actual CAD model of the scaffold, the HSDS file is generated for two different commercial 3D printing machines namely Dimension 1200es made by Stratasys and Hyrel Hydra made by Hyrel 3D. It should be noted here, that the proposed file format is generic and can be used by any machine control system which is also independent of material.   Only infill of the model is printed and the infill printing speed is used as 30 mm/sec and 50 mm/sec for Dimension 1200es and Hyrel Hydra respectively. The raster width for both machine is considered as 1.13mm and the layer thickness is considered as 0.2 mm and 0.30 mm for Dimension 1200es and Hyrel Hydra respectively. The HSDS is generated considering the layer thickness 0.25 mm consisting of 12 layers where the Dimension 1200es needs 15 layers and Hyrel Hydra needs 10 layers to be fabricated to get the 3.0 mm build height of the object. Since the object is cylindrical, the similarity index for each consecutive contours is 0. Therefore the API has added three more contours in HSDS for Dimensions 1200es where it eliminates two contours from HSDS for Hyrel Hydra and updated the HSDS file accordingly to fabricate the same object using the two different machines. Finally the object is fabricated with Dimension using the ABS model and support material respectively and with Hyrel Hydra using ABS and PLA respectively as shown in Figure 27. An example of how the proposed methodology can be applied in cloud manufacturing is also shown in Figure 28**.** This same process plan framework is used to bio-print for this thesis which are shown in later chapters.
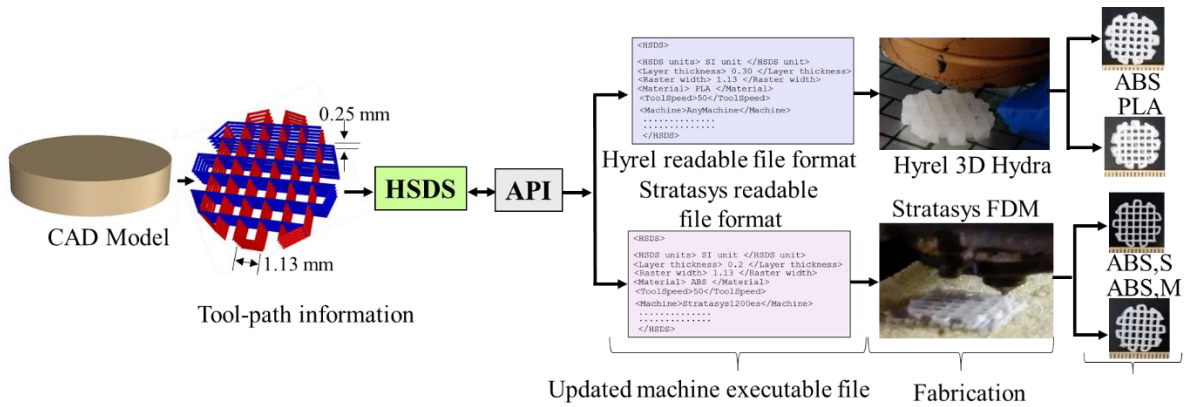
Figure 27: Same digital scaffold model fabricated using two different AM machines.
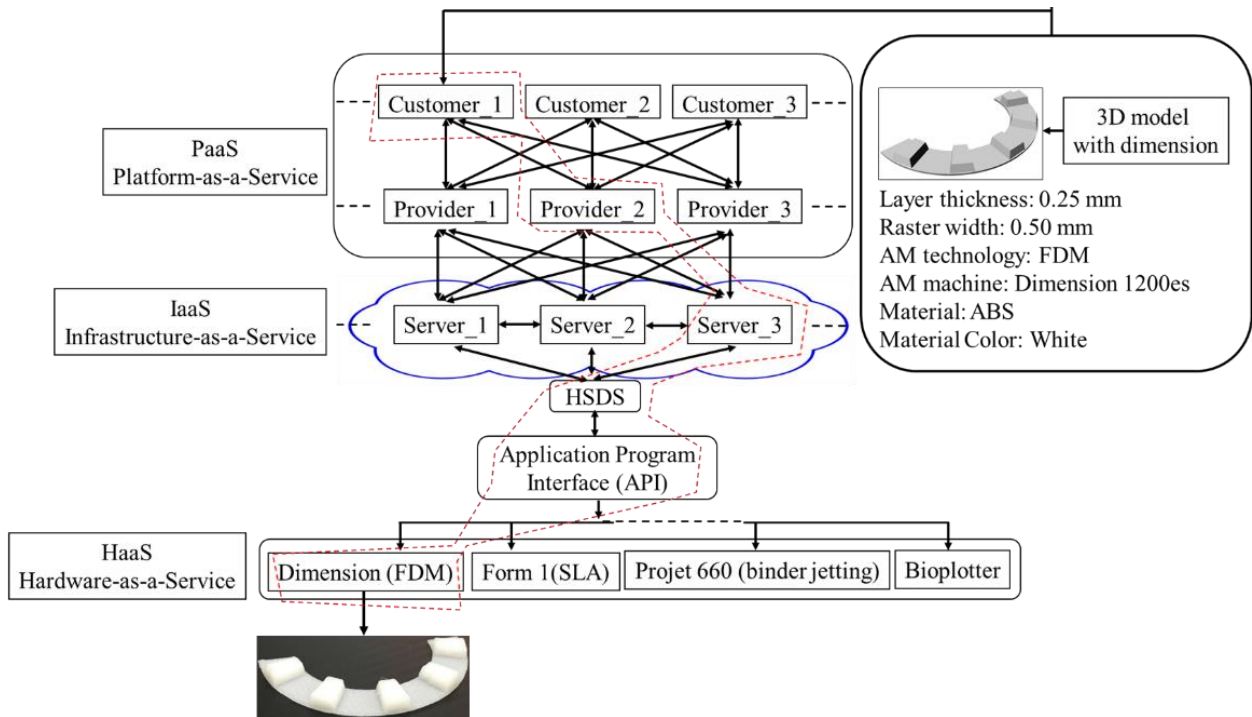
Figure 28: An example of cloud manufacturing applicability.

Total time needed to implement the methodology on the example 1, 2 and 3 are approximately 5, 12 and 10 seconds per iteration respectively. However, required time can be reduced significantly by parallel processing or increasing the computational power. The raster width used to fabricate the model and support is considered 0.5 mm and .75mm respectively for both proposed methodology and commercial software. Layer thickness is considered as 0.254

51

mm for both model and support. The infill printing speed is considered as 20 mm/sec. Sequential

point information is stored in the HSDS format as discussed. Then the proposed API is used to

create the printer specific .sml file and the models are fabricated as shown in Figure 29**.**

(a)   (b)   (c)
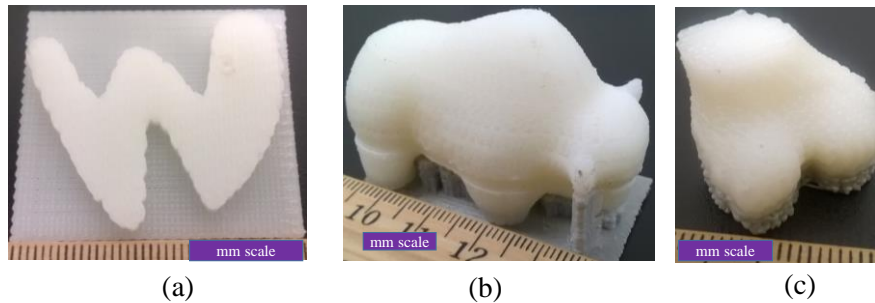
Figure 29: Fabricated parts: (a) example 1, (b) example 2, and (c) example 3.

3.4.2. Remarks of file format

A generic digital file format is proposed that store the information of sequential toolpath

points. An API is implemented to read the generic file for creating the printer specific deposition

instruction. The proposed HSDS data structure contains generic process plan data in a

hierarchical structure and can be accessed remotely. Such framework can support the cloud

manufacturing as well as repeatability between bio-printers.

4. 3D PRINTABILITY OF ALGINATE-CARBOXYMETHYL CELLULOSE HYDROGEL

Sodium alginate is a seaweed-extracted naturally derived polysaccharide, has been used in 3D bio-printing for several years because of its good biocompatibility. The inclusion of calcium ions directs cross-linking of the carboxylate groups of sodium alginate to achieve excellent gelation without hampering biocompatible environment [242]. Due to the high water content, it allows the good exchange of waste products and nutrients. Various cell types such as fibroblast [243], myoblast, endothelial [244], chondrocytes [153], and schwann [245] have been encapsulated into alginate for culturing. The dissipation of Ca^{2+} ions in physiological conditions results in water-soluble, nontoxic alginate and eventually the gradual degradation of Ca-alginate gel [246]. However, achieving the intricate internal porous architecture with predefined shape, size and dimensional integrity using hydrogels material is limited.

To fabricate large scaffold with accurate pore size and geometry, other biomaterials are often mixed with alginate to prepare a hybrid hydrogel. Carboxymethyl cellulose (CMC), is a high-molecular-weight water-soluble polysaccharide used for viscosity modifier or thickener. It has been reported that the binding of CMC's matrix protein assists in cell migration and cell attachment [247]. Moreover, alginate-CMC (alg-CMC) hybrid hydrogel has been used to fabricate beads for various drug delivery experiments [248, 249]. However, to our best knowledge, the combination of alg-CMC has not been explored for 3D bio-printing which is examined in this research. The extrusion-based in-house bio-printing system is used to fabricate 3D scaffold structures with special features. Dispensing material used in this technique requires a suitable viscosity and density as well as the shape fidelity retaining capability and high cell viability during and after printing [53]. A set of systematic quantitative characterization tests

such as rheological and mechanical test, filament collapse and fusion test, the effects of air pressure and print distance on filament width will be conducted to validate its printability, shape fidelity. Afterwards, 3D scaffold structures will be fabricated with various cell lines and the cell viability is recorded. The outcome of all these experiments and cell viability measurement will indicate the capability of this hybrid hydrogel as a candidate biomaterial for 3D bio-printing process.

4.1. Materials and methods

4.1.1. Preparation of bio-printer and scaffold toolpath

A three-axis in-house modified 3D bio-printer is used to fabricate the acellular and cell-laden scaffold under sterile condition. The hydrogel is stored in a disposable barrel reservoir (EFD, Nordson) and dispensed pneumatically through a dosing nozzle (EFD, Nordson, the inner diameter 410 μm) on a stationary print bed as shown in Figure 7. The hydrogel flow rate and width of filament are controlled by dispensing pressure, nozzle speed and print distance (i.e., the distance from the nozzle tip to build plane). The vectorized tool-path of the scaffold is programmed and converted into the machine-readable language with a visual basic based scripting language. The toolpath of the scaffold is designed and machine readable file format is prepared using the methodology described in chapter 3. The scaffold is fabricated layer-upon-layer where the hydrogel filaments of succeeding layer are deposited in a $0°/90°$ fashion into petri-dish. The spray of $CaCl_2$ ensures the physical cross-linking of the fabricated scaffold. The total solid loading of the material composition is restricted $\leq 10\%$ (w/v), because more than that solid content may reduce the cell viability than 80% [6, 46]. The weight percentage of alginate is kept constant at 4% due to prior reporting [45, 202] of high cell viability in up to 4% alginate solution. Even though 4% alginate shows good shear thinning behavior, only this percentage was

not a successful candidate to fabricate a defined 3D scaffold [45]. Therefore, various percentage of CMC is mixed with 4% alginate to get better cell viability and printability. For various compositions of alg-CMC (4:1; 2:1, 4:3 and 1:1), 1D line, 2D grid and 3D scaffolds are printed, and the filament width and pore size are measured using ImageJ software unless and otherwise stated. For each data of filament width and pore size, three random measurements (n = 3) are taken from random locations, and the data are represented as a mean ± standard deviation.

4.1.2. Preparation of hybrid hydrogel

The bio-materials used for scaffold fabrication are alginate (alginic acid sodium salt from brown algae; Sigma-Aldrich) and carboxymethyl cellulose (CMC) (Sigma-Aldrich). The chemical structures of that two material are shown in Figure 1 (a) and 1 (b) respectively. Alginate is a common biopolymer, composed of $(1-4)$-linked β-D mannuronic (M) and α-L guluronic acids (G) as shown in Figure 30 (a). This material is a negatively charged linear copolymer (M and G blocks) which is soluble in the water and supports cell growth and exhibits high biocompatibility. The G-block of this material assists to form gels and GM and M blocks improve the flexibility. Carboxymethylcellulose (CMC) is an anionic water-soluble biopolymer derived naturally or through chemical reaction from cellulose. It is a copolymer of β-D-glucose and β-D-glucopyranose-2-O-(carboxymethyl)-monosodium salt which are connected via β-1,4-glucosidic bonds [190]. The chemical formula of CMC is shown in Figure 30 (b). This material is non-toxic and non-allergenic, is widely used as thickener [250]. Each glucose monomer has three hydroxyl groups which can be substituted by a carboxyl group. More substitution of the hydroxyl group by carboxyl makes the cellulose more soluble, thicken and stable [190].
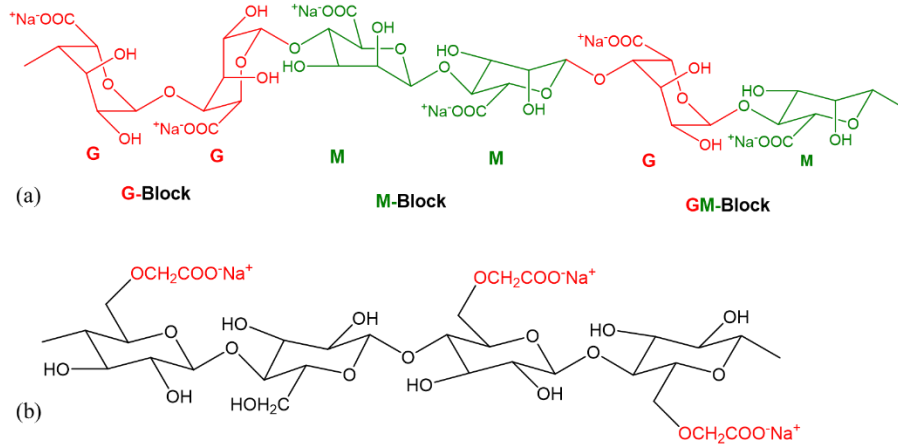
Figure 30: Chemical formula of (a) Alginate, (b) Carboxymethyl Cellulose.

A pure alginate and mixture of alginate and carboxymethyl cellulose (alg-CMC) solutions are prepared following the steps shown in Figure 31. Since both alginate and CMC are polar solute, they are soluble in water. These two materials make intermolecular action through the formation of hydrogen bonds and consequently compatible blended hybrid hydrogel. 4% (w/v) $CaCl_2$ (Sigma-Aldrich) is prepared with 0.2 μm filtered deionized (DI) water and used as chemical cross-linker. The extrusion-based bio-printing system needs fast gelation. Since, alginate contains carboxyl group (-COO-), this part of the hybrid hydrogel is cross-linked with the application of divalent cation, e.g., Ca^{2+}. Ca^{2+} generates ionic inter-chain bridges with G and M blocks and assists to achieve fast gelation. CMC also contains carboxyl group (-COO-) which forms calcium complex with the presence of Ca^{2+}. Hence, this hybrid hydrogel aids the fast formation of gel during fabrication and encapsulates the cells. Moreover, mixing CMC with alginate will increase the solution viscosity which will improve the printability.

56
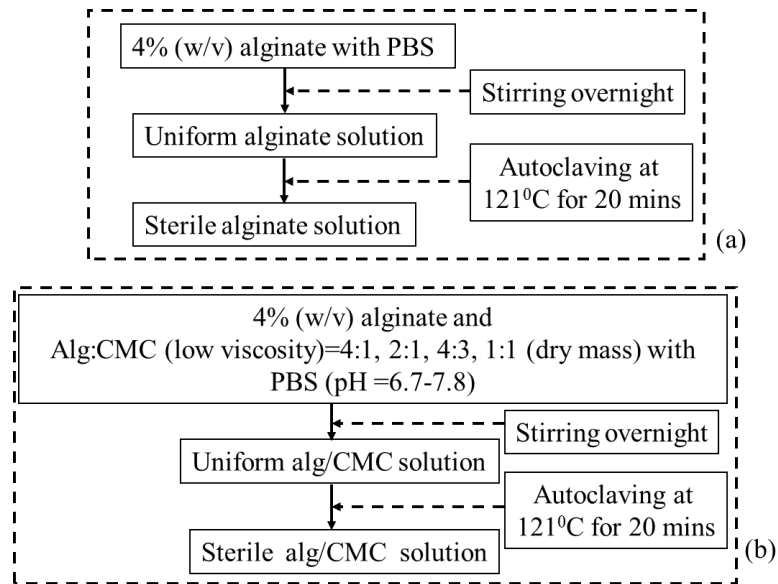
Figure 31: Preparation of hydrogel composed with: (a) Alginate, and (b) Alginate-CMC.

4.1.3. Rheological test of hybrid hydrogel

Rheological measurements were performed using a rotational rheometer (ARES-LS2, TA instruments, New Castle, DE, USA) with parallel plate geometry (20 mm flat plate). All measurements were recorded with a 1.0 mm gap width at 25^0C. The viscosities and shear stress of different concentrations were assessed using rotational test at a stress rate of 0.1 to 100 s^{-1}. The dynamic sweep stress test is done at stress rate of 0.1 to 100% to determine the solid and liquid-like state of different bio-inks. The frequency sweep test (0.1 to $100s^{-1}$) and three interval thixotropic test (3iTT) (stress rate of 0.1 to 100%) were also performed to characterize the bio-ink.The rheological properties i.e. viscosities, shear stress of bio-ink with different alginate and CMC compositions were assessed by different rheological measurements. The impact of the different concentrations of CMC on rheological behavior with respect to the shear rate and frequencies is determined by steady rate sweep test, dynamic stress sweep test, frequency sweep test and three point interval thixotropic test.

4.1.4. Mechanical test of hybrid hydrogel

The Young's modulus of the specimens is determined using the Nano-indentation equipment. Indentation is recorded at six random spots (n = 6) during each run of the experiment. Measurements are carried out at room temperature with an Atomic Force Microscopy, i.e., AFM (Dimension 3100, Veeco, USA). The indenter used in this test is a rectangular 0.01-0.025 Ωcm Anatomy (n) doped Si tip (RTESPA-300, Bruker, USA). The resonance frequency and an average spring constant of the indenter are about 300 kHz and 40 N/m respectively. The radius of curvature at the tip is nominally 8nm and tip half angle is 20^0. The test indentation on sapphire (Bruker, USA) determines the deflection sensitivity of the indenter. Once Young's modulus is determined, the reduced modulus is calculated using the following equation:

$$\frac{1}{E_r} = \frac{1-\nu^2}{E} + \frac{1-\nu_i^2}{E_i} \qquad (9)$$

Where E_r is reduced modulus, E_i=150 GPa and $\nu_i = 0.17$ is Poisson's ratio of the probe respectively, E and ν are Young's modulus and Poisson's ratio of the sample. The Poisson's ratio of the sample is considered as $\nu = 0.5$.

4.1.5. Scanning electron microscope

The microstructure of fabricated scaffold is analyzed by scanning electron microscopy (JEOL, JSM-6010LA, analytical Scanning electron microscope). The accelerating voltage, spot size (SS), and working distance (WD) used in this imaging are 10kV, 50mm and 13-14 mm respectively with magnifications of x27, x130, x160, x180, x700 scale. The samples have been washed three times with PBS containing Ca^{2+} and Mg^{2+} and dehydrated using a gradation series of ethanol/distilled water solutions.

4.1.6. Swelling test

The swelling test is done following the protocol described in the literature [251]. Briefly, sample filaments with various material compositions i.e. 4% alginate, 4% alginate-1% CMC, 4% alginate-2% CMC, 4% alginate-3% CMC, 4% alginate-4% CMC has length of 1 cm are printed with a diameter of 250 µm dispensing nozzle. The sample number for each material combination is n = 3. Before storing them in liquid media, the weight of all the filaments is recorded and denoted as dry weight (W_d). All of the printed filaments are immersed in the culture media and incubator having ideal culture condition, i.e., 37^0C and 5% CO_2. The weights of the filaments are recorded every day up to 11 days and denoted this weight as wet weight (W_w). Using the following equation, % of swelling rate of these filaments is determined:

$$\% \text{ of swelling rate} = \frac{W_w - W_d}{W_d} \times 100 \tag{10}$$

4.1.7. Shape fidelity test

Alginate and CMC are mixed together for having accurate pore size and geometry during bio-printing. This hybrid hydrogel may enable to achieve physical gelation characteristics and solidified filament morphology after extrusion to support the successive layers. To investigate the capability of this hybrid hydrogel in term of printability and shape fidelity, a set of systematic qualitative and quantitative characterization tests such as filament fusion and collapse test, the effects of air pressure and print distance on filament width, lateral pore collapse test will be conducted in this section.

4.1.7.1. Filament fusion test

Four consecutive layers of various alg-CMC compositions are fabricated layer-upon-layer without applying $CaCl_2$ to conduct the filament fusion test. The fabricated scaffold follows

0^0-90^0 pattern which captures the 2D effect and increasing filament to filament distance (FD). The range of filament to filament distance used here is 1-5 mm with 1 mm increments. After considering the filament diameter (d_f), the raster width is defined as, $R_w = FD - d_f$ as shown in Figure 32. To facilitate the visualization, each composition is mixed with different colors. To avoid the undesirable surface tension, measurement is recorded from two top layers. Air pressure, nozzle speed, nozzle diameter and print distance used in this test are respectively 8 psi, 5 mm/s, 0.41 mm and 0.7 mm. Pictures of fabricated scaffolds are taken with canon (EOS Rebel T6) high-resolution camera right after the fabrication to avoid the unwanted material spreading. Two different factors, i.e., the percentage of diffusion rate (rate of material spreading) (Df_r) and printability (P_r) [6] are determined respectively using equations (11) and (12) during filament fusion test shown below. The plotted values represent the 3 repetitions of measurements for each alg-CMC composition.

$$Df_r = \frac{A_t - A_a}{A_t} \times 100\% \tag{11}$$

$$P_r = \frac{L^2}{16 A_c} \tag{12}$$

Where, A_t and A_a are a theoretical and actual areas of pore respectively, L is the perimeter of the pore. The diffusion rate of a pore without any material spreading is 0 (i.e. $A_t = A_a$) and for a perfect square pore, the printability is 1.0.
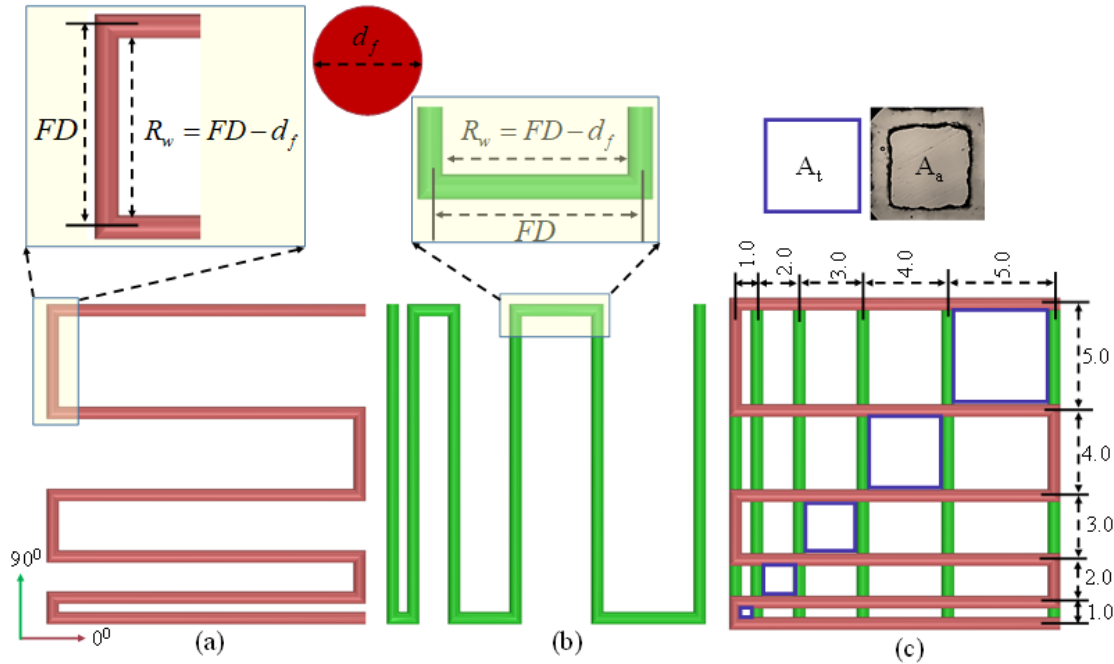
Figure 32: Filament deposited along (a) 0^0, (b) 90^0 and (c) 0^0-90^0.

4.1.7.2. Filament collapse test

The filament collapse test is conducted following our prior work (ref JMP pilling)work by Therriault *et al.* [252], where the mid-span deflection of a suspended filament of hydrogel was analyzed. A platform consisting of seven pillars with a known space of 1, 2, 3, 4, 5, 6 mm are modeled with a CAD software Rhino 5.0 as shown in Figure 33 (a). The dimension of five pillars situated in the middle is 2x10x6 mm, and the dimension of the two corner pillars is 5x10x6 mm. The platform is fabricated using "Dimension 1200es" 3D printer made by Stratasys with ABS material as shown in Figure 33 (a). A single filament of various compositions is deposited on this platform as shown in Figure 33(b).
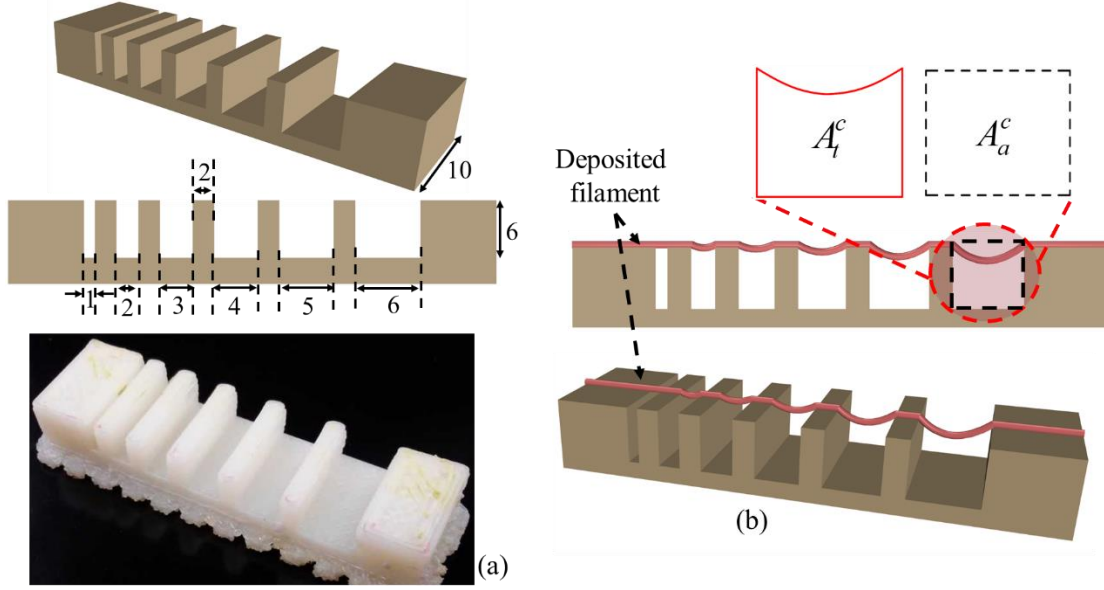
Figure 33: (a) Model and fabricated part of the platform, (b) Determination of collapse area factor.

The picture of the deposited filament is taken with canon (EOS Rebel T6) high-resolution camera right after the suspension to avoid the unwanted material deflection. Air pressure, nozzle diameter and nozzle speed used for this test are respectively 8 psi, 5mm/s, and 0.41mm. Collapse area factor (C_f), i.e., the percentage of the actual area after deflecting the suspended filament with respect to the theoretical area is determined using the following equation:

$$C_f = \frac{A_a^c}{A_t^c} \times 100\% \tag{13}$$

Where, A_a^c and A_t^c are actual and theoretical area respectively as shown in Figure 33 (b). If the material is too viscous and unable to make a bridge between two pillars, the actual area is considered as zero and so as the collapse area factor. On the other hand, if filament does not collapse and makes a straight bridge between two consecutive pillars, then $A_a^c = A_t^c$ and consequently the collapse area factor is 100%. The plotted values represent the 3 repetitions of measurements for each alg-CMC composition.

4.1.7.3. Effect of nozzle speed, air pressure, and print distance on filament width

For each composition of the hydrogel, a line having 10 mm length is deposited (three layers) with various nozzle speed, i.e., 4, 5, 6, 7, 8, 9, 10 mm/s. The air pressure and print distance used for this test are 8 psi and 0.7mm respectively. To determine the effect of air pressure and print distance on filament width, a line having 10 mm length is deposited (three layers) with the material composition of 4% alg-2% CMC and 4% alg-4% CMC. A range of pneumatic pressure (5, 6, 8, 10, 12, and 15 psi) is selected from prior literature and the prints are analyzed to find the effect of air pressure. The nozzle speed, print distance are used for this test is 5 mm/s and 0.7 mm respectively. Various print distances, *e.g.*, 0.4, 0.7, 0.9, 1.1, 1.3, and 1.5 mm are used to demonstrate the effect of print distance on filament width. The nozzle speed and air pressure used for this test are 5 mm/s and 8 psi respectively. For our tests, 0.41mm nozzle diameter is used. The width of the filament is recorded with Zeiss bright field inverted microscope for each of this test. The plotted values represent the 3 repetitions of measurements for statistical significance.

4.1.7.4. Qualitative and quantitative test for lateral pore

Two different qualitative tests are conducted during fabrication of scaffold. Firstly, each of the compositions is suspended in open air with an 8 psi air pressure and 10 mm print distance and observed if it makes continuous filament or just droplets. If any composition makes continuous filament, this is defined as proper gelation as shown in Figure 34(a). The composition making proper gelation potentially may maintain the shape fidelity of the fabricated scaffold. On the other hand, the composition making droplet during suspension is defined as under-gelation as shown in Figure 34(a) which loses the shape fidelity during the progress of scaffold fabrication. Secondly, the lateral porosity of the fabricated scaffold with each of the compositions is visually

63

observed to see the difference. Scaffold fabricated with the composition having a lower viscosity will collapse in the overhang region between two consecutive filaments of the lower layer, and eventually, the lateral pore may diminish.
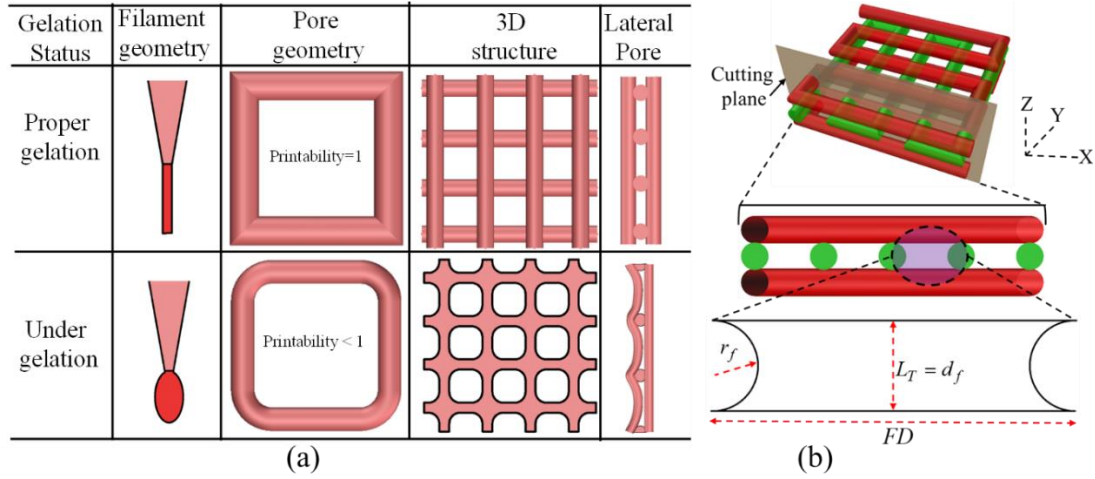
Figure 34: (a) Qualitative, and (b) Quantitative test of lateral pore.

The shape fidelity can be described quantitatively in term of the lateral porosity as shown in Figure 34(b). The lateral collapse area factor, i.e., the percentage of the actual lateral area of each lateral pore with respect to the theoretical lateral pore area, is determined using the following equation:

$$C_f^l = \frac{A_a^l}{FD \times LT - \pi r_f^2} \times 100\% \tag{14}$$

Where, A_a^l is the actual area of the lateral pore, LT and r_f are theoretical layer thickness and theoretical radius of filament respectively as shown in Figure 34(b). If the lateral pore is diminished after fabrication of the scaffold, i.e. $A_a^l = 0$ and so as the lateral collapse area factor. The higher value of $C_f^l \to 1$ reflecting the better preservation of lateral pore and so as the scaffold shape fidelity.

The list of tests proposed in this section will assist to find the material compositions to fabricate large scale scaffold with proper printability and shape fidelity.

64

4.1.8. Cell culture and cell-laden scaffold fabrication

BxPC3, the human pancreatic cancer cell, human embryonic kidney cell (HEK 293) are cultured and maintained in high glucose DMEM, 2 mM Glutamine, and 10% Fetal Bovine Serum (FBS) with 100 µg /ml penicillin and 100 µg/ml streptomycin (Sigma-Aldrich) in 5% CO_2 at 37^0C incubator. Prostate stem cancer cell is cultured and maintained in high glucose Prostate cancer cell media, 2 mM Glutamine, and 10% Fetal Bovine Serum (FBS) with 100 µg /ml penicillin and 100 µg/ml streptomycin (Sigma-Aldrich) in 5% CO_2 at 37^0C incubator. Finally, Porc1 cell is cultured and maintained in high glucose DMEM/F12, 10% Fatal Bovine Serum (FBS), with 100 µg /ml penicillin and 100µg/ml streptomycin (Sigma-Aldrich) in 5% CO_2 and 37^0C incubator. The culture medium is changed twice a week. Cells in passage 3-5 are used for the 3D bio-printing. For cell-laden scaffold fabrication, 2×10^6 to 6×10^6 cells/ml are mixed with alginate and alg-CMC solutions respectively into disposable barrel reservoir (EFD, Nordson) and dispensed pneumatically through a dosing nozzle (EFD, Nordson, the inner diameter 250 µm) as shown in Figure 35(a). A 0^0-90^0 deposition direction is followed to dispense ten layers of cell-laden scaffold with a dimension of 10mm×10mm×2.0mm with1.0 mm filament to filament distance.

The cell-laden scaffold is preserved in 5% CO_2, and 37^0C incubator with the same medium used for cell culture referred in above. The medium was changed twice in a week. Bio-printing of cell-laden scaffold and incubation are schematically shown in Figure 35 (b) and Figure 35 (c) respectively.
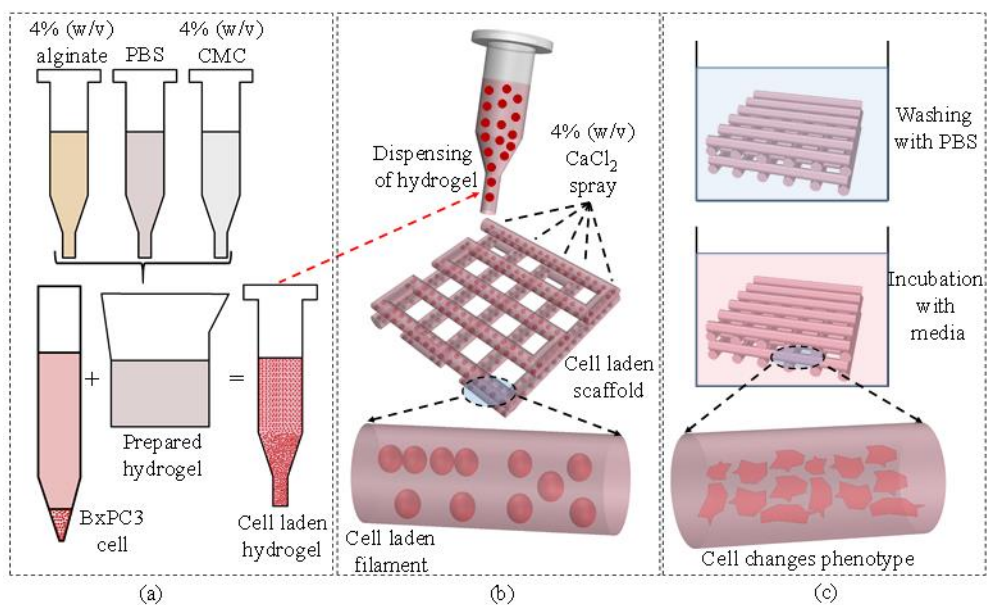
Figure 35: (a) Preparation of cell-laden hydrogel, (b) bio-printing of the cell-laden hydrogel, and (c) incubation of fabricated scaffold.

4.2. Results and discussion

4.2.1. Rheological test result

Various rheological tests *i.e.* steady rate sweep test, dynamic stress sweep test, frequency sweep test, 3-interval thixotropic tests are conducted to detemine the suitable combination of alginate and CMC. The outcome of each rheological test is analyzed in this section to suggest a suitable combination of alginate and CMC which will be able to hold the shape of fabricated large scaffold with proper prinability and shape fidelity.

4.2.1.1. Steady rate sweep test

Figure 36 (a) and Figure 36 (b) show the log-log plot of viscosity and shear stress vs shear strain rate respectively. Viscosity decreases with increasing the shear rate whereas the shear stress increases with increasing the shear rate. This phenomenon demonstrates the shear thinning behavior of all the compositions. However, the addition of CMC with suspension increases the viscosity as well as the shear stress. Zero-shear viscosity value of alginate hydrogel

66

with 4% CMC composition increases almost from 1 Pa.S to 600 Pa.s with respect to only 4% alginate. This might happen because of increasing the cross-linking rate with increased amount of CMC into the suspension.
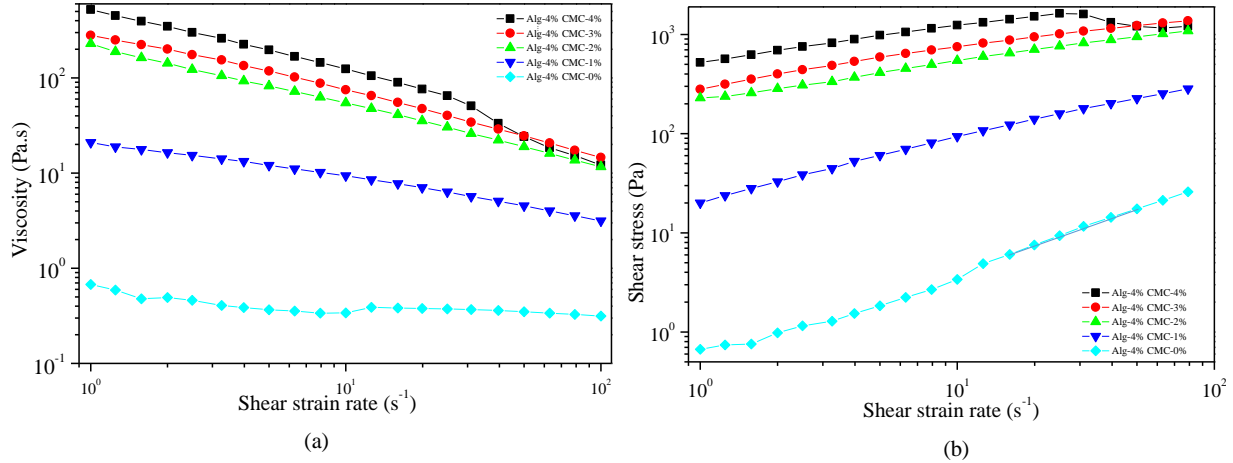
Figure 36: Evaluation of shear thinning behavior of hydrogels: (a) Viscosity vs shear strain rate, (b) Shear stress vs shear strain rate.

The shear thinning behavior of all pseudo-plastic materials can be approximated by the following Herschel-Bulkley model [253, 254]:

$$\tau = \tau_o + K\dot{\gamma}^n \tag{15}$$

Where, τ and τ_0 are the static and dynamic yield shear stress (Pa) respectively, K is the model factor (consistency index in Pa.s^n) and $\dot{\gamma}$ is the shear rate (s^{-1}) and n is the flow index. Graph from Figure 36(b) is fitted to this model with 95% confidence interval. R^2-value varies from 95 to 99 as shown in Table 6. Value of n less than 1 demonstrates that all the compositions are non-Newtonian fluid. Addition of CMC from 1-4% with alginate hydrogel shifts the Newtonian characteristics to shear thinning, because the n-value is dropped down from 0.98 to 0.71 and yield shear stress is increased from 0.43 Pa to almost 512 Pa. This phenomenon reveals that mixing CMC leads to stronger mechanical strength and achieves better ability to retain the shape

67

fidelity after material deposition. The model factor K reflects the viscosity component (Pa.s^n) which increases with increasing the percentage of CMC. Therefore, alginate with 4% CMC shows better extrudability through nozzle due to reduce the viscosity with the application of shear stress.

Table 6: Herschel-Bulkley model parameters for the curve shear stress vs shear strain rate for various compositions.

Composition	τ_o (Pa)	K (Pa.s^n)	n	R^2
Alg-4% CMC-4%	511.9	126	0.71	96
Alg-4% CMC-3%	301	69.24	0.76	95
Alg-4% CMC-2%	221.8	44.23	0.81	97
Alg-4% CMC-1%	22.13	7.43	0.91	98
Alg-4%	0.43	0.23	0.98	99
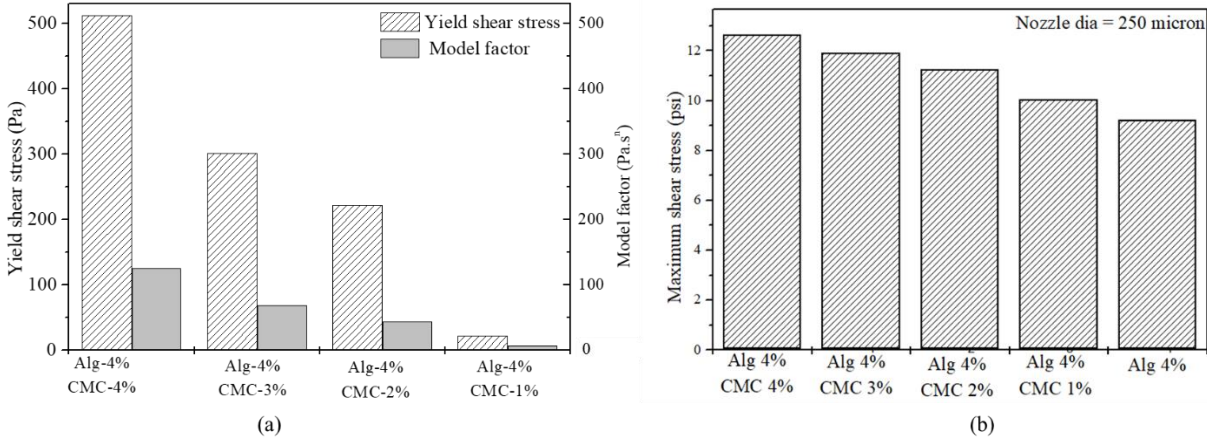
Figure 37: (a) Yield stress and model factor and (b) Maximum shear stress.

The flow rate of all the compositions with respect to corresponding n, shear strain rate (γ_0) and viscosity (η_0) is determined using the following equation:

$$Q = \left(\frac{n}{3n+1}\right) \pi \gamma_0^{\frac{n-1}{n}} \left(\frac{\partial P/\partial z}{2\eta_0}\right) R^{\frac{3n+1}{n}}$$

(16)

Where, $\partial P / \partial z$ is the pressure gradient which is a unique value for a given deposition system, R=125 µm, is the radius of the nozzle. Finally, the maximum shear stress of all the compositions for corresponding n value is determined using the following equation as shown in Figure 37 (b):

$$\tau_{max} = \left(\frac{n}{3n+1}\right)^n \frac{D}{4} \frac{\partial P}{\partial z} \tag{17}$$

Where D is the diameter of the nozzle.

4.2.1.2. Dynamic stress sweep test

One of the characterizing factors for viscoelastic suspension is their complex shear modulus (G^*) which is expressed by the following equation:

$$G^* = G' + iG'' \tag{18}$$

Where G' is the elastic (or storage) modulus, the real component and G'' viscous (or loss) modulus, the imaginary component of equation (1). The dynamic stress sweep test for various compositions of the hydrogel at 1 Hz is represented the outcome of G' and G'' vs shear strain (%) in Figure 38. It is clear from the figure that with increasing the percentage of CMC into the alginate suspension, the physical state of the hydrogel is transferred from liquid-like to solid-like state. With 0-2% of CMC, value of G'' dominates G' at each shear strain. Thereby, the liquid-like state is persisted for these two hydrogel compositions. With increasing the amount of CMC in the suspension from 3 to 4%, G' dominates G'' up to a certain level of shear strain and then intersects. This certain level is called as linear viscoelastic range (LVR) which determines the limit at which the suspension preserves the sedimentation within the sample without permanent deformation. This resembles the solid-like behavior of the suspension before the intersecting point. After the intersecting point, both moduli are decreased with the dominancy of G'' i.e. the liquid-like phase. In the co-existence of liquid and solid-like phase, increasing the percentage of

69

CMC increases the LVR as shown in Figure 38 (iii-v). To provide more insight into solid and

liquid-like behavior of hydrogel, dynamic mechanical loss tangent ($\tan\delta = G''/G'$) is implied as

shown in Figure 38(vi). Tangent value smaller than 1 predominantly reflects the elastic behavior,

and greater than 1 predominantly indicates viscous behavior. It is clear from the Figure 38 (vi)

that alginate with 4% CMC shows predominant solid-like behavior up to 60% shear strain.

Besides, alginate with 3% CMC shows solid-like behavior up to 0.3% and 8% strain rate

respectively.
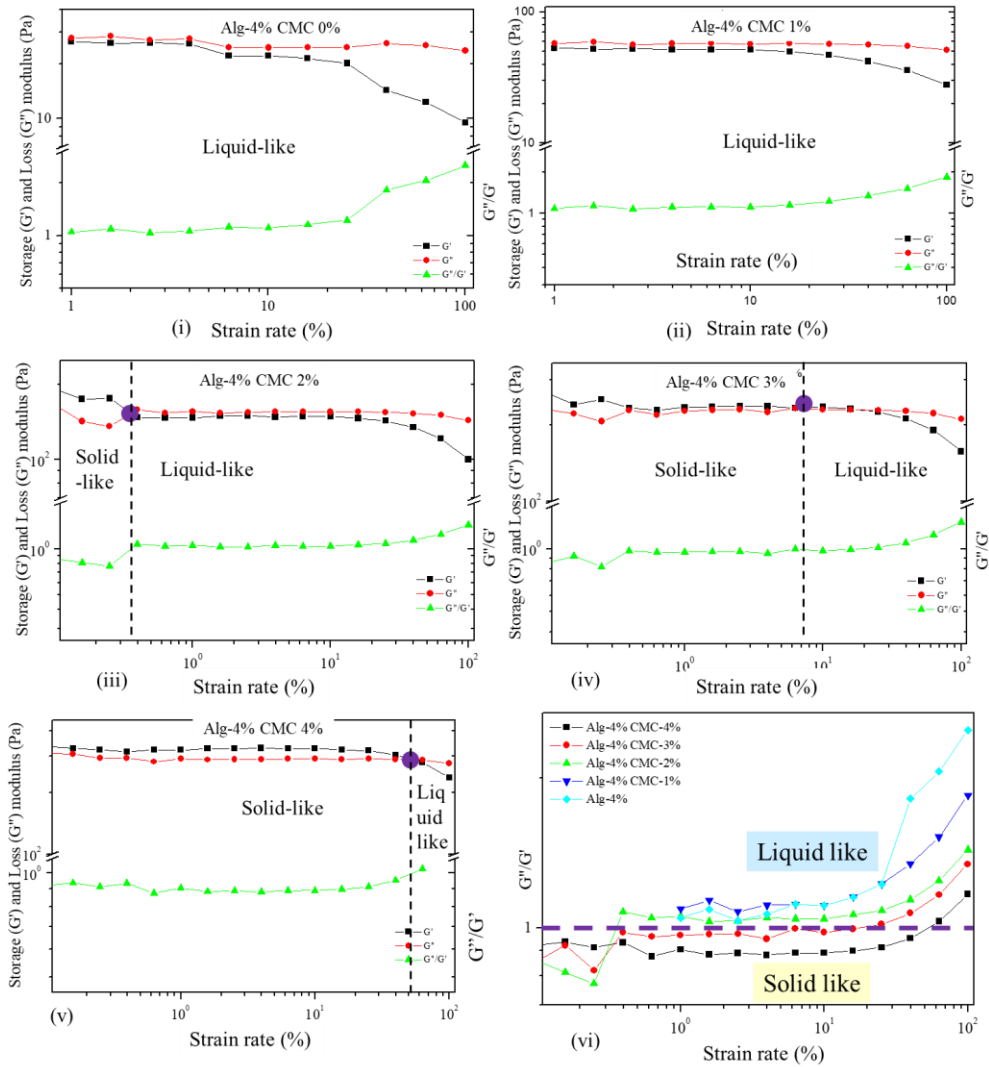
Figure 38: (a) Dynamic strain sweep test.

4.2.1.3. Frequency sweep test

The outcome from frequency sweep test offers more insight about the interactions among hydrogel particles which is known as colloidal force. Here, with increasing the frequency, G' shows dominating character than G''. However, G' and G'' values for 4% CMC is at least one order higher than other compositions as shown in Figure 39. The phenomenon reflects more particle to particle interaction i.e. colloidal force into the hydrogel due to the presence of CMC. This behavior makes this composition more suitable for extrusion-based bio-printing.
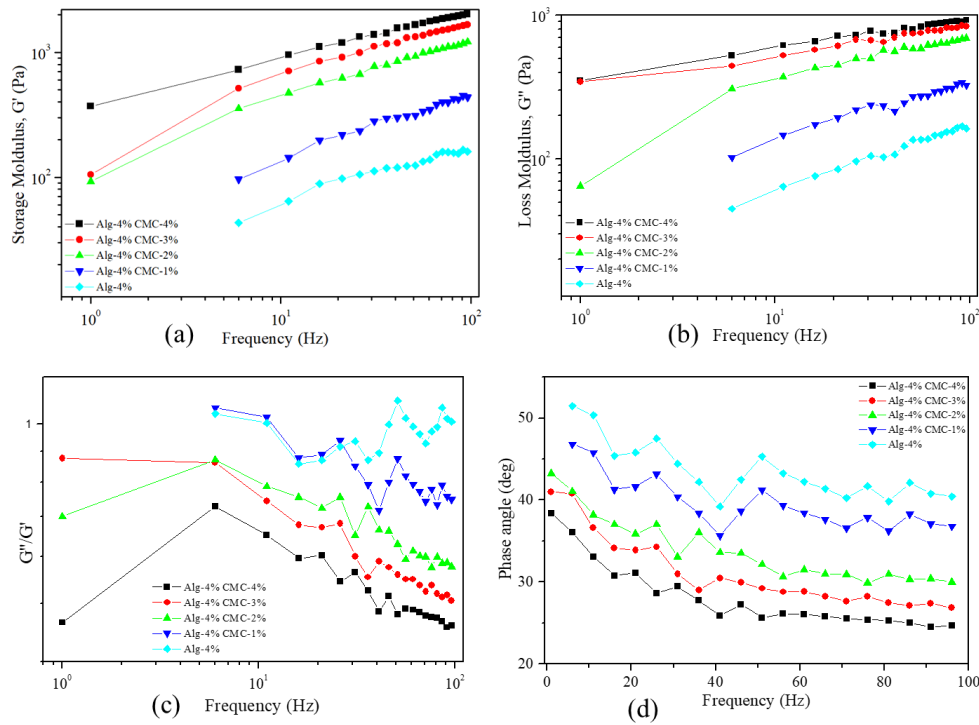
Figure 39: Result of frequency sweep test for various compositions: (a) Storage modulus vs frequency, (b) Loss modulus vs frequency, and (c) Dynamic mechanical loss vs frequency, and (d) Phase angle vs frequency.

4.2.1.4. Three point interval thixotropic test

To provide more understanding of the real scenario during extrusion of hydrogel, 3-interval-thixotropy-tests are also conducted on various compositions. In this test, the first interval imitates the at-rest state of sample, the second interval resembles the hydrogel decomposition

71

under high shear i.e. experienced high shear during extrusion, and third interval reflects the structure retention after hydrogel extrusion as shown in Figure 40 (a). The stress-shear rate loop shown in Figure 40 (c) demonstrates the shear history of alginate with 4% CMC. A stress is applied on the at-rest hydrogel which breaks down the initial network structures of the hydrogel. After the hydrogel is extruded through the nozzle at a certain shear rate, it takes time to recover the internal network. In most cases, when the shear is released, the stress path lags forming a hysteresis loop as shown in Figure 40 (c). The area within the hysteresis loop signifies the energy consumed in the internal network breakdown. From Figure 40 (b), it is clear that alginate with 4% CMC consumes more energy to break down the internal network than other compositions.
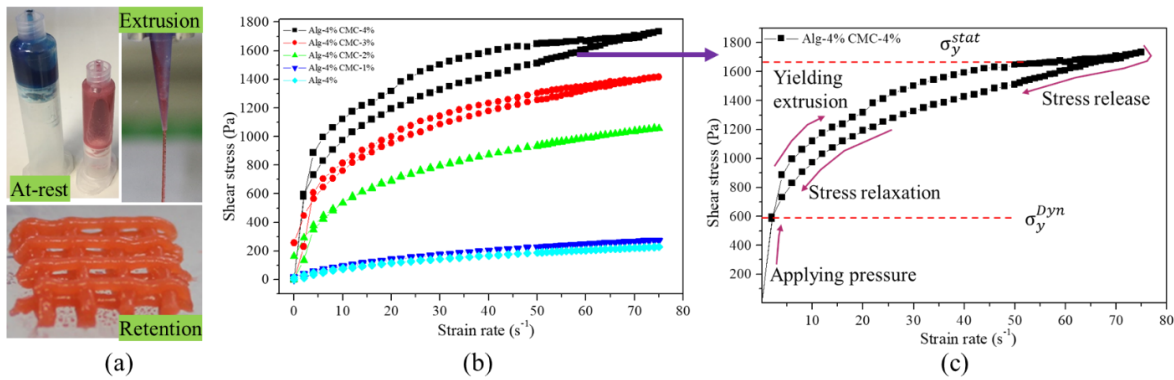
Figure 40: (a) Representation of three states during extrusion, (b-c) Result of 3-Interval-thixotropic-tests.

The viscosity and shear stress are also determined of some other compositions of alginate and CMC e.g. A_2C_5, A_3C_5, A_4C_5, A_2C_6 rather than the five candidates considered above to explore if they are suitable for 3D bio-printing as shown in Figure 41. Moreover, the viscosity is also compared with different alginate-CMC compositions having similar solid content e.g. 8%. It is clear from Figure 42 that, CMC has more effect on viscosity than alginate.
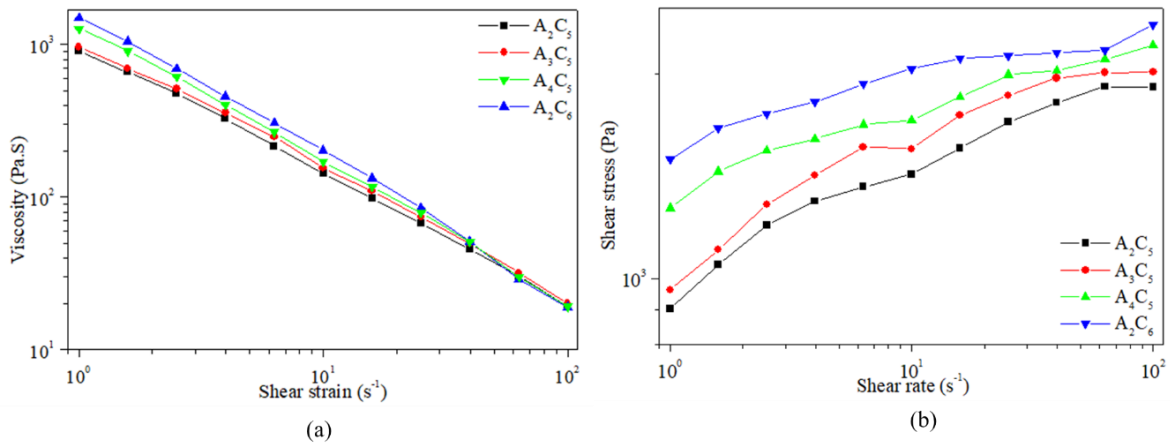
Figure 41: (a) Viscosity and shear stress of various composition of alginate and CMC.
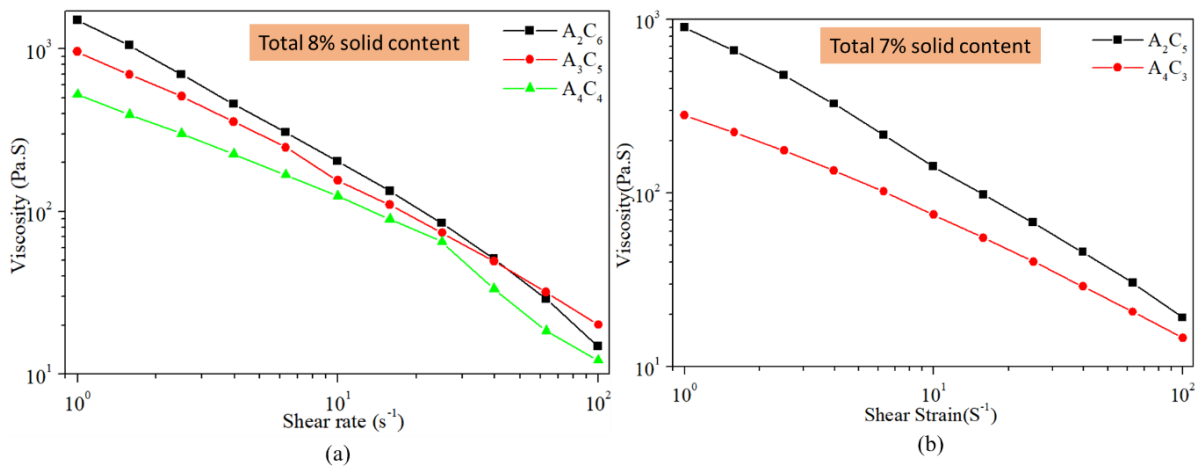
Figure 42: Viscosity of various alginate and CMC compositions having solid content of (a) 8% and (b) 7%.

4.2.1.5. Remarks for rheological test

Once all the rheological tests are done, it is clear from the result that the viscosity is solid content dependent. However, for similar percentage of solid content, CMC has more effect of the enhancement of viscosity. Here, 4% alginate-4% CMC is considered as optimum composition because it has moderate level of viscosity that will require comparatively less amount of air pressure to dispense. Moreover, other three rheological tests are also demonstrating that 4% alginate-4% CMC has better potential to maintain proper printability and shape fidelity during

large scaffold fabrication. Composition having higher viscosity may improve the printability more, but will create negative effect of encapsulated cell.

4.2.2. Mechanical testing

Mixing of CMC with alginate has increased the Young's and Reduced Modulus of the blended hydrogel as shown in Figure 43. Mean value of the response, i.e., Young's modulus of various material concentrations is significantly different (p-value =0 with 95% confidence interval). Incorporation of CMC into alginate increases the crosslinking density by increasing the $Ca^{2+}/-COO^-$ ionic interaction as shown in Figure 43. Moreover, the hydrogen bond between the same $-COO^-$ ion of alginate and CMC makes the hybrid hydrogel stronger. Hence, with the increment of CMC percentage leads the upward trend of the Young's and reduced modulus as shown in Figure 43.
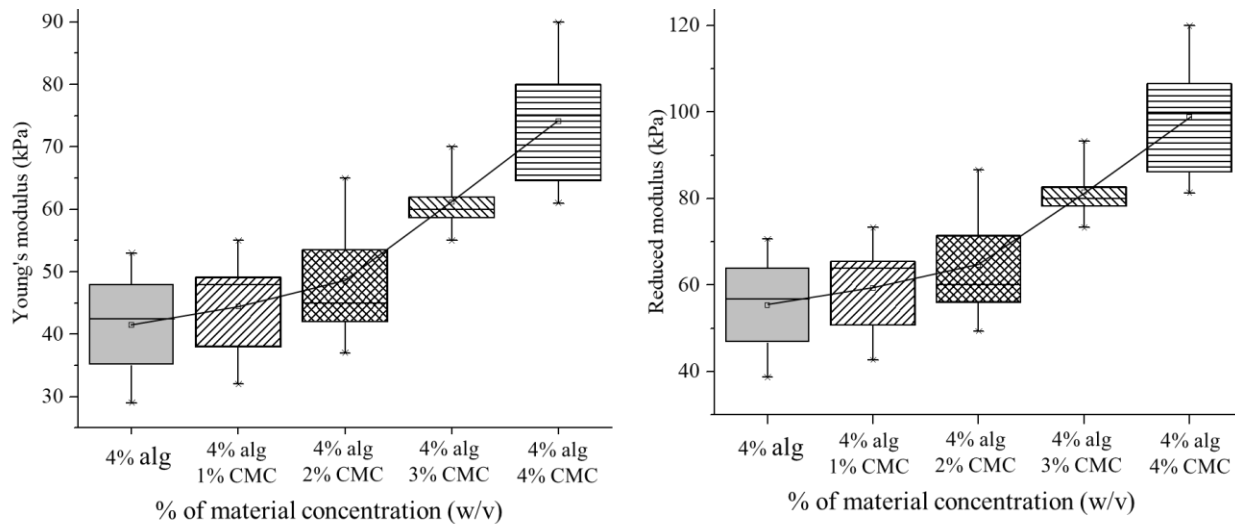
Figure 43: Young's and Reduced Modulus.

4.2.3. Microstructure of materials

To study the influence of CMC on the filament microstructure, SEM imaging is performed with novel hybrid hydrogel 4% alg-4% CMC in comparison to pure 4% alginate as

74

shown in Figure 44. The cross-linked filament surface of pure alginate is smooth because of

forming a primary membrane with Ca^{2+} as shown in Figure 44 (b). On the other hand, the

filament surface fabricated with alg-CMC hydrogel is highly porous as shown in Figure 44 (c)

assists potentially more to supply the nutrients and oxygen to the encapsulated cell. The filament

incubated 3 days showing more pores as shown in Figure 44 (d-f) indicating more release of

CMC.
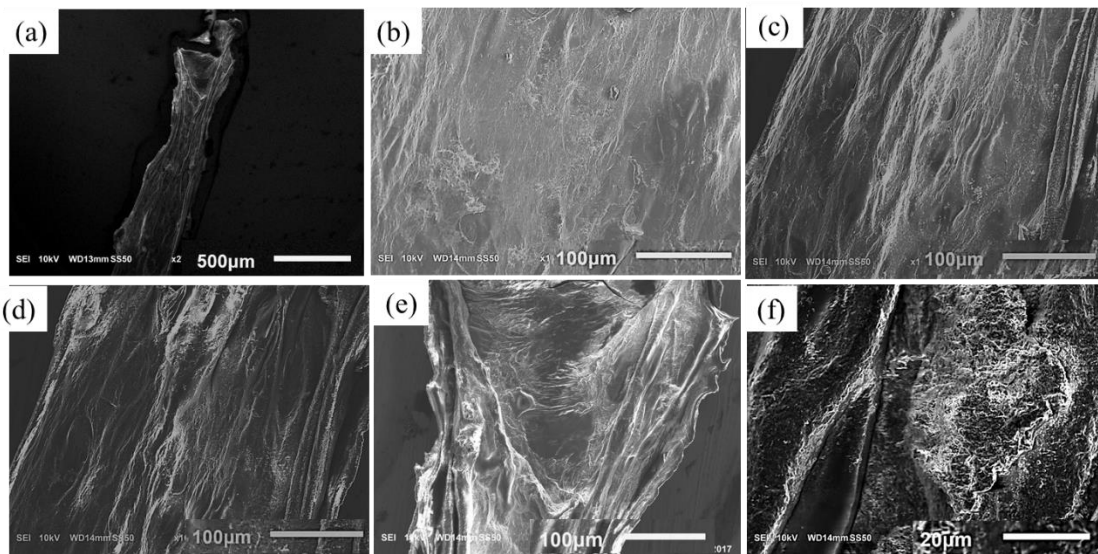
Figure 44: Scanning electron microscopy of filament with (a-b) 4%Alg and (c) 4%Alg-4% CMC
before incubation, (d-f) 4%Alg-4% CMC after 3 days of incubation.

4.2.4. Swelling of material

All the compositions of material exhibit an upward trend of the swelling rate with the

changes of time as shown in Figure 45. The mean swelling rate of each material combination at

different time periods, i.e., at day 1, 3, 5, 7, 9, 11 is significantly different (p-value=0 with 95%

confidence interval). Likewise, various material compositions show a significant difference in

swelling rate among them as shown in Figure 45. Reducing the percentage of CMC increases the

swelling rate, and pure alginate shows maximum swelling. The reason behind this behavior is the

addition of CMC increases the crosslinking density. Hence, the water absorption decreases and eventually the swelling rate.
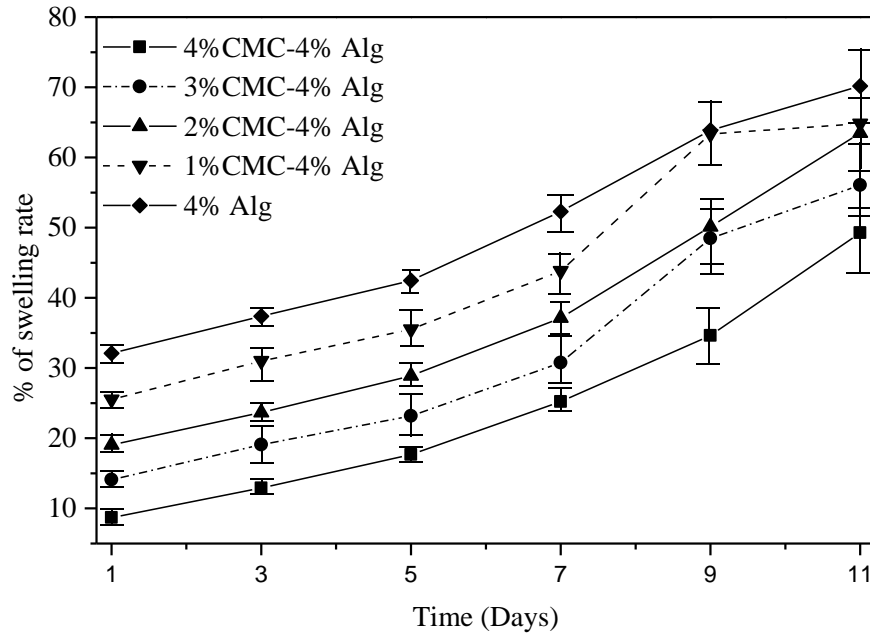
Figure 45: Swelling rate of different compositions of material.

4.2.5. Shape fidelity test result

The outcome of shape fidelity test will exhibit the capability of the considered material compositions' shape holding capacity. Specifically, the fusion test will determine the diffusion or spreading rate and measurement of printability of material compositions. The collapse test will identify the shape holding capacity of the deposited filament without support. The lateral pore collapse test will determine the capability to hold the lateral pore of the material compositions. How the nozzle speed, print distance, air pressure affect the filament width will also be identified from this test result.

4.2.5.1. Filament fusion and printability

To evaluate the effect of filament fusion and pore closure for each composition of the hydrogel, the area of the designed variational pore of the fabricated scaffold is measured as

shown in Figure 46. The diffusion rate and printability of each pore are determined following the equation (2) and (3) respectively. The diffusion rate shows decreasing trend where the printability shows an increasing trend with increasing the pore size for each composition of material as shown in Figure 47. Qualitatively, the 4% alg-4%CMC shows good pore size and geometry than other material compositions. The quantitative analysis of diffusion rate validates that the composition of 4% alg-4% CMC shows minimum material spreading, i.e. minimum diffusion rate than other compositions. The range of printability of 4% alg-4%CMC is 0.78 to 0.92 for the pore size 2mm to 5 mm which demonstrates almost square geometry of the pore. During diffusion test, the changes of layer thickness is also analyzed. Compared to 4% alg-4% CMC, the total build height of the scaffold fabricated with A_4C_3, A_4C_2, A_4C_1, and A_4C_0 are reduced by 22%, 33%, 40% and 59% respectively. This result indicates that compositions with less solid content diffuses more on xy-plane and undermine the filament stacking capacity which is also stated in existing literatures [38, 189].
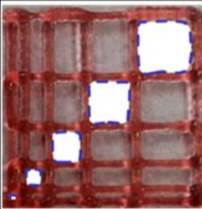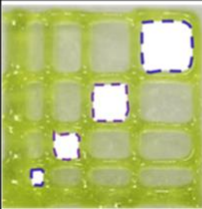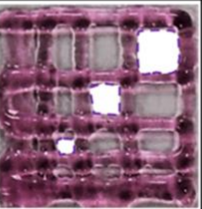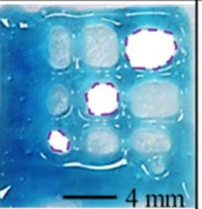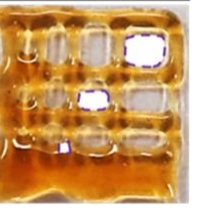
Figure 46: Filament fusion test.
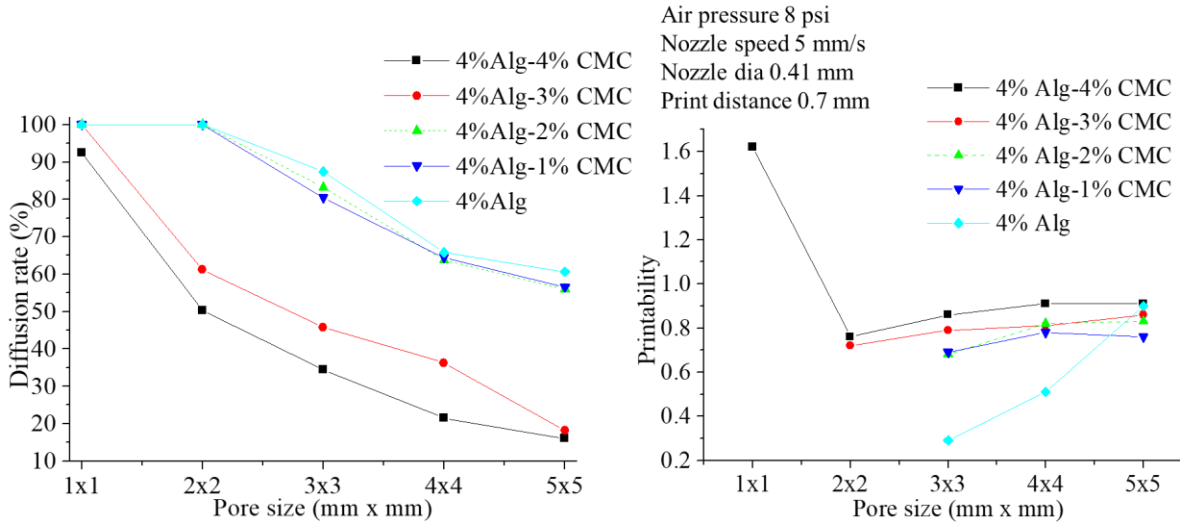
Figure 47: Diffusion rate and printability in filament fusion test.

To explore qualitatively, the same scaffold is fabricated with some other compositions of alginate and CMC e.g. A_2C_5, A_3C_5, A_4C_5, A_2C_6 rather than the five candidates considered above for fusion test as shown in Figure 48.

Figure 48: Filament fusion test at various air pressure.

It is clear from the Figure 48 that none of the considered composition is able to dispense continuous filament with even 12 psi where A_4C_4 is dispensing continuous filament with 8 psi air pressure. Requirement of such higher air pressure to dispense the continuous filament with A_2C_5, A_3C_5, A_4C_5, and A_2C_6 is supporting the viscosity result of these compositions shown in Figure 41. Hence, A_4C_4 qualifies as optimum composition in term of printability and diffusion rate because of dispensing continuous filament with 8 psi air pressure. Therefore, in rest of the experiments A_2C_5, A_3C_5, A_4C_5, A_2C_6 are not considered as potential candidates.

4.2.5.2. Filament collapse

The qualitative observation of the collapse test for various compositions of material identifies that with increasing the percentage of CMC leads minimum deflection of the suspended filament as shown in Figure 49(a). Composition with 4% alg-4% CMC generates almost straight filament on the pillars situated at various distances. The collapse area factor for each distance value of each material composition is determined using the equation (4). With increasing the pillar to pillar distance, the collapse area factor shows decreasing trend as shown in Figure 49 (b). The graph indicates the composition with 4% alg-4% CMC has minimum collapse area factor even with increasing the distance value. Composition with 4% alg-1% CMC is not able to hold the filament geometry and breaks away even at 4mm distance value. The same scenario happens for 4% alg at 3mm distance value. Hence, this event results in zero collapse area factors for these two compositions.
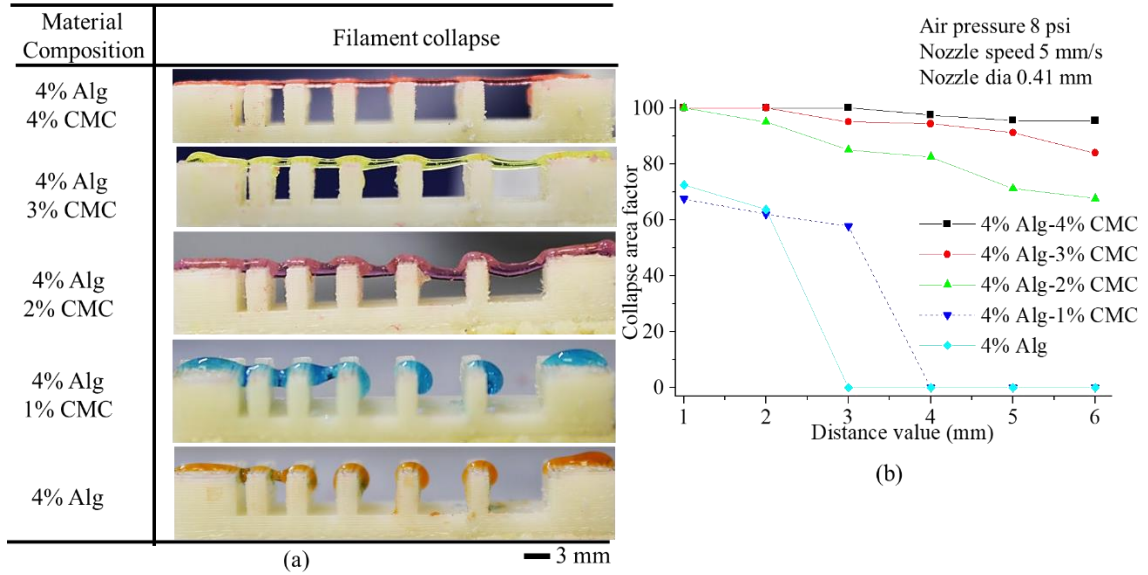
Figure 49: (a) Filament collapse test, and (b) Collapse area factor.

4.2.5.3. Effect of nozzle speed, air pressure and print distance on filament width

The nozzle speed directly influences the filament width for all types of material compositions as shown in Figure 50 (a). With increasing the nozzle speed, the filament width reduces for all material compositions as shown in Figure 50 (b).
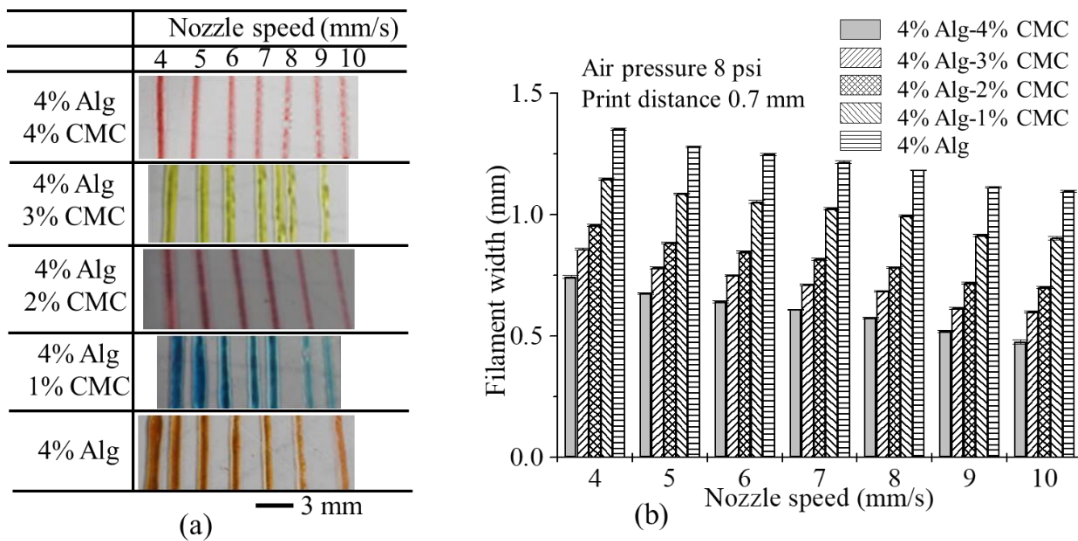
Figure 50: (a) Printed filaments at different nozzle speed, (b) the effect of nozzle speed on filament width.

With increasing the nozzle speed, the suspended filament experiences tension along deposition direction and become thinner. Higher nozzle speed may break down the filament results in a discontinuous material deposition. For each composition, the filament width is greater than the nozzle diameter because of material expansion after extrusion. The addition of CMC with alginate reduces the expansion of material after extrusion which results in less difference of the filament width with respect to original nozzle diameter at various nozzle speeds as shown in Figure 50 (b). Hence, composition with 4% alg-4% CMC shows minimum filament width than other compositions.

		4% Alg-2% CMC				4% Alg-4% CMC		
PD	PF	Corner	Deposition	Filament	PF	Corner	Deposition	Filament
0.4		Sharp	Normal	Straight		Sharp	Normal	Straight
0.7		Sharp	Normal	Straight		Sharp	Normal	Straight
0.9		Sharp	Over	Curvy		Sharp	Normal	Straight
1.1		Round	Over	Curvy		Sharp	Normal	Straight
1.3		Round	Over	Curvy		Round	Over	Curvy
1.5		Round	Over	Curvy		Round	Over	Curvy

(a)

Air pressure (psi)

| | 5 | 6 | 8 | 10 | 12 | 15 |

4% Alg 2% CMC

4% Alg 4% CMC

(b)

Figure 51: Qualitative effect of (a) print distance, (b) air pressure.

The effect of print distance on filament width is shown in Figure 51(a) and Figure 52 (a). With increasing the print distance, the filament width is increasing. Apparently, the corner of the deposited filament changes from sharp to round with increasing print distance. Filament deposited from a higher distance get less contact with the build plane which leads the starting point of the deposition further away and results in accumulation of material. This event also creates curvy filament as shown in Figure 52 (a). With increasing the portion of CMC, the

changes of filament width reduces with increasing the print distance. Composition with 4% alg-4% CMC shows a better corner and filament geometry, and material deposition than a composition with 4% alg-2% CMC.
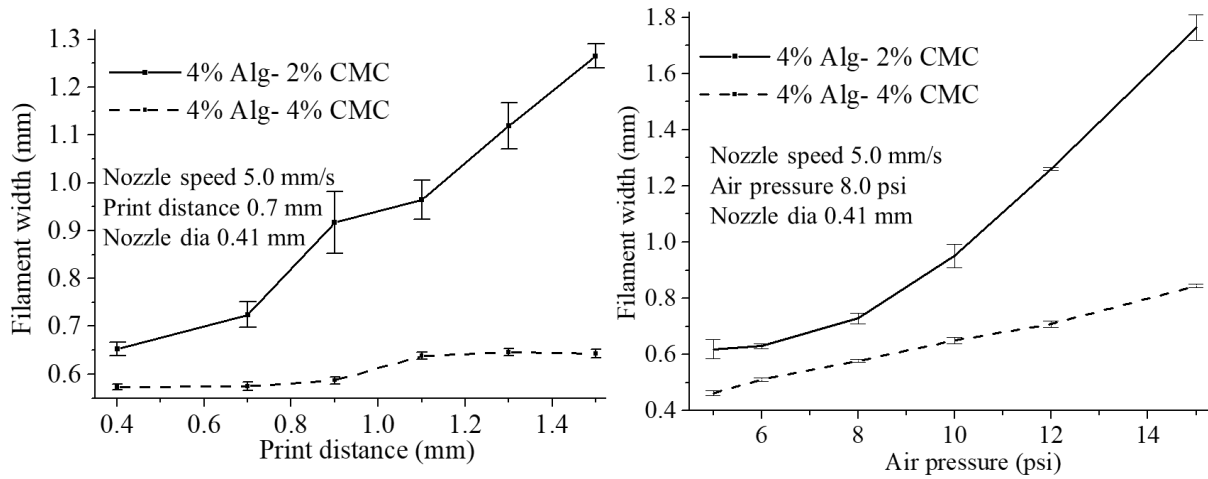
Figure 52: Effect of print distance and air pressure on filament width.

With increasing the air pressure, the filament width of 4% alg-2% CMC and 4% alg-4% CMC composition increases as shown in Figure 51(b) and Figure 52(b). However, the increased amount of CMC into alginate will reduce the changes of the filament width as shown in Figure 52 (b). Applying less air pressure may not exceed the surface tension of the material with the nozzle and eventually will not deposit continuous filament. Besides, over material deposition may happen due to high air pressure. Thereby, applying optimum air pressure for different material compositions will assure the continuous filament deposition as well as uniform filament width.

4.2.5.4. Qualitative and quantitative test of lateral pore

Scaffolds having a filament to filament distance of 3 mm are fabricated (10 layers) with compositions of 4%alg-4%CMC and 4%alg-2% CMC as shown in Figure 53(a). Qualitatively, each pore of the scaffold fabricated by former composition is almost square. On the other hand,

the pore geometry of scaffold fabricated by later composition is almost circular. To visualize the

lateral pore in the scaffold structure clearly, the scaffold is cut laterally and observed the lateral

pore macroscopically and microscopically. The presence of lateral pore in the scaffold fabricated

by 4%alg-4%CMC is quite clear. However, due to the higher collapse of the filament and

comparatively less viscosity, lateral pore in the scaffold fabricated by 4%alg-2%CMC was

almost invisible. Therefore, it can be claimed that scaffold fabricated by 4%alg-4%CMC

maintains the lateral pore as well.
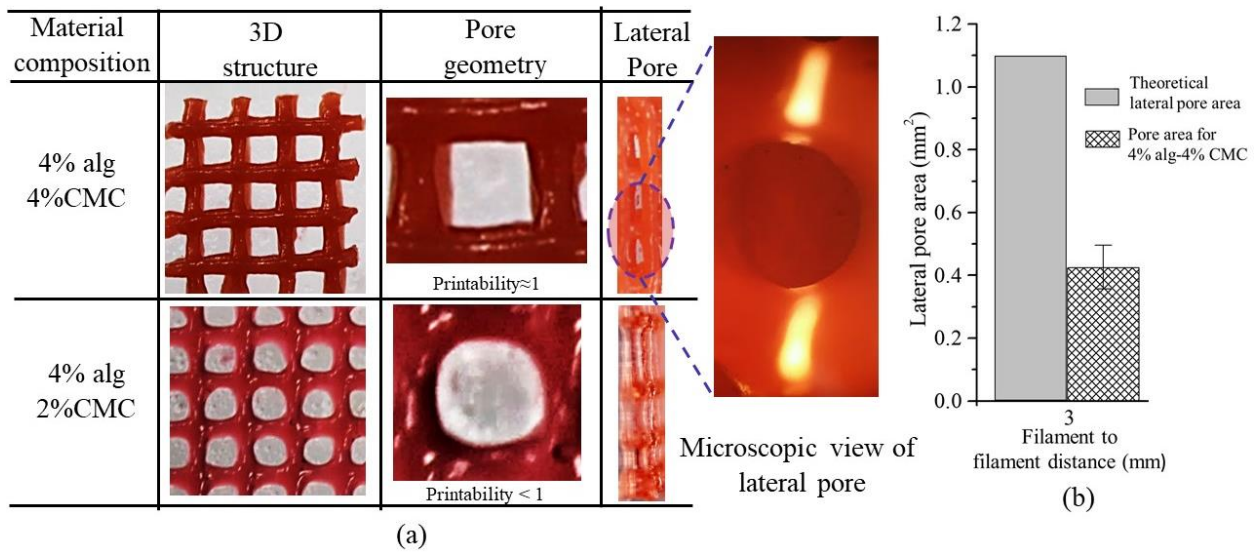
Figure 53: (a) Qualitative, and (b) Quantitative test for lateral pore.

For given 3mm filament to filament distance and 0.41 mm nozzle diameter, the

theoretical lateral pore area is calculated as 1.1 mm^2. The lateral pore area presented in the

scaffold fabricated by 4% alg-4%CMC is measured (n = 5) and compared with theoretical pore

area. Using equation (5), the lateral collapse area factor is determined as 37% for this specific

filament to filament distance and nozzle diameter. Since, there was no lateral pore in the

scaffold fabricated with 4% alg-2% CMC, lateral collapse area factor for this composition is

zero.

4.2.5.5. Remarks for shape fidelity

After doing a set of systematic qualitative and quantitative characterization tests, it is clear that 4% alginate-4% CMC maintains good printability and shape fidelity. This result indicates that 4% alginate-4% CMC can be a good candidate for the fabrication of large-scale scaffold.

4.2.6. Fabrication of large scaffold

Once the aforementioned characterization tests are done, it is revealed, the composition of 4%alg-4%CMC shows good printability and shape fidelity. Therefore, this composition is used to fabricate acellular large scale scaffolds as shown in Figure 54. Using this material composition, authors were able to fabricate the scaffold having a build height of 1.4 cm. The represented scaffold figures demonstrate the capability of this composition to hold the shape fidelity of large-scale scaffold fabrication.
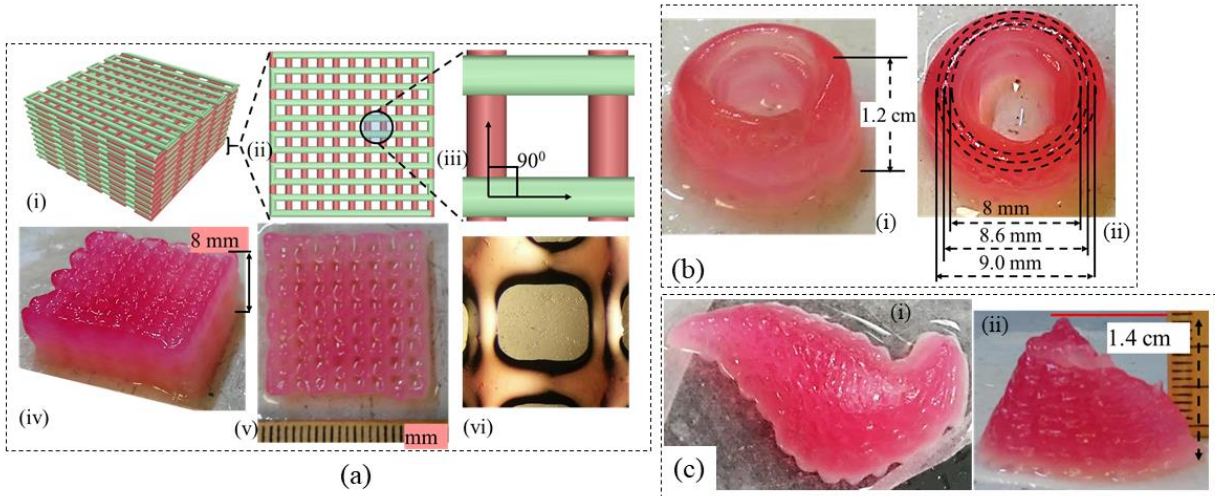
Figure 54: Large-scale scaffold fabricated by 4%alg-4%CMC.

4.2.7. Fabrication of scaffolds with multi-material

To demonstrate the capability of the modified bio-printer to fabricate the scaffold with multiple materials, same hydrogel material i.e. alginate-CMC with two different colors is used in

two dispensing nozzles. The machine readable file is generated following *Process flow diagram* of Figure 14. The generated toolpath and fabricated scaffold are shown in Figure 55**.**

(a)   (b)
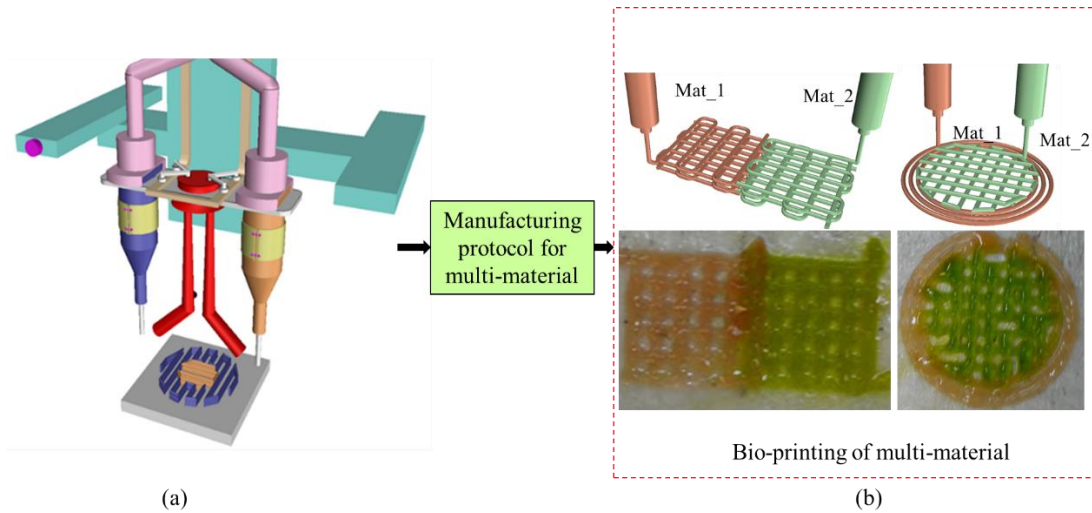
Figure 55: Schematic representation of multi-nozzle bio-printer, and (b) fabricated scaffold using multiple materials.

4.2.8. Fabrication of filament having micro-channel using co-axial nozzle system

Even though the significant advances happen in engineering complex tissues in vitro, there are still critical challenges for the development of vascular networks within engineered scaffolds. Insertion of vascular networks in vitro has been shown to facilitate the integration of tissue constructs with the host vasculature via rapid anastomosis [255]. Similarly, rapid fabrication of three dimensional microchannel networks in cell-laden hydrogels has widespread applications for in vitro models of drug discovery and organs on a chip platforms [256]. The primary requirement to fabricate the scaffold having vascular network is having the ability of extrusion based bio-printer to dispense the filament having micro-channel. To do that, a dispensing system having co-axial nozzle is necessary which is designed and assembled in this research as shown in chapter 3. Using this facility, acellular and cell-laden filament with micro-channel are fabricated in this research as shown in Figure 56**.**
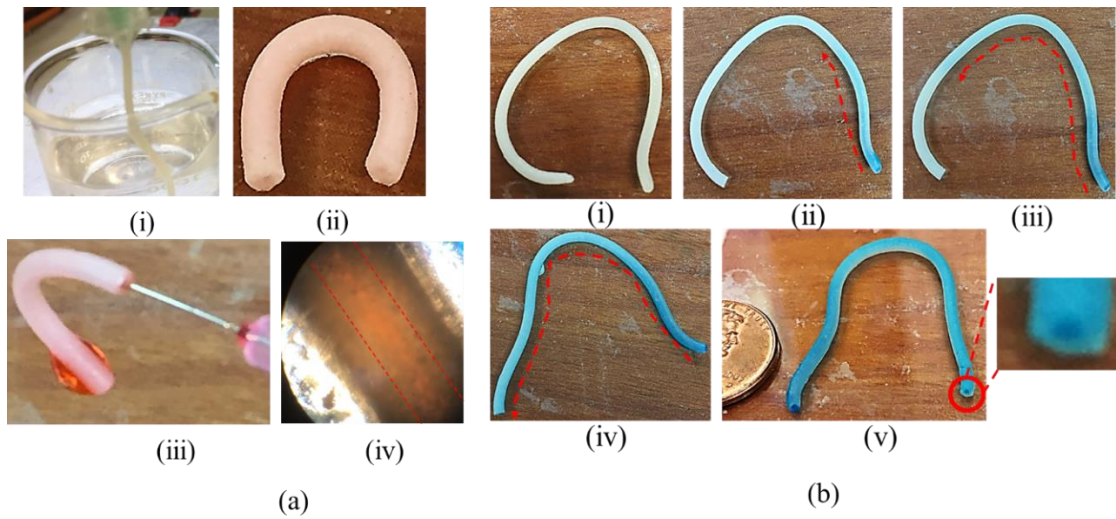
Figure 56: Fabrication of filament having micro-channel, and (b) Fluid flow through the fabricated filament having micro-channel.

To demonstrate the cell survivability of the fabricated cell-laden filament having micro-channel, filament is fabricated encapsulating BxPC3 cell line and incubated in 37^0C and 5% CO_2 for seven days. After that, the cross-section of the filament is stained with DAPI, GFP and phase contrast as shown in Figure 57. It is clear identified from this imaging that the encapsulated cells are surviving into this micro-channeled filament. Cell-laden filament fabrication capability having micro-channel will take this system one step ahead to fabricate functional tissue scaffold having vascular network in long run.
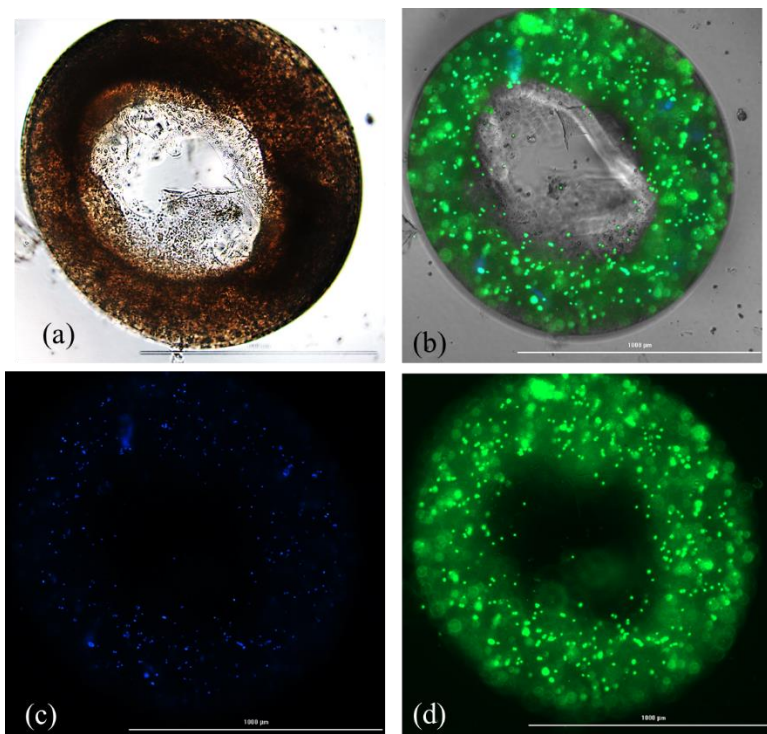
Figure 57: Staining of cell laden filament having micro-channel using (a) Phase contrast, (b) GFP (live cell) (c) DAPI (dead cell) and (d) Live GFP-DAPI (live and dead cell).

4.2.9. Analysis of cell survivability

4.2.9.1. Cell-laden scaffold fabrication with non-functional cell

BxPC3 cell is encapsulated into 4%alg-4%CMC using magnetic stirrer immediately prior to dispensing the hydrogel to fabricate the scaffold. Fabricated cell-laden scaffold is showing in Figure 58 .The cell viability and bio-compatibility of the encapsulated cells are conducted using LIVE/DEAD assay after the printing and at the different time period. Following the manufacturers protocol, ReadyProbes™ Cell Viability Imaging Kit, Blue/Green (Thermofisher, Waltham, MA, USA) was used. Cell encapsulated scaffold was imaged using Lionheart FX automated live cell imager (Biotek, Winooski, VT, USA). Using 50 μm layer thickness, the z-stack images are captured. The protocol is defined accordingly and beacon (n = 5) is selected randomly. Laser power and other detector parameters are kept constant throughout

the imaging of the different beacons. The percentage of cell viability is determined with the ratio of total number of live cell to the total number cells presented in the focused area. Viability at different predefined time periods, i.e., day 1, 5, 15, 23 using staining of the live/dead cell is determined. A significant amount of live and dead cell is observed after dispensing and cross-linking the hydrogels with $CaCl_2$ as shown in Figure 59 and Figure 60**.** At the first day, the percentage of viability for alginate and alginate/CMC was almost similar and there was no significant difference. However, the cell viability into an alginate-CMC blend was higher and significantly different than into alginate at day 15 and 23 as shown in Figure 60 and Figure 61**.** From the SEM image, it is quite clear that presence of CMC induces more porosity into the structure over time. Thereby, the cell-laden filament fabricated with 4% alg-4%CMC allows more exchange of required growth factor and removal of waste material which drives towards higher cell viability.
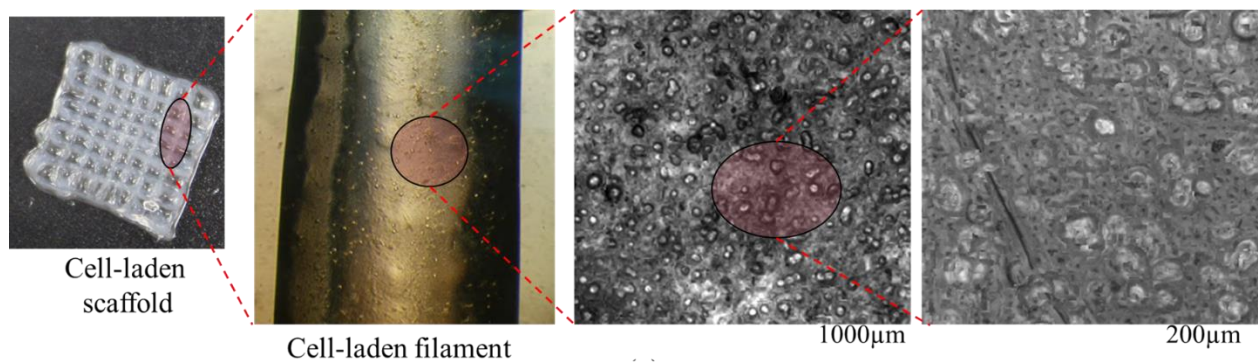
Figure 58: Cell-laden scaffold and filament.
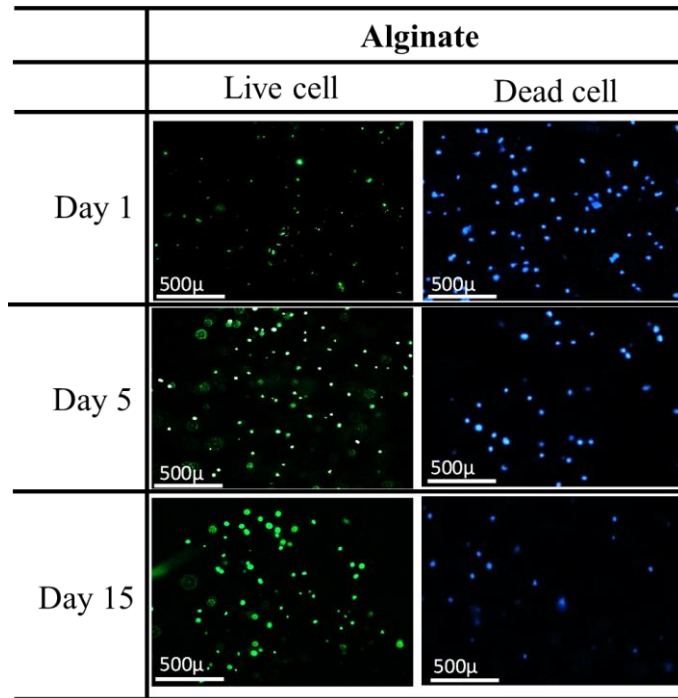
Figure 59: Live/dead staining of BxPC3 cell encapsulated in alginate at different time periods.
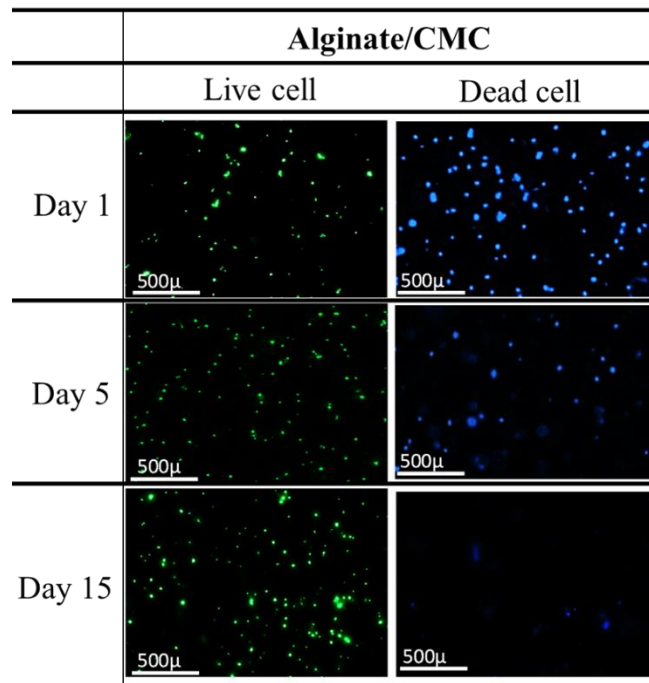
Figure 60: Live/dead staining of BxPC3 cell encapsulated in alg-CMC hydrogel at different time periods.
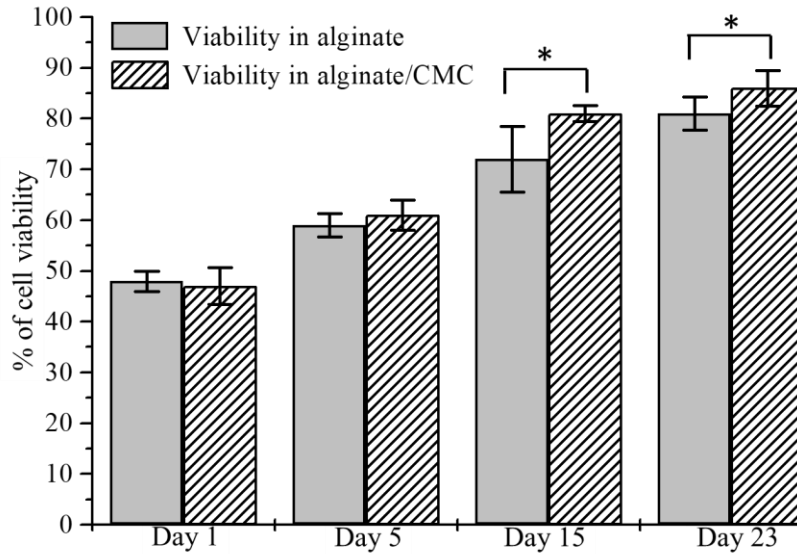
Figure 61: Comparison of cell viability into alginate and alg-CMC at the different time.

The morphology of BxPC3 cell is observed by phase contrast at different time periods into alginate and alginate/CMC. Minimum of five spots of spheroid morphology is visualized in each sample of alginate/CMC, and the diameter of the spheroid is continued to increase as shown in Figure 62.
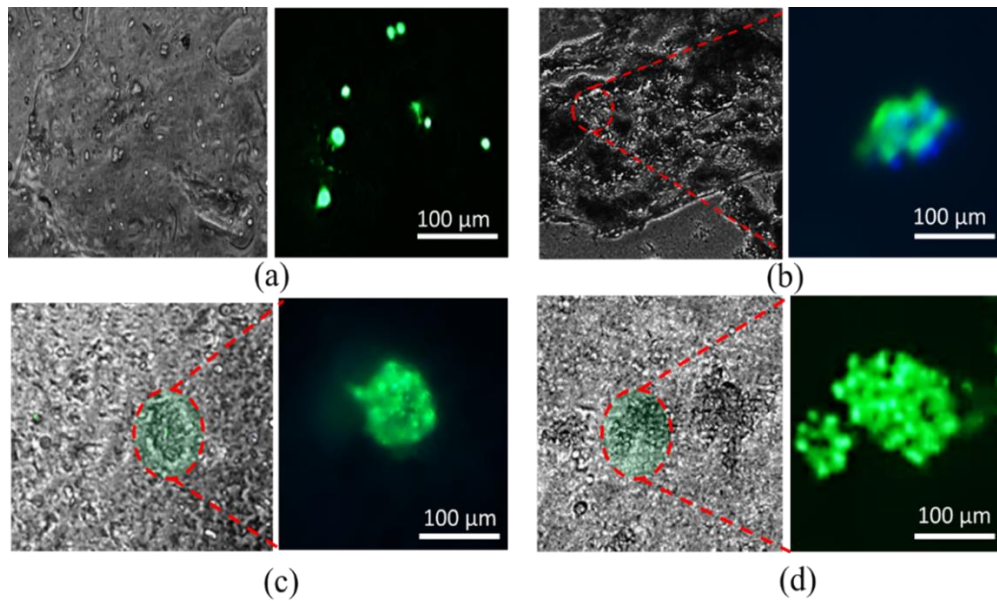
Figure 62: Generation of cell spheroid at day (a) 1, (b) 5, (d) 15, and (e) 23; (c) Cell morphology on 2D culture plate as control, and (f) Cell morphology after 23 days into scaffold.

Different types of cell line e.g. prostate cancer stem cell; and human embryonic kidney, HEK 293 cell are also mixed with 4% Alg-4% CMC composition using magnetic stirrer to evaluate the cell survivability. Scaffold with a dimension of 10mm×10mm×2mm and raster width of 2 mm is fabricated using this cell laden hydrogel. The cell viability of those cell lines into the scaffold is determined after 15 days as shown in Figure 63 (a). All the cell lines show almost similar amount of cell viability i.e. around 90% as shown in Figure 63 (b). This phenomenon indicates good survivability of different type of cells into this material composition.
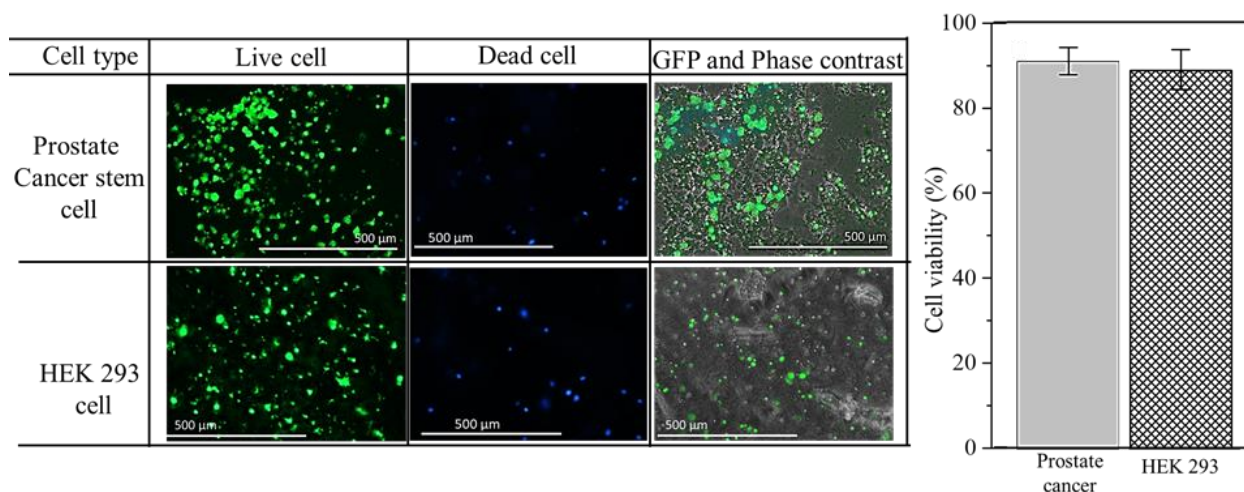
Figure 63: (a) Cell survivability of various cell line into 4% (w/v) Alg-4% (w/v) CMC hydrogel material (b) Cell viability of various cell line.

4.2.9.2. Cell-laden scaffold fabrication with functional cell

Porc1, a functional type of tracheal cell which has the contractile and expansion capacity, is mixed with 4% Alg-4% CMC composition to evaluate the cell survivability and functionality into this material composition. After 15 days of incubation, the encapsulated cell was showing its morphological change into the material as shown in Figure 64. Therefore, this material composition also exhibits the capability to allow the functionality of the cell. However, the arrangement of the cell into the scaffold is random which may hinder to achieve the contractile

91

effect of the scaffold as shown in Figure 64 (d). Therefore, we will continue our study to find out a component of bio-ink which will drive the cell along a specific direction.
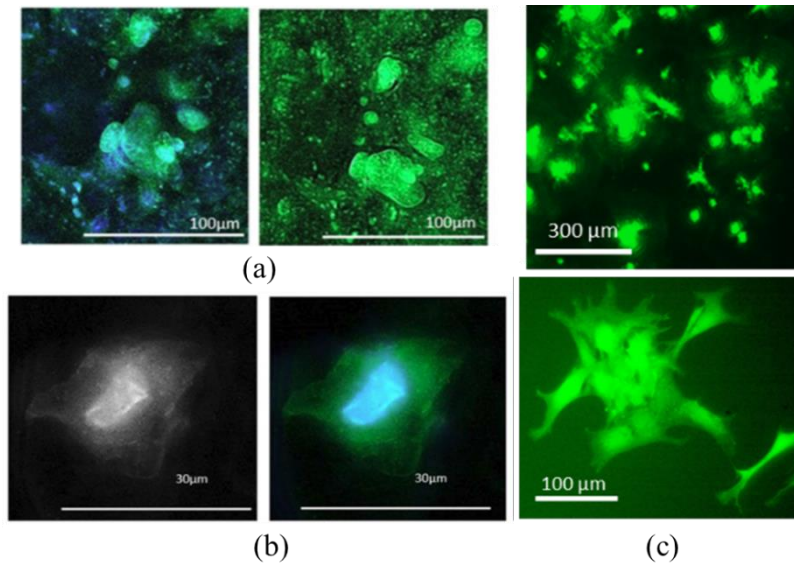
Figure 64: Imaging of scaffold encapsulating Porc1 cell: (a) DAPI, (b) GFP, and (c) Confocal, and (d) randomly distributed cell.

4.2.9.3. Effect of pore size on cell survivability

In tissue engineering and regenerative medicine, porous materials can provide a temporary microenvironment to promote cell adhesion, proliferation and differentiation to guide the formation of new tissues and organs [58]. The efficiency of cell viability and proliferation can be varied depending on scaffold pore size [57]. The pore size should be in a range that facilitates cell penetration and migration during cell seeding, nutrient diffusion and removal of metabolic substances, and provides a three-dimensional microenvironment inducing cell assembly and differentiation [27]. To investigate the pore size on the overall cell survivability, scaffolds having pore size of 250, 500 and 1000 µm are fabricated using the alginate-CMC material encapsulating BxPC3 cell line in this research. The scaffold is stained after 15 incubation days with GFP, DAPI and phase contrast. From Figure 65, Figure 66 and Figure 67, it is clearly identified that, there is effect of pore size on cell proliferation and smaller pore size

facilitates more cell proliferation than larger pore size. A round cell morphology is typical observed for encapsulated BxPC3 cells, and homogeneous cell distribution facilitates tissue formation. The scaffolds having smaller pore size provide the cells more favorable microenvironment, which is a better choice for spheroid formation.
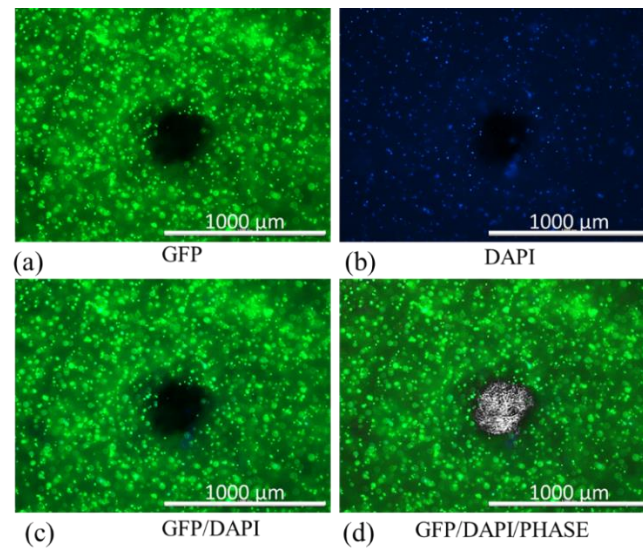
Figure 65: Imaging of scaffold having pore size of 250 µm: (a) GFP, (b) DAPI, and (c) GFP/DAPI, and (d) GFP/DAPI/Phase contrast.
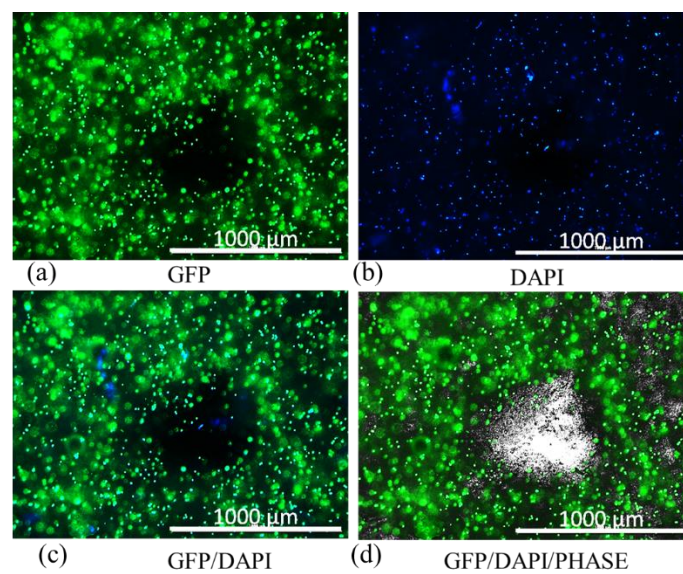
Figure 66: Imaging of scaffold having pore size of 500 µm: (a) GFP, (b) DAPI, and (c) GFP/DAPI, and (d) GFP/DAPI/Phase contrast.
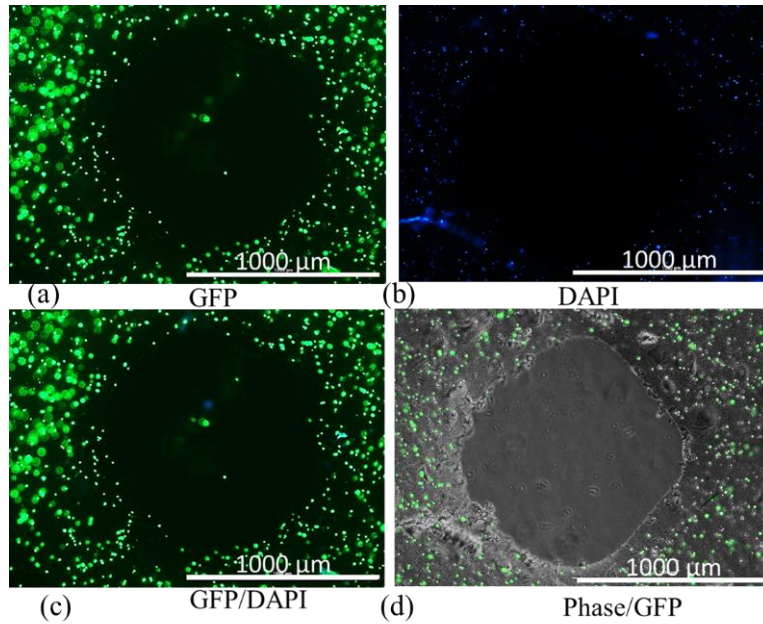
Figure 67: Imaging of scaffold having pore size of 1000 µm: (a) GFP, (b) DAPI, and (c) GFP/DAPI, and (d) GFP/DAPI/Phase contrast.

4.2.9.4. 4D printing with Alginate and CMC

Despite the tremendous potential of 3D bio-printing techniques toward the fabrication of highly complex biological structures and the flourishing progress in 3D bio-printing, fabricating complex free form scaffold is still challenging. Sometime to fabricate those complex freeform scaffolds, the dynamically reconfigurable architectures with tunable functionality and responsiveness are important. The phenomenon of dynamically reconfigurable architectures of the fabricated scaffold by 3D bio-printing process by the presence of suitable internal or external stimuli is called 4D printing [257]. This advanced technology offers great potential for the creation of sophisticated dynamical structures with high resolution, otherwise inaccessible through the 3D bio-printing techniques. The efficacy of the 4D printing method relies on the ability of swelling anisotropies by local control of the orientation of filament fabricated by alginate-CMC. The longitudinal filament direction shows different swelling behavior than

94

transverse direction. This swelling anisotropies subsequently result different elastic moduli. The extent of the magnitude of the anisotropic swelling depends on the filament direction, nozzle diameter and printing speed. Harnessing anisotropic swelling allows precise control over the curvature in bilayer [258].

To demonstrate the potential of this alginate-CMC material for 4D bio-printing, a set of acellular scaffolds with various geometries is designed and fabricated as shown in Figure 68 to Figure 70 using the proposed extrusion based bio-printing methodology. Due to the anisotropy in the swelling rate of alginate and CMC, they dynamically reconfigure at different direction depending on the deposition direction. Hence, depending on the scaffold geometry, they show different final configurations at the presence of water as shown in Figure 68, Figure 69 and Figure 70. The proper designing of deposition direction and controlling of process parameters can give more control over dynamic reconfiguration of the 3D bio-printed scaffold [259]. The successful trial of 4D printing with this material can allow the fabrication of more intricate scaffolds in future.
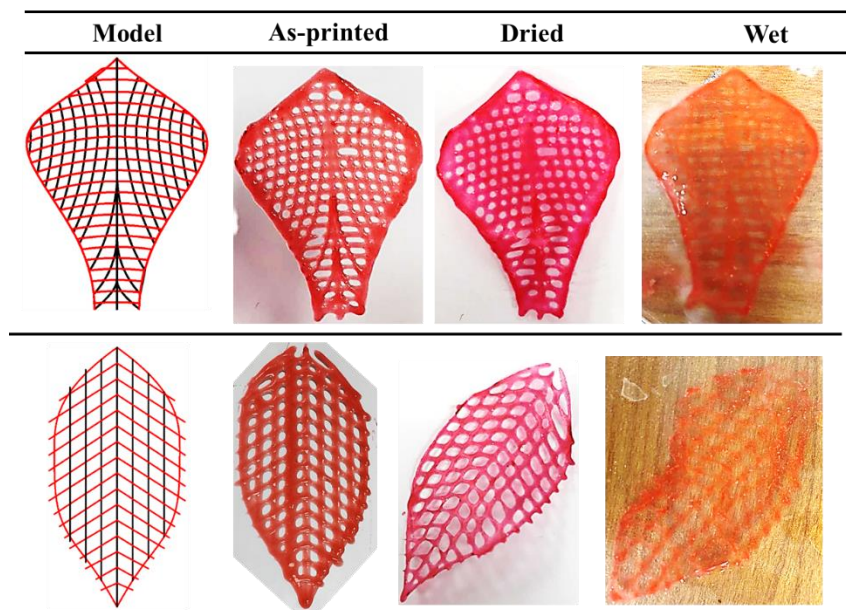
Figure 68: Designing and fabrication of free-form scaffold for 4D printing demonstration.

Model	As-printed	Dried	Wet
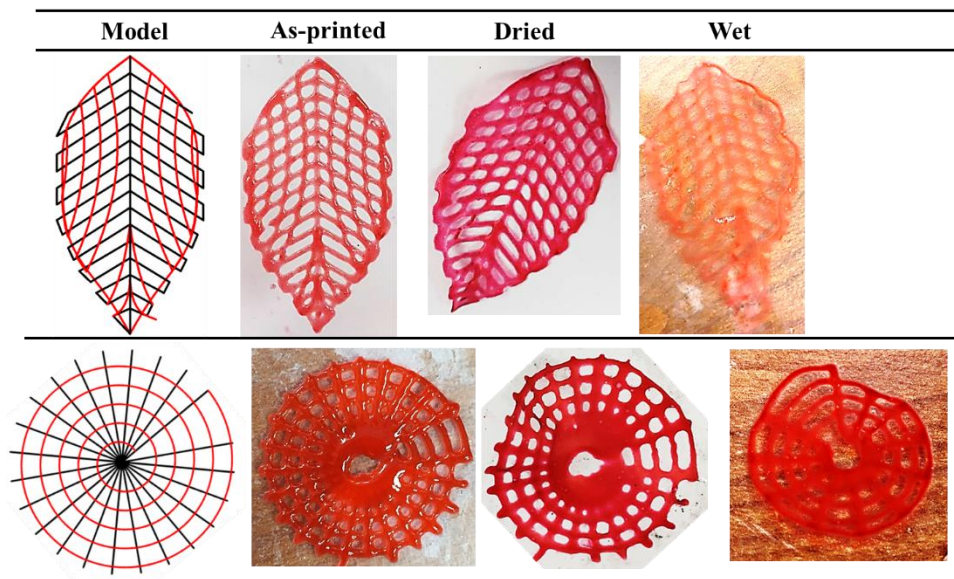
Figure 69: Designing and fabrication of various scaffold for 4D printing demonstration.

Model	As-printed	Dried	Wet

Less denser
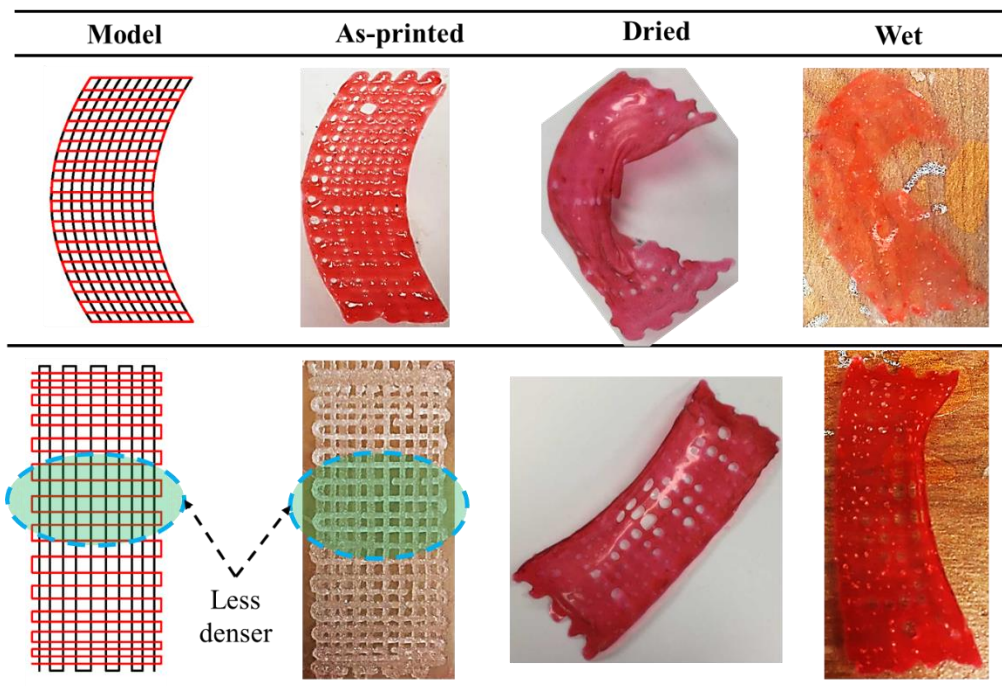
Figure 70: Designing and fabrication of scaffold having various porosity for 4D printing demonstration.

4.2.10. Remarks for material-Alginate and CMC

From the aforementioned qualitative and quantitative analysis, it is clear that the combination of alginate and CMC can be a good candidate for large scale scaffold fabrication and cell encapsulation. Set of tests also determines that 4% alginate and 4% CMC is an optimum material composition to fulfil the both requirement i.e. large scale scaffold fabrication and better cell survivability. However, the maximum build height of the fabricated scaffold with this material composition is 1.4 cm which can be increased by the appropriate selection of another element into this bio-ink. That will be discussed in the next chapter. Moreover, the arrangement of the cell into the scaffold is random which may not be helpful to achieve the contractile effect of the scaffold. Therefore, this study will be continued to find out a component of bio-ink which will drive the cell proliferation along a specific direction and that will be discussed in chapter 6.

5. DEVELOPMENT OF CLAY BASED NOVEL BIO-INK FOR 3D PRINTING PROCESS

In the previous chapter, the capability of the combination of alginate and CMC to fabricate large scale scaffold and cell survivability have been discussed. Adding nano particle in the bio-material is popular idea to improve the mechanical properties in both pre-printing and post-printing stage. Adding nano- material may improve the diffusion rate after dispensing which is 32% for alginate and CMC. It may also leave more lateral pore space where the combination of alginate and CMC leaves only 19%. In this chapter, the focus will be to find out the material combination and composition contained with natural hydrogel which will allow less diffusion with good shape fidelity and subsequently to fabricate 3d scaffold structure. The cytotoxicity of the material composition will also be determined at the end of this section.

Recently, different types of nano-clay e.g. laponite [260-262], montmorillonite (MMT) [263, 264] are widely used for tissue engineering. This material augments the cell spreading and osteogenesis into fabricated scaffolds [161]. To fabricate scaffold in centimeter scale using 3D bio-printing, nano-clay is used as an element into the composition of alginate and methyl cellulose for demonstrating the skeletal application [46]. MMT is a layered structure nano-clay consisting of an octahedral alumina sheet embedded by two tetrahedral silica sheets [260] as shown in Figure 71. Specific properties of MMT i.e. high capacity of cation exchange, adsorption, high surface area, and swelling behavior define it as a good candidate of tissue engineering application and drug delivery material [265]. Therefore, in several reported works, MMT is combined with alginate to prepare beads to analyze the drug delivery [266-268]. However, to our best knowledge, the combination of alginate-CMC-MMT has not been explored for 3D bio-printing process. In this chapter, montmorillonite nano-clay is blended with previously developed hybrid hydrogel alginate and CMC to investigate its capability to fabricate

98

large scaffold and cytotoxicity. A set of systematic quantitative characterization tests such as rheological and mechanical test, filament collapse and fusion test, the effects of air pressure and print distance on filament width will be conducted in this section as well to validate its printability, shape fidelity. Afterwards, 3D scaffold structures are fabricated with cell-laden bio-ink and its viability is recorded. The outcome of all these experiments and cell viability measurement will indicate the capability of this hybrid hydrogel as a candidate biomaterial for 3D bio-printing process.
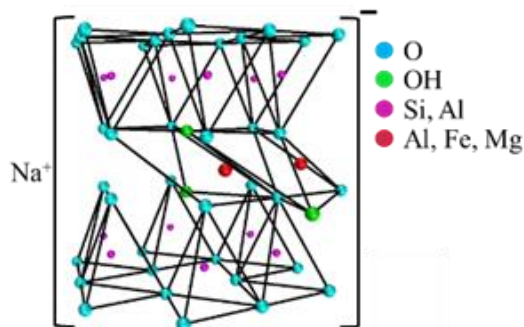
Figure 71: Chemical formula of Na-MMT.

5.1. Materials and methods

5.1.1. Preparation of hydrogel

The materials and their compositions used in this chapter to prepare the hydrogel is shown in Table 7 where letter 'A', 'C' and 'M' represents Sodium alginate,   carboxy methyl cellulose (Sigma-Aldrich) and sodium montmorillonite; and the numerical subscript represent their weight percentage respectively. In this research, five different composition i.e. $A_4C_0M_0$, $A_4C_0M_4$, $A_4C_1M_4$, $A_4C_2M_4$, $A_4C_3M_4$ is considered where $A_4C_0M_0$ is used as control. The weight percentage of Sodium alginate is kept constant at 4% due to prior reporting [45, 202] of high cell viability in upto 4% alginate solution. To maintain reasonable number of experiment, only 4% weight percentage of MMT is considered and this will expose potential of CMC in favor of

99

alginate and carboxymethyl cellulose in the composition. The percentages of material shown in Table 7 are dissolved into 0.2 μm filtered deionized (DI) water and stirred overnight to prepare the bio-ink gel. 4% (w/v) $CaCl_2$ (Sigma-Aldrich) is prepared with 0.2 μm filtered deionized (DI) water and used as chemical cross-linker to assure quick gelation of the deposited bio-ink.

Table 7: Percentage of material used to prepare bio-ink.

Label	Alginate (A) % (w/v)	CMC (C) % (w/v)	MMC(M) % (w/v)
$A_4C_0M_0$	4	0	0
$A_4C_0M_4$	4	0	4
$A_4C_1M_4$	4	1	4
$A_4C_2M_4$	4	2	4
$A_4C_3M_4$	4	3	4

Since alginate, CMC and MMT are polar solute, they are soluble in water. It is reported that alginate and MMT has chemical interaction due to the intermolecular hydrogen bonds and electrostatic attraction force [266, 267]. Moreover, it is stated that alginate attracts CMC via hydrogen bond into solution [190]. Therefore, possibly these materials are interacting among them in the aqueous solution via intermolecular hydrogen bonds and electrostatic attraction at numerous points to form gel as shown in Figure 72 (d) and eventually this formation of gel makes this hybrid bio-ink printable.
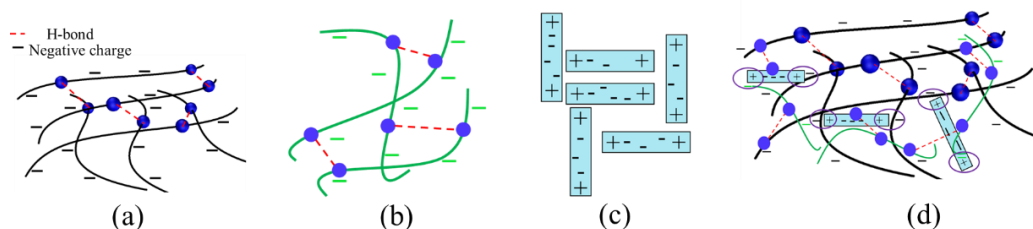
Figure 72: Chemical interaction: (a) Into alginate, (b) Into carboxymethyl cellulose, (c) Into Na-montmorillonite, and (d) Among alginate, carboxymethyl cellulose, and Na-montmorillonite.

5.1.2. Characterization tests

The same instruments, protocols as discussed in chapter three, have been used in this chapter to conduct the rheological test, scanning electron microscope, swelling test, shape fidelity test.

5.2. Results and discussion

5.2.1. Rheological test result

Various rheological tests *i.e.* steady rate sweep test, dynamic stress sweep test, frequency sweep test, 3-interval thixotropic tests are conducted to detemine the suitable combination of alginate, CMC and MMT. The outcome of each rheological test is analyzed in this section to suggest a suitable combination of alginate, CMC and MMT which will be able to hold the shape of fabricated large scaffold with proper prinability and shape fidelity.

5.2.1.1. Steady rate sweep test

The log-log plot of viscosity and shear stress vs shear strain rate is shown in Figure 73 (a) and (b) respectively. With increasing the shear rate, viscosity decreases whereas the shear stress increases. This phenomenon demonstrates the shear thinning behavior of all the compositions. However, the addition of CMC with suspension increases the viscosity as well as the shear stress. Zero-shear viscosity value of alginate hydrogel with 2% CMC composition increases almost from 4 Pa.S to 879 Pa.s with respect to only 4% alginate-4% MMT. This might happen because of increasing the cross-linking rate with increased amount of CMC into the suspension.
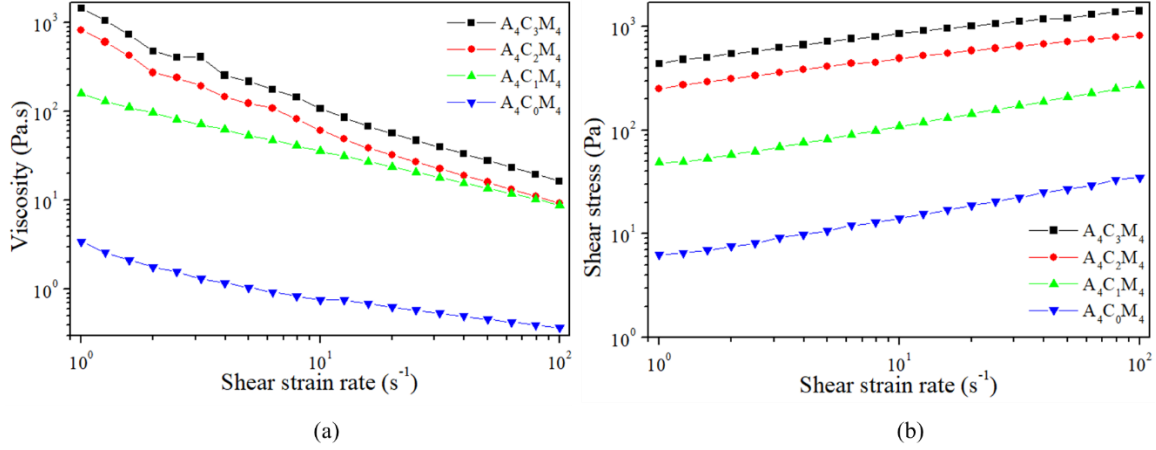
Figure 73: Evaluation of shear thinning behavior of hydrogels: (a) Viscosity vs shear strain rate, (b) Shear stress vs shear strain rate.

5.2.1.2. Dynamic stress sweep test

The dynamic stress sweep test for various compositions of the hydrogel at 1 Hz is represented the outcome of G' and G'' vs shear strain (%) in Figure 74. It is clear from the figure that with increasing the percentage of CMC into the alginate-MMT suspension, the physical state of the hydrogel is transferred from liquid-like to solid-like state. At the beginning of shear strain, the value of G' dominates G'' for all compositions other than $A_4C_0M_0$. With increasing the amount of CMC in the suspension from 1 to 3%, G' dominates G'' up to a certain level of shear strain and then intersects. This certain level is called as linear viscoelastic range (LVR) which determines the limit at which the suspension preserves the sedimentation within the sample without permanent deformation. This resembles the solid-like behavior of the suspension before the intersecting point. After the intersecting point, both moduli are decreased with the dominancy of G'' i.e. the liquid-like phase. In the co-existence of liquid and solid-like phase, increasing the percentage of CMC increases the LVR as shown in Figure 74. To provide more insight into solid and liquid-like behavior of hydrogel, dynamic mechanical loss tangent ($\tan\delta = G''/G'$) is

102

implied as shown in Figure 74 (i-vi). Tangent value smaller than 1 predominantly reflects the elastic behavior, and greater than 1 predominantly indicates viscous behavior.
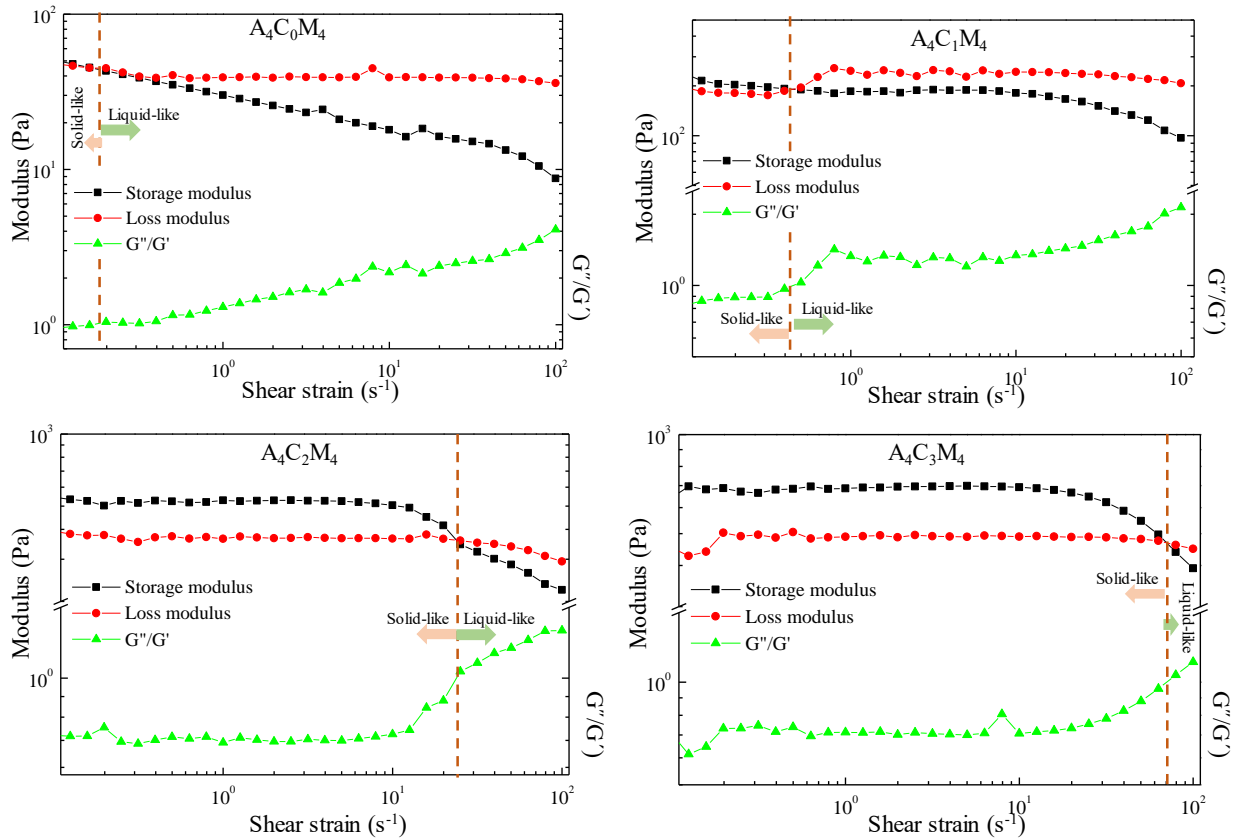
Figure 74: Dynamic strain sweep test.

5.2.1.3. Three point interval thixotropic test

Three point-interval-thixotropic-tests are conducted on various compositions to provide more understanding of the real scenario during extrusion of hydrogel. In this test, the first interval imitates the at-rest state of sample, the second interval resembles the hydrogel decomposition under high shear i.e. experienced high shear during extrusion, and third interval reflects the structure retention after hydrogel extrusion as shown in Figure 75. The stress-shear rate loop shown in Figure 75 demonstrates the shear history of alginate with 4% CMC. A stress is applied on the at-rest hydrogel which breaks down the initial network structures of the hydrogel. After the hydrogel is extruded through the nozzle at a certain shear rate, it takes time to

recover the internal network. In most cases, when the shear is released, the stress path lags forming a hysteresis loop as shown in Figure 75. The area within the hysteresis loop signifies the energy consumed in the internal network breakdown. From Figure 75, it is clear that alginate with 4% CMC consumes more energy to break down the internal network than other compositions.
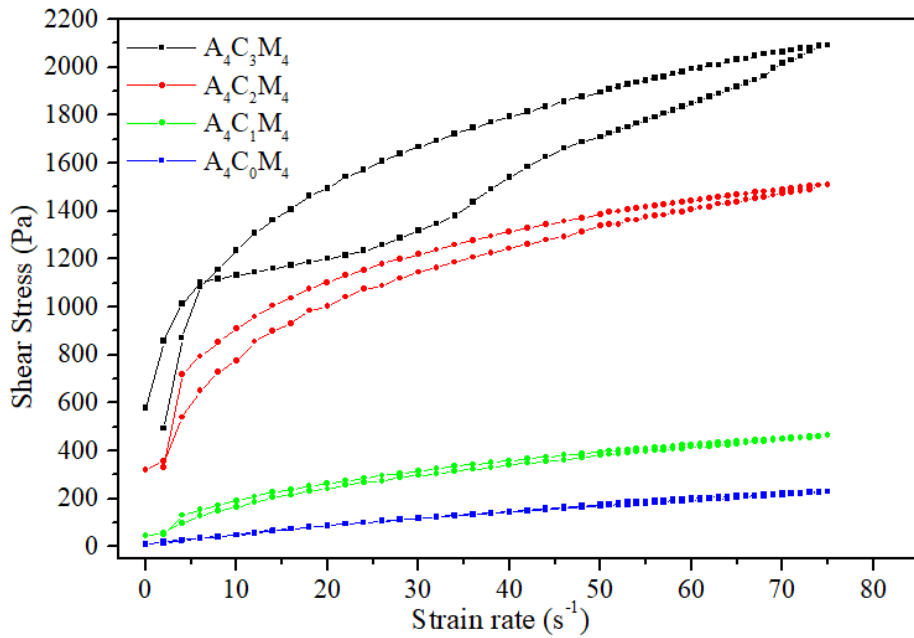
Figure 75: Result of 3 point-Interval-thixotropic-tests.

5.2.1.4. Remarks for rheological test

Once all the rheological tests are done, it is clear from the result that the viscosity is solid content dependent, because 4% alginate-4% CMC-3% MMT is showing highest viscosity. However, material with higher viscosity demands more shear stress which hinders the overall cell viability. Composition containing 4% alginate-4% CMC-2% MMT, has better potential to maintain proper printability and shape fidelity during large scaffold fabrication. Since, it has comparatively less viscosity, it has higher potential to encapsulate the cell.

5.2.2. Swelling test result

The swelling test is done following the protocol described in [251]. Briefly, sample scaffolds (n=3) are fabricated with material composition $A_4C_2M_4$ as shown in Figure 76 (a). Qualitatively, it is clear that the filament width of the incubated scaffold increases with time as shown in Figure 76 (c-d). However, the geometry of the scaffold and morphology of the macro-pore are seldom changed which indicates the capability of holding the shape fidelity of the scaffold in incubation period. The upward trend of the percentage of swelling graph shown in Figure 76 (e) exhibits high swelling capability of this material composition in proper incubation environment with respect to time. This time-dependent higher percentage of swelling creates more porosity in the structure which leads more exchange of nutrient and waste element of encapsulated cells during incubation period.
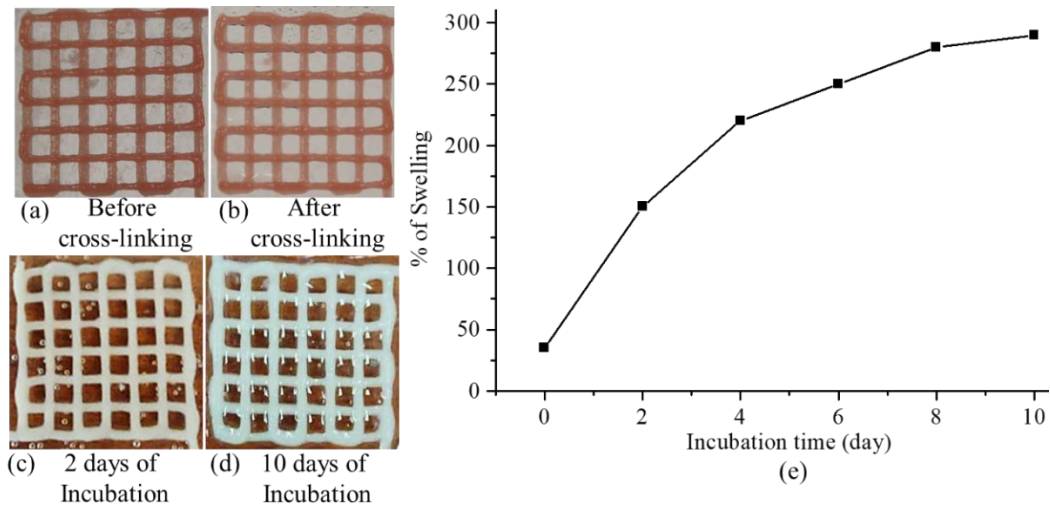
Figure 76: Fabricated scaffold (a) Before cross-linking, (b) After cross-linking, (c) with 2 days of incubation, (d) with 10 days of incubation, and (e) Percentage of swelling with respect to incubation time.

5.2.3. Scanning electron microscope

The SEM images of filament fabricated by various material compositions are shown in Figure 77. Since $A_4C_0M_4$ doesn't make proper gelation, it shows cracks on the filament surface after it get dried. With increasing the percentage of CMC, the materials get proper gelation and shows smooth filament surface. The image of the cross-section of filament shows with increasing the percentage of CMC, the amount of micro-pores increase. The presence of those micro-pores will potentially improve the nutrients and growth factor supply in case of cell laden scaffold fabrication.
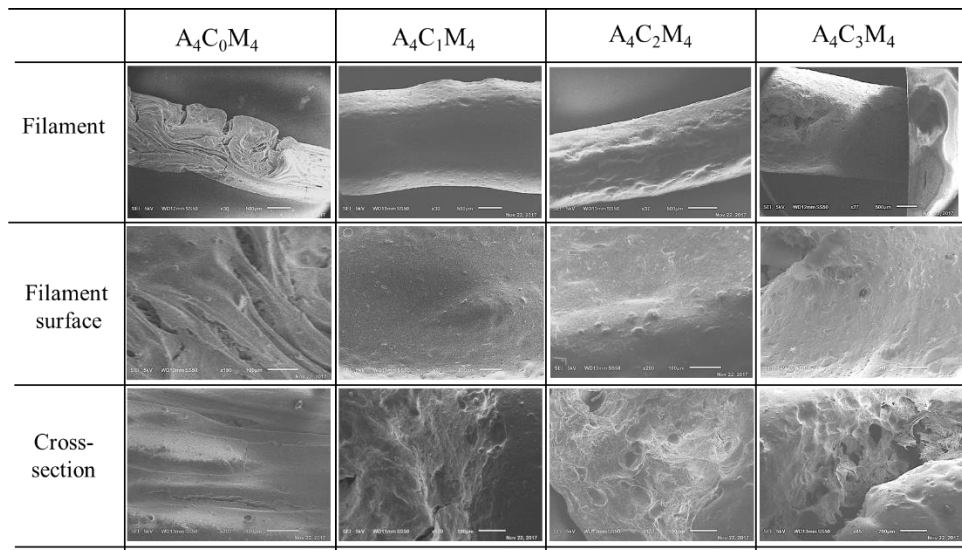
Figure 77: SEM images of deposited filaments composted with various material compositions.

5.2.4. Shape fidelity test result

The outcome of shape fidelity test will exhibit the capability of the considered material compositions' shape holding capacity. Specifically, the fusion test will determine the diffusion or spreading rate and measurement of printability of material compositions. The collapse test will identify the shape holding capacity of the deposited filament without support. The lateral pore collapse test will determine the capability to hold the lateral pore of the material compositions.

How the nozzle speed, print distance, air pressure affect the filament width will also be identified from this test result.

5.2.4.1. Filament fusion test

To evaluate the effect of filament fusion and pore closure for each composition of bio-ink, the area of each pore of the fabricated scaffold is measured and the diffusion rate and printability of each pore is determined following the equation (3) and (4). The diffusion rate shows decreasing trend where the printability shows increasing trend with increasing the pore size for each composition of material as shown in Figure 78 and Figure 79. Qualitatively, $A_4C_2M_4$ and $A_4C_3M_4$ show good pore geometry, sharp filament corner and less material diffusion at the intersections of consecutive layers than other material compositions. The quantitative analysis of diffusion rate validates that $A_4C_2M_4$ and $A_4C_3M_4$ show minimum material spreading i.e. minimum diffusion rate than other compositions. The range of printability of $A_4C_2M_4$ and $A_4C_3M_4$ are 0.76-1.03 and 0.82-1.10 which demonstrates almost square geometry of the pore. With decreasing the concentration of CMC and MMT, pores with smaller dimension are closed. Therefore, this test indicates that $A_4C_2M_4$ and $A_4C_3M_4$ can maintain good printability and shape fidelity. However, the geometry of the filament generated from $A_4C_3M_4$ is not uniform throughout the scaffold due to over gelation. Applying increased amount of air pressure and reducing printing speed may facilitate to gain the uniform filament geometry. Still, the higher air pressure exerts undesirable amount of shear stress on the encapsulated cell, leads more cell damage. Hence, $A_4C_2M_4$ can be a good candidate to maintain good printability, shape fidelity and safe environment for encapsulated cell.

	$A_4C_0M_0$	$A_4C_0M_4$	$A_4C_1M_4$	$A_4C_2M_4$	$A_4C_3M_4$
Bi-layer					
1x1 pore 3x3 pore					
Filament intersection					
Filament corner					
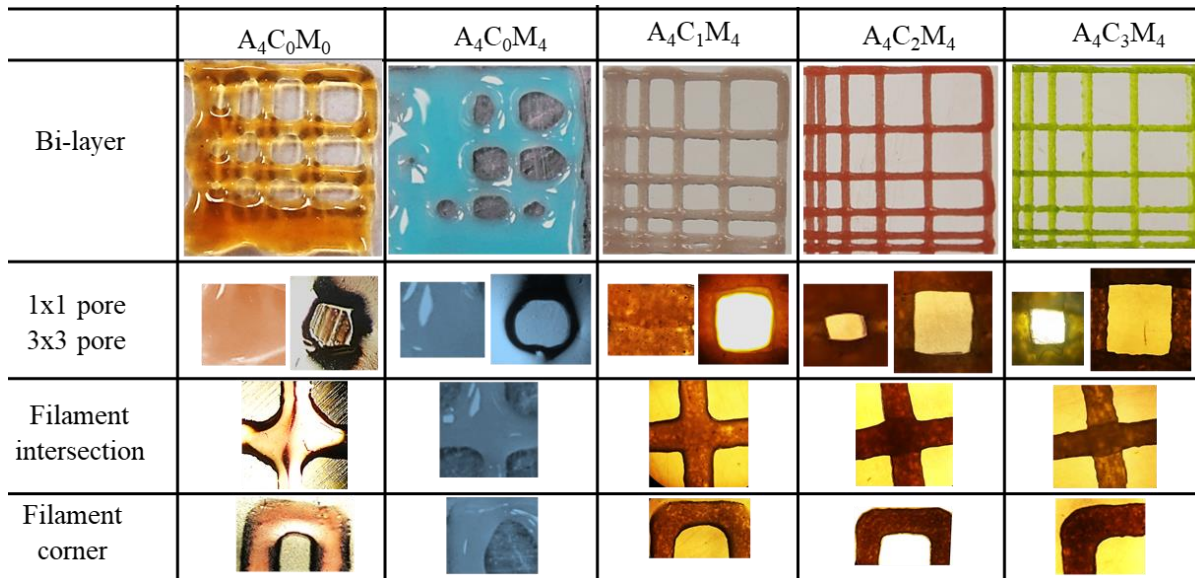
Figure 78: Filament fusion test.
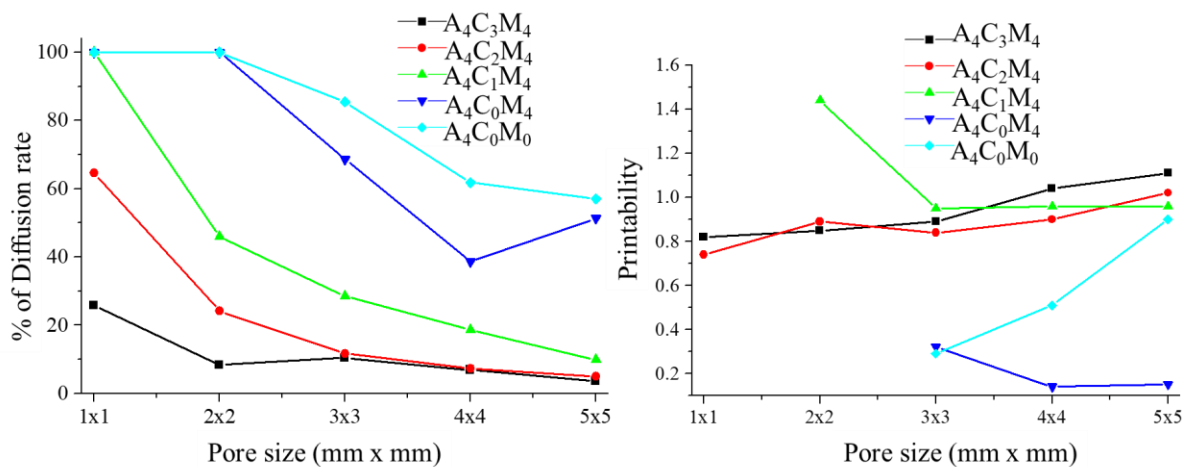
Figure 79: (a) Percentage of diffusion rate, and (b) printability of various material compositions.

5.2.4.2. Filament collapse test

The qualitative observation of the collapse test for various compositions of material identifies that with increasing the percentage of CMC up to 2, the bio-ink transformed from under gelation to proper gelation state which leads the bridge formation on the pillars with minimum or zero deflection as shown in Figure 80. Hence, the material composition with higher

108

percentage of CMC resembles quantitatively less percentage of collapse factor as shown in Figure 80 (b). For example, composition $A_4C_2M_4$ generates almost straight filament on the consecutive pillars located at various distances which indicates zero collapse of the filament as shown in Figure 80 (b). Increasing the percentage of CMC more than 2% transform the gelation status to over gelation and generates curvy filament.
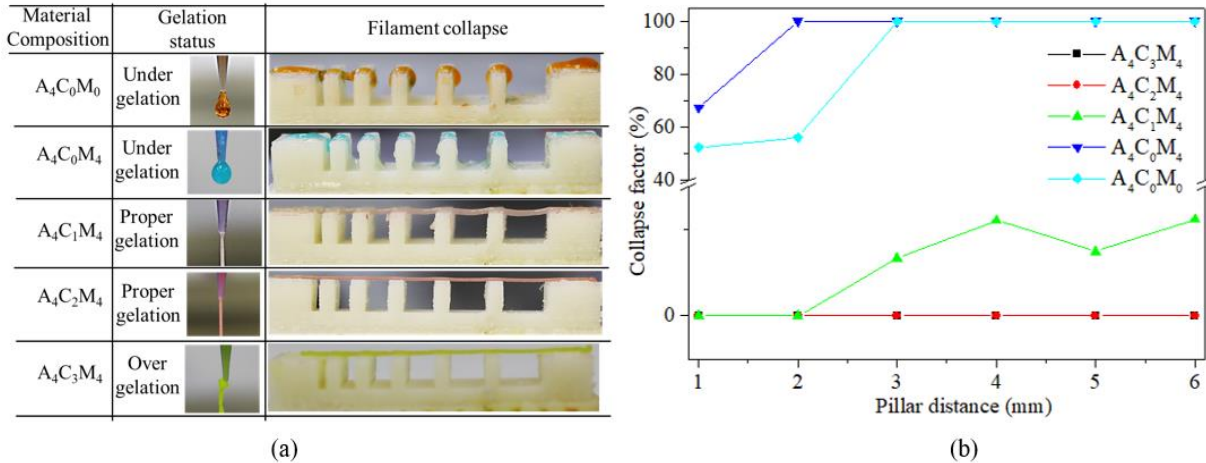
Figure 80: (a) Filament collapse test of different material compositions, (b) Collapse area factor at different distance.

5.2.4.3. Effect of air pressure on filament width

To determine the effect of air pressure on filament width, $A_4C_1M_4$ and $A_4C_2M_4$ are chosen as candidate compositions due to better printability and less fusion and collapse rate. A line having 10 mm length is deposited (three layers) with 5mm/s nozzle speed and 0.7mm print distance. Various air pressure *e.g.* 10, 12, 14, 16, and 20 psi are used during the inspection of the effect of air pressure on filament width as shown in Figure 81 (a). The width of the filament is recorded with Zeiss bright field inverted microscope for each of this test. The plotted values represent the 3 repetitions of measurements.
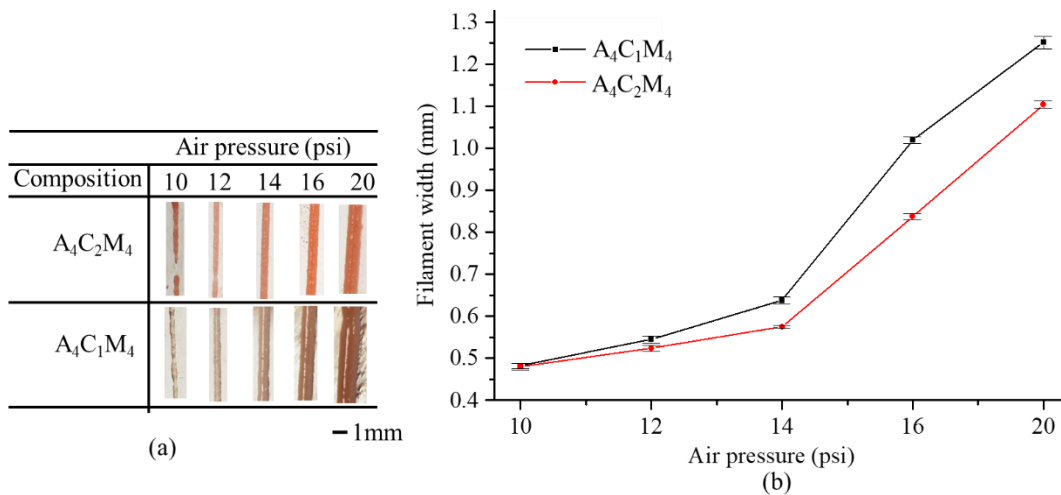
Figure 81: (a) Printed filaments at various air pressure, and (b) The effect of air pressure on filament width.

With increasing the air pressure, the filament width of $A_4C_1M_4$ and $A_4C_2M_4$ composition increases as shown in Figure 81 (b). However, it is clear from the graph, the increased amount of CMC in bio-ink will reduce the changes of the filament width. Lower amount of air pressure may not exceed the surface tension of the material with the nozzle and eventually will not deposit continuous filament. Therefore, the filaments generated at 10 psi from both of compositions are discontinuous as shown in Figure 81 (a). However, over material deposition may happen due to high air pressure. Thereby, applying optimum air pressure for different material compositions will assure the continuous filament deposition as well as uniform filament width.

5.2.4.4. Qualitative and quantitative test of lateral pore

Scaffolds having filament to filament distance of 3 mm is fabricated (10 layers) with compositions $A_4C_1M_4$ and $A_4C_2M_4$. Qualitatively, each pore of the scaffold fabricated by later composition is almost square in shape as shown in Figure 82. To visualize the lateral pore in the scaffold structure clearly, the scaffold is cut laterally and observed the lateral pore macroscopically and microscopically (with Zeiss bright field inverted microscope). Scaffolds fabricated with those

compositions collapse in overhang region between two consecutive filaments of the lower layer and eventually the lateral pore shrinks as shown in Figure 82. The lateral pore diminishes absolutely in the scaffold fabricated by less viscous bio-ink. Therefore, it can be claimed visually, scaffold fabricated by $A_4C_2M_4$ maintains better lateral pore geometry than $A_4C_1M_4$.

	Top view (Macroscopic)	Pore geometry (Microscopic)	Lateral Pore	Lateral pore geometry
$A_4C_2M_4$		Printability≈1		
$A_4C_1M_4$		Printability < 1		

Figure 82: Qualitative test of lateral pore.

The shape fidelity can be described quantitatively in term of the lateral porosity as shown in Figure 83 (a). The lateral collapse area factor i.e. percentage of area collapsed right after the scaffold fabrication with respect to the theoretical lateral pore area is determined using equation (2). The theoretical area of lateral pore is represented as $A_t^l = DF \times LT - \pi r_f^2$ where LT and r_f are theoretical layer thickness and radius of filament respectively as shown in Figure 83 (a). If the lateral pore is diminished after fabrication of the scaffold, $A_a^l = 0$. The greater value of lateral collapse area factor reflects the less preservation of lateral pore and so as the scaffold shape fidelity. For given 3mm filament to filament distance and 0.41 mm nozzle diameter, the theoretical lateral pore area is calculated as 1.1 mm^2. The lateral pore area presented in the scaffold fabricated by $A_4C_1M_4$ and $A_4C_2M_4$ is measured (n=3) and compared with theoretical pore area. Using

111

equation (2), the lateral collapse area factor is determined as shown in Figure 83 (b). It is clear from the graph that the lateral pore collapses significantly with decreasing the percentage of CMC.
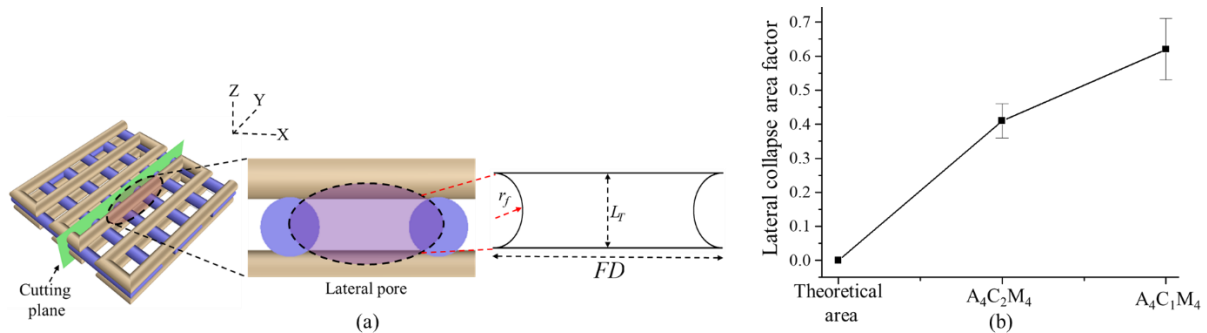
Figure 83: (a) Theoretical representation of lateral pore, and (b) Lateral collapse area factor.

During lateral pore area test, the changes of layer thickness is also analyzed. Compared to $A_4C_2M_4$ the total build height of the scaffold fabricated with $A_4C_1M_4$ is reduced by 23%. This result indicates that compositions with less solid content diffuses more on xy-plane and undermine the filament stacking capacity which is also stated in some existing literatures [38, 189].

5.2.4.5. *Remarks for shape fidelity test*

After doing a set of systematic qualitative and quantitative characterization, it is clear that the composition, $A_4C_2M_4$ maintains good printability and shape fidelity. This result indicates that $A_4C_2M_4$ can be a good candidate for the fabrication of large-scale scaffold.

5.2.5. Fabrication of large scaffold

Once the characterization tests described above are done, it is revealed, composition $A_4C_2M_4$ shows good printability and shape fidelity. Therefore, this composition is used to fabricate large scale acellular scaffolds with various pattern using the 14 psi air pressure and 0.7mm print distance unless otherwise stated. A cuboidal scaffold with a dimension of $25 \times 25 \times 14$ mm^3 is fabricated following 0^0-90^0 deposition orientations shown in Figure 84 (b). The

fabricated scaffold maintains uniform geometry of the macro-pores throughout the structure even after 75 layers as shown in Figure 84 (b). As it is stated above, increased air pressure and slower print speed may provide uniform filament geometry with $A_4C_3M_4$ composition. To investigate, a cuboidal scaffold with a dimension of $30\times30\times18$ mm^3 is fabricated with $A_4C_3M_4$which required 20 psi air pressure and 4 mm/s print speed as shown in Figure 85 (b). $CaCl_2$ is sprayed after finishing the fabrication of whole model for both compositions of $A_4C_2M_4$ and $A_4C_3M_4$.
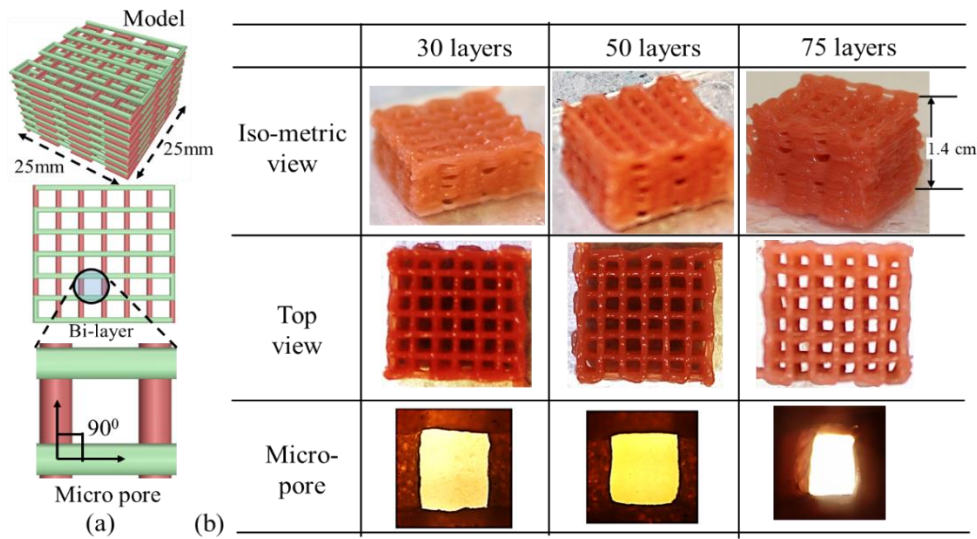
Figure 84: (a) Design of cuboidal scaffold, (b) Fabricated scaffold with the composition $A_4C_2M_4$.
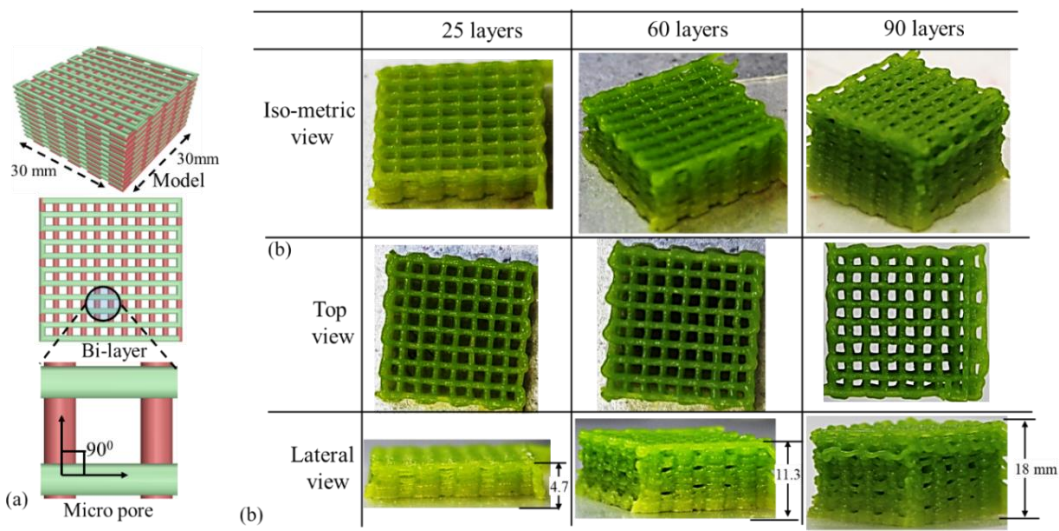
Figure 85: (a) Design of cuboidal scaffold, (b) Fabricated scaffold with the composition $A_4C_2M_3$.

A tubular scaffold having 10 mm diameter is fabricated up to 20 mm height without any shape deformity using the composition $A_4C_2M_4$ as shown in Figure 86. Some other deposition orientations i.e. 0^0-45^0, 0^0-45^0-90^0 are also used to fabricate scaffolds with composition $A_4C_2M_4$ to validate the capability to yield different pore geometry as shown in Figure 87 (a) and (c). This indicates the competence of this material to achieve and control the intricate internal geometry of the fabricated scaffold. The microscopic view of the pore geometries shown in Figure 87 (b) and (d) validates the capability of this composition to maintain the desired complex pore geometry resulted from various deposition orientations.
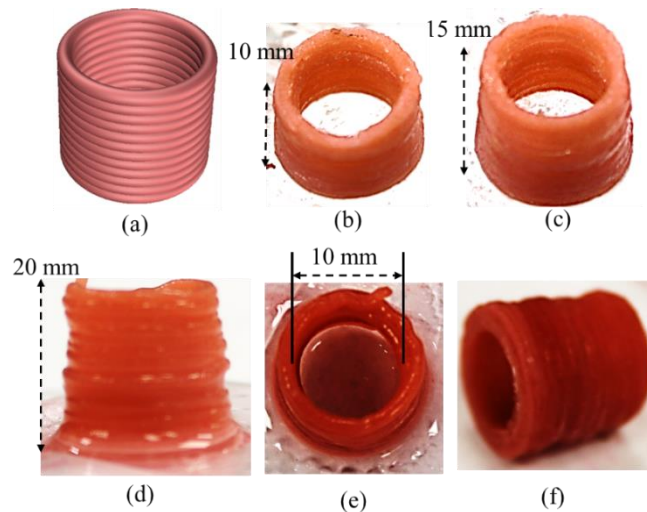
Figure 86: (a) Model of tubular scaffold; fabricated scaffold with (b) 10 mm, (c) 15 mm, (d) 20 mm build height, (e-f) Top view of the scaffold having 20 mm build height, and (f) Flipping the scaffold on build plane after fabrication having 20 mm build height.
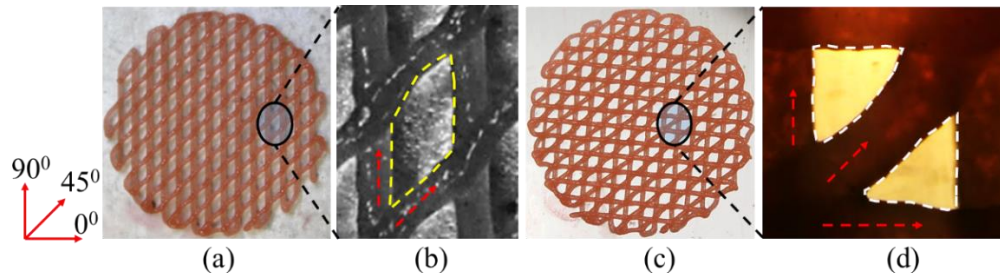
Figure 87: (a) Scaffold and (b) its pore geometry having deposition orientation 0^0-45^0, (c) Scaffold and (d) its pore geometry having deposition orientation 0^0-45^0-90^0.

114

This material is deposited to fabricate complex layer geometry instead of depositing it for regular geometry i.e. square, circle, and rectangle to validate the ability to maintain the shape fidelity for complex 3D object. A bi-layer toolpath is designed for vertebra incorporating variational pore size and fabricated with this composition as shown in Figure 89. A kidney model is fabricated up to 30 layers following the deposition orientation of 45^0-90^0 as shown in Figure 88. All of the fabricated scaffold demonstrated in this paper indicates the good potential of this composition to be implemented as new type of bio-ink in 3D bio-printing process.
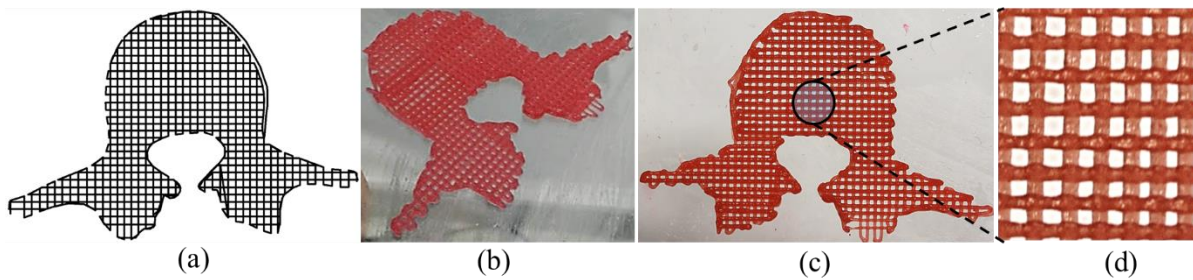
Figure 88: (a) Bi-layer toolpath orientation of vertebra with variational pore size, (b-c) Fabricated scaffold, and (d) Variational pore size.
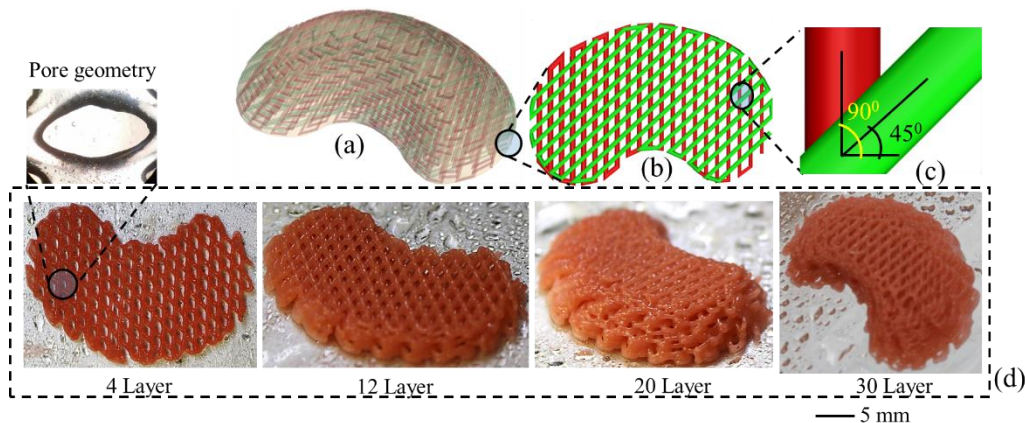
Figure 89: (a) Kidney model, (b) Bi-layer orientation, (c) Filament disposition orientation, and (d) Fabricated scaffold with different layer numbers.

5.2.6. Assessing cytotoxicity

BxPC3, the human pancreatic cancer cells are cultured and maintained in high glucose DMEM, 2 mM Glutamine, and 10% Fetal Bovine Serum (FBS) with 100 µg /ml penicillin and

100 µg/ml streptomycin (Sigma-Aldrich) in 5% CO_2 at 37^0C incubator. The culture medium is

changed twice a week. Cells at passage 5 are used for 3D bio-printing. For cell-laden scaffold

fabrication, 2×10^6 cells/ml are mixed with $A_4C_2M_4$ solution into disposable barrel reservoir

(EFD, Nordson) and dispensed pneumatically through a dosing nozzle (EFD, Nordson, the inner

diameter 410 µm). The cell-laden scaffold is preserved in 5% CO_2, and 37^0C incubator with the

same medium used for cell culture.

During deposition the cell-laden filament through dispensing nozzle, the cell experiences

shear stress, which could be potentially harmful to the cell. Thereby, the cell viability and

cytotoxicity is conducted using LIVE/DEAD assay after 7 days. ReadyProbes™ Cell Viability

Imaging Kit, Blue/Green (Thermofisher, USA) was used following the manufacturers protocol.

The filament with the cells was imaged using Lionheart FX automated live cell imager (Biotek,

USA). The z-stack images are captured using 50 µm layer thickness. The protocol is defined

accordingly and beacon (n=5) is selected randomly. Laser power and other detector parameters

are kept constant throughout the imaging of the different beacons. The demonstration of

LIVE/DEAD assay is shown in Figure 90. From the figure it is clear that 84% of live cell are

presented in the scaffold after 7 days. The percentage of cell viability for this proposed bio-ink is

compared with existing bio-ink in Table 8.

Table 8: Comparison of cell viability with proposed and existing bio-ink.

Bio-ink constituents	Cell viability (%)
Pure alginate [155]	80
Alg-Laponite-Methyl Cellulose [46]	70-75
Alg-Methyl Cellulose [155]	78
Alg-CMC-MMT (proposed)	84
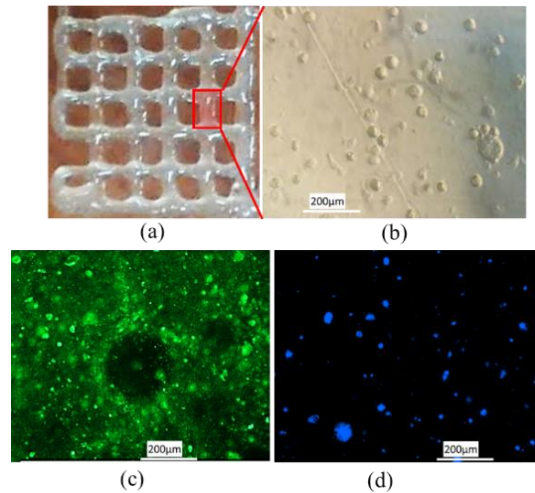
Figure 90: (a) Cell-laden scaffold, (b) Phase-contrast view, (c) Live cell, and (d) Dead cell after seven days.

5.2.7. Remarks for material-Alginate, CMC and MMT

The presented hybrid bio-ink indicates an attractive alternative for 3D bio-printing materials for extrusion based system. The outcome of a set of characterization tests validate that MMT and CMC can be employed as a hydrogel filler for multiple polymeric platforms. The characterization tests and fabrication demonstration with 4% (w/v) alginate, 2% (w/v) CMC and 4% (w/v) MMT makes this composition a novel type of bio-ink in 3D bio-printing process. It is clear that this hybrid bio-ink can be a potential biomaterial suitable for 3D bio-printing process and the outlined characterization techniques open an avenue directing reproducible printability and shape fidelity. Furthermore, 7 days of cell culture result shows 84% cell viability which proves it bio-compatibility as well. However, it is clearly identified that, the encapsulated cell is not changing its morphology which is one of the main requirements to regenerate the tissue. Therefore, in the next chapter, another element will be found out and mixed with alginate and CMC to provide better cell viability, proliferation and morphological change.

6. DEVELOPMENT OF NANO-FIBER INFILLED BIO-INK FOR 3D PRINTING PROCESS

Recently, the increasing interest on hydrogel nano-materials and nano-composites in biomedical, pharmaceutical and tissue engineering applications [269] brings nano-fibrillated cellulose (NFC) on top of the list [270, 271]. NFC is a high aspect ratio natural, sustainable material derived from the most abandoned renewable polymer on earth i.e. plant [272, 273] which has a versatile application span in coatings, biomedical, energy, construction and specialty chemical industries [274]. NFC is composed with β (1-4) linked D-glucose units and partially to fully crystalline which exhibits remarkable mechanical properties [275, 276], hydrophilicity and tunable surface chemistries and biocompatibility [152, 277]. Typically, the individual fibrils of NFC are 3-5 nm in diameter and several micrometers in length [278]. The chemical structure of NFC is shown in Figure 91.

Since, NFC forms gel at very low concentration into water, this rheology is used in several works to explore the 3D printing. Pure NFC (2% wt) is used as base material to fabricate the 3D object and freeze dried to analyze the potential of this material in additive manufacturing [279]. This material is also used in 3D bio-printing to fabricate 3D scaffold for culturing human pluripotent cells and liver cells [280, 281]. NFC is used with other hydrogels as filler or thickener to increase the viscosity to conduct the 3D bio-printing. Several works are published to demonstrate the 3D printability and biocompatibility of various concentration of alginate (0.25-1.0 % w/v) and NFC (1.50-2.25 % w/v) hydrogel including chondrocytes cell to identify the potential to regenerate the cartilage tissue [152, 282]. In another work, human-derived induced pluripotent stem (iPS) cells are used with alginate-NFC and hyaluronic acid-NFC compositions to fabricate cartilage engineered tissue using 3D bio-printing technique [283]. Recently, NFC-

alginate hydrogel is used as coating of surgical sutures as cell carrier and result demonstrates the potential of therapeutic cell delivery [284]. However, the non-uniformity of network entanglements in the pure NFC gel made them highly difficult to make them 3D printable because the erratic nature of pressure requirement [285]. Therefore, 3D printed object with this material shows poor shape control. To enhance the uniformity, dispersibility, homogeneity and printability of NFC based gel, the surface of this material is modified by oxidizing with 2,2,6,6 tetramethyl-1-piperidinyloxy (TEMPO) to add negatively charged carboxylate ion. TEMPO-mediated oxidation is one of the chemical pretreatment methods to modify selectively the surface of native NFC under aqueous and mild condition. This method selectively introduces anionic carboxylate groups on the surface of each cellulose fibril [286, 287]. This oxidization method proceeds with the addition of NaClO to aqueous NFC suspensions in the presence of catalytic amount of 2,2,6,6 tetramethyl-1-piperidinyloxy (TEMPO) and NaBr at pH 10-11 at room temperature [288]. The primary hydroxyl groups of C6 are selectively oxidized into aldehyde groups and consequently converted to carboxylate groups as shown in Figure 91. TEMPO mediated oxidized NFC will be denoted as TO-NFC in this paper.
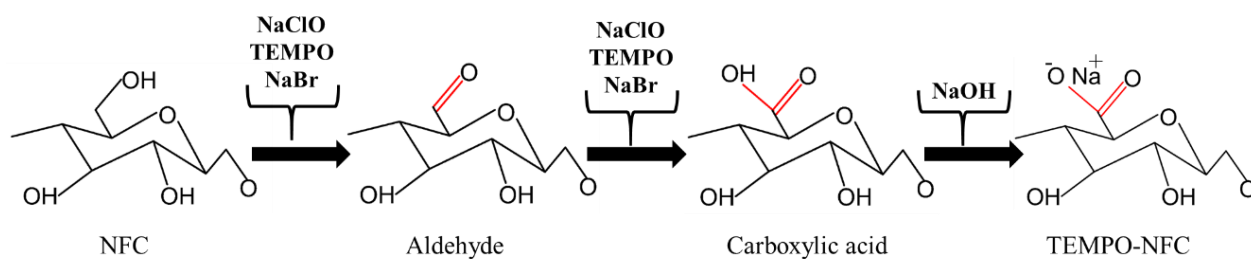
Figure 91: Mechanism of TEMPO pretreatment to NFC.

This negatively charged carboxylated NFC has the capacity to disperse into the water at the individual nano-fibril level because of the electrostatic repulsion effect [289]. Because of its

119

larger surface area compared to pure micro-fibrillated cellulose (MFC), the smaller amount of TO-NFC i.e.0.2% (g/ml) can form gel by forming the hydrogen bond among fibers [192]. Various percentage of TO-NFC i.e. 0.2-0.4 % (g/ml) shows the dominating amount of storage modulus compared to loss modulus [192] which reflects the shape holding capacity of this material after casting or bio-printing. In another work, the shear thinning behavior of TO-NFC is identified [275] which is also a critical property of any biomaterial to be 3D-printable. Moreover, the application of mono-, di- and trivalent cations into TO-NFC triggers the gelation due to strong ionic interactions between carboxylate group and metal ion [192, 290]. This phenomenon also encourages the authors to use this material as a conjugate of alginate to explore the 3D bio-printing. In order to determine the biocompatibility, TO-NFC is administered with glucose and glyceryl trioleate to mice and investigated the blood insulin and GIP content [291]. TO-NFC (1% w/v) and the combination of carboxymethylation and periodate oxidized NFC (0.5 % w/v) is used to prepare gel and deposit using extrusion 3D-bioprinting system for wound dressing applications [292]. However, the pure TO-NFC does not show better shape fidelity compared to other hydrogel used in [292]. Recently, a work is reported to demonstrate the 3D printability of pure TO-NFC (2.8% w/v) to fabricate light weight large scale 3D scaffold. After fabrication, the scaffold is freeze dried and it achieved almost 98% porosity [285]. However, the cytotoxicity of this material is not considered in this paper. The addition of anionic group i.e. carboxylate with NFC improves the cytokine secretion which eventually assist to attach and proliferate the cell on the fiber surface [293]. Recent, several works reported that, to fabricate the functional tissue construct, the alignment of functional cell and cell to cell interaction are imperative [294-296].

Though the 3D-bioprintability and biocompatibility of TO-NFC are demonstrated [291, 292], the distribution and orientation of fiber into 3D printed scaffold are not explored yet. In

extrusion based bio-printing process the bio-ink passes through the dispensing nozzle and the shear generated within the nozzle may provide a partial alignment of the reinforced fiber along the deposition direction. Such oriented distribution in scaffold structure may control its' mechanical properties [275, 276], hydrophilicity, surface chemistries and biocompatibility [277, 297]. Even though, the flow induced fiber alignment have been reported for synthetic polymer (i.e. carbon and glass fiber) [298-300], but alignment of natural fiber (e.g. cellulose nano-fiber) has not been studied yet. Since, the short fiber can be aligned with the application of shear, the controlled alignment of TO-NFC can drive the encapsulated functional cell towards its own direction as shown in Figure 92 (c). Therefore, TO-NFC is considered as third element and blended with previously developed bio-ink of alginate and CMC in this chapter.
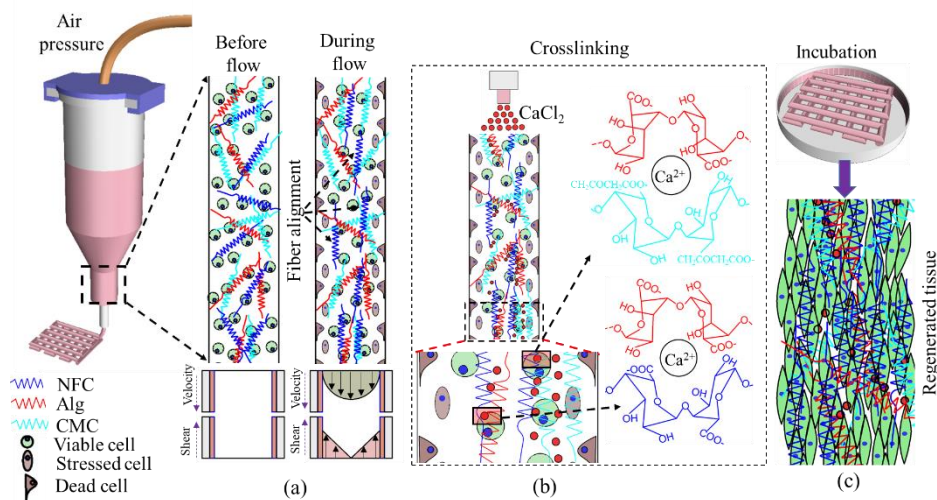
Figure 92: (a) Deposition of short fiber filled hydrogel, (a) Cross-linking of hydrogel, (c) Incubation and aligned cell proliferation for tissue regeneration.

6.1. Materials and methods

6.1.1. Preparation of TO-NFC

TEMPO nano-fibrillated dry cellulose (0.2-2.0 mmol/g carboxylate level) is acquired from University of Maine (Orono, Maine, USA). The size of TO-NFC is achieved by following

the protocol described in Saito et al.[287]. TO-NFC with 1% (w/v) solid content is mixed into 10

ml deionized water and agitated using a magnetic stirrer bar with 1500 rpm for different period

of time i.e. 2, 4, 6, 8, 10, 12, 23 and 28 hours at room temperature. About 30 μl of slurry is

placed in between of two cover slips to make the fiber planar. The cover slip is placed under the

CK Olympus bright field microscope (Tokyo, Japan) and captured the distribution of fiber for

each TO-NFC sample. Each image is imported into ImageJ, an image processing software and

"segmented line" option is used to determine the length of the randomly selected fibers (n=10).

The length of the fibers stirred for 2, 4, 6, 8, 10, 12, 23 and 28 hours are 219.13 ± 14.81 μm,

128.8± 7.51 μm, 104.54± 6.11 μm, 87.83 ± 6.10 μm, 85.93 ± 6.73 μm, 62.49 ± 8.72 μm, 46.47 ±

3.16 μm, and 34.69 ± 2.96 μm respectively. The diameter of the nanofibers is measured as 82 ±

11 nm. After stirring, the TO-NFC slurry is stored at 4^0C before further analysis. The flow

diagram of overall processing of TO-NFC is shown in Figure 93 (a).
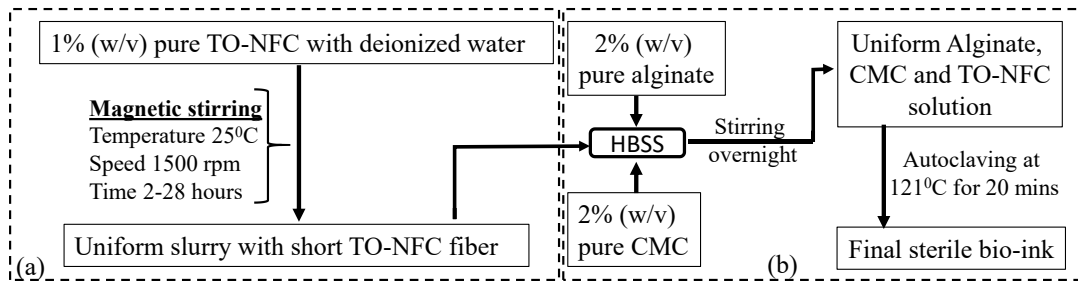
Figure 93: (a) Preparation of TO-NFC (b) Preparation of bio-ink using alginate, CMC and TO-NFC.

6.1.2. Preparation of hydrogel

TO-NFC slurry achieved after the stirring of 28 hours is selected as candidate fiber. This

slurry is poured into HBSS with hybrid hydrogel (Alginate and Carboxymethyl cellulose-CMC)

developed in chapter three , stirred overnight until the solution turns into viscous and

homogeneous solution and autoclaved at 121^0C for 20 minutes for the further experiment as

shown in Figure 1(b). TN represents TO-NFC and the numerical subscripts represent the weight percentage of the material mixed. As a physical cross-linker, 4% (w/v) calcium chloride ($CaCl_2$) (Sigma-Aldrich, St. Louis, MO, USA) is prepared with 0.2 µm filtered deionized (DI) water. The percentages of material shown in Table 9 are dissolved into 0.2 μm filtered deionized (DI) water and stirred overnight to prepare the bio-ink gel. 4% (w/v) $CaCl_2$ (Sigma-Aldrich) is prepared with 0.2 μm filtered deionized (DI) water and used as chemical cross-linker to assure quick gelation of the deposited bio-ink.

Table 9: Composition of samples with weight percentage.

Sample	Alg (A) (g)	CMC(C) (g)	TO-NFC (TN) (g)	Alg/CMC/TO-NFC (ACTN) (%)	Water content (wt%)
$A_0C_0TN_1$	0.0	0.0	1.0	0/0/100	99.0
$A_1C_1TN_1$	1.0	1.0	1.0	33/33/33	97.0
$A_2C_2TN_1$	2.0	2.0	1.0	40/40/20	95.0
$A_2C_2TN_{0.5}$	2.0	2.0	0.5	45/45/10	95.5

6.1.3. Fiber direction and deposited into deposited filament

The shear induced deposition of soft material reinforced with the short fiber may affect the orientation of the fiber [301, 302]. In [301, 302], increase in fiber orientation is described by reducing the mean fiber angle relative to the direction of force exertion i.e. the deposition direction. To analyze this phenomenon, a single filament is extruded using the selected process parameters shown in Figure 94 (a). Material under simple shear flow condition through the nozzle may result two different layers called core layer and skin or frozen layer as shown in Figure 94 (b) [302, 303]. These two layers are defined by the fiber orientation. The fiber in the skin layer tends to be oriented parallel to the applied load or deposition direction whereas the

fiber in the core layer orients perpendicular to deposition direction [304]. The distribution of fiber for filament is captured by CK Olympus bright field microscope (Tokyo, Japan).

Process parameters	
Nozzle dia (μm)	250, 310
Air pressure (psi)	8, 10, 12
Nozzle speed(mm/s)	4
Print distance (mm)	0.7

(a)

(b)
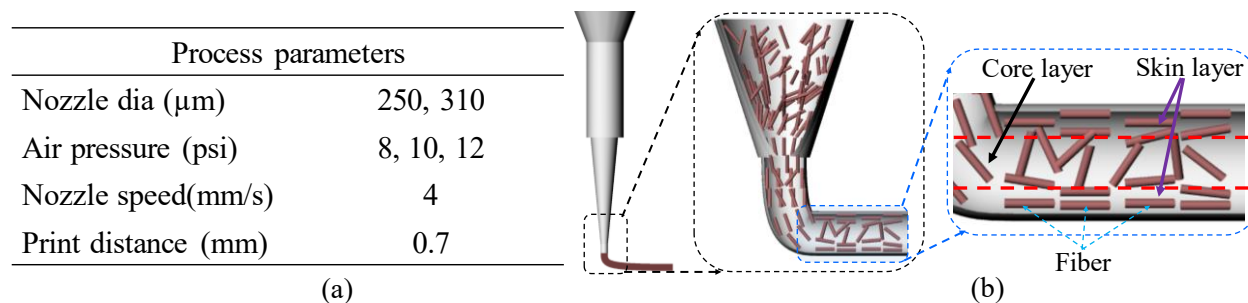
Figure 94: Material compositions and process parameters used to analyze the effect of air pressure and (b) core layer and skin layer.

6.1.4. Fourier transformation infrared (FTIR) spectroscopy

Fourier transform infrared spectra were obtained using Nicolet 8700 FTIR spectrometer (Thermofisher, Waltham, MA) and KBr discs in the spectra range 7800-350 cm^{-1} with an optical resolution of 0.09 cm^{-1} and an accumulation of 27 scans per analysis.

6.1.5. Characterization tests

The same instruments, protocols as discussed in chapter three have been used in this chapter to conduct the rheological test, scanning electron microscope, swelling test, shape fidelity test.

6.2. Result and discussion

6.2.1. TO-NFC fiber length

About 30 μl of slurry is placed in between of two cover slips to make the fiber planar as shown in Figure 95 (a-b). The cover slip is placed under the CK Olympus bright field microscope (Tokyo, Japan) and captured the distribution of fiber for each TO-NFC sample. Each image is imported into ImageJ, an image processing software and "segmented line" option is used to determine the length of the randomly selected fibers (n=10). The fiber length is expressed

as "mean± standard deviation". The microscopic view and the average length of the fiber size at different stirring time are shown in Figure 95 and Figure 96 (c) respectively. From those figures, it is clear that the fiber size is showing a decreasing trend ranging from 219 ± 14.81 µm to 34.7 ± 3 µm with respect to the stirring time.
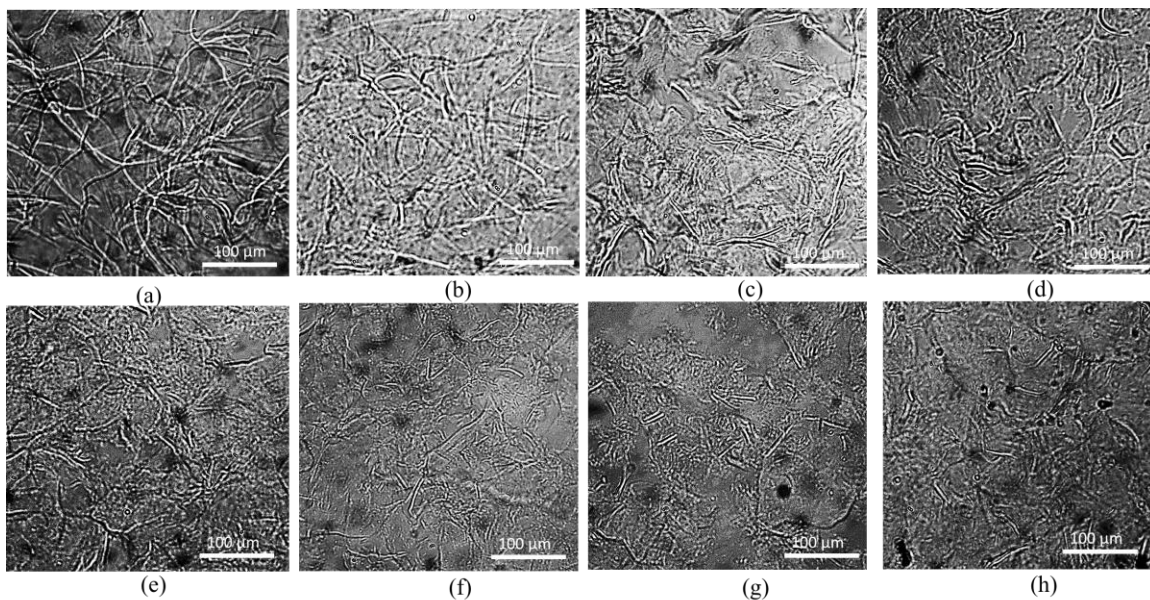
Figure 95: Microscopic view of fiber size at stirring time of (a) 2 hours, (b) 4 hours, (c) 6 hours, (d) 8 hours, (e) 10 hours, (f) 12 hours, (g) 23 hours, and (h) 28 hours.
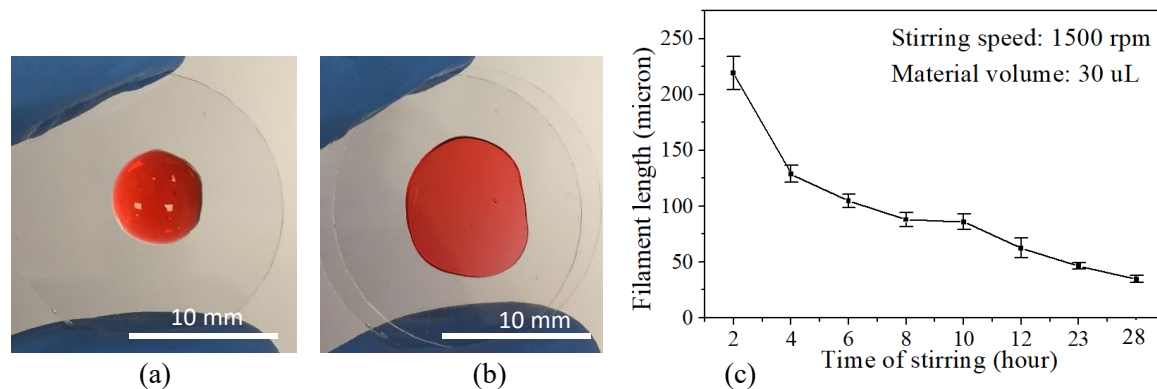
Figure 96: (a-b) 30 µl of TO-NFC into the cover slip for microscopic capture, and (c) changes of fiber size with respect to stirring time.

6.2.2. Rheological test result

Various rheological tests *i.e.* steady rate sweep test, dynamic stress sweep test, frequency sweep test, 3-interval thixotropic tests are conducted to detemine the suitable combination of alginate, CMC and TO-NFC. The outcome of each rheological test is analyzed in this section to suggest a suitable combination of alginate, CMC and TO-NFC which will be able to hold the shape of fabricated large scaffold with proper prinability and shape fidelity.

6.2.2.1. Steady rate sweep test

The log-log plots of viscosity vs shear strain rate and shear stress vs shear strain rate are shown in Figure 97 (a) and Figure 97 (b) respectively. Viscosity decreases with increasing the shear rate whereas the shear stress increases with increasing the shear rate. This phenomenon demonstrates the shear thinning behavior of all the compositions. However, the addition of solid content with the suspension increases the overall viscosity as well as the shear stress. Therefore, the composition, $A_2C_2TN_1$ shows higher viscosity and shear stress. Zero-shear viscosity value of composition, $A_2C_2TN_1$ increases almost from 0.4 Pa.S to 300 Pa.S with respect to only pure TO-NFC. This might happen because of increasing the cross-linking rate with increased amount of solid content. The elements of the composition, $A_2C_2TN_1$ having high solid content are containing the polar group C=O which drives towards high rate of cross-linking.
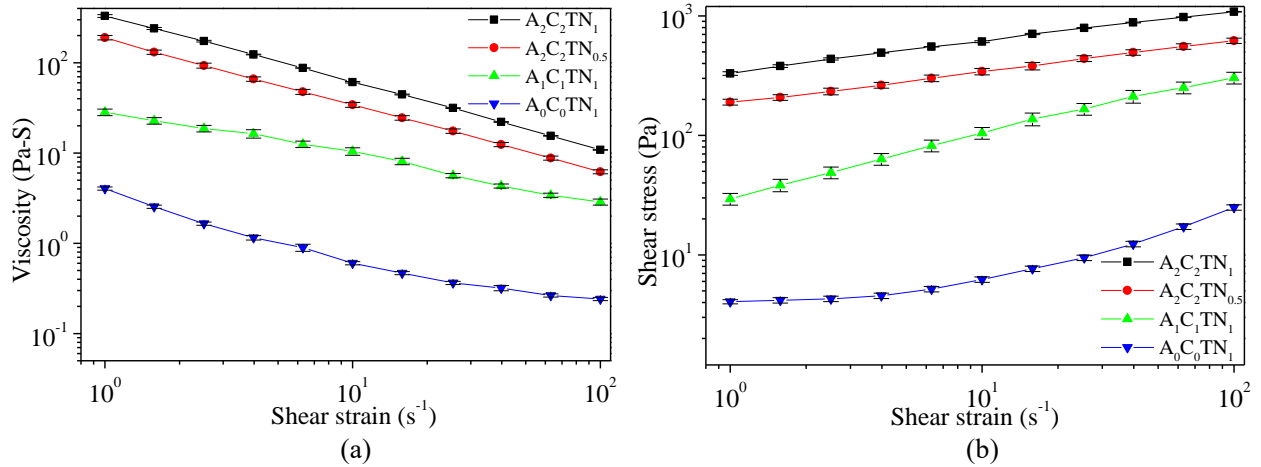
Figure 97: Evaluation of shear thinning behavior of hydrogels: (a) Viscosity vs shear strain rate, (b) Shear stress vs shear strain rate.

6.2.2.2. Dynamic stress sweep test

The dynamic stress sweep test for various compositions of the hydrogel at 1 Hz is represented the outcome of G' and G'' vs shear strain (%) in Figure 98. It is clear from the figure that with increasing the percentage of solid content into the suspension, the physical state of the hydrogel is transferred from liquid-like to solid-like state. In case of pure TO-NFC, value of G'' dominates G' at each shear strain as shown in Figure 98 (a). Thereby, the liquid-like state is persisted for this hydrogel. With increasing the amount of alginate, CMC in the suspension from 1 to 2 %, G' dominates G'' up to a certain level of shear strain and then intersects. This certain level is called as linear viscoelastic range (LVR) which determines the limit at which the suspension preserves the sedimentation within the sample without permanent deformation. This resembles the solid-like behavior of the suspension before the intersecting point. After the intersecting point, both moduli are decreased with the dominancy of G'' i.e. the liquid-like phase. In the co-existence of liquid and solid-like phase, increasing the solid content increases the LVR as shown in Figure 98 (b-d). To provide more insight into solid and liquid-like behavior of

127

hydrogel, dynamic mechanical loss tangent ($\tan \delta = G''/G'$) is also included in each graph as shown in Figure 98 (a-d). Tangent value smaller than 1 predominantly reflects the elastic behavior, and greater than 1 predominantly indicates viscous behavior. It is clear from the figures that $A_2C_2TN_1$ and $A_2C_2TN_{0.5}$ shows predominant solid-like behavior up to almost 47% and 9 % strain rate respectively.
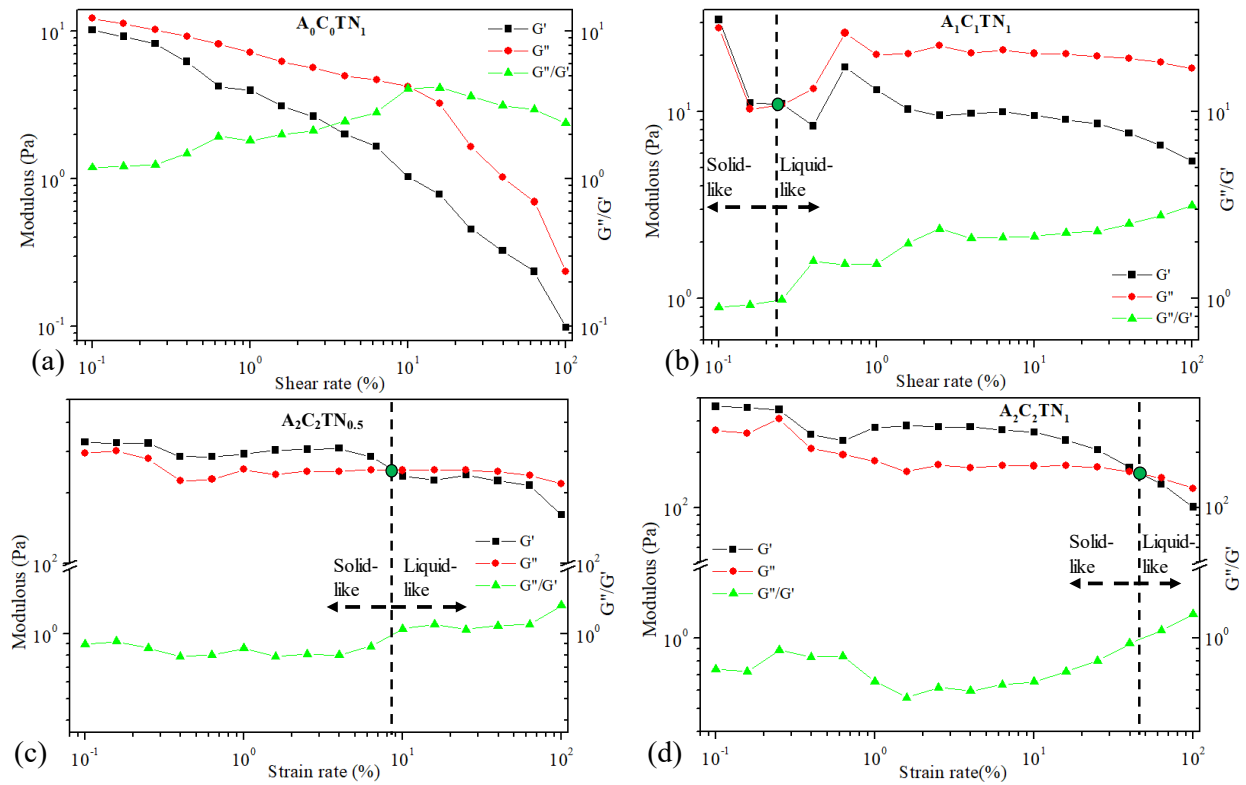
Figure 98: Dynamic strain sweep test for (a) Pure TO-NFC, (b) $A_1C_1TN_1$, (c) $A_2C_2TN_{0.5}$, and (d) $A_2C_2TN_1$.

6.2.2.3. Three point interval thixotropic test

To provide more understanding of the real scenario during extrusion of hydrogel, 3-interval-thixotropy-tests are also conducted on various compositions. In this test, the first interval imitates the at-rest state of sample, the second interval resembles the hydrogel decomposition under high shear i.e. experienced high shear during extrusion, and third interval reflects the

128

structure retention after hydrogel extrusion as shown in Figure 99 (a). The stress-shear rate loop shown in Figure 99 (c) demonstrates the shear history of the compositions. A stress is applied on the at-rest hydrogel which breaks down the initial network structures of the hydrogel during extrusion. After the hydrogel is extruded through the nozzle at a certain shear rate, the initial internal network of the hydrogel is reformed as shown in Figure 99. From Figure 99 (b), it is clear that, the direction of the viscosity of the hydrogel is upward right after the extrusion which indicates the retention of the broken internal bond of the deposited hydrogel.
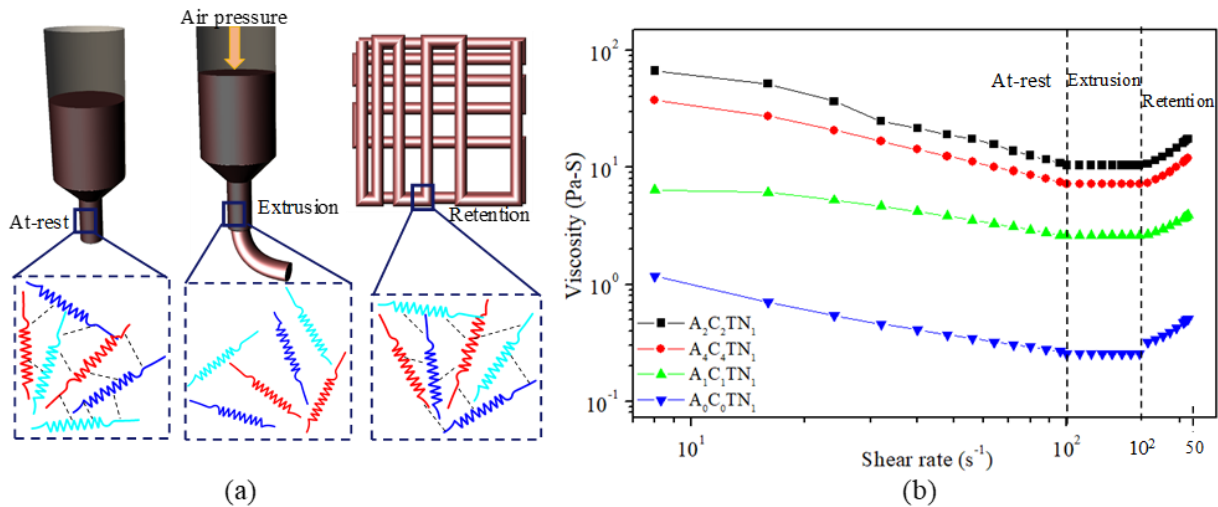
Figure 99: (a) Representation of three states during extrusion, (b) Result of 3-Interval-thixotropic-tests.

It is revealed from the result of the above mentioned rheological experiments that compositions $A_2C_2TN_1$ and $A_2C_2TN_{0.5}$ have higher viscosity and eventually better solid-like state during exertion of shear. Therefore, these two compositions will be used for the rest of the research for further analysis unless otherwise stated.

6.2.2.4. Remarks for rheological test

Once all the rheological tests are done, it is clear from the result that the viscosity is solid content dependent, because 2% alginate-2% CMC-1% TO-NFC is showing highest viscosity.

However, material with higher viscosity demands more shear stress which hinders the overall cell viability. Composition containing 2% alginate-2% CMC-1% TO-NFC, has better potential to maintain proper printability and shape fidelity during large scaffold fabrication as well as cell viability.

6.2.3. FTIR result

Figure 100 represents the infrared spectra of pure TO-NFC, $A_2C_2TN_1$ and $A_2C_2TN_{0.5}$. The asymmetric stretching band at 1613 cm^{-1} of the FTIR spectra indicated chains modified by carboxyl groups. Moreover, the stretching vibration band of the C-H at 2920 cm^{-1} and stretching vibration band of the -O-H groups near 3393 cm^{-1}. A signal at 1040 cm^{-1} is corresponding to C-O stretching vibrations.
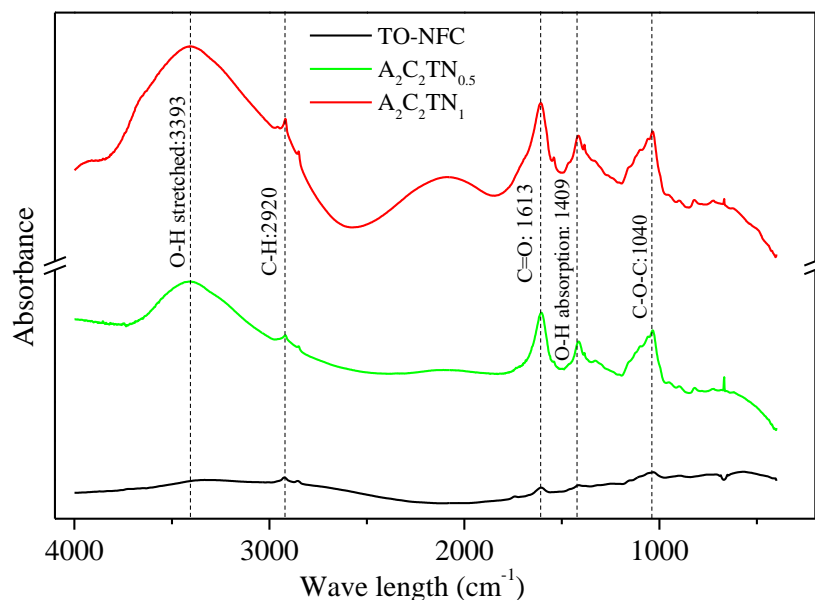
Figure 100: FTIR spectrum of various candidate materials.

6.2.4. Fiber directionality

The distribution of TO-NFC into the final solution of $A_2C_2TN_{0.5}$ and $A_2C_2TN_1$ is shown in Figure 101 (a-b) which is apparently random. The determination of angle of the individual fiber with respect to the deposition direction is shown in Figure 101(c). The effect of the air

130

pressure on the deposited filament width and the orientation of the fiber are analyzed in this

paper. The graph shown in Figure 101 (d) demonstrates the increasing tread of the filament

diameter with increasing the air pressure for both 250 µm and 310 µm nozzle dia for $A_2C_2TN_1$

composition. Due to the change of the filament width, the orientation of the fiber changes which

eventually affect the thickness of core and skin layer [304].

The filament fabricated with $A_2C_2TN_1$ through 250 µm and 310 µm nozzle at various air

pressure and their fiber distribution are shown in Table 10 and Table 11. The absolute angle

between the randomly selected TO-NFC fibers and the deposition direction is shown in Figure

102 (a) and (b) for 250 µm and 310 µm nozzle respectively. The fiber distribution for the

filament generated by 250 µm nozzle and 10 psi air pressure shows almost 84% fiber disperse

within 0^0-30^0 range with respect to the deposition direction. The result is shown in Figure 102

(c).
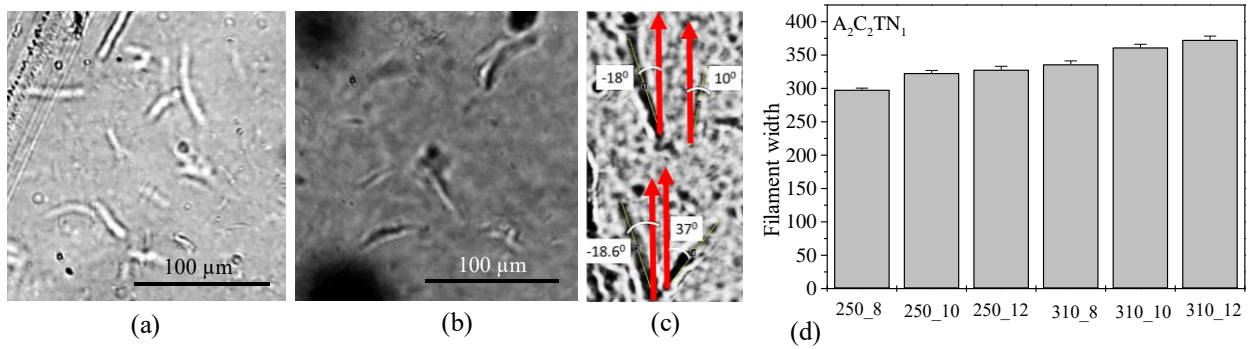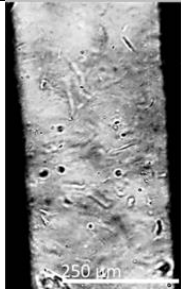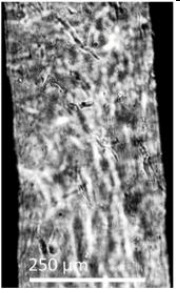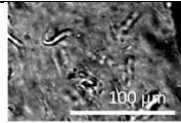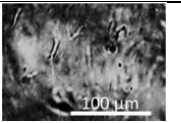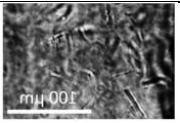
Figure 101: Distribution of TO-NFC into the final solution of (a) $A_2C_2TN_1$, (2) $A_4C_4TN_1$ and (c)
angle between TO-NFC and deposition direction, and (d) changes of fiber width with respect to
air pressure for $A_2C_2TN_1$ composition.

The fiber distribution for the filament generated by the same nozzle with 8 psi and 12 psi

shows 46% and 54% within 0^0-30^0 range respectively with respect to the deposition direction.

Even though, the core layer of the filament generated by 8 psi is smaller than the core layer of

filament generated by10 psi and 12 psi, the shear induced by 10 psi and 12 psi influence more to
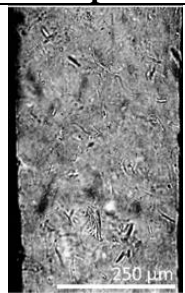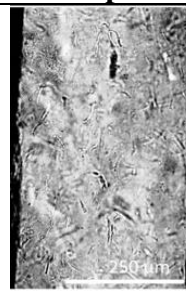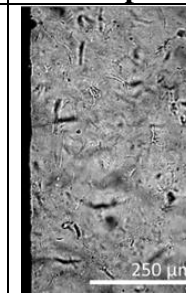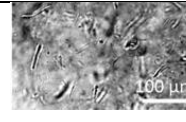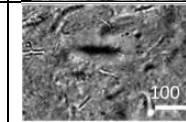
align the fiber along deposition direction [28]. However, the fiber alignment stands better for 10

psi because of the influence of the smaller core layer than 12 psi. The fiber distribution of the

filament fabricated through 310 µm nozzle and 8, 10, and 12 psi is around 49, 43, and 32%

respectively within 0^0-30^0 range with respect to the deposition direction.

Table 10: 3D Printed filament and fiber distribution for 250 µm nozzle diameter at various air pressures.

Nozzle dia 250 µm	8 psi	10 psi	12 psi
3D printed filament			
Fiber distribution			

The result is shown in Figure 102 (c). It is showing the decreasing trend of the fiber

alignment with respect to the deposition direction. Because, with increasing the air pressure, the

core layer of the filament increases than its skin layer which disrupts the fiber alignment along

force exertion direction. Therefore, the filament fabricated through 250 µm nozzle and 10 psi air

pressure offers better fiber alignment by maintaining the optimum core layer and required shear.

Table 11: 3D Printed filament and fiber distribution for 310 µm nozzle diameter at various air pressures.

Nozzle dia 310 µm	8 psi	10 psi	12 psi
3D printed filament			
Fiber distribution			

Figure 102: (a-b) Orientation of randomly selected fiber with respect to deposition direction through 250 µm and 310 µm respectively, (c) percentage of fiber orientation distribution, and (d) cumulative percentage of fiber orientation distribution.

133

6.2.5. Swelling of material

For the swelling test two sample candidates e.g. $A_2C_2TN_{0.5}$ and $A_2C_2TN_1$ are used. The fabricated scaffolds with the compositions of $A_2C_2TN_{0.5}$ and $A_2C_2TN_1$ are shown in Figure 103 (a,c). All the material compositions used for swelling test show increasing trend of percentage of swelling and pore closure with respect to the incubation day as shown in Figure 103 (b,d). The mean of the percentage of swelling and pore closure is significantly different (p-value=0 with 95% confidence interval) for different days. The swelling rate and pore closure of the composition $A_2C_2TN_{0.5}$ is greater than $A_2C_2TN_1$ for each day. Because composition $A_2C_2TN_1$ has more TO-NFC which forms more chemical bonds into solution and restrict the entry of water during incubation time.
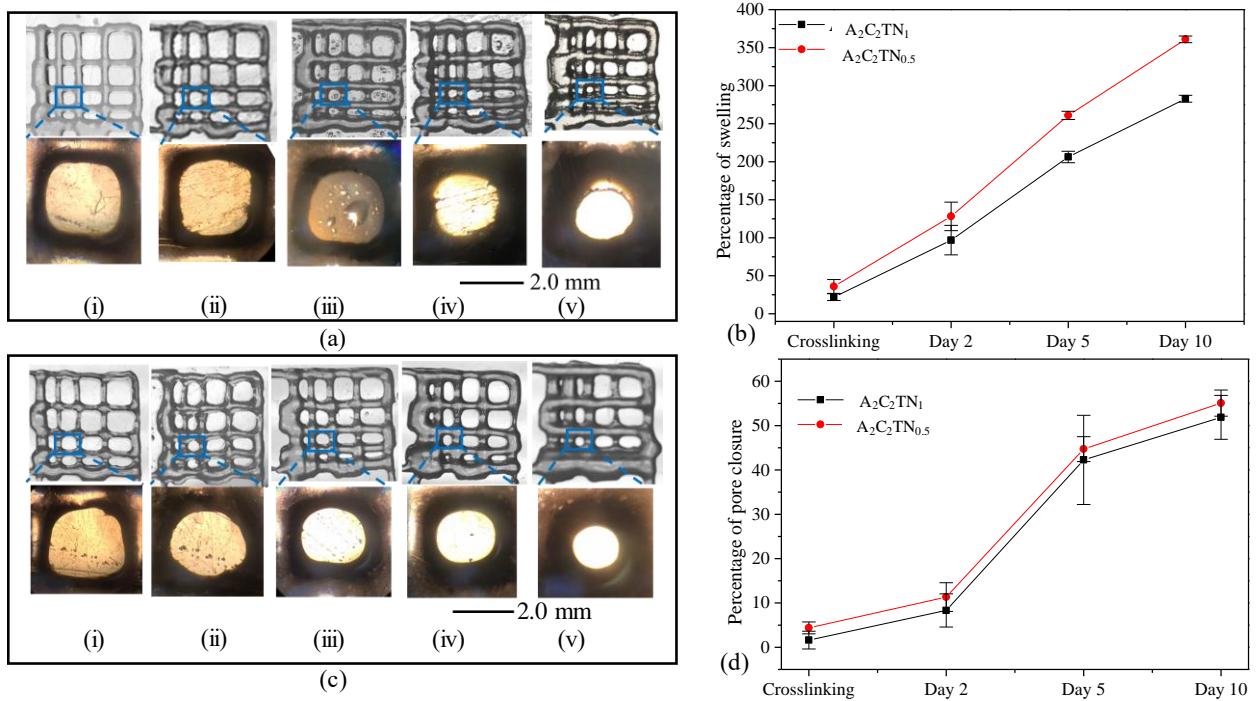
Figure 103: (a,c) Fabricated scaffolds and their microscopic pore geometry: (i) After the printing, (ii) After crosslinking, (iii) at day 2, (iv) at day 5, and (v) at day 10. (b) Percentage of swelling, and (d) Percentage of pore closure.

6.2.6. Microstructure of material

The image shown in Figure 104 (a-b) demonstrates the fiber distribution on the planar surface of the pure TO-NFC. It is clear from the Figure 104 (a-b) that the fiber distributes randomly into the film. The prepared film is broken into two pieces images of the cross-sectional surface of the broken film are captured. The image of the cross-sectional surface shown in Figure 104 (c-d) indicates the fiber distribution along lateral direction which is almost uniform. The cross-section of some of the fiber seems irregular because those fibers are not perfectly situated on X-Y plane.

| (a) | (b) | (c) | (d) |
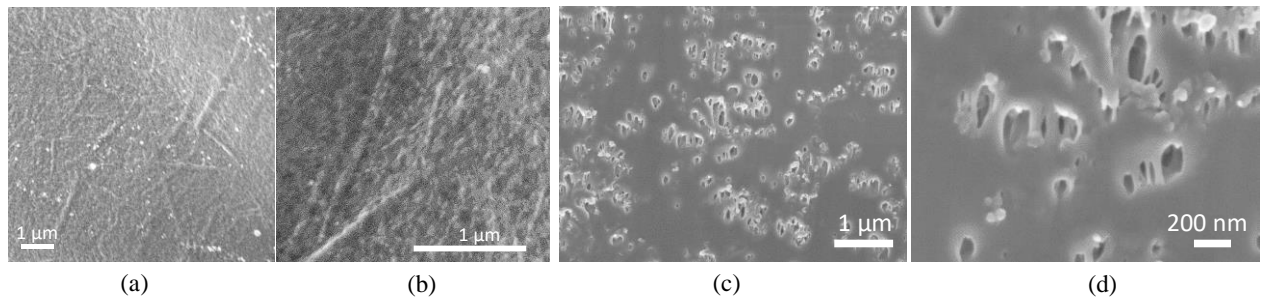
Figure 104: Image of the Pure TO-NFC (a-b) planar Surface and (c-d) Cross section.

SEM is also conducted on the compositions of $A_2C_2TN_1$ and $A_2C_2TN_{0.5}$ to analyze the microstructure morphologically as shown in Figure 105 (a-b). A smooth cell structure and homogeneous distribution of alginate, CMC and TO-NFC are observed. This homogeneous distribution is resulted from the strong chemical interaction between alginate, CMC and TO-NFC.

| (a) | (b) |
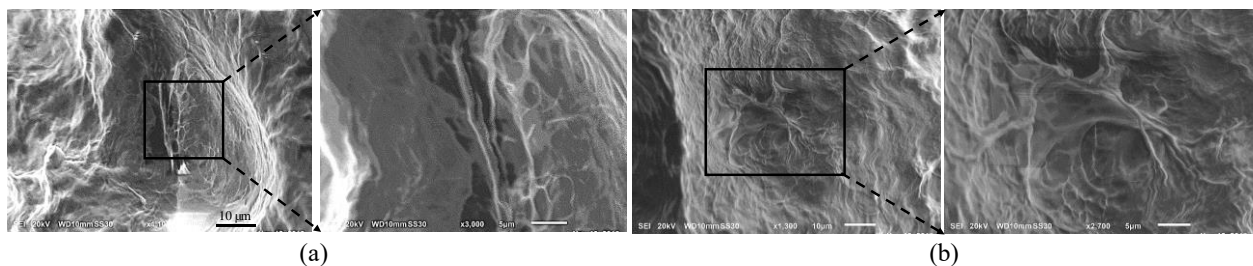
Figure 105: SEM images of the composition of (a) $A_2C_2TN_1$, and (b) $A_2C_2TN_{0.5}$.

135

6.2.7. Shape fidelity test

6.2.7.1. Filament width

To investigate the manufacturability i.e. 3D printability of the sample candidates, an acellular filament is deposited with pure TO-NFC, $A_1C_1TN_1$, $A_2C_2TN_{0.5}$ and $A_2C_2TN_1$. The images of fabricated filament are captured using the CK Olympus bright field microscope (Tokyo, Japan). The width of the filament is determined using ImageJ as shown in Figure 106 (a). Figure 106 (b) indicates that with increasing the solid content into the composition, the diffusion of the filament is decreasing i.e. properly holding the geometry of the filament which eventually will improve the overall shape fidelity of the fabricated scaffold.
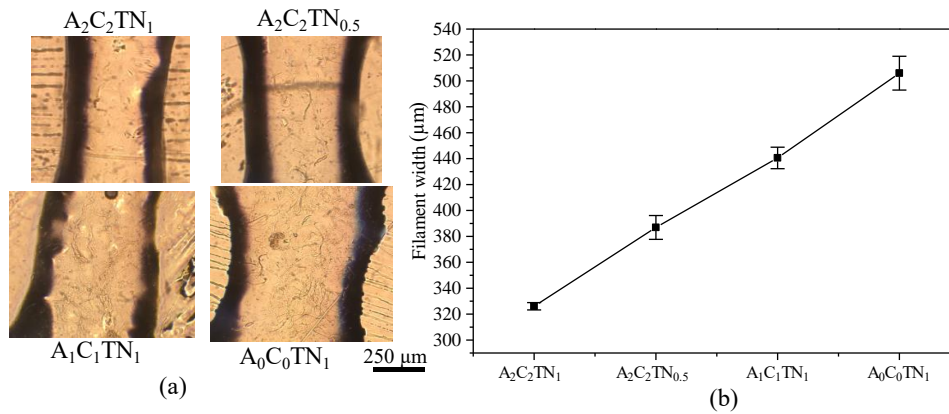
Figure 106: (a) Filament fabricated with four different samples and (b) Filament width of different samples.

Depending on the difference of air pressure, the filament width will also change. The graph shown in Figure 107 demonstrates the increasing trend of the filament width with increasing the air pressure for both 250 µm and 310 µm nozzle diameter. In each case, the diameter of the deposited filament is higher than the nozzle diameter because of material deformation and expansion after deposition. The trend of this result is in accordance with other works related to the effect of air pressure on filament width [305, 306]. The changes of filament width fabricated with $A_2C_2TN_1$ are 19-30% extruded through 250 µm nozzle at various air

pressures, which reflect the good shape holding capacity of the filament fabricated with this material composition. The changes of filament width, fabricated with the composition of $A_2C_2TN_{0.5}$ and through the nozzle of 250 µm, at different air pressure are 34-49% which is undermining the shape holding capacity of this composition. The overall filament width fabricated with the composition and nozzle of $A_2C_2TN_1$ and 310 µm respectively is larger than the filament fabricated with the same material composition and 250 µm nozzle size. Due to the excessive increase in deposited filament width, only $A_2C_2TN_1$ composition will be considered in remaining section.
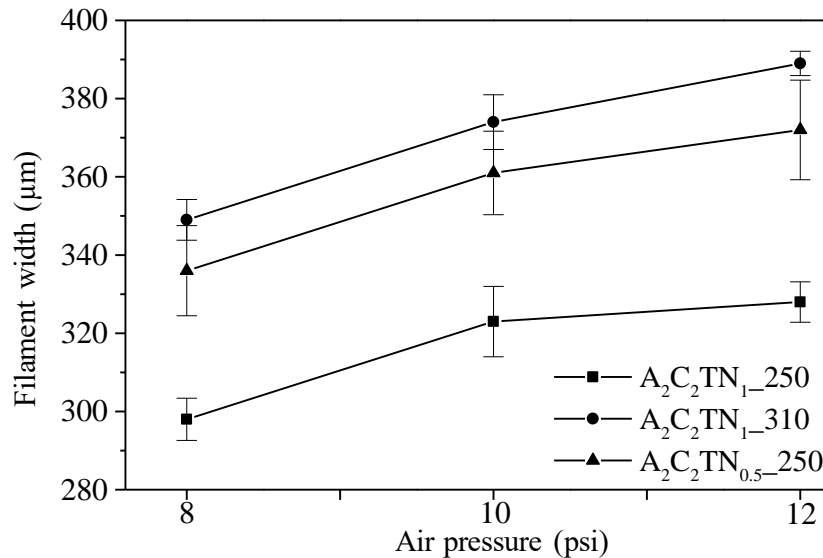
Figure 107: Changes of fiber width with respect to air pressure.

6.2.7.2. Filament fusion

The actual pore area is measured using ImageJ software. Quantitatively, the diffusion rate shows a decreasing trend with increasing the pore size as shown in Figure 108. The fabricated scaffold and quantitative result indicate that the diffusion rate of composition $A_2C_2TN_1$ is only 33% for 3×3 pore size. On the other hand, for the same size of pore, the diffusion rates are 63%,

100% and 100% for $A_2C_2TN_{0.5}$, $A_1C_1TN_1$ and TO-NFC respectively. With less solid content, the material diffuses more on xy-plane and undermine the filament stacking capacity which is also stated in some existing literatures [38, 189].

(a)

(b)
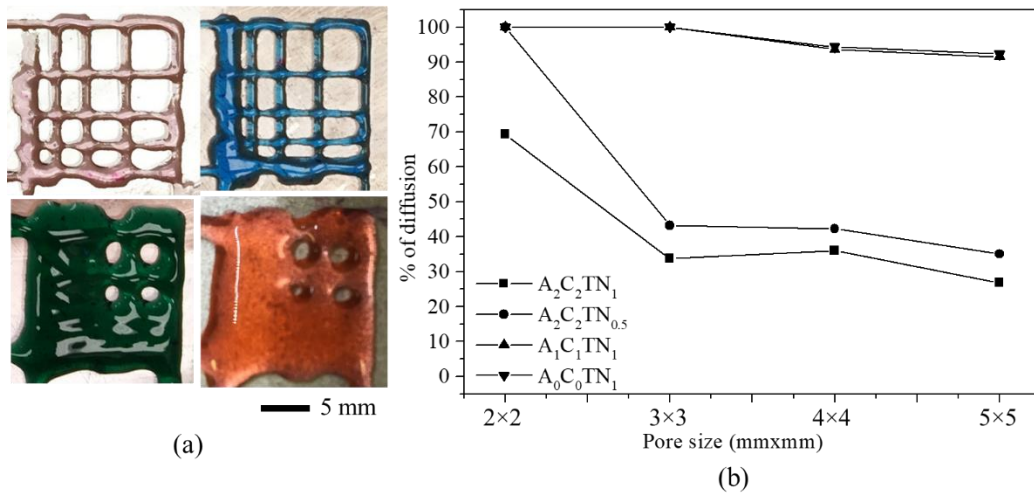
Figure 108: Fabricated scaffold for fusion test using compositions (a) $A_2C_2TN_1$, $A_2C_2TN_{0.5}$, $A_1C_1TN_1$, Pure TO-NFC, and (b) Result for fusion test.

6.2.7.3. Filament collapse

The qualitative observation of the collapse test for various compositions of material indicates that increasing the percentage of solid content leads minimum deflection of the suspended filament as shown in Figure 109. With increasing the pillar to pillar distance, percentage of collapse is increasing. Quantitatively, composition $A_2C_2TN_1$ shows only 23% of collapse while pure TO-NFC and $A_1C_1TN_1$ shows 100% and 88% collapse respectively. Composition $A_2C_2TN_1$ also shows better result than $A_2C_2TN_{0.5}$. Therefore, it can be concluded from this test that composition $A_2C_2TN_1$ is able to hold the filament geometry during 3D bio-printing. The result of collapse test is shown in Figure 109.
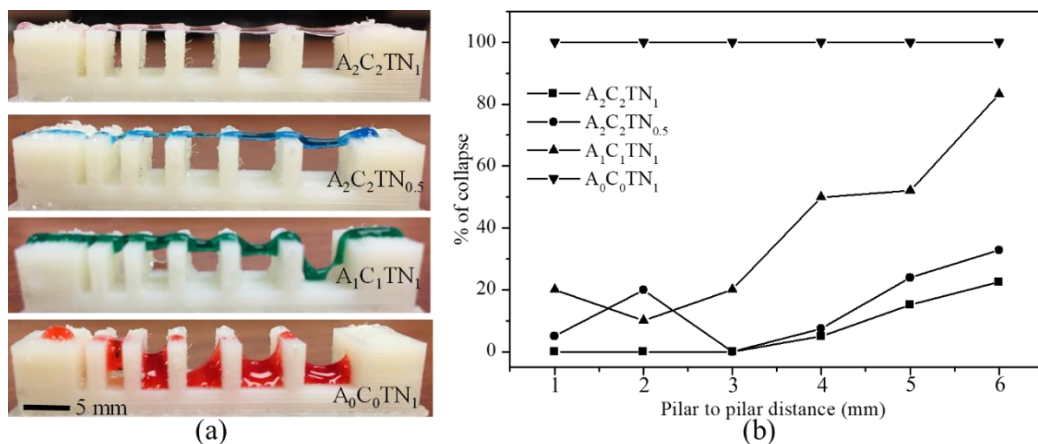
Figure 109: Deposited filament for collapse test using compositions (a) $A_2C_2TN_1$, $A_2C_2TN_{0.5}$, $A_1C_1TN_1$, Pure TO-NFC, and (d) Result of collapse test.

6.2.7.4. Remarks for shape fidelity test

After doing a set of systematic qualitative and quantitative characterization, it is clear that the composition, $A_2C_2TN_1$ maintains good printability and shape fidelity. This result indicates that $A_2C_2TN_1$ can be a good candidate for the fabrication of large-scale scaffold.

6.2.8. Fabrication of large scaffold

Once all the characterization tests i.e. viscosity, filament width, collapse test and fusion test are done, it is clear that composition $A_2C_2TN_1$ is able to assist the scaffold to maintain the structural integrity. Therefore, $A_2C_2TN_1$ is used to fabricate acellular scaffold to demonstrate the 3D printability of large and freeform scaffold. A cuboidal scaffold having a dimension of 25mm×25mm with a raster width of 2.5 mm is fabricated up to 32 layers with a build height of 8.75 mm with good shape fidelity as shown in Figure 110. This material composition can also be used to fabricate the free-form shape assuring the pore geometry as shown in Figure 111. After that, the structure starts to lose its fidelity because of increasing material weight on top of the structure. Authors have run the fabrication up to 42 layers with this material composition.

139
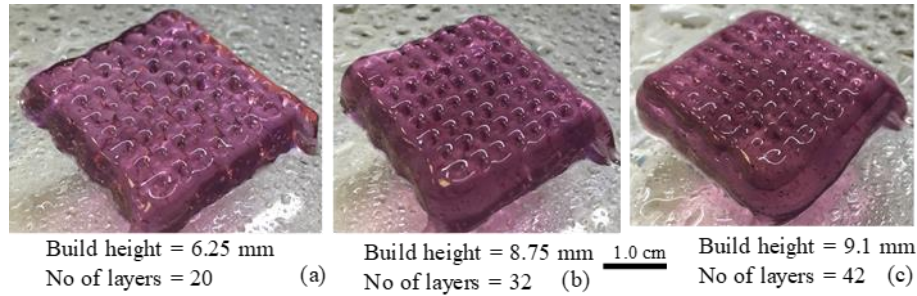
Figure 110: Fabrication of large scaffold using composition $A_2C_2TN_1$.
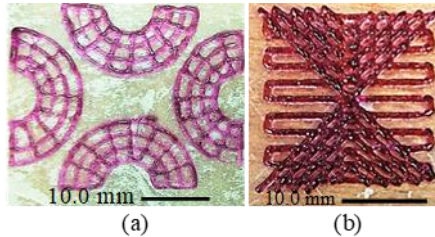
Figure 111: Fabrication of freeform scaffold.

6.2.9. Analysis of cell survivability

6.2.9.1. Cell directionality with fiber direction

The Cell viability of the fabricated filament (n=3) with different compositions and process parameters is determined at 1, 5 and 10 incubation days. Regardless of different material compositions, process parameters and incubations days, cells are surviving into those 3D printed filaments as shown in Table 12, Table 13, Table 14 and respectively. However, filaments fabricated with various air pressures i.e. 8, 10, and 12 psi show different cell viability as shown in Figure 112. Filament fabricated with 8, 10 and 12 psi shows almost 84%, 82% and 73% cell viability respectively after 1 day of incubation. These percentage will increase up to 90%, 89% and 81% respectively for 8, 10 and 12 psi after 10 days of incubation which reflects the proof of cell proliferation into the filament. The encapsulated cell into all the filaments fabricated with 8 and 10 psi demonstrates elongated morphology at different incubation days depicted at Table 12 and Table 13.

Table 12: Live and dead cell with 8 psi air pressure at incubation days 1, 5, and 10.

8psi	Day 1	Day 5	Day 10
Live cell	500 µm	500 µm	500 µm
Dead cell	500 µm	500 µm	500 µm
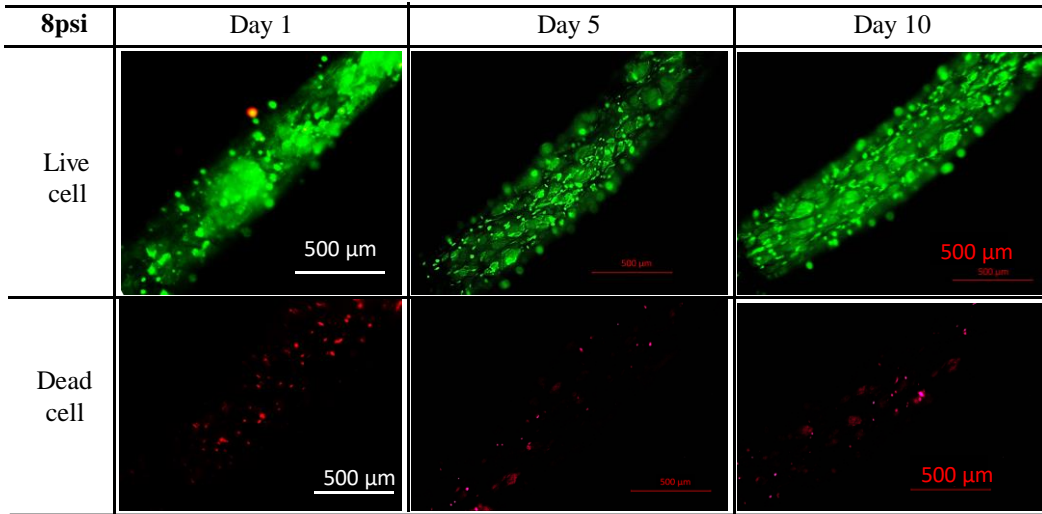
Table 13: Live and dead cell with 10 psi air pressure at incubation days 1, 5, and 10.

10 psi	Day 1	Day 5	Day 10
Live cell	500 µm	500 µm	500 µm
Dead cell	500 µm	500 µm	500 µm
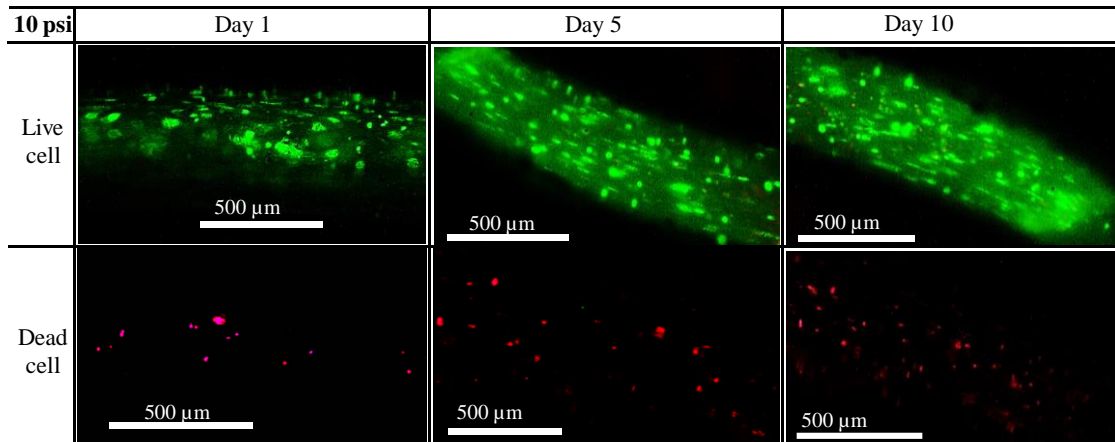
The encapsulated cell into the filament fabricated with 12 psi demonstrates round morphology at the incubation day of 1 and 5. This may happen because of high shear effect on the encapsulated cell. However, the cells are recovering its morphology and shows elongated shape at the incubation day of 10 as shown in Table 14. The reason behind this phenomenon may be the addition of anionic group i.e. carboxylate with NFC improves the cytokine secretion which eventually assist to attach and proliferate the cell on the fiber surface [293]. To investigate

141

the attachment and proliferation of the cell on the fiber surface, porc1 cell is seeded on the pure

TO-NFC surface and the cell morphology is observed at various incubation days.

Table 14: Live and dead cell with 12 psi air pressure at incubation days 1, 5, and 10.
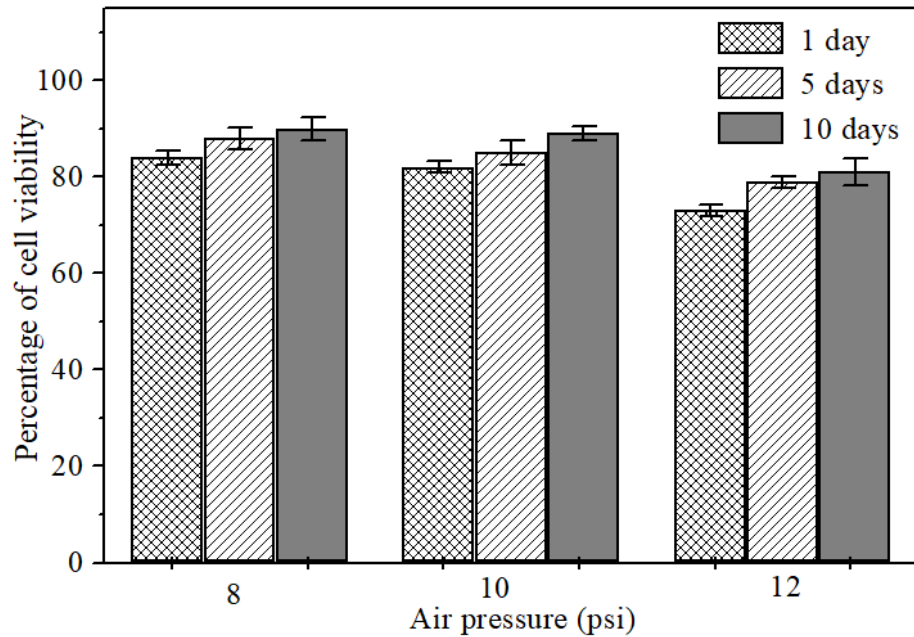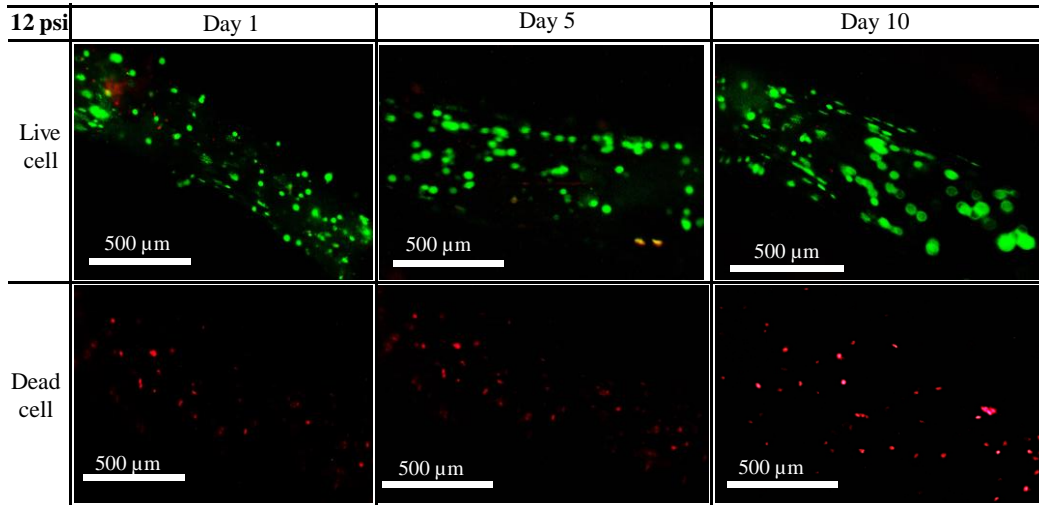
Figure 112: Percentage of cell viability at different air pressures and incubation days.

This action proves the cell attachment and proliferation on the TO-NFC surface as shown

in Figure 113. Moreover, this cell spreading can be expedite by applying poly-l-lysine as shown

in Figure 114. The reason is poly-Lysine enhances electrostatic interaction between negatively-charged ions of the cell membrane and positively-charged surface ions of attachment factors on the culture surface. It increases the number of positively-charged sites available for cell binding when adsorbed to the culture surface.
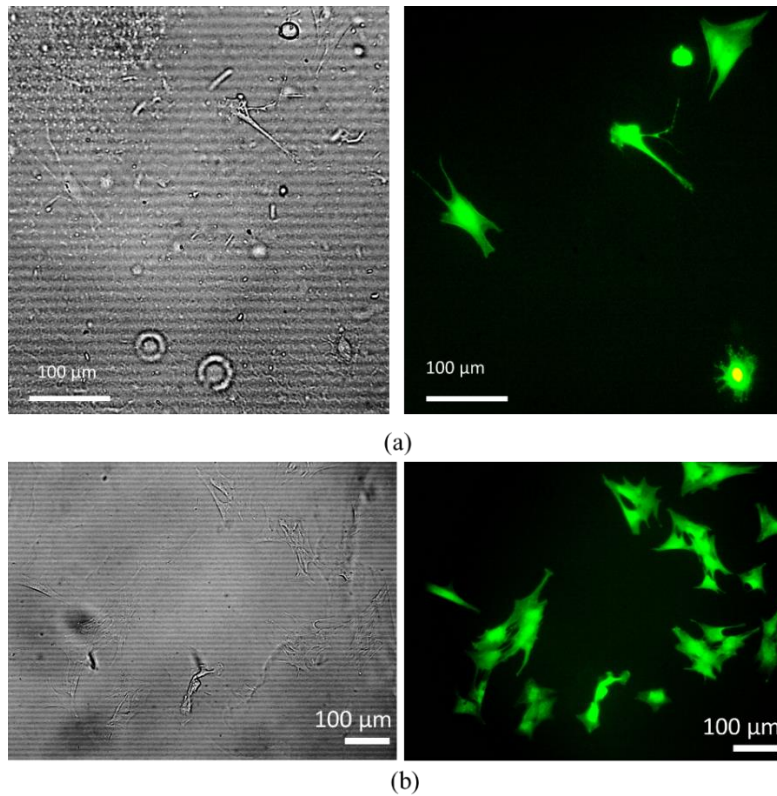
Figure 113: Cell attachment on TO-NFC surface: at incubation day (a) 5 and (b) 15.
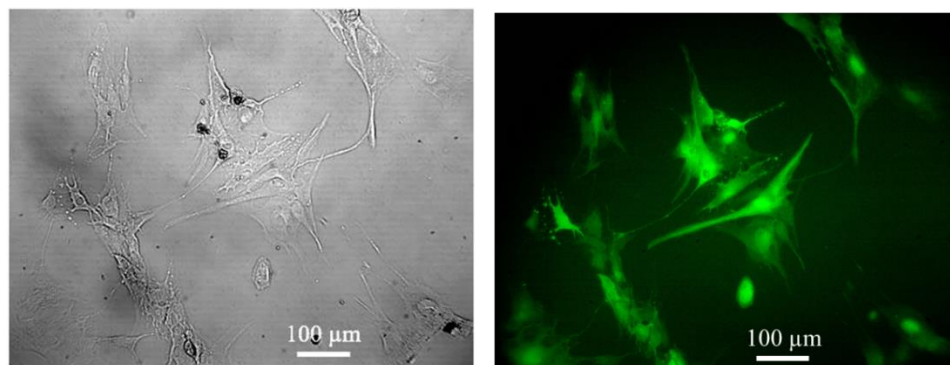
Figure 114: Cell attachment on TO-NFC surface: at incubation day 7 after applying poly-l-lysine.

As it is analyzed that, in extrusion based bio-printing process, the TO-NFC filled biomaterial ink passes through the dispensing nozzle generate shear which provides alignment of the reinforced fiber along the deposition direction. Such oriented distribution in scaffold structure may control its' mechanical properties [275, 276], hydrophilicity, surface chemistries and biocompatibility [277, 297]. Therefore, it is clearly identified from Figure 115 and 116, the porc1 cell proliferating following the TO-NFC fiber into the deposited filament.
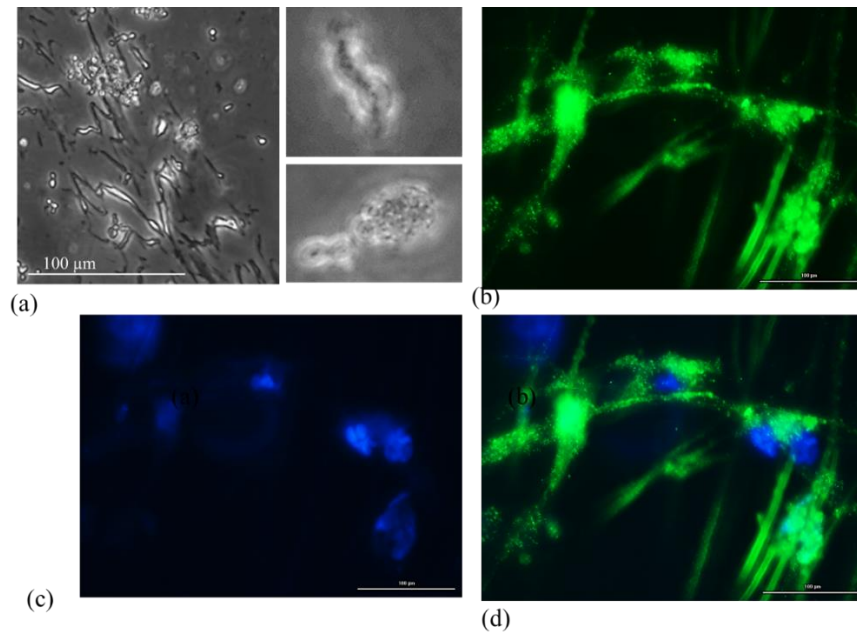
Figure 115: (a) Proliferation of cell along the TO-NFC fiber, (b) Live cell attached with fiber, (c) Dead cell, (d) Live and dead cell.
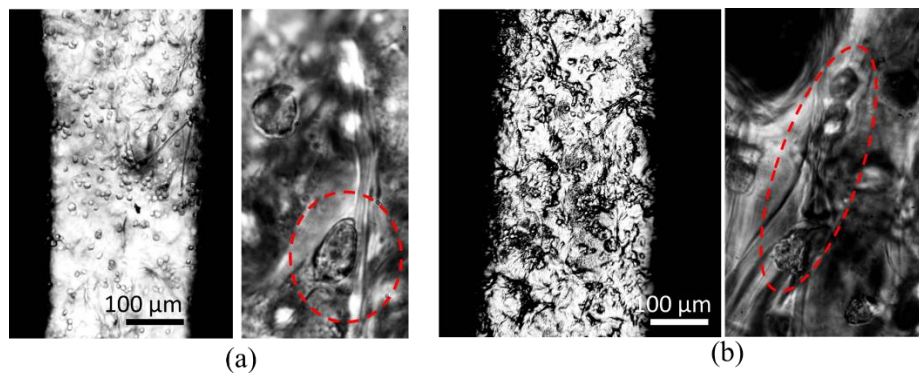
Figure 116: Proliferation of cell along the TO-NFC fiber captured by bright field microscope.

6.2.9.2. Effect of fiber length on cell viability

TO-NFC prepared by stirring at three different time e.g. 4, 12 and 28 hours are used as candidate element and blended into alginate and CMC to prepare the bio-ink. The Cell viability of the fabricated filament (n=3) with different compositions is determined after 6 incubation days. Regardless of different material compositions prepared by different fiber size, cells were surviving into those 3D printed filaments as shown in Figure 117 (a). However, filaments fabricated with various compositions show different cell viability as shown in Figure 118 (b). It is clear from the viability result that, the filament fabricated with composition having smaller fiber size i.e. fiber generated by the stirring of 28 hours shows better cell viability. Material with shorter fiber size represents more fibrous texture into the composition which creates highly micro-level porous environment for the encapsulated cell. Scaffold environment having micro-porosity will allow the transportation of necessary growth media and gas. Moreover the fibrous texture provides larger effective surface to attach the cell. This microenvironment can partially mimic the topographical features of the natural ECM and influence the cell activity [307]. Eventually, this phenomenon triggers better cell-matrix interaction resulting intrinsic physical forces into the cell and that may influence the cell division as previously shown on other types of substrate [308]. Hence, more cell cluster is visible for the composition of $A_2C_2TN_{1-28}$ due to the increased cell-cell interactions as shown in the inset of Figure 117 (c). Due to the chemical treatment of NFC to generate TO-NFC, the structural chain forms mechanically strong crystallinity by hydrogen bond which will also make this bio-ink one of the better choice to fabricate larger 3D scaffold by bio-printing process [280].
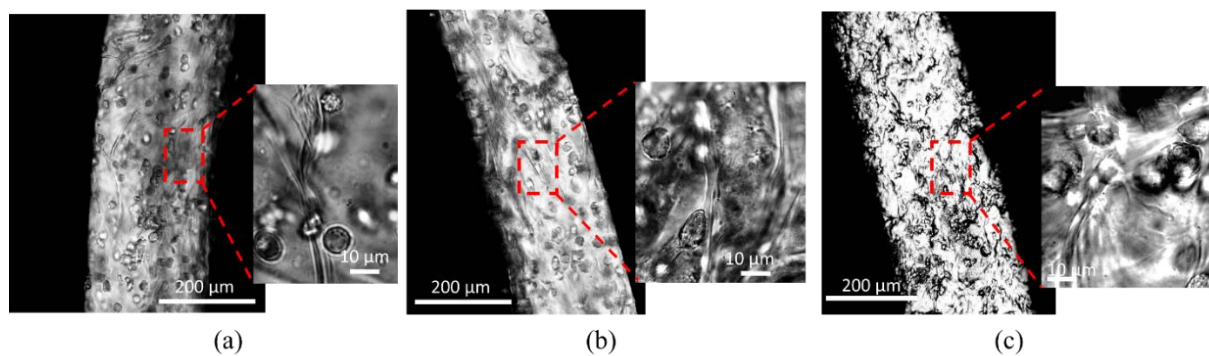
Figure 117: Cell laden filament fabricated with the composition of (a) $A_2C_2TN_{1-4}$, (b) $A_2C_2TN_{1-12}$, and (c) $A_2C_2TN_{1-28}$.
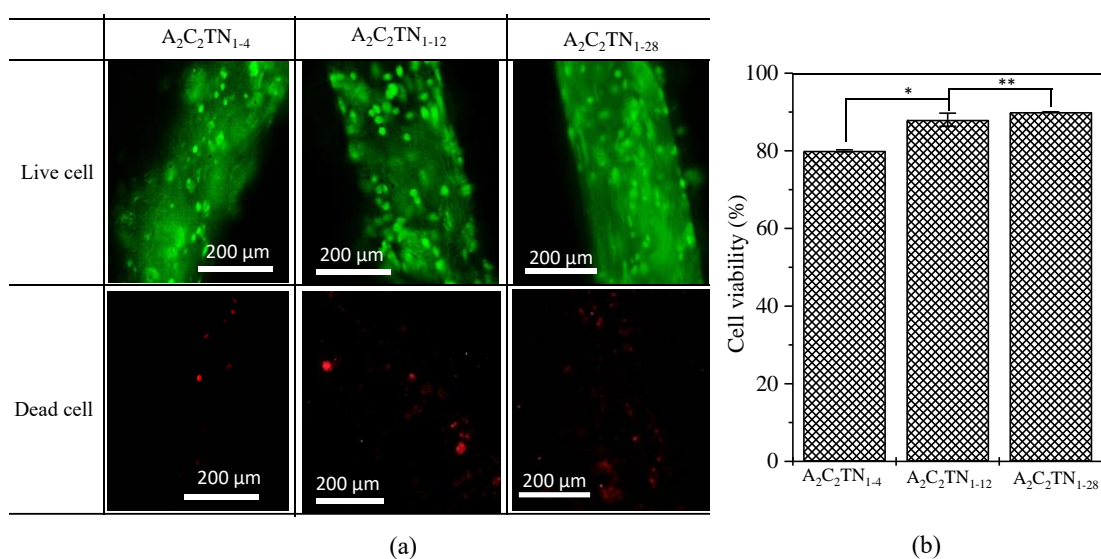
Figure 118: (a) Live cell, dead cell and (b) Percentage of cell viability.

6.2.9.3. Remarks for material-alginate, CMC, and TO-NFC

From the aforementioned qualitative and quantitative analysis, it is clear that the combination of alginate, CMC and TO-NFC can be a good candidate for large scale scaffold fabrication and cell encapsulation. Set of tests also determines that 2% alginate, 2% CMC and 1% TO-NFC is an optimum material composition to fulfil the both requirements i.e. large scale scaffold fabrication and better cell survivability. The capability of shear induced fiber alignment opens a new possibility of directing encapsulated cell proliferation. The formation of cell to cell network will give a maturation towards regeneration of functional tissue. To get the actuation of

146

the fabricated scaffold in long run, the confluence of the cell should be more, which is still an on-going research. Therefore, this study will be continued to improve the cell proliferation which will drive towards higher cell confluence to get the contractile effect in long run.

7. OVERALL DISCUSSION

7.1. Comparison of viscosity

In this whole research process three different types of hybrid hydrogels with various compositions are considered as shown in Table 15. In the hybrid hydrogel composed with alginate-CMC and alginate-CMC-MMT, we have fixed the alginate amount of 4%, because of prior reporting [45, 202] of high cell viability at this percentage. To maintain reasonable number of experiment, only 4% weight percentage of MMT is considered in alginate-CMC-MMT and this has exposed potential of CMC in favor of alginate and carboxymethyl cellulose in the composition. In alginate-CMC-TO-NFC hybrid hydrogel, all the elements have been varied and TO-NFC is considered up to 1 %, because small amount of TO-NFC can significantly increase the viscosity of the solution [192].

Table 15: Composition of samples with weight percentage.

Alginate and CMC	Alginate, CMC and MMT	Alginate, CMC and TO-NFC
A_4C_0	$A_4C_0M_0$	$A_0C_0TN_1$
A_4C_1	$A_4C_0M_4$	$A_1C_1TN_1$
A_4C_2	$A_4C_1M_4$	$A_2C_2TN_{0.5}$
A_4C_3	$A_4C_2M_4$	$A_2C_2TN_1$
A_4C_4	$A_4C_3M_4$	

Rheological measurements were performed using a rotational rheometer (ARES-LS2, TA instruments, New Castle, DE, USA) with parallel plate geometry (20 mm flat plate). All measurements were recorded with a 1.0 mm gap width at 25^0C. The viscosities and shear stress of different concentrations were assessed using rotational test at a stress rate of 1.0 to 100 s^{-1}. The dynamic sweep stress test is done at stress rate of 1.0 to 100% to determine the solid and liquid-like state of different bio-inks. The frequency sweep test (1.0 to 100s^{-1}) and three interval thixotropic test (3iTT) (stress rate of 0.1 to 100%) were also performed to characterize the bio-

ink. The rheological properties i.e. viscosities, shear stress of bio-ink with different alginate and CMC compositions were assessed by different rheological measurements. The impact of the different concentrations of alginate, CMC, MMT and TO-NFC on rheological behavior with respect to the shear rate and frequencies is determined by steady rate sweep test, dynamic stress sweep test, frequency sweep test and three interval thixotropic test in the previous chapters. The overall viscosity of all the compositions of each hybrid hydrogel is enlisted in Table 16 and graphically shown in Figure 119.

Table 16: Viscosity of different compositions.

Alginate and CMC	Viscosity at 1.0 s^{-1} (Pa.S)	Alginate, CMC and MMT	Viscosity at 1.0 s^{-1} (Pa.S)	Alginate, CMC and TO-NFC	Viscosity at 1.0 s^{-1} (Pa.S)
A_4C_0	0.67	$A_4C_0M_0$	0.67	$A_0C_0TN_1$	4.0412
A_4C_1	20.95	$A_4C_0M_4$	3.44	$A_1C_1TN_1$	28.3023
A_4C_2	229	$A_4C_1M_4$	160.574	$A_2C_2TN_{0.5}$	190.065
A_4C_3	280.080	$A_4C_2M_4$	827.76	$A_2C_2TN_1$	329.65
A_4C_4	522.47	$A_4C_3M_4$	1452.22		
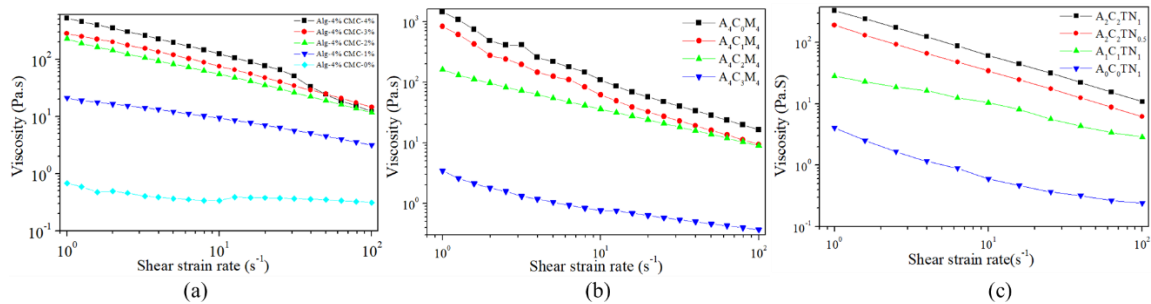
Figure 119: Viscosity with respect to various shear strain rate for (a) Alginate and CMC, (b) Alginate, CMC and MMT, and (c) Alginate, CMC and TO-NFC.

For all types of compositions shown in graph, it is clear that the viscosity is solid content dependent. Therefore, the viscosity of $A_4C_2M_4$ is almost 36% and 60% more than A_4C_4 and $A_2C_2TN_1$ respectively. This viscosity measurement gives a preliminary insight of the

qualification of any composition to fulfil the objective of this research i.e. fabricating large scale scaffold with proper shape fidelity and better cell viability for a longer period of time.

7.2. Comparison of shape fidelity

A set of shape fidelity related characterization tests e.g. filament fusion test, collapse test, lateral pore size test narrows down the set of candidate compositions to achieve the research objective. In the whole experiment process, it is clear that highest amount of viscosity may increase the shape fidelity of the final structure. However, that may elevate the requirement of air pressure which leaves negative impact on the overall cell survivability. Therefore, we needed to consider both the capability of fabricating large scaffold preserving shape fidelity and maintaining better cell viability during selection of optimum composition from each hybrid hydrogel. Under these considerations, A_4C_4, $A_4C_2M_4$, and $A_4C_4TN_1$ are qualified as optimum compositions from the hybrid hydrogels of alginate-CMC, alginate-CMC-MMT and alginate-CMC-TO-NFC respectively.

From the qualitative comparison of fusion test among the optimum candidates of three hybrid hydrogels shown in Figure 120, it is clear A_4C_4 and $A_4C_2M_4$ are preserving pore geometry better (almost square) than $A_2C_2TN_1$. The printability of all these three compositions are almost similar and very close to 1.0 which reflects very good potential of these compositions to maintain the shape fidelity of the final scaffold. The diffusion rate is totally solid content dependent, therefore $A_4C_2M_4$ shows less amount of spread than A_4C_4 and $A_2C_2TN_1$ as shown in Table 17. All the compositions are containing carboxyl group and more presence of this group generate more hydrogen bond into the solution and eventually it facilitates to hold the filament geometry. This fusion test result is also co-related with the viscosity result of these compositions.

150
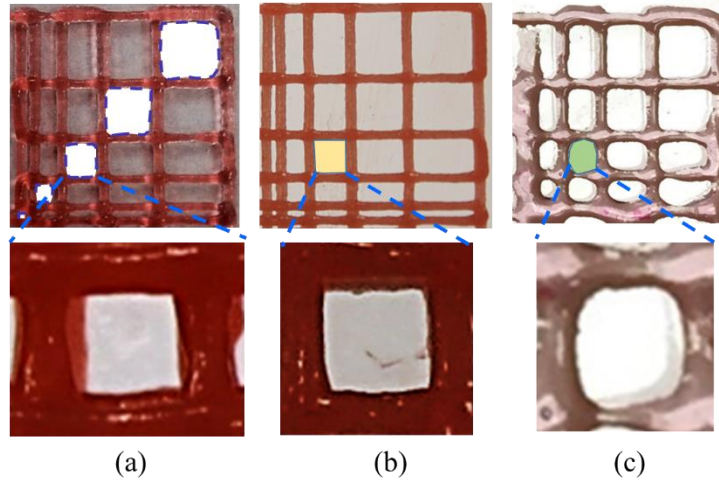
Figure 120: Scaffolds fabricated for fusion test with the compositions of (a) A_4C_4, (c) $A_4C_2M_4$, and (c) $A_2C_2TN_1$.

Table 17: Fusion test result of the composition of A_4C_4, $A_4C_2M_4$, and $A_4C_4TN_1$.

3X3 pore size	A_4C_4	$A_4C_2M_4$	$A_2C_2TN_1$
Diffusion rate (%)	33.0	12.0	35.0
Printability	0.88	0.83	0.85

The collapse test reflects the capability of any composition to maintain the lateral pore geometry without deflecting along build direction. Normally, researchers are considering the pore geometry on XY plane which is creating the vascularization to flow the growth media and gases. However, the preservation of lateral pore may allow the flow of nutrients from multi-direction which may improve the cell viability and proliferation. From the qualitative comparison of collapse test among the optimum candidates of three hybrid hydrogels as shown in Figure 121(a), it is clear A_4C_4 and $A_4C_2M_4$ are deflecting less than $A_2C_2TN_1$. $A_4C_2M_4$ preserving more lateral pore than A_4C_4 as shown in Figure 121(b). Quantitatively, $A_4C_2M_4$ is able to preserve the lateral pore almost 60% where A_4C_4 is preserving only 19%. $A_2C_2TN_1$ is not able to leave any lateral pore. The comparison of this collapse test result of these compositions also reflects the significance of their viscosity.
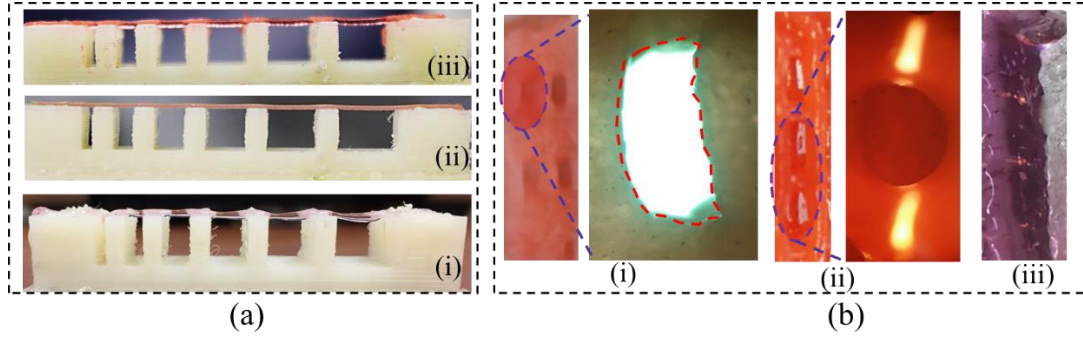
Figure 121: (a) Single filament deposited for collapse test and (b) Lateral pore preservation capacity of (i) A_4C_4, (ii) $A_4C_2M_4$, and (iii) $A_2C_2TN_1$.

Table 18: Collapse result of the composition of A_4C_4, $A_4C_2M_4$, and $A_4C_4TN_1$.

3mm pillar distance	A_4C_4	$A_4C_2M_4$	$A_2C_2TN_1$
Collapse rate (%)	0	0	0
L. Collapse rate (%)	81	40	100

7.3. Comparison of build height

Once all the characterization tests described above are done, it is revealed, composition A_4C_4 $A_4C_2M_4$, and $A_2C_2TN_1$ have higher prospect to fabricate large structure. Therefore, these three compositions are used for large scaffold fabrication as shown in Figure 122. It is clear from the Figure 122 and Table 19 that the build height of the scaffold fabricated by the composition of $A_4C_2M_4$ is 2.0 cm which is highest among three. The viscosity of $A_4C_2M_4$ is almost 36% and 60% more than A_4C_4 and $A_2C_2TN_1$ respectively. Subsequently, the build height of the scaffold fabricated by $A_4C_2M_4$ is almost 30% and 55% more than A_4C_4 and $A_2C_2TN_1$ respectively. Therefore, here, the result of the viscosity test is supporting the build height result. Moreover, the shape fidelity related characterization tests also show the potential of $A_4C_2M_4$ composition to fabricate large structure with proper shape fidelity because of having less diffusion and collapse rate.
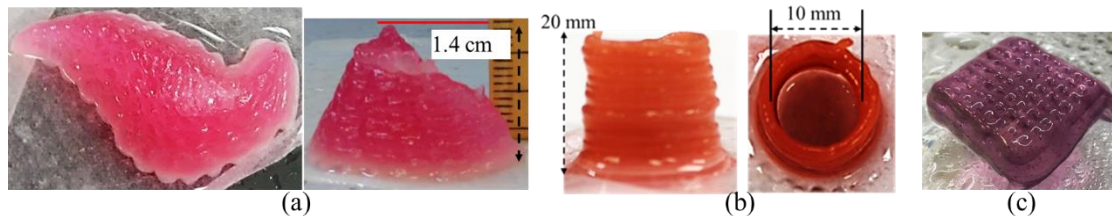
Figure 122: Large scaffolds fabricated by the compositions of (a) A_4C_4, (b) $A_4C_2M_4$, and (c) $A_2C_2TN_1$.

Table 19: Comparison of build height of the scaffold fabricated by the composition of A_4C_4, $A_4C_2M_4$, and $A_4C_4TN_1$.

	A_4C_4	$A_4C_2M_4$	$A_2C_2TN_1$
Build height (cm)	1.4	2.0	0.9

7.4. Comparison of cell survivability

To investigate the cytotoxicity of the compositions of A_4C_4, $A_4C_2M_4$, and $A_2C_2TN_1$, various cell lines e.g. BxPC3 (pancreatic cancer cell), prostate stem cancer cell, HEK293, Porc1 cells are encapsulated into these compositions and the cell viability is analyzed using the live/dead assay as shown in Figure 123. The cell viability result reveals that composition $A_4C_2M_4$ has less amount of cell viability i.e. 84% than A_4C_4 and $A_2C_2TN_1$. Another drawback with $A_4C_2M_4$ composition is, the cell was not changing its morphology as shown in Figure 123 (b). Since, the cell-laden scaffold fabricated with $A_4C_2M_4$ is used 14 psi air pressure, it may create the shear effect on the cell and results more cell death. Moreover, higher viscosity may not allow enough room for the encapsulated cell to expose its functionality. However, this cell viability is higher than pure alginate and some other existing cellulose and clay based bio-ink as compared in Table 20. Adding some protein origin polymer e.g. fibrin, collagen with the composition of $A_4C_2M_4$ may increase the cell adhesion site into the composition which will be one of the future study of this research.
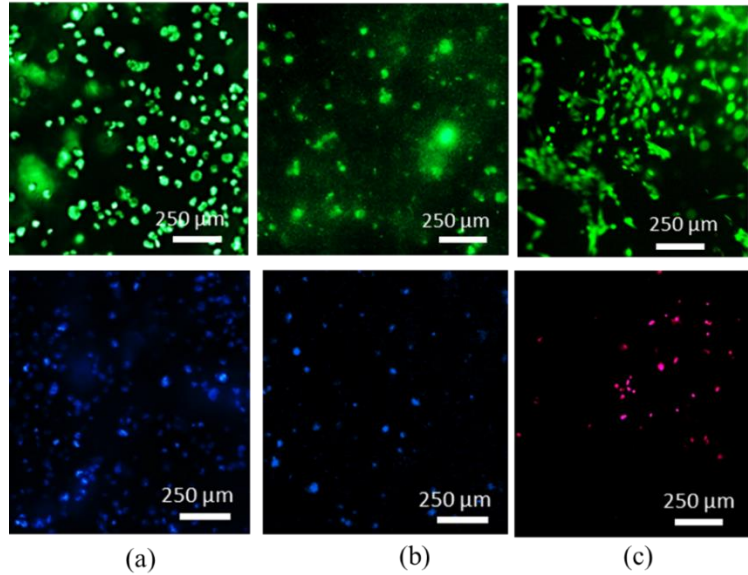
Figure 123: Live dead assay of cell encapsulated into (a) A_4C_4, (b) $A_4C_2M_4$, and (c) $A_2C_2TN_1$.
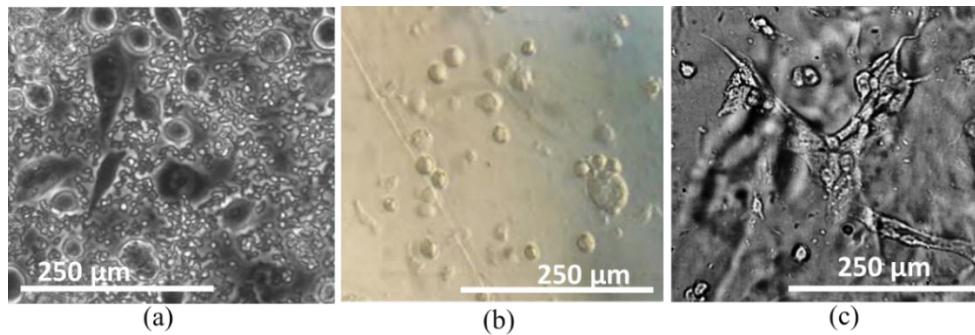
Figure 124: Cell phenotype after 10 days of incubation: (a) Prostate cancer cell encapsulated into A_4C_4, (a) Prostate cancer cell encapsulated into $A_4C_2M_4$, and (c) Porc1 cell encapsulated into $A_2C_2TN_1$.

Table 20: Comparison of cell viability with the composition of $A_4C_2M_4$ and existing bio-ink.

Bio-ink constituents	Cell viability (%)
Pure alginate [155]	80
Alg-Laponite-Methyl Cellulose [46]	70-75
Alg-Methyl Cellulose [155]	78
Alg-CMC-MMT (proposed)	84

A_4C_4 and $A_2C_2TN_1$ are showing almost similar amount of cell viability i.e. around 90% which is higher than the reported cell viability i.e. 40-86% [93] using extrusion based bio-printing process. The encapsulated cells are also showing morphological change into A_4C_4 and

154

$A_2C_2TN_1$ as shown in Figure 124 (a) and Figure 124 (c). However, to achieve the actuation, the encapsulated functional cell should be connected. Recently, several works related to the functional tissue construction have been published and outlined that the alignment of functional cell and cell to cell interaction are imperative [294-296]. From Figure 124 (a) and Figure 124 (c), it is clear that even the cell is changing its morphology into A_4C_4, it is not connected. On the other hand, cell is making network into $A_2C_2TN_1$ which is showing better possibility to regenerate the tissue. Finally, utilizing the shear during extrusion, reinforced TO-NFC is getting aligned along the deposition direction as shown in Figure 125 (a). Since, the addition of anionic group i.e. carboxylate with NFC improves the cytokine secretion, this phenomenon eventually improves the attachment and proliferate of the cell on the fiber surface [293]. It is clear from the Figure 125 (b) that the encapsulated functional cell is changing its morphology along the deposition direction and proliferating. Therefore, the alignment of the short fiber resulted from the shear during extrusion can be a directed avenue of encapsulated cell to get connected, proliferate along a specific direction and regenerate the functional tissue in long run.
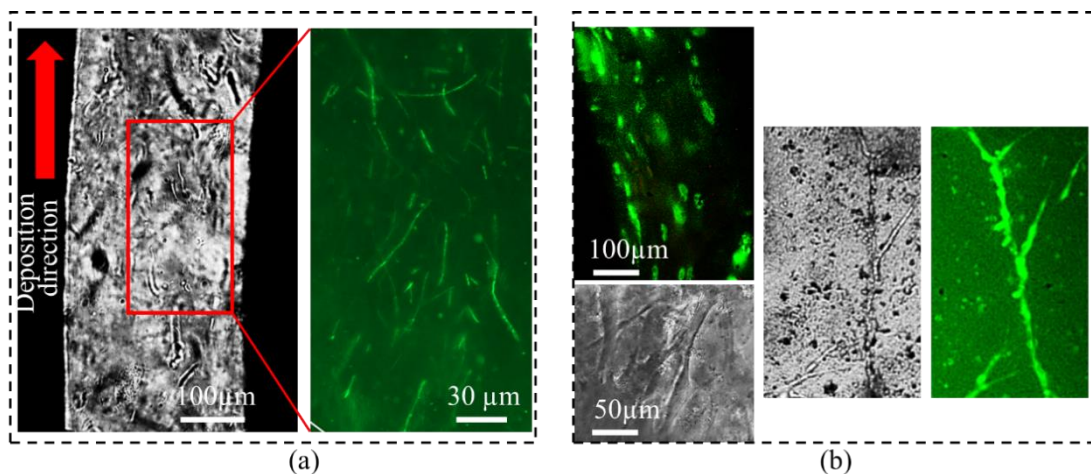
Figure 125: (a) Aligning short fiber applying shear force, and (b) Directing the cell proliferation along deposition direction.

8. CONCLUSION AND FUTURE WORK

8.1. Conclusion

In this research, a novel bio-ink composed with hybrid hydrogels is designed which is capable of maintaining proper printability, shape fidelity and higher cell viability. To determine the best elements of bio-ink, first of all alginate with carboxymethyl cellulose (CMC) is considered. All the characterization tests related to material properties, printability, and shape fidelity and cell viability identify that bio-ink containing 4% alginate and 4% CMC is the optimum composition. This bio-ink is showing 86% cell viability even after 21 days of incubation. The maximum build height with this composition is 1.4 cm. However, during the analysis of cell proliferation and functionality, it is revealed that, the cell is spreading randomly and does not following any alignment which is one of the important factors for functional tissue regeneration. To improve the printability and shape fidelity and eventually build height of the scaffold, another element i.e. MMT is added into alginate-CMC. All the characterization tests related to material properties, printability, shape fidelity and cell viability detemine that bio-ink containing 4% alginate, 4% CMC and 2% MMT is the optimum composition. This bio-ink is showing 84% cell viability after 7 days of incubation. The maximum build height with this composition is 2.0 cm. However, during the analysis of cell proliferation and functionality, it is identified that, the cell is not changing its morphology which is necessary for functional tissue regeneration. Therefore, we have concluded that addition of some protein origin polymers can improve the cell attachment site into the scaffold and can improve the cell viability of this bio-ink. To control the cell proliferation i.e. achieving the cell alignment, we have added one more element i.e. TO-NFC in alginate-CMC. We have taken the advantage of shear induced fiber alignment phenomenon using extrusion based bio-printing process to align the infilled fiber

156

during deposition of filament. The characterization tests conducted related to material properties, printability, shape fidelity and cell viability, reveal that bio-ink containing 2% alginate, 2% CMC and 1% NO-NFC is the optimum composition. This approach has successfully aligned almost 84% fiber dispersion within 0^0-30^0 range with respect to the deposition direction. Moreover, the encapsulated cell creates the connectivity during proliferation in incubation period. The cell proliferation along the fiber shows the potential of controlling the direction of encapsulated cell. Therefore, to fabricate large scale functional tissue scaffold, this hybrid hydrogel can be a potential bio-ink in 3D bio-printing process. The machine readable files for all the scaffolds are generated following the proposed HSDS file format system. This proposed file format can be used for different existing bio-printers. At different situations, the printability of the bio-materials are defined by different factors e.g. viscosity or tanδ or swelling rate or diffusion rate separately without considering the manufacturing parameters. The bio-compatibility is defined by the viability rate or cell morphology changes. This work establishes a processing bounds of different output i.e. viscosity, tanδ, diffusion and collapse rate, printability, swelling rate and cell viability as shown in Table 21 altogether. For example, in several works, the printability and shape fidelity of bio-ink are defined by viscosity where the viscosity value at 1.0 s^{-1} shear rate were around 350 Pa.S [309], 500 Pa.S [196], 800 Pa.S [24]. These values are comparable with our proposed bound of viscosity. The appropriate printability value for various bio-ink are selected as 0.84 and 0.95 [6], which is also comparable with our proposed printability range. Actually, the manufacturing parameters are interrogated and correlated with fidelity and reproducibility of the 3D scaffold during the bio-ink design process in this work.

Table 21: Upper and lower limit of different output to suggest the 3D printability of new bio-ink.

Output	Lower bound	Upper bound
Viscosity (Pa.S)	329.65	827.76
Loss tangent (tanδ)	0.69	0.99
Diffusion rate (%)	11.62	34.44
Collapse factor (%)	0	5
Printability	0.80	0.95
Swelling rate (%)	17.68	227
Cell viability (%)	84	91

This complete package of quantifiable limit of different output opens an avenue to develop new bio-ink for extrusion based bio-printing process. Adjusting the outlined output within this limit will define a good 3D bio-printability of the developed bio-ink without compromising the structural integrity of the fabricated scaffold and better cell viability. Moreover, the outlined systematic quantitative characterization tests can be conducted to design material for other application where confirming printability is important e.g. medical devices, soft robotics, 3D printed electronics using extrusion based printing process. Finally, we hope the framework of this research will accelerate the future bio-ink development for extrusion based bio-printing process with more efficiency, repeatability and reliability.

8.2. Future work

A mathematical model relating different input parameters e.g. material concentration, air pressure, print speed, and print distance and different outputs e.g. printability and cell viability will be established based on experimental data in future. This model can be developed using design of experiment (DoE) method. It is expected, this model will be able to predict the 3D bio-printability of new candidate of bio-ink more systematically considering the material characteristics and fabrication parameters. To improve the fiber alignment for the bio-ink consisting alginate, CMC and TO-NFC, various combination of nozzle diameters, nozzle length,

and mechanical vibration will be used in future. Because, it is stated that, dispensing nozzle having variational diameter [310], extensional flow fields [311], and linear oscillatory mechanism [302] can improve the short fiber alignment during material release. Even though, bio-ink prepared with alginate, CMC and TO-NFC show good cell viability, cell to cell connection, and cell proliferation along deposition direction, its contractile effect is still not achieved due to less cell confluence. To improve the cell confluence, different protein origin polymers e.g. collagen, fibrin, thrombin will be added at various percentage into the existing alginate, CMC and TO-NFC based bio-ink. Once, the confluence of the encapsulated cell is improved and the contractile effect is achieved, this improved bio-ink will be used to fabricate large scaffold encapsulating functional cell. Another important factor to achieve the in-vitro functional tissue, is incorporating the vascularization encapsulating HUVEC cell as shown in Figure 126 (b). To accomplish the vascularization into the fabricated scaffold, a manufacturing system having the capability of releasing multiple materials encapsulating multiple cell will be necessary as schematically shown in Figure 126 (a). The work of designing and developing this system will be another future work.
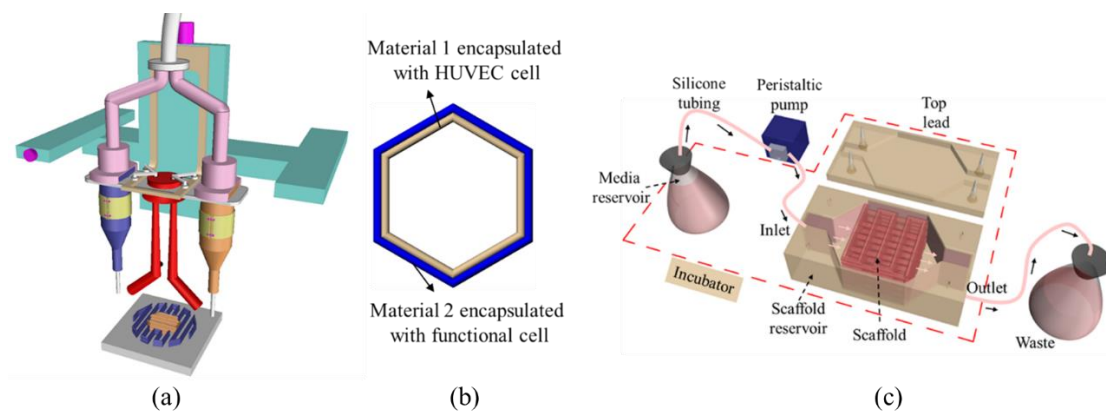
Figure 126: (a) An extrusion-based bio-printer having the capability of depositing multiple material, (b) Scaffold fabricating with multiple materials encapsulating multiple cells, and (c) Schematic representation of perfusion-based bio-reactor.

Finally, the dynamic supply of fresh growth factor during incubation i.e. perfusion based bio-reactor will also be designed and manufactured to incubate the fabricated scaffold in future as schematically shown in Figure 126 (c).

REFERENCES

1. Murphy, S.V. and A. Atala, *3D bioprinting of tissues and organs.* Nature biotechnology, 2014. **32**(8): p. 773-785.
2. Jia, W., et al., *Direct 3D bioprinting of perfusable vascular constructs using a blend bioink.* Biomaterials, 2016. **106**: p. 58-68.
3. Axpe, E. and M.L. Oyen, *Applications of alginate-based bioinks in 3D bioprinting.* International Journal of Molecular Sciences, 2016. **17**(12): p. 1976.
4. Skardal, A. and A. Atala, *Biomaterials for integration with 3-D bioprinting.* Annals of biomedical engineering, 2015. **43**(3): p. 730-746.
5. Khoda, A., I.T. Ozbolat, and B. Koc, *A functionally gradient variational porosity architecture for hollowed scaffolds fabrication.* Biofabrication, 2011. **3**(3): p. 034106.
6. Ouyang, L., et al., *Effect of bioink properties on printability and cell viability for 3D bioplotting of embryonic stem cells.* Biofabrication, 2016. **8**(3): p. 035020.
7. Groll, J., et al., *A definition of bioinks and their distinction from biomaterial inks.* Biofabrication, 2018. **11**(1): p. 013001.
8. Malda, J., et al., *25th anniversary article: engineering hydrogels for biofabrication.* Advanced materials, 2013. **25**(36): p. 5011-5028.
9. Ozbolat, I.T., et al., *Hybrid tissue scaffolds for controlled release applications: A study on design and fabrication of hybrid and heterogeneous tissue scaffolds for controlled release applications is presented in this paper.* Virtual and Physical Prototyping, 2012. **7**(1): p. 37-47.
10. Xu, T., et al., *Complex heterogeneous tissue constructs containing multiple cell types prepared by inkjet printing technology.* Biomaterials, 2013. **34**(1): p. 130-139.
11. Xu, T., et al., *Inkjet printing of viable mammalian cells.* Biomaterials, 2005. **26**(1): p. 93-99.
12. Iwami, K., et al., *Bio rapid prototyping by extruding/aspirating/refilling thermoreversible hydrogel.* Biofabrication, 2010. **2**(1): p. 014108.
13. Shor, L., et al., *Precision extruding deposition (PED) fabrication of polycaprolactone (PCL) scaffolds for bone tissue engineering.* Biofabrication, 2009. **1**(1): p. 015003.
14. Barron, J., et al., *Biological laser printing: a novel technique for creating heterogeneous 3-dimensional cell patterns.* Biomedical microdevices, 2004. **6**(2): p. 139-147.
15. Guillemot, F., et al., *High-throughput laser printing of cells and biomaterials for tissue engineering.* Acta biomaterialia, 2010. **6**(7): p. 2494-2500.
16. Guillotin, B., et al., *Laser assisted bioprinting of engineered tissue with high cell density and microscale organization.* Biomaterials, 2010. **31**(28): p. 7250-7256.
17. Peltola, S.M., et al., *A review of rapid prototyping techniques for tissue engineering purposes.* Annals of medicine, 2008. **40**(4): p. 268-280.
18. Murphy, S.V., A. Skardal, and A. Atala, *Evaluation of hydrogels for bio-printing applications.* Journal of Biomedical Materials Research Part A, 2013. **101**(1): p. 272-284.
19. Benoit, D.S., et al., *Small functional groups for controlled differentiation of hydrogel-encapsulated human mesenchymal stem cells.* Nature materials, 2008. **7**(10): p. 816-823.
20. Ahearne, M., *Introduction to cell–hydrogel mechanosensing.* Interface focus, 2014. **4**(2): p. 20130038.

21.   Murphy, C.M., M.G. Haugh, and F.J. O'Brien, *The effect of mean pore size on cell attachment, proliferation and migration in collagen–glycosaminoglycan scaffolds for bone tissue engineering.* Biomaterials, 2010. **31**(3): p. 461-466.

22.   Perez, R.A. and G. Mestres, *Role of pore size and morphology in musculo-skeletal tissue regeneration.* Materials Science and Engineering: C, 2016. **61**: p. 922-939.

23.   Vijayavenkataraman, S., et al., *Design of three-dimensional scaffolds with tunable matrix stiffness for directing stem cell lineage specification: An in silico study.* Bioengineering, 2017. **4**(3): p. 66.

24.   Li, H., et al., *3D bioprinting of highly thixotropic alginate/methylcellulose hydrogel with strong interface bonding.* ACS applied materials & interfaces, 2017. **9**(23): p. 20086-20097.

25.   Wang, L., et al., *Iterative feedback bio-printing-derived cell-laden hydrogel scaffolds with optimal geometrical fidelity and cellular controllability.* Scientific reports, 2018. **8**(1): p. 2802.

26.   Gaetani, R., et al., *Cardiac tissue engineering using tissue printing technology and human cardiac progenitor cells.* Biomaterials, 2012. **33**(6): p. 1782-1790.

27.   Loh, Q.L. and C. Choong, *Three-dimensional scaffolds for tissue engineering applications: role of porosity and pore size.* Tissue Engineering Part B: Reviews, 2013. **19**(6): p. 485-502.

28.   Chen, S., et al., *Gelatin scaffolds with controlled pore structure and mechanical property for cartilage tissue engineering.* Tissue Engineering Part C: Methods, 2016. **22**(3): p. 189-198.

29.   Neufurth, M., et al., *Engineering a morphogenetically active hydrogel for bioprinting of bioartificial tissue derived from human osteoblast-like SaOS-2 cells.* Biomaterials, 2014. **35**(31): p. 8810-8819.

30.   Li, V.C.-F., et al., *Direct Ink Write (DIW) 3D Printed Cellulose Nanocrystal Aerogel Structures.* Scientific Reports, 2017. **7**(1): p. 8018.

31.   Ribeiro, A., et al., *Assessing bioink shape fidelity to aid material development in 3D bioprinting.* Biofabrication, 2017.

32.   He, Y., et al., *Research on the printability of hydrogels in 3D bioprinting.* Scientific reports, 2016. **6**: p. 29977.

33.   Gao, T., et al., *Optimization of gelatin–alginate composite bioink printability using rheological parameters: a systematic approach.* Biofabrication, 2018. **10**(3): p. 034106.

34.   Habib, A., et al., *3D printability of alginate-carboxymethyl cellulose hydrogel.* Materials, 2018. **11**(3): p. 454.

35.   Li, Y., et al., *pH sensitive Laponite/alginate hybrid hydrogels: swelling behaviour and release mechanism.* Soft Matter, 2011. **7**(13): p. 6231-6238.

36.   Lin, H.-H., et al., *Preparation and characterization of a biodegradable polyurethane hydrogel and the hybrid gel with soy protein for 3D cell-laden bioprinting.* Journal of Materials Chemistry B, 2016. **4**(41): p. 6694-6705.

37.   Li, H., S. Liu, and L. Lin, *Rheological study on 3D printability of alginate hydrogel and effect of graphene oxide.* International Journal of Bioprinting, 2016. **2**(2): p. 163-175.

38.   Ahn, G., et al., *Precise stacking of decellularized extracellular matrix based 3D cell-laden constructs by a 3D cell printing system equipped with heating modules.* Scientific Reports, 2017. **7**(1): p. 8624.

39.	Chang, R., J. Nam, and W. Sun, *Effects of dispensing pressure and nozzle diameter on cell survival from solid freeform fabrication–based direct cell writing.* Tissue Engineering Part A, 2008. **14**(1): p. 41-48.

40.	Zhao, Y., et al., *The influence of printing parameters on cell survival rate and printability in microextrusion-based 3D cell printing technology.* Biofabrication, 2015. **7**(4): p. 045002.

41.	Seol, Y.-J., et al., *Bioprinting technology and its applications.* European Journal of Cardio-Thoracic Surgery, 2014. **46**(3): p. 342-348.

42.	Zhang, M., et al., *Dual-responsive hydrogels for direct-write 3D printing.* Macromolecules, 2015. **48**(18): p. 6482-6488.

43.	Chang, C.C., et al., *Direct-write bioprinting three-dimensional biohybrid systems for future regenerative therapies.* Journal of Biomedical Materials Research Part B: Applied Biomaterials, 2011. **98**(1): p. 160-170.

44.	Di Giuseppe, M., et al., *Mechanical behaviour of alginate-gelatin hydrogels for 3D bioprinting.* Journal of the mechanical behavior of biomedical materials, 2018. **79**: p. 150-157.

45.	Chung, J.H., et al., *Bio-ink properties and printability for extrusion printing living cells.* Biomaterials Science, 2013. **1**(7): p. 763-773.

46.	Ahlfeld, T., et al., *Development of a clay based bioink for 3D cell printing for skeletal application.* Biofabrication, 2017. **9**(3): p. 034103.

47.	Ding, H. and R. Chang, *Printability study of bioprinted tubular structures using liquid hydrogel precursors in a support bath.* Applied Sciences, 2018. **8**(3): p. 403.

48.	Ouyang, L., et al., *3D printing of HEK 293FT cell-laden hydrogel into macroporous constructs with high cell viability and normal biological functions.* Biofabrication, 2015. **7**(1): p. 015010.

49.	Hong, S., et al., *3D printing of highly stretchable and tough hydrogels into complex, cellularized structures.* Advanced Materials, 2015. **27**(27): p. 4035-4040.

50.	Wang, N., et al., *Mechanical behavior in living cells consistent with the tensegrity model.* Proceedings of the National Academy of Sciences, 2001. **98**(14): p. 7765-7770.

51.	Clark, E.A. and J.S. Brugge, *Integrins and signal transduction pathways: the road taken.* Science, 1995. **268**(5208): p. 233.

52.	Khalil, S. and W. Sun, *Bioprinting endothelial cells with alginate for 3D tissue constructs.* Journal of biomechanical engineering, 2009. **131**(11): p. 111002.

53.	Blaeser, A., et al., *Biofabrication under fluorocarbon: a novel freeform fabrication technique to generate high aspect ratio tissue-engineered constructs.* BioResearch open access, 2013. **2**(5): p. 374-384.

54.	Dee, K.C., D.A. Puleo, and R. Bizios, *An introduction to tissue-biomaterial interactions.* 2003: John Wiley & Sons.

55.	Arahira, T. and M. Todo, *Effects of proliferation and differentiation of mesenchymal stem cells on compressive mechanical behavior of collagen/β-TCP composite scaffold.* Journal of the mechanical behavior of biomedical materials, 2014. **39**: p. 218-230.

56.	da Silva, M.A., et al., *Chitosan/polyester-based scaffolds for cartilage tissue engineering: assessment of extracellular matrix formation.* Acta Biomaterialia, 2010. **6**(3): p. 1149-1157.

57.	Han, K.-S., et al., *Effect of pore sizes of silk scaffolds for cartilage tissue engineering.* Macromolecular Research, 2015. **23**(12): p. 1091-1097.

58. Zhang, Q., et al., *Pore size effect of collagen scaffolds on cartilage regeneration.* Acta biomaterialia, 2014. **10**(5): p. 2005-2013.

59. Hao, L., et al., *Enhanced human osteoblast cell adhesion and proliferation on 316 LS stainless steel by means of CO2 laser surface treatment.* Journal of Biomedical Materials Research Part B: Applied Biomaterials: An Official Journal of The Society for Biomaterials, The Japanese Society for Biomaterials, and The Australian Society for Biomaterials and the Korean Society for Biomaterials, 2005. **73**(1): p. 148-156.

60. Rouabhia, M., et al., *Surface treatment with amino acids of porous collagen based scaffolds to improve cell adhesion and proliferation.* The Canadian Journal of Chemical Engineering, 2018. **96**(10): p. 2236-2242.

61. Bhora, F., et al., *Effect of growth factors on cell proliferation and epithelialization in human skin.* Journal of Surgical Research, 1995. **59**(2): p. 236-244.

62. Rodrigues, M., L.G. Griffith, and A. Wells, *Growth factor regulation of proliferation and survival of multipotential stromal cells.* Stem cell research & therapy, 2010. **1**(4): p. 32.

63. Carletti, E., A. Motta, and C. Migliaresi, *Scaffolds for tissue engineering and 3D cell culture*, in *3D cell culture*. 2011, Springer. p. 17-39.

64. Yusop, A.H.M., et al., *Controlling the degradation kinetics of porous iron by poly (lactic-co-glycolic acid) infiltration for use as temporary medical implants.* Scientific reports, 2015. **5**: p. 11194.

65. Yang, Q., et al., *Preparation of polycaprolactone tissue engineering scaffolds by improved solvent casting/particulate leaching method.* Journal of Macromolecular Science, Part B: Physics, 2006. **45**(6): p. 1171-1181.

66. Johnson, T., et al., *Fabrication of highly porous tissue-engineering scaffolds using selective spherical porogens.* Bio-medical materials and engineering, 2010. **20**(2): p. 107-118.

67. Choudhury, M., S. Mohanty, and S. Nayak, *Effect of different solvents in solvent casting of porous PLA scaffolds—In biomedical and tissue engineering applications.* Journal of Biomaterials and Tissue Engineering, 2015. **5**(1): p. 1-9.

68. Haugh, M.G., C.M. Murphy, and F.J. O'Brien, *Novel freeze-drying methods to produce a range of collagen–glycosaminoglycan scaffolds with tailored mean pore sizes.* Tissue Engineering Part C: Methods, 2009. **16**(5): p. 887-894.

69. Lowe, C.J., et al., *Production of highly aligned collagen scaffolds by freeze-drying of self-assembled, fibrillar collagen gels.* ACS biomaterials science & engineering, 2016. **2**(4): p. 643-651.

70. Offeddu, G.S., et al., *Multi-scale mechanical response of freeze-dried collagen scaffolds for tissue engineering applications.* journal of the mechanical behavior of biomedical materials, 2015. **42**: p. 19-25.

71. Chen, W., et al., *Gas-foaming calcium phosphate cement scaffold encapsulating human umbilical cord stem cells.* Tissue Engineering Part A, 2011. **18**(7-8): p. 816-827.

72. Kim, H.J., et al., *Gas foaming fabrication of porous biphasic calcium phosphate for bone regeneration.* Tissue Engineering and Regenerative Medicine, 2012. **9**(2): p. 63-68.

73. Huang, Y.-C. and D.J. Mooney, *Gas foaming to fabricate polymer scaffolds in tissue engineering*, in *Scaffolding in tissue engineering*. 2005, CRC press. p. 161-173.

74. Li, W.-J., et al., *Fabrication and characterization of six electrospun poly (α-hydroxy ester)-based fibrous scaffolds for tissue engineering applications.* Acta biomaterialia, 2006. **2**(4): p. 377-385.

75. Jun, I., et al., *Electrospun fibrous scaffolds for tissue engineering: viewpoints on architecture and fabrication.* International journal of molecular sciences, 2018. **19**(3): p. 745.

76. Lannutti, J., et al., *Electrospinning for tissue engineering scaffolds.* Materials Science and Engineering: C, 2007. **27**(3): p. 504-509.

77. Aljohani, W., et al., *Bioprinting and its applications in tissue engineering and regenerative medicine.* International journal of biological macromolecules, 2018. **107**: p. 261-275.

78. Zhang, Y.S., et al., *3D bioprinting for tissue and organ fabrication.* Annals of biomedical engineering, 2017. **45**(1): p. 148-163.

79. Wang, Z., et al., *3D bioprinted functional and contractile cardiac tissue constructs.* Acta biomaterialia, 2018. **70**: p. 48-56.

80. Bertassoni, L.E., et al., *Hydrogel bioprinted microchannel networks for vascularization of tissue engineering constructs.* Lab on a Chip, 2014. **14**(13): p. 2202-2211.

81. Mohebi, M.M. and J.R. Evans, *A drop-on-demand ink-jet printer for combinatorial libraries and functionally graded ceramics.* Journal of combinatorial chemistry, 2002. **4**(4): p. 267-274.

82. Cui, X., et al., *Direct human cartilage repair using three-dimensional bioprinting technology.* Tissue Engineering Part A, 2012. **18**(11-12): p. 1304-1312.

83. Tasoglu, S. and U. Demirci, *Bioprinting for stem cell research.* Trends in biotechnology, 2013. **31**(1): p. 10-19.

84. Hopp, B., et al., *Survival and proliferative ability of various living cell types after laser-induced forward transfer.* Tissue Engineering, 2005. **11**(11-12): p. 1817-1823.

85. Gruene, M., et al., *Laser printing of stem cells for biofabrication of scaffold-free autologous grafts.* Tissue Engineering Part C: Methods, 2010. **17**(1): p. 79-87.

86. Koch, L., et al., *Laser printing of skin cells and human stem cells.* Tissue Engineering Part C: Methods, 2009. **16**(5): p. 847-854.

87. Fedorovich, N.E., et al., *Evaluation of photocrosslinked lutrol hydrogel for tissue printing applications.* Biomacromolecules, 2009. **10**(7): p. 1689-1696.

88. Jakab, K., et al., *Three-dimensional tissue constructs built by bioprinting.* Biorheology, 2006. **43**(3, 4): p. 509-513.

89. Visser, J., et al., *Biofabrication of multi-material anatomically shaped tissue constructs.* Biofabrication, 2013. **5**(3): p. 035007.

90. Jones, N., *Science in three dimensions: the print revolution*. 2012.

91. Mironov, V., et al., *Organ printing: tissue spheroids as building blocks.* Biomaterials, 2009. **30**(12): p. 2164-2174.

92. Marga, F., et al., *Toward engineering functional organ modules by additive manufacturing.* Biofabrication, 2012. **4**(2): p. 022001.

93. Nair, K., et al., *Characterization of cell viability during bioprinting processes.* Biotechnology journal, 2009. **4**(8): p. 1168-1177.

94. Smith, C.M., et al., *Three-dimensional bioassembly tool for generating viable tissue-engineered constructs.* Tissue engineering, 2004. **10**(9-10): p. 1566-1576.

95. Duan, B., et al., *3D bioprinting of heterogeneous aortic valve conduits with alginate/gelatin hydrogels.* Journal of biomedical materials research Part A, 2013. **101**(5): p. 1255-1264.

96. Smith, C.M., et al., *Characterizing environmental factors that impact the viability of tissue-engineered constructs fabricated by a direct-write bioassembly tool.* Tissue engineering, 2007. **13**(2): p. 373-383.

97. Mata, A., et al., *A three-dimensional scaffold with precise micro-architecture and surface micro-textures.* Biomaterials, 2009. **30**(27): p. 4610-4617.

98. Hollinger, J.O., *An introduction to biomaterials*. 2011: CRC press.

99. Williams, D.F., *On the mechanisms of biocompatibility.* Biomaterials, 2008. **29**(20): p. 2941-2953.

100. Sabnis, A., et al., *Cytocompatibility studies of an in situ photopolymerized thermoresponsive hydrogel nanoparticle system using human aortic smooth muscle cells.* Journal of Biomedical Materials Research Part A, 2009. **91**(1): p. 52-59.

101. Norotte, C., et al., *Scaffold-free vascular tissue engineering using bioprinting.* Biomaterials, 2009. **30**(30): p. 5910-5917.

102. Ozbolat, I. and H. Gudapati, *A review on design for bioprinting.* Bioprinting, 2016. **3**: p. 1-14.

103. Hersel, U., C. Dahmen, and H. Kessler, *RGD modified polymers: biomaterials for stimulated cell adhesion and beyond.* Biomaterials, 2003. **24**(24): p. 4385-4415.

104. Karp, J.M., et al., *Controlling size, shape and homogeneity of embryoid bodies using poly (ethylene glycol) microwells.* Lab on a Chip, 2007. **7**(6): p. 786-794.

105. Wegrzyn, T.F., M. Golding, and R.H. Archer, *Food Layered Manufacture: A new process for constructing solid foods.* Trends in Food Science & Technology, 2012. **27**(2): p. 66-72.

106. Panesar, A., et al., *Design Framework for Multifunctional Additive Manufacturing: Placement and Routing of Three-Dimensional Printed Circuit Volumes.* Journal of Mechanical Design, 2015. **137**(11): p. 111708-111708.

107. Krola, T.A., M.F. Zaehb, and C. Seidela, *Optimization of supports in metal-based additive manufacturing by means of finite element models*, in *Proceedings of the Solid Freeform Fabrication Symposium.* 2012: Houston, Texas.

108. Ahsan, A.N., R. Xie, and B. Khoda, *Direct Bio-printing with Heterogeneous Topology Design.* Procedia manufacturing, 2017. **10**: p. 945-956.

109. Khoda, A., I.T. Ozbolat, and B. Koc, *Modeling of variational gradient porous architecture with multi-directional filament deposition in 3D scaffolds.* Computer-Aided Design and Applications, 2013. **10**(3): p. 445-459.

110. Endres, M., et al., *Osteogenic induction of human bone marrow-derived mesenchymal progenitor cells in novel synthetic polymer–hydrogel matrices.* Tissue engineering, 2003. **9**(4): p. 689-702.

111. Jeong, C.G. and S.J. Hollister, *A comparison of the influence of material on in vitro cartilage tissue engineering with PCL, PGS, and POC 3D scaffold architecture seeded with chondrocytes.* Biomaterials, 2010. **31**(15): p. 4304-4312.

112. Bartnikowski, M., et al., *Effects of scaffold architecture on mechanical characteristics and osteoblast response to static and perfusion bioreactor cultures.* Biotechnology and bioengineering, 2014. **111**(7): p. 1440-1451.

113. Stukel, J., et al., *Polyethlyene glycol microgels to deliver bioactive nerve growth factor.* Journal of Biomedical Materials Research Part A, 2015. **103**(2): p. 604-613.

114. Carvalho, C., R. Landers, and R. Muelhaupt, *Soft and hard implant fabrication using 3D-BioplottingTM.* 2004.

115. Choi, N.S. and J. Heller, *Drug delivery devices manufactured from poly (orthoesters) and poly (orthocarbonates)*. 1978, Google Patents.

116. Okada, M., *Chemical syntheses of biodegradable polymers.* Progress in polymer science, 2002. **27**(1): p. 87-133.

117. Farng, E. and O. Sherman, *Meniscal repair devices: a clinical and biomechanical literature review.* Arthroscopy: The Journal of Arthroscopic & Related Surgery, 2004. **20**(3): p. 273-286.

118. Choueka, J., et al., *Canine bone response to tyrosine-derived polycarbonates and poly (L-lactic acid).* Journal of Biomedical Materials Research: An Official Journal of The Society for Biomaterials and The Japanese Society for Biomaterials, 1996. **31**(1): p. 35-41.

119. Kim, J., et al., *Tyrosine-derived polycarbonate scaffolds for bone regeneration in a rabbit radius critical-size defect model.* Biomedical materials, 2015. **10**(3): p. 035001.

120. Cortizo, M.S., M.S. Molinuevo, and A.M. Cortizo, *Biocompatibility and biodegradation of polyester and polyfumarate based-scaffolds for bone tissue engineering.* Journal of tissue engineering and regenerative medicine, 2008. **2**(1): p. 33-42.

121. Lu, Y. and S. Chen, *Micro and nano-fabrication of biodegradable polymers for drug delivery.* Advanced drug delivery reviews, 2004. **56**(11): p. 1621-1633.

122. Kim, T.K., et al., *Gas foamed open porous biodegradable polymeric microspheres.* Biomaterials, 2006. **27**(2): p. 152-159.

123. Borden, M., et al., *Tissue engineered microsphere-based matrices for bone repair:: design and evaluation.* Biomaterials, 2002. **23**(2): p. 551-559.

124. Ueda, H. and Y. Tabata, *Polyhydroxyalkanonate derivatives in current clinical applications and trials.* Advanced drug delivery reviews, 2003. **55**(4): p. 501-518.

125. Schuurman, W., et al., *Bioprinting of hybrid tissue constructs with tailorable mechanical properties.* Biofabrication, 2011. **3**(2): p. 021001.

126. Bakarich, S.E., et al., *Three-dimensional printing fiber reinforced hydrogel composites.* ACS applied materials & interfaces, 2014. **6**(18): p. 15998-16006.

127. Woodfield, T.B., et al., *Design of porous scaffolds for cartilage tissue engineering using a three-dimensional fiber-deposition technique.* Biomaterials, 2004. **25**(18): p. 4149-4161.

128. Xu, W., et al., *A polyurethane-gelatin hybrid construct for manufacturing implantable bioartificial livers.* Journal of Bioactive and Compatible Polymers, 2008. **23**(5): p. 409-422.

129. Moroni, L., J. De Wijn, and C. Van Blitterswijk, *Three-dimensional fiber-deposited PEOT/PBT copolymer scaffolds for tissue engineering: Influence of porosity, molecular network mesh size, and swelling in aqueous media on dynamic mechanical properties.* Journal of biomedical materials research Part A, 2005. **75**(4): p. 957-965.

130. Schagemann, J., et al., *Poly-ϵ-caprolactone/gel hybrid scaffolds for cartilage tissue engineering.* Journal of biomedical materials research Part A, 2010. **93**(2): p. 454-463.

131. Jang, C.H., et al., *Effect of umbilical cord serum coated 3D PCL/alginate scaffold for mastoid obliteration.* International journal of pediatric otorhinolaryngology, 2014. **78**(7): p. 1061-1065.

132. Yao, Q., et al., *Design, construction and mechanical testing of digital 3D anatomical data-based PCL–HA bone tissue engineering scaffold.* Journal of Materials Science: Materials in Medicine, 2015. **26**(1): p. 1-9.

133.   Han, L.-H., et al., *Fabrication of three-dimensional scaffolds for heterogeneous tissue engineering.* Biomedical microdevices, 2010. **12**(4): p. 721-725.

134.   Domingues, R.M., et al., *Enhancing the biomechanical performance of anisotropic nanofibrous scaffolds in tendon tissue engineering: reinforcement with cellulose nanocrystals.* Advanced healthcare materials, 2016. **5**(11): p. 1364-1375.

135.   Liu, Q., et al., *Preparation and Properties of 3D Printed Alginate–Chitosan Polyion Complex Hydrogels for Tissue Engineering.* Polymers, 2018. **10**(6): p. 664.

136.   Demirtaş, T.T., G. Irmak, and M. Gümüşderelioğlu, *A bioprintable form of chitosan hydrogel for bone tissue engineering.* Biofabrication, 2017. **9**(3): p. 035003.

137.   Emami, Z., et al., *Controlling alginate oxidation conditions for making alginate-gelatin hydrogels.* Carbohydrate polymers, 2018. **198**: p. 509-517.

138.   Luo, Y., et al., *3D printing of concentrated alginate/gelatin scaffolds with homogeneous nano apatite coating for bone tissue engineering.* Materials & Design, 2018. **146**: p. 12-19.

139.   Chang, R., J. Nam, and W. Sun, *Direct cell writing of 3D microorgan for in vitro pharmacokinetic model.* Tissue Engineering Part C: Methods, 2008. **14**(2): p. 157-166.

140.   Kulseng, B., et al., *TRANSPLANTATION OF ALGINATE MICROCAPSULES: Generation of Antibodies Against Alginates and Encapsulated Porcine Islet-Like Cell Clusters1.* Transplantation, 1999. **67**(7): p. 978-984.

141.   Kong, H.J., et al., *Controlling rigidity and degradation of alginate hydrogels via molecular weight distribution.* Biomacromolecules, 2004. **5**(5): p. 1720-1727.

142.   Boontheekul, T., H.-J. Kong, and D.J. Mooney, *Controlling alginate gel degradation utilizing partial oxidation and bimodal molecular weight distribution.* Biomaterials, 2005. **26**(15): p. 2455-2465.

143.   Cohen, D.L., et al., *Direct freeform fabrication of seeded hydrogels in arbitrary geometries.* Tissue engineering, 2006. **12**(5): p. 1325-1335.

144.   Daly, A.C., et al., *A comparison of different bioinks for 3D bioprinting of fibrocartilage and hyaline cartilage.* Biofabrication, 2016. **8**(4): p. 045002.

145.   Billiet, T., et al., *The 3D printing of gelatin methacrylamide cell-laden tissue-engineered constructs with high cell viability.* Biomaterials, 2014. **35**(1): p. 49-62.

146.   Zhang, T., et al., *Three-dimensional gelatin and gelatin/hyaluronan hydrogel structures for traumatic brain injury.* Journal of bioactive and compatible polymers, 2007. **22**(1): p. 19-29.

147.   Lee, V.K., et al., *Creating perfused functional vascular channels using 3D bio-printing technology.* Biomaterials, 2014. **35**(28): p. 8092-8102.

148.   Zhang, B., et al., *High-resolution 3D bioprinting system for fabricating cell-laden hydrogel scaffolds with high cellular activities.* Procedia Cirp, 2017. **65**: p. 219-224.

149.   Li, Z., et al., *Tuning alginate-gelatin bioink properties by varying solvent and their impact on stem cell behavior.* Scientific reports, 2018. **8**(1): p. 8020.

150.   You, F., X. Wu, and X. Chen, *3D printing of porous alginate/gelatin hydrogel scaffolds and their mechanical property characterization.* International Journal of Polymeric Materials and Polymeric Biomaterials, 2017. **66**(6): p. 299-306.

151.   Daly, A.C., et al., *3D bioprinting of developmentally inspired templates for whole bone organ engineering.* Advanced healthcare materials, 2016. **5**(18): p. 2353-2362.

152.   Markstedt, K., et al., *3D bioprinting human chondrocytes with nanocellulose–alginate bioink for cartilage tissue engineering applications.* Biomacromolecules, 2015. **16**(5): p. 1489-1496.

153.   Kundu, J., et al., *An additive manufacturing-based PCL–alginate–chondrocyte bioprinted scaffold for cartilage tissue engineering.* Journal of tissue engineering and regenerative medicine, 2015. **9**(11): p. 1286-1297.

154.   Jia, J., et al., *Engineering alginate as bioink for bioprinting.* Acta biomaterialia, 2014. **10**(10): p. 4323-4331.

155.   Schütz, K., et al., *Three-dimensional plotting of a cell-laden alginate/methylcellulose blend: towards biofabrication of tissue engineering constructs with clinically relevant dimensions.* Journal of tissue engineering and regenerative medicine, 2017. **11**(5): p. 1574-1587.

156.   Zhao, Y., et al., *Three-dimensional printing of Hela cells for cervical tumor model in vitro.* Biofabrication, 2014. **6**(3): p. 035001.

157.   Jang, C.H., et al., *A MSCs-laden polycaprolactone/collagen scaffold for bone tissue regeneration.* RSC Advances, 2016. **6**(8): p. 6259-6265.

158.   Izadifar, Z., et al., *Analyzing biological performance of 3D-printed, cell-impregnated hybrid constructs for cartilage tissue engineering.* Tissue Engineering Part C: Methods, 2015. **22**(3): p. 173-188.

159.   Fedorovich, N.E., et al., *Three-dimensional fiber deposition of cell-laden, viable, patterned constructs for bone tissue printing.* Tissue Engineering Part A, 2008. **14**(1): p. 127-133.

160.   Xu, W., et al., *Rapid prototyping three-dimensional cell/gelatin/fibrinogen constructs for medical regeneration.* Journal of Bioactive and Compatible Polymers, 2007. **22**(4): p. 363-377.

161.   Xavier, J.R., et al., *Bioactive nanoengineered hydrogels for bone tissue engineering: a growth-factor-free approach.* ACS nano, 2015. **9**(3): p. 3109-3118.

162.   Kang, H.-W., et al., *A 3D bioprinting system to produce human-scale tissue constructs with structural integrity.* Nature biotechnology, 2016. **34**(3): p. 312-319.

163.   Wüst, S., et al., *Tunable hydrogel composite with two-step processing in combination with innovative hardware upgrade for cell-based three-dimensional bioprinting.* Acta biomaterialia, 2014. **10**(2): p. 630-640.

164.   Grigore, A., et al., *Behavior of encapsulated MG-63 cells in RGD and gelatine-modified alginate hydrogels.* Tissue Engineering Part A, 2014. **20**(15-16): p. 2140-2150.

165.   Schuurman, W., et al., *Gelatin-methacrylamide hydrogels as potential biomaterials for fabrication of tissue-engineered cartilage constructs.* Macromolecular bioscience, 2013. **13**(5): p. 551-561.

166.   Wang, X., et al., *Tumor-like lung cancer model based on 3D bioprinting.* 3 Biotech, 2018. **8**(12): p. 501.

167.   Hong, Y., et al., *Covalently crosslinked chitosan hydrogel: properties of in vitro degradation and chondrocyte encapsulation.* Acta biomaterialia, 2007. **3**(1): p. 23-31.

168.   Yan, Y., et al., *Fabrication of viable tissue-engineered constructs with 3D cell-assembly technique.* Biomaterials, 2005. **26**(29): p. 5864-5871.

169.   Seidel, J., et al., *Green bioprinting: extrusion-based fabrication of plant cell-laden biopolymer hydrogel scaffolds.* Biofabrication, 2017. **9**(4): p. 045011.

170. Kesti, M., et al., *A versatile bioink for three-dimensional printing of cellular scaffolds based on thermally and photo-triggered tandem gelation.* Acta biomaterialia, 2015. **11**: p. 162-172.

171. Duan, B., et al., *Three-dimensional printed trileaflet valve conduits using biological hydrogels and human valve interstitial cells.* Acta biomaterialia, 2014. **10**(5): p. 1836-1846.

172. Xu, T., et al., *Hybrid printing of mechanically and biologically improved constructs for cartilage tissue engineering applications.* Biofabrication, 2012. **5**(1): p. 015001.

173. Atala, A., F.K. Kasper, and A.G. Mikos, *Engineering complex tissues.* Science translational medicine, 2012. **4**(160): p. 160rv12-160rv12.

174. Shim, J.-H., et al., *Bioprinting of a mechanically enhanced three-dimensional dual cell-laden construct for osteochondral tissue engineering using a multi-head tissue/organ building system.* Journal of Micromechanics and Microengineering, 2012. **22**(8): p. 085014.

175. Müller, M., et al., *Alginate sulfate–nanocellulose bioinks for cartilage bioprinting applications.* Annals of biomedical engineering, 2017. **45**(1): p. 210-223.

176. Nakamura, M., et al., *Biomatrices and biomaterials for future developments of bioprinting and biofabrication.* Biofabrication, 2010. **2**(1): p. 014110.

177. Faulkner-Jones, A., et al., *Bioprinting of human pluripotent stem cells and their directed differentiation into hepatocyte-like cells for the generation of mini-livers in 3D.* Biofabrication, 2015. **7**(4): p. 044102.

178. Hinton, T.J., et al., *Three-dimensional printing of complex biological structures by freeform reversible embedding of suspended hydrogels.* Science advances, 2015. **1**(9): p. e1500758.

179. Rutz, A.L., et al., *A multimaterial bioink method for 3D printing tunable, cell-compatible hydrogels.* Advanced Materials, 2015. **27**(9): p. 1607-1614.

180. Schloßmacher, U., et al., *Alginate/silica composite hydrogel as a potential morphogenetically active scaffold for three-dimensional tissue engineering.* RSC Advances, 2013. **3**(28): p. 11185-11194.

181. Zhang, Y.S., et al., *Bioprinting 3D microfibrous scaffolds for engineering endothelialized myocardium and heart-on-a-chip.* Biomaterials, 2016. **110**: p. 45-59.

182. Shanjani, Y., et al., *A novel bioprinting method and system for forming hybrid tissue engineering constructs.* Biofabrication, 2015. **7**(4): p. 045008.

183. Kang, H.-W., et al., *A 3D bioprinting system to produce human-scale tissue constructs with structural integrity.* Nature biotechnology, 2016. **34**(3): p. 312.

184. Bhattacharjee, T., et al., *Writing in the granular gel medium.* Science advances, 2015. **1**(8): p. e1500655.

185. Kyle, S., et al., *'Printability'of Candidate Biomaterials for Extrusion Based 3D Printing: State-of-the-Art.* Advanced healthcare materials, 2017. **6**(16): p. 1700264.

186. Jungst, T., et al., *Strategies and molecular design criteria for 3D printable hydrogels.* Chemical reviews, 2015. **116**(3): p. 1496-1539.

187. Mouser, V.H., et al., *Yield stress determines bioprintability of hydrogels based on gelatin-methacryloyl and gellan gum for cartilage bioprinting.* Biofabrication, 2016. **8**(3): p. 035003.

188. Paxton, N.C., et al., *Proposal to Assess Printability of Bioinks for Extrusion-Based Bioprinting and Evaluation of Rheological Properties Governing Bioprintability.* Biofabrication, 2017.

189. M'barki, A., L. Bocquet, and A. Stevenson, *Linking Rheology and Printability for Dense and Strong Ceramics by Direct Ink Writing.* Scientific Reports, 2017. **7**(1): p. 6017.

190. Han, Y. and L. Wang, *Sodium alginate/carboxymethyl cellulose films containing pyrogallic acid: physical and antibacterial properties.* Journal of the Science of Food and Agriculture, 2017. **97**(4): p. 1295-1301.

191. Kim, Y.B., et al., *Mechanically reinforced cell-laden scaffolds formed using alginate-based bioink printed onto the surface of a PCL/alginate mesh structure for regeneration of hard tissue.* Journal of colloid and interface science, 2016. **461**: p. 359-368.

192. Masruchin, N., et al., *Characteristics of TEMPO-oxidized cellulose fibril-based hydrogels induced by cationic ions and their properties.* Cellulose, 2015. **22**(3): p. 1993-2010.

193. Maji, K., et al., *Preparation and evaluation of gelatin-chitosan-nanobioglass 3D porous scaffold for bone tissue engineering.* International journal of biomaterials, 2016. **2016**.

194. Kiyotake, E.A., et al., *Development and quantitative characterization of the precursor rheology of hyaluronic acid hydrogels for bioprinting.* Acta biomaterialia, 2019.

195. Diamantides, N., et al., *Correlating rheological properties and printability of collagen bioinks: the effects of riboflavin photocrosslinking and pH.* Biofabrication, 2017. **9**(3): p. 034102.

196. Jang, J., et al., *Tailoring mechanical properties of decellularized extracellular matrix bioink by vitamin B2-induced photo-crosslinking.* Acta biomaterialia, 2016. **33**: p. 88-95.

197. Lee, D.-Y., et al., *Phage as versatile nanoink for printing 3-D cell-laden scaffolds.* Acta biomaterialia, 2016. **29**: p. 112-124.

198. Wilson, S.A., et al., *Shear-thinning and thermo-reversible nanoengineered inks for 3D bioprinting.* ACS applied materials & interfaces, 2017. **9**(50): p. 43449-43458.

199. Law, N., et al., *Characterisation of hyaluronic acid methylcellulose hydrogels for 3D bioprinting.* Journal of the mechanical behavior of biomedical materials, 2018. **77**: p. 389-399.

200. Datta, P., B. Ayan, and I.T. Ozbolat, *Bioprinting for Vascular and Vascularized Tissue Biofabrication.* Acta Biomaterialia, 2017.

201. Kolesky, D.B., et al., *3D bioprinting of vascularized, heterogeneous cell-laden tissue constructs.* Advanced materials, 2014. **26**(19): p. 3124-3130.

202. Colosi, C., et al., *Microfluidic Bioprinting of Heterogeneous 3D Tissue Constructs Using Low-Viscosity Bioink.* Advanced Materials, 2016. **28**(4): p. 677-684.

203. Gao, Q., et al., *Coaxial nozzle-assisted 3D bioprinting with built-in microchannels for nutrients delivery.* Biomaterials, 2015. **61**: p. 203-215.

204. Pati, F., et al., *Extrusion bioprinting*, in *Essentials of 3D biofabrication and translation.* 2015, Elsevier. p. 123-152.

205. *Crump SS, Inventor Stratasys Inc., Minneapolis, MN, assignee. Apparatus and method for creating three-dimensional objects. US patent US 5,121,329. 1992.*

206. Ahsan, A.N., R. Xie, and B. Khoda, *Direct Bio-printing with Heterogeneous Topology Design.* 2017, Procedia Manufacturing (In-press).

207. Alexander P, A.S., Dutta D, *Part orientation and build cost determination in layered manufacturing.* . 1998: Computer-Aided Design, 30(5) p. 343–56.

208. Byun, H.-S. and K.H. Lee, *Determination of the optimal build direction for different rapid prototyping processes using multi-criterion decision making.* Robotics and Computer-Integrated Manufacturing, 2006. **22**(1): p. 69-80.

209. Frank, D. and G. Fadel, *Expert system-based selection of the preferred direction of build for rapid prototyping processes.* Journal of Intelligent Manufacturing, 1995. **6**(5): p. 339-345.

210. Pham, D., S. Dimov, and R. Gault, *Part orientation in stereolithography.* The International Journal of Advanced Manufacturing Technology, 1999. **15**(9): p. 674-682.

211. Thrimurthulu, K., P.M. Pandey, and N.V. Reddy, *Optimum part deposition orientation in fused deposition modeling.* International Journal of Machine Tools and Manufacture, 2004. **44**(6): p. 585-594.

212. Hildebrand, K., B. Bickel, and M. Alexa, *Orthogonal slicing for additive manufacturing.* Computers & Graphics, 2013. **37**(6): p. 669-675.

213. Smith, T.S., et al., *Optimal slicing of free-form surfaces.* Computer Aided Geometric Design, 2002. **19**(1): p. 43-64.

214. Habib, A. and B. Khoda, *Attribute driven process architecture for additive manufacturing.* 2016: Robotics and Computer Integrated Manufacturing (In-press).

215. Habib, A., N. Ahsan, and B. Khoda, *Optimizing Material Deposition Direction for Functional Internal Architecture in Additive Manufacturing Processes.* Procedia Manufacturing, 2015. **1**: p. 378-392.

216. DING, D.-H., et al., *Process Planning Strategy for Wire and Arc Additive Manufacturing.*

217. Han, W., et al., *Tool path-based deposition planning in fused deposition processes.* Journal of manufacturing science and engineering, 2002. **124**(2): p. 462-472.

218. Muller, P., J.-Y. Hascoet, and P. Mognol, *Toolpaths for additive manufacturing of functionally graded materials (FGM) parts.* Rapid Prototyping Journal, 2014. **20**(6): p. 511-522.

219. Choi, K.-H., et al. *Study on Path Generation and Control based on Dual Laser in Solid Freefrom Fabrication System.* in *SICE-ICASE, 2006. International Joint Conference.* 2006. IEEE.

220. Ahsan, A.M.M.N., M.A. Habib, and B. Khoda, *Resource based process planning for additive manufacturing.* Computer-Aided Design, 2015. **69**: p. 112-125.

221. Es-Said, O.S., et al., *Effect of Layer Orientation on Mechanical Properties of Rapid Prototyped Samples.* Materials and Manufacturing Processes, 2000. **15**(1): p. 107-122.

222. Khoda, A.K.M.B. and B. Koc, *Functionally heterogeneous porous scaffold design for tissue engineering.* Computer-Aided Design, 2013. **45**(11): p. 1276-1293.

223. Khoda, A.K.M., I.T. Ozbolat, and B. Koc, *Designing heterogeneous porous tissue scaffolds for additive manufacturing processes.* Computer-Aided Design, 2013. **45**(12): p. 1507-1523.

224. Jin, G.Q., et al., *A hybrid and adaptive tool-path generation approach of rapid prototyping and manufacturing for biomedical models.* Computers in industry, 2013. **64**(3): p. 336-349.

225. Jacob, G.G., C.C. Kai, and T. Mei, *Development of a new rapid prototyping interface.* Computers in Industry, 1999. **39**(1): p. 61-70.

226. Jamieson, R. and H. Hacker, *Direct slicing of CAD models for rapid prototyping.* Rapid Prototyping Journal, 1995. **1**(2): p. 4-12.

227. Bøhn, J.H. and M.J. Wozny. *Automatic CAD-model repair: shell-closure*. in *Proc. Symp. on Solid Freeform Fabrication*. 1992.

228. Makela, I. and A. Dolenc. *Some efficient procedures for correcting triangulated models*. in *Solid Freeform Fabrication Symposium Proceedings*. 1993. DTIC Document.

229. Kumar, V. and D. Dutta, *An assessment of data formats for layered manufacturing.* Advances in Engineering Software, 1997. **28**(3): p. 151-164.

230. Chua, C.K. and K.F. Leong, *Rapid prototyping: principles and applications*. Vol. 1. 2003: World Scientific.

231. ASTM, *Standard Specification for Additive Manufacturing File Format (AMF)*, in *ISO/ASTM 52915: 2013(E) V 1.1*. 2013, ASTM International: PA.

232. ASTM, A., *F2915-13 Standard Specification for Additive Manufacturing File Format (AMF) Version 1.1, ASTM International*. 2014.

233. Hardwick, M., *On STEP-NC and the complexities of product data integration.* Journal of Computing and Information Science in Engineering, 2004. **4**(1): p. 60-67.

234. Zhou*, M., *STEP-based approach for direct slicing of CAD models for layered manufacturing.* International journal of production research, 2005. **43**(15): p. 3273-3285.

235. *http://3mf.io/what-is-3mf/*.

236. de Figueiredo Leite, J.V., J.M.X.N. Teixeira, and V. Teichrieb. *Optimizing 3D Object Visualization on the Web*. in *International Conference on Virtual, Augmented and Mixed Reality*. 2016. Springer.

237. Nassar, A. and E. Reutzel. *A proposed digital thread for additive manufacturing*. in *Solid Freeform Fabrication Symposium Proceedings, University of Texas, Austin, TX*. 2013.

238. Hiller, J.D. and H. Lipson. *STL 2.0: a proposal for a universal multi-material Additive Manufacturing File format*. in *Solid Freeform Fabrication Symposium, Austin, TX, Aug*. 2009. Citeseer.

239. Habib, A. and B. Khoda, *Hierarchical Scanning Data Structure for Additive Manufacturing*. 2017: 45th North American Manufacturing Research Conference (in-press).

240. Wu, D., D.W. Rosen, and D. Schaefer, *Cloud-based design and manufacturing: status and promise*, in *Cloud-Based Design and Manufacturing (CBDM)*. 2014, Springer. p. 1-24.

241. Habib, M.A. and B. Khoda, *Attribute driven process architecture for additive manufacturing.* Robotics and Computer-Integrated Manufacturing, 2017. **44**: p. 253-265.

242. Gasperini, L., J.F. Mano, and R.L. Reis, *Natural polymers for the microencapsulation of cells.* Journal of the royal society Interface, 2014. **11**(100): p. 20140817.

243. Hunt, N.C., et al., *Calcium-alginate hydrogel-encapsulated fibroblasts provide sustained release of vascular endothelial growth factor.* Tissue engineering Part A, 2012. **19**(7-8): p. 905-914.

244. Sapir, Y., et al., *The promotion of in vitro vessel-like organization of endothelial cells in magnetically responsive alginate scaffolds.* Biomaterials, 2012. **33**(16): p. 4100-4109.

245. Mosahebi, A., et al., *A novel use of alginate hydrogel as Schwann cell matrix.* Tissue engineering, 2001. **7**(5): p. 525-534.

246. Hunt, N., et al., *Encapsulation of fibroblasts causes accelerated alginate hydrogel degradation.* Acta Biomaterialia, 2010. **6**(9): p. 3649-3656.

247. Garrett, Q., et al., *Carboxymethylcellulose binds to human corneal epithelial cells and is a modulator of corneal epithelial wound healing.* Investigative ophthalmology & visual science, 2007. **48**(4): p. 1559-1567.

248. Kim, M.S., et al., *Ionically crosslinked alginate–carboxymethyl cellulose beads for the delivery of protein therapeutics.* Applied Surface Science, 2012. **262**: p. 28-33.

249. Agarwal, T., et al., *Calcium alginate-carboxymethyl cellulose beads for colon-targeted drug delivery.* International journal of biological macromolecules, 2015. **75**: p. 409-417.

250. Tongdeesoontorn, W., et al., *Effect of carboxymethyl cellulose concentration on physical properties of biodegradable cassava starch-based films.* Chemistry Central Journal, 2011. **5**(1): p. 6.

251. You, F., et al., *3D printing of porous cell-laden hydrogel constructs for potential applications in cartilage tissue engineering.* ACS Biomaterials Science & Engineering, 2016. **2**(7): p. 1200-1210.

252. Therriault, D., S.R. White, and J.A. Lewis, *Rheological behavior of fugitive organic inks for direct-write assembly.* Applied Rheology, 2007. **17**(1): p. 10112-11411.

253. Shao, Y., et al., *Use of microfibrillated cellulose/lignosulfonate blends as carbon precursors: Impact of hydrogel rheology on 3D printing.* Industrial & Engineering Chemistry Research, 2015. **54**(43): p. 10575-10582.

254. Costakis Jr, W.J., et al., *Additive manufacturing of boron carbide via continuous filament direct ink writing of aqueous ceramic suspensions.* Journal of the European Ceramic Society, 2016. **36**(14): p. 3249-3256.

255. Leong, M.F., et al., *Patterned prevascularised tissue constructs by assembly of polyelectrolyte hydrogel fibres.* Nature communications, 2013. **4**: p. 2353.

256. Annabi, N., et al., *25th anniversary article: Rational design and applications of hydrogels in regenerative medicine.* Advanced materials, 2014. **26**(1): p. 85-124.

257. Li, Y.-C., et al., *4D bioprinting: the next-generation technology for biofabrication enabled by stimuli-responsive materials.* Biofabrication, 2016. **9**(1): p. 012001.

258. Aharoni, H., E. Sharon, and R. Kupferman, *Geometry of thin nematic elastomer sheets.* Physical review letters, 2014. **113**(25): p. 257801.

259. Gladman, A.S., et al., *Biomimetic 4D printing.* Nature materials, 2016. **15**(4): p. 413-418.

260. Varma, R.S., *Clay and clay-supported reagents in organic synthesis.* Tetrahedron, 2002. **58**(7): p. 1235-1255.

261. Wang, C., et al., *Preparation of laponite bioceramics for potential bone tissue engineering applications.* PloS one, 2014. **9**(6): p. e99585.

262. Tao, L., et al., *In vitro and in vivo studies of a gelatin/carboxymethyl chitosan/LAPONITE® composite scaffold for bone tissue engineering.* RSC Advances, 2017. **7**(85): p. 54100-54110.

263. Demir, A.K., A.E. Elçin, and Y.M. Elçin, *Strontium-modified chitosan/montmorillonite composites as bone tissue engineering scaffold.* Materials Science and Engineering: C, 2018. **89**: p. 8-14.

264. Haroun, A.A., A. Gamal-Eldeen, and D.R. Harding, *Preparation, characterization and in vitro biological study of biomimetic three-dimensional gelatin–montmorillonite/cellulose scaffold for tissue engineering.* Journal of Materials Science: Materials in Medicine, 2009. **20**(12): p. 2527-2540.

265. Itadani, A., et al., *Al-pillared montmorillonite clay minerals: Low-pressure CO adsorption at room temperature.* Journal of colloid and interface science, 2007. **313**(2): p. 747-750.

266. Adzmi, F., et al., *Preparation, characterisation and viability of encapsulated Trichoderma harzianum UPM40 in alginate-montmorillonite clay.* Journal of microencapsulation, 2012. **29**(3): p. 205-210.

267. Kevadiya, B., et al., *Montmorillonite-alginate composites as a drug delivery system: Intercalation and In vitro release of diclofenac sodium.* Indian journal of pharmaceutical sciences, 2010. **72**(6): p. 732.

268. Iliescu, R.I., et al., *Montmorillonite–alginate nanocomposite as a drug delivery system– incorporation and in vitro release of irinotecan.* International journal of pharmaceutics, 2014. **463**(2): p. 184-192.

269. Gaharwar, A.K., N.A. Peppas, and A. Khademhosseini, *Nanocomposite hydrogels for biomedical applications.* Biotechnology and bioengineering, 2014. **111**(3): p. 441-453.

270. Klemm, D., et al., *Nanocelluloses: a new family of nature-based materials.* Angewandte Chemie International Edition, 2011. **50**(24): p. 5438-5466.

271. Charreau, H., M. L Foresti, and A. Vázquez, *Nanocellulose patents trends: a comprehensive review on patents on cellulose nanocrystals, microfibrillated and bacterial cellulose.* Recent patents on nanotechnology, 2013. **7**(1): p. 56-80.

272. Moon, R.J., et al., *Cellulose nanomaterials review: structure, properties and nanocomposites.* Chemical Society Reviews, 2011. **40**(7): p. 3941-3994.

273. Sehaqui, H., et al., *Wood cellulose biocomposites with fibrous structures at micro-and nanoscale.* Composites Science and Technology, 2011. **71**(3): p. 382-387.

274. De France, K.J., T. Hoare, and E.D. Cranston, *Review of hydrogels and aerogels containing nanocellulose.* Chemistry of Materials, 2017. **29**(11): p. 4609-4631.

275. Fukuzumi, H., et al., *Dispersion stability and aggregation behavior of TEMPO-oxidized cellulose nanofibrils in water as a function of salt addition.* Cellulose, 2014. **21**(3): p. 1553-1559.

276. Abe, K. and H. Yano, *Cellulose nanofiber-based hydrogels with high mechanical strength.* Cellulose, 2012. **19**(6): p. 1907-1912.

277. Roman, M., *Toxicity of cellulose nanocrystals: a review.* Industrial Biotechnology, 2015. **11**(1): p. 25-33.

278. Siró, I. and D. Plackett, *Microfibrillated cellulose and new nanocomposite materials: a review.* Cellulose, 2010. **17**(3): p. 459-494.

279. Håkansson, K.M., et al., *Solidification of 3D printed nanofibril hydrogels into functional 3D cellulose structures.* Advanced Materials Technologies, 2016. **1**(7): p. 1600096.

280. Bhattacharya, M., et al., *Nanofibrillar cellulose hydrogel promotes three-dimensional liver cell culture.* Journal of controlled release, 2012. **164**(3): p. 291-298.

281. Lou, Y.-R., et al., *The use of nanofibrillar cellulose hydrogel as a flexible three- dimensional model to culture human pluripotent stem cells.* Stem cells and development, 2013. **23**(4): p. 380-392.

282. Ávila, H.M., et al., *3D bioprinting of human chondrocyte-laden nanocellulose hydrogels for patient-specific auricular cartilage regeneration.* Bioprinting, 2016. **1**: p. 22-35.

283. Nguyen, D., et al., *Cartilage tissue engineering by the 3D bioprinting of iPS cells in a nanocellulose/alginate bioink.* Scientific reports, 2017. **7**(1): p. 658.

284. Laurén, P., et al., *Nanofibrillar cellulose-alginate hydrogel coated surgical sutures as cell-carrier systems.* PloS one, 2017. **12**(8): p. e0183487.

285. Li, V.C., et al., *Direct Ink Write 3D Printed Cellulose Nanofiber Aerogel Structures with Highly Deformable, Shape Recoverable, and Functionalizable Properties.* ACS Sustainable Chemistry & Engineering, 2018. **6**(2): p. 2011-2022.

286. Saito, T., et al., *Homogeneous suspensions of individualized microfibrils from TEMPO-catalyzed oxidation of native cellulose.* Biomacromolecules, 2006. **7**(6): p. 1687-1691.

287. Saito, T., et al., *Cellulose nanofibers prepared by TEMPO-mediated oxidation of native cellulose.* Biomacromolecules, 2007. **8**(8): p. 2485-2491.

288. Missoum, K., M.N. Belgacem, and J. Bras, *Nanofibrillated cellulose surface modification: a review.* Materials, 2013. **6**(5): p. 1745-1766.

289. Saito, T. and A. Isogai, *TEMPO-mediated oxidation of native cellulose. The effect of oxidation conditions on chemical and crystal structures of the water-insoluble fractions.* Biomacromolecules, 2004. **5**(5): p. 1983-1989.

290. Dong, H., et al., *Cation-induced hydrogels of cellulose nanofibrils with tunable moduli.* Biomacromolecules, 2013. **14**(9): p. 3338-3345.

291. Shimotoyodome, A., et al., *Regulation of postprandial blood metabolic variables by TEMPO-oxidized cellulose nanofibers.* Biomacromolecules, 2011. **12**(10): p. 3812-3818.

292. Rees, A., et al., *3D bioprinting of carboxymethylated-periodate oxidized nanocellulose constructs for wound dressing applications.* BioMed research international, 2015. **2015**.

293. Hua, K., et al., *Surface chemistry of nanocellulose fibers directs monocyte/macrophage response.* Biomacromolecules, 2015. **16**(9): p. 2787-2795.

294. Tijore, A., et al., *Bioprinted gelatin hydrogel platform promotes smooth muscle cell contractile phenotype maintenance.* Biomedical microdevices, 2018. **20**(2): p. 32.

295. Shadrin, I.Y., et al., *Cardiopatch platform enables maturation and scale-up of human pluripotent stem cell-derived engineered heart tissues.* Nature communications, 2017. **8**(1): p. 1825.

296. Jackman, C.P., et al., *Engineered cardiac tissue patch maintains structural and electrical properties after epicardial implantation.* Biomaterials, 2018. **159**: p. 48-58.

297. Baker, B.M. and R.L. Mauck, *The effect of nanofiber alignment on the maturation of engineered meniscus constructs.* Biomaterials, 2007. **28**(11): p. 1967-1977.

298. Compton, B.G. and J.A. Lewis, *3D-printing of lightweight cellular composites.* Advanced materials, 2014. **26**(34): p. 5930-5935.

299. Zhong, W., et al., *Short fiber reinforced composites for fused deposition modeling.* Materials Science and Engineering: A, 2001. **301**(2): p. 125-130.

300. Lee, H., et al., *Direct alignment and patterning of silver nanowires by electrohydrodynamic jet printing.* Small, 2014. **10**(19): p. 3918-3922.

301. Yunus, D.E., et al., *Shear induced alignment of short nanofibers in 3D printed polymer composites.* Nanotechnology, 2016. **27**(49): p. 495302.

302. Yunus, D.E., et al., *Short fiber reinforced 3d printed ceramic composite with shear induced alignment.* Ceramics International, 2017. **43**(15): p. 11766-11772.

303. Fung, C.-P., J.-R. Hwang, and C.-C. Hsu, *The effect of injection molding process parameters on the tensile properties of short glass fiber-reinforced PBT.* Polymer-Plastics Technology and Engineering, 2003. **42**(1): p. 45-63.

304. Papthanasiou, T. and D.C. Guell, *Flow-induced alignment in composite materials*. 1997: Elsevier.

305. Habib, A. and B. Khoda, *Development of clay based novel hybrid bio-ink for 3D bio-printing process.* Journal of Manufacturing Processes, 2019. **38**: p. 76-87.

306. Jin, Y., et al., *Self-Supporting Nanoclay as Internal Scaffold Material for Direct Printing of Soft Hydrogel Composite Structures in Air.* ACS Applied Materials & Interfaces, 2017. **9**(20): p. 17456-17465.

307. Guo, Z., et al., *Effect of Fiber Diameter on Proliferation and Differentiation of MC3T3-E1 Pre-Osteoblasts.* Journal of Biomaterials and Tissue Engineering, 2017. **7**(2): p. 162-169.

308. Skardal, A., et al., *Substrate elasticity controls cell proliferation, surface marker expression and motile phenotype in amniotic fluid-derived stem cells.* Journal of the mechanical behavior of biomedical materials, 2013. **17**: p. 307-316.

309. Lepowsky, E., M. Muradoglu, and S. Tasoglu, *Towards preserving post-printing cell viability and improving the resolution: past, present, and future of 3D bioprinting theory.* Bioprinting, 2018: p. e00034.

310. Mittal, N., et al., *Multiscale Control of Nanocellulose Assembly: Transferring Remarkable Nanoscale Fibril Mechanics to Macroscale Fibers.* ACS nano, 2018.

311. Nunes, J., et al., *Dripping and jetting in microfluidic multiphase flows applied to particle and fibre synthesis.* Journal of physics D: Applied physics, 2013. **46**(11): p. 114002.